The ammonia, carbon dioxide and water ternary system

Christopher Howard

A dissertation submitted in partial fulfillment

of the requirements for the degree of

Doctor of Philosophy

of

University College London.

Department of Earth Sciences

University College London

March 19, 2019

I, Christopher Howard, confirm that the work presented in this thesis is my own. Where information has been derived from other sources, I confirm that this has been indicated in the work.

Abstract

Interactions between simple molecules are of fundamental interest across diverse areas of the physical sciences, and the ternary system $NH_3 + CO_2 \pm H_2O$ is no exception. In the outer solar system, interaction of CO_2 with aqueous ammonia is likely to occur, synthesising 'rock-forming' minerals, with CO_2 perhaps playing a role in ammonia-water oceans and cryomagmas inside icy planetary bodies. In the same context, ammonium carbonates may have some astrobiological relevance, since removal of water leads to the formation of urea. On Earth, combination of CO_2 with aqueous ammonia has relevance to carbon capture schemes, and there is interest in using such materials for hydrogen storage in fuel cells.

Consequently, from earthly matters of climate change to the study of extraterrestrial ices, understanding the structures and properties of ammonium carbonates are important. Despite this, our knowledge of ammonium carbonates is limited, even under ambient conditions of pressure and temperature, and is entirely absent at the higher pressures, severely limiting our ability to model the behaviour of $NH_3 + CO_2 \pm H_2O$ solids and fluids in planetary environments.

This work reports the results of several experiments using variable pressure and temperature neutron diffraction work on ammonium bicarbonate [NH_4HCO_3] and ammonium carbamate [$[NH_4]^+[NH_2CO_2]^-$], with complementary Density Functional Theory (DFT) calculations. The excellent agreement between experiments and DFT calculations obtained so far adds weight to the accuracy of calculated material properties of ammonium carbonate monohydrate [$(NH_4)_2CO_2 \cdot H_2O$], ammonium sesquicarbonate monohydrate [$(NH_4)_4(H_2(CO_3)_3) \cdot H_2O$] and several polymorphs of urea [$CO(NH_2)_2$] where little empirical data exists. These experimental and computational studies provide the structural and thermoelastic information required for accurate planetary modelling and remote identification of these material on planetary surfaces.

Impact statement

Interactions between the simplest of molecules are of fundamental interest across diverse areas of the physical sciences, as well as underpinning a number of important industrial processes, and the ternary system $NH_3 + CO_2 \pm H_2O$ is no exception. A range of computational and experimental techniques have helped to understand and characterise the behaviour of the compounds forming in this system at conditions relevant to cold planetary environments and large industrial processes.

Combination of CO_2 with aqueous ammonia has relevance to carbon capture schemes, where the so-called 'chilled ammonia process' has come to the forefront during the past decade as a low-energy alternative to capture by amines. The process traps not only carbon emissions in the solid state but also hydrogen, and there is interest in using such materials for hydrogen storage in fuel cells, since they are relatively stable and do not suffer from slow hydrogen release unlike other storage materials.

On a planetary scale, interaction of CO_2 with aqueous ammonia in the outer solar system is likely to occur; these small molecules are known to be abundant in astrophysical ices (e.g. comets) and reactions between them will produce the compounds in this ternary system. It is highly likely that ammonium carbonates are 'rock-forming' minerals in the outer solar system and that CO_2 plays a major role (as a dissolved volatile) in ammonia-water oceans and cryomagmas inside icy planetary bodies.

In the same context, ammonium carbonates may have some astrobiological relevance, since removal of water leads to urea. It is known from laboratory analogue experiments that the organic molecules produced photochemically in the atmosphere of Saturn's giant satellite Titan may be hydrolyzed in aqueous ammonia to form both urea and amino acids.

The use of neutron diffraction, using the ISIS neutron spallation source of the STFC Rutherford Appleton Laboratory, and complementary computational studies

have provided important findings that may be useful in various applications. The identification of polymorphism present in this system as a function of pressure and temperature is important to understand in various industrial applications, since each polymorph will have unique physical properties. It has also determined thermoelastic parameters of each compound, which is necessary for use in modelling these materials in planetary environments.

This work has also determined evidence of unusual mechanical properties in these materials, including negative linear expansivity and negative area expansivity, and negative linear compressibility. These unusual and rare phenomena could have a wide range of applications, such as in the design of pressure sensors, artificial muscles and actuators, and are seemingly commonplace in the compounds in this ternary system.

This work, therefore, is of importance to: planetary scientists, especially those with interests in the icy bodies of the outer solar system; industrial chemists and materials scientists working on carbon-capture, hydrogen storage materials and the hydrogen and/or ammonia energy economies; chemists and materials scientists interested in understanding hydrogen bonded systems, in particular those applying quantum-mechanical modelling.

Acknowledgements

I would like to acknowledge STFC for financial support in the form of a postgraduate studentship.

To Dr. Dominic Fortes (ISIS) and Prof. Ian Wood (UCL), I thank them both for providing me with the opportunity to undertake my PhD, for their endless knowledge and advice throughout the project, for keeping me sane on the days spent doing experiments at ISIS, and for the continuing support.

From ISIS, I thank Dr. Kevin Knight, Dr. Craig Bull, Dr. Nick Funnell and Dr. Matthias Gutmann, for their great efforts and patience during my various experiments at the ISIS neutron spallation source.

There are people that have been a big part of the PhD journey. Matthew Dodd, a great friend, always up for a drink, and owner of a rather comfy couch to spend a few nights on. Rehemat Bhatia, who has provided valuable insight to the requirements of the PhD and provides great excuses for some procrastination. Geoffrey Baron, a really nice guy, and provided much needed company and discussions through the various experiments we've encountered. Martha Pamato, another really nice person and fellow Earth Materials demonstrator. To you all, a very big thank you.

Of course, there are many fellow students, postdocs and friends that I have met during this project, and I cannot being to mention all these people. But those people will know who they are and know that they deserve a very big thank you.

Finally, I would like to thank my parents and my sister for their love and support, especially during those particularly stressful moments. Without them, this journey, from undergraduate through PhD, would not have been possible.

Contents

List of Figures

List of Tables

Chapter 1

The $NH_3 + CO_2 \pm H_2O$ ternary system

The ternary system in this thesis, NH_3 + CO_2 $\pm$ H_2O, has been studied to constrain the physical properties of ammonium carbonates across the solar system by computational and experimental methods. By better understanding the properties of this system, models of planetary and satellite interiors can be constrained to better determine the evolution of icy bodies.

The importance of this system shall be outlined for both earthly matters (section 1.2.2) and planetary matters (section 1.2.3), along with information already known and deduced from past studies of similar systems, and how this work has tackled gathering the necessary data to bridge the gap in the current knowledge (section 1.3). To begin however, the compounds that constitute this ternary system shall be introduced.

1.1 The 'ammonium carbonates'

The ternary system NH_3 + CO_2 $\pm$ H_2O (see Figure 1.1) contains both the CO_2 - H_2O (left hand side of the plot) and NH_3 - H_2O systems (right hand side of the plot), which have both been studied extensively. The solids that form in the centre of this ternary system are collectively known as the 'ammonium carbonates'. These carbonates are stable at temperatures below 300 K in the most part; above this temperature, the carbonates break down due to the volatility of ammonia. The formation of ammonium carbonates is relatively straightforward; the addition of the constituent parts in various amounts leads to the formation of stable carbonates (Table 1.1), which include:

1. ammonium carbonate monohydrate[1] [$(NH_4)_2CO_3 \cdot H_2O$],

2. ammonium sesquicarbonate monohydrate[1] [$(NH_4)_4(H_2(CO_3)_3) \cdot H_2O$],

3. ammonium bicarbonate[1] [NH_4HCO_3],

4. ammonium carbamate (α / β) [$[NH_4]^+[NH_2CO_2]^-$],

5. urea[2] (*I, II, III, IV, V*) [$CO(NH_2)_2$].

Table 1.1
Formation reactions, based on the three components of the ternary system of NH_3, CO_2 and H_2O, of the ammonium carbonates.

Compound	Reaction
1. Ammonium carbonate monohydrate	$2NH_3 + 2H_2O + CO_2 \longrightarrow (NH_4)_2CO_3H_2O$
2. Ammonium sesquicarbonate monohydrate	$4NH_3 + 4H_2O + 3CO_2 \longrightarrow (NH_4)_4(H_2(CO_3)_3) \cdot H_2O$
3. Ammonium bicarbonate	$NH_3 + H_2O + CO_2 \longrightarrow NH_4HCO_3$
4. Ammonium carbamate	$2NH_3 + CO_2 \longrightarrow [NH_4]^+[NH_2CO_2]^-$
5. Urea *	$NH_4CO_2NH_2 \rightleftharpoons CO(NH_2)_2 + H_2O$

* Note the reversible reaction between ammonium carbamate and urea via addition or subtraction of water

Of these, ammonium bicarbonate and urea are the only compounds to occur naturally on Earth. Ammonium bicarbonate forms the mineral teschemacherite, found in layers of guano in South Africa and South America [136], and in geothermal waters from New Zealand [21]. Urea is a common by-product in biological systems, serving an important role in the metabolism of nitrogen-bearing compounds by animals and is the main nitrogen-bearing substance in the urine of mammals. Due to the volatility of some of the solids, particularly in ammonium carbonate monohydrate, ammonium sesquicarbonate monohydrate and ammonium carbamate, the likely localities where ammonium carbonates will be found is in cold environments, such as in cold polar regions or glacial environments.

Whilst there has been much focus on the NH_3-H_2O and the CO_2-H_2O systems, the solids that form in the centre of this ternary system (NH_3 + CO_2 $\pm$ H_2O) have mostly been overlooked in the literature. The first literature published was in 1800 [32], and yet over the past 200 years the knowledge of these solids are still limited. Indeed, the first crystal structure to be determined by modern methods (principally

[1]Referred to historically as 'normal' 1., 'half-acid' 2. and 'acid' 3. respectively
[2]Referred to historically as carbamide

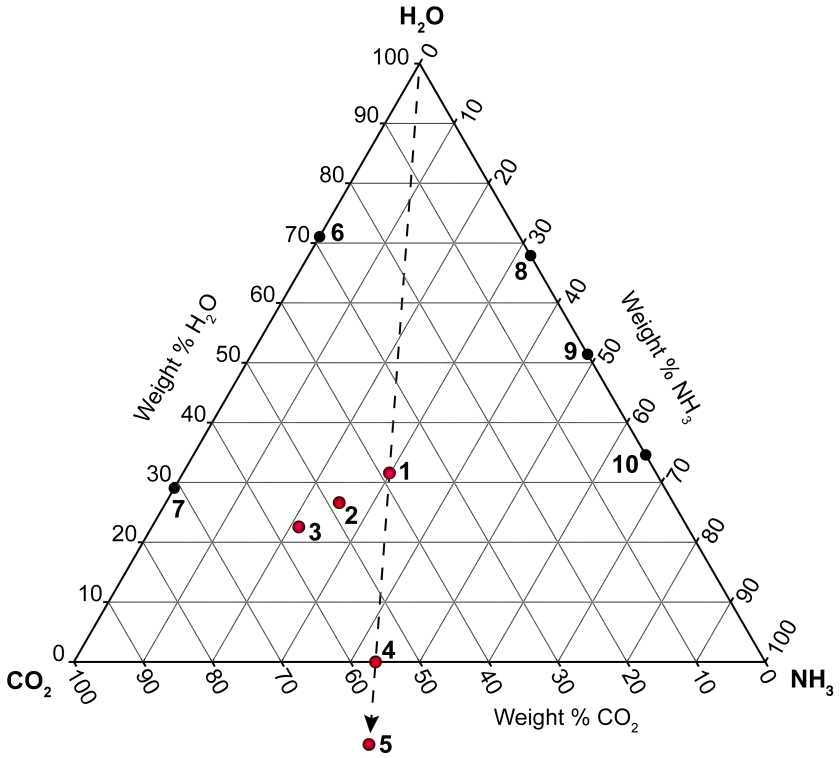

Figure 1.1
The ternary system of NH_3 + CO_2 ± H_2O. The compositions of compounds to form in this system are given by wt%, with an exception made for crystalline end members (water ice, dry ice, and solid ammonia). The numbers correspond to phases: (1) ammonium carbonate monohydrate; (2) ammonium sesquicarbonate monohydrate; (3) ammonium bicarbonate; (4) ammonium carbamate; (5) urea; (6) CO_2 clathrate hydrate; (7) solid carbonic acid; (8) ammonia dihydrate; (9) ammonia monohydrate; (10) ammonia hemihydrate.

X-ray diffraction) was that of urea [67], then ammonium bicarbonate [99], with ammonium carbamate 40 years later [2]. Ammonium sesquicarbonate monohydrate was only discovered in 2003 [91]; the existence of the β-phase of ammonium carbamate was discovered in 2007 [82]; and finally, a diffraction pattern of ammonium carbonate monohydrate was measured just a few years ago in a single crystal neutron diffraction experiment [53].

Furthermore, there has been much discussion and contradictory observations regarding both the correct compositions (*cf.* [39]) and accurate solid phase equilibria (*cf.* [53]) of the carbonates in the published work. It is likely due to the instability of these carbonates when handled at room temperature, and the tendency for a mixture of different phases to be present at any given time. Combine this with the similarity of the morphology between crystals - which are typically small, semi-transparent and elongated [113], and sometimes just a solid white mass containing a mixture of

phases is observed - it makes visual identification between crystals difficult, leading to easy misidentification. Commercially available 'ammonium carbonate' exacerbates this problem as it is not typically pure, and can even be the wrong composition entirely - usually ammonium carbamate [128, 82, 53].

It seems rather curious as to why there has been so little interest in these solids, since there have been extensive studies of related compounds of toxic ammonium oxalate and explosive ammonium chlorate and ammonium nitrate [53]. There has been detailed work on the decomposition of ammonium carbonate, ammonium bicarbonate, and ammonium carbamate at room temperatures and above. There has, however, been no work on these materials at low temperatures. We know relatively little about some of these carbonates, which could be useful for a variety of purposes from planetary modelling to large scale industrial processes.

1.2 Justification of this work

Despite the lack of work, there are interesting properties and uses for the solids that form in this system. Uses in industry will be discussed (section 1.2.2), such as use in carbon-capture schemes, followed by how the solids are likely to form in planetary environments (section 1.2.3). Firstly though, is a discussion of some of the importance from a crystallographic point of view.

1.2.1 Hydrogen bonding

The hydrogen bond, a medium strength intermolecular or intramolecular force, is an important directional interaction in organic and inorganic compounds, hydrous minerals, and in biological systems [107, 130]. The International Union of Pure and Applied Chemistry (IUPAC) recommendation gives a definition of a hydrogen bond as "*an attractive interaction between a hydrogen atom from a molecule or a molecular fragment* X-H *in which* X *is more electronegative than* H, *and an atom or group of atoms in the same or a different molecule, in which there is evidence of bond formation*" [8].

A typical hydrogen bond is given in the form X-H$\cdots$Y-Z, where X-H is the hydrogen bond donor and the Y-Z is the acceptor. The X-H bond is a shorter, stronger covalent bond than the H$\cdots$Y hydrogen bond, with Y either an atom (in this case -Z is not present), a fragment or a molecule. In some cases, X and Y are the same. The

strength of the hydrogen bond depends on the donor and acceptor atoms; a stronger H···Y bond is shorter, and stretches the X-H distance; the H···Y is strongest when X-Ĥ···Y = 180 °. The strongest hydrogen bonds occur when the central hydrogen atom is equidistant from its neighbouring atoms - a symmetrical hydrogen bond. Hydrogen bond distances are greater than the length of covalent bonds or ionic pair separations, but are less than Van der Waals interactions.

However, the variance in the properties of hydrogen bonding led to a more compact, broad definition as "*a hydrogen bond is a weak chemical bond between a valence-saturated* XH *group of one molecule and a valence-saturated* Y *atom in the same or different molecule*" [54].

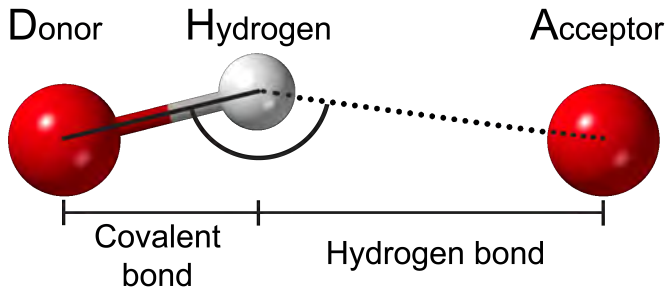

Figure 1.2
The hydrogen bond. Notation of this form of bond is usually given as X-H···Y. The X-H bond is between the donor and hydrogen, and the H···Y is between the hydrogen and acceptor. The X-H covalent bond is typically ∼1 Å, and the H···Y bond is ≥X-H bond. The angle is usually given in the notation form as X-Ĥ···Y.

Hydrogen bonds play an important role in the behaviour of a material. The hydrogen-bonded nature of materials inherently makes them more compressible due to the weaker hydrogen bonds controlling the strain response of the structure to an applied stress. Since soft, compressible materials can behave in interesting ways, such as large anisotropy, interesting bonding geometries, optical applications, anisotropic thermal behaviour, and polymorphism [150, 51], determining the position of hydrogen atoms, especially in extensively hydrogen bonded materials, is central to understanding a material's behaviour.

Therefore, the extensive hydrogen-bonded nature of the solids to form in this ternary system, with varying hydrogen bond geometries comprising their structures (see Figure 1.3) makes them interesting to study. Urea, in particular, is considered a prototypical hydrogen bonded crystal due to the simplicity of the structure, with sig-

nificant scientific and practical importance, especially with reference to phase stability of hydrogen bonded molecular solids [156]. Furthermore, the chemical behaviour of the elements C, H, N, and O, form the basis for most chemistry in biological systems. There is plenty of literature that goes into much more detail of the importance of hydrogen bonding in material science than is given here (for example [107, 130]).

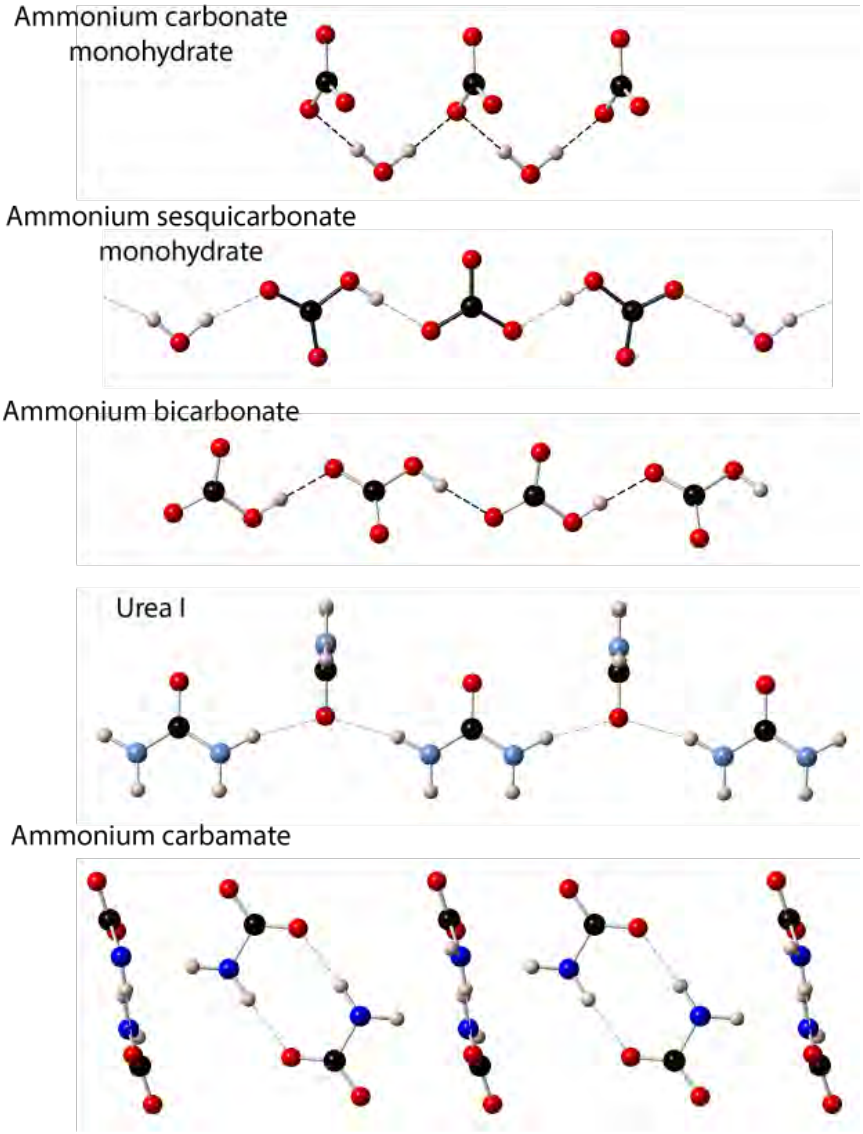

Figure 1.3
Comparison of hydrogen bonding in selected ammonium carbonates. Atoms are: oxygen (red), nitrogen (blue), carbon (black), and hydrogen (cream). The dotted lines show long range hydrogen bonding. To scale. This work will show that highly directional hydrogen bonding leads to highly anisotropic properties.

Due to the extensive hydrogen bonding, this system is suited ideally to neutron diffraction techniques, due to the greater accuracy that can be achieved in hydrogen atom positions over the use of X-rays. Unlike neutron diffraction, which gives a di-

rect measure of the position of the hydrogen atom's nucleus, X-rays sense the electron density located inward along the covalent bond to the nucleus itself, hence O-H bond lengths reported in X-ray studies are much shorter than when measured with neutron diffraction (the details of diffraction techniques will be described in Chapter 2).

Despite this, there is a considerable lack of neutron diffraction data reported in the literature of the ammonium carbonates. It is also interesting to see how *ab initio* calculations using density functional theory (DFT) reproduce the structural details and predict the properties of these solids, considering that it does not describe hydrogen bonding in structures (Chapter 2 has greater detail on the *ab initio* calculations).

1.2.2 Industrial uses of the ammonium carbonates

Ammonium carbonate has been implemented into industrial processes, with uses currently under investigation including; hydrogen storage capabilities of ammonium for use in fuel cells; separation of rare earth elements (REE) due to solubility variability; use as an additive in solutions to inhibit the growth of certain polymorphs, allowing synthesis of pure polymorphic substances. Perhaps the most promising technological use however, lies with carbon-capture and storage schemes (CCS). In the past, carbon-capture has relied on monoethanolamine (MEA) technology, but now more interest in ammonium-based technologies has surfaced due to greater efficiencies in reusing the ammonium in the processes over monoethanolamine processes.

1.2.2.1 Carbon-Capture schemes

The importance of reducing greenhouses gases into the environment has become one of the defining issues in modern science, with many schemes put forward as a viable method to reduce emissions in order to meet targets of less than 2 °C warming by the end of the 21st century.

One promising technology to drastically reduce emissions at fixed energy sources (i.e. power plants) is carbon-capture and storage schemes, by which waste CO_2 is removed from waste gases and not released into the atmosphere. There have been several different methods offered, from pumping CO_2 into deep underground reservoirs to using materials to store the waste gases. The latter has been seen to be a more promising technology, due to the lesser expense and greater ease of capturing the gases in all environments. Captured CO_2 has already been used for the production of urea and

enhanced oil recovery [65]. For example, ammonium carbamate and ammonium bicarbonate, formed from ammonia-based CO_2 capture, can be converted into urea-based compounds by heating, which are useful products in agrochemical, pharmaceutical, dye chemicals, and precursors of isocyanates and raw materials of polyurethanes [13].

Many different materials have been suggested for use as the absorber of CO_2, including amines, amino acids, carbonates, and various liquids (see Table 1.2). Amines have typically been regarded as the most mature and promising technologies, based on their reliability and extensive use, but suffer from issues such as high regeneration energies, degradation, and high corrosive nature.

Whilst there have been extensive studies trying to overcome these issues, a perhaps more promising technology is based on the ammonia-water system. The potential to store large volumes of carbon dioxide within the ammonia-water system at room temperatures holds an exciting and promising future for carbon-capture technology. Flue gases containing CO_2 - that would normally be released to the atmosphere - are instead fed through an aqueous ammonia solution, typically 10 - 30 wt% NH_3, forming ammonium carbonates, which can then be extracted as a solid, with the remaining liquid to be reused for further capture. This 'solid' can be physically stored, but in most cases is chemically reacted to separate the CO_2. Ammonia-based carbon-capture technologies offer many advantages over the mature amine technology: $\sim$99 % pure CO_2; high capture capacity; lack of thermal degradation; cheaper absorbent costs; and high chemical stability.

Carbon-capture using ammonia-based technologies has proved to be viable; the question for a number of years has been how feasible it is that it can be made into a commercial success. Full scale pilot schemes have shown that CO_2 capture is possible in large scale projects (Table 1.3). However, there are issues that need to be addressed and challenges that need to be overcome before ammonia-based carbon-capture becomes commercially successful.

One such challenge, and arguably the main issue facing ammonia-based carbon-capture technologies, involves the volatility of ammonia at ambient temperatures and pressures, known as ammonia slip. The suppression of ammonia slip is of primary importance for the successful development of ammonia-based technologies, both technically and economically, since ammonia slip is inconvenient and costly to control.

Table 1.2

A summary of the key points of different solvents used in carbon-capture and storage (taken from Mumford *et al.*, 2015 [102]).

Type	Company	Solvents	Benefit	Disadvantage	Future work	Reference
Advanced Amine	Hitachi; Dow; KEPCO; MHI; Fluor; Shell	H3-1; UCARSOL^{TM} FGC 3000; RS-1, RS-2, RS-3; Cansolv; CASTOR 1 & 2; KS-1, KS-2, KS-3; Fluor Econamines FG Plus^{SM}	Extensive operational/design experience available; An extra degree of freedom determining the compositions of amine mixtures to optimise its performance	Corrosion; Solvent degradation; Form heat stable salts with SO_2 and NO; Amine emission; Viscous	Develop novel amine based solvents to lower regeneration energy required, oxidative degradation, corrosion, and increase reaction kinetics and absorption capacity; Heat integration; Equipment innovation such as intercooling system	[84, 93, 41, 120]
Amino acid salt	Siemens; BASF	PostCap; Puratreat	Low vapour pressure; Low oxidative degradation and emission; Reactive towards CO_2; Low environmental impact; Similar rate constants to MEA	Forms heat stable salts with SO_2 and NO; High heat of regeneration	Performance should be examined on a larger scale and in a real industrial situation	[84, 153, 132, 117, 149]
Carbonate system	UNOTechnology	UNO MK3	Low vapour pressure; Non-volatile; No oxidative degradation; Low toxicity; Low regeneration energy; Low environmental life-cycle impact; Multi-impurity capture; FGD unnecessary; Low manufacture cost	Reduced kinetics	Scale up of plant based trials; Process of design of large scale systems; Examine new promoter systems; Slurry handling system design and simulation	[84, 101, 58]
Aqueous ammonia	Alstom; CSIRO; PowerSpan	CAP	Does not decompose, high capacity, high purity product, competitive heat of regeneration	High ammonia vapour pressure; Slower kinetics than MEA; Solid ammonium bicarbonate formation; Ammonia emission; Harsh conditions duo to operating temperature	Additives to enhance CO_2 absorption rate and suppress ammonia vapour, re-engineering industrial ammonium bicarbonate fertiliser production and combined capture of CO_2 and SO_2	[84, 157, 154, 3, 124, 158, 159]
Immiscible liquid	3H Company	Self-concentrating absorbent CO_2 capture process	Low regeneration energy; Non-aqueous environment to mitigate corrosion, degradation and formation of stable salts	Mechanism and chemistry unsure; Low maturity	Develop new system using different liquids; More testing and research on bench scale should be conduced	[84]
Ionic liquid	Notre Dame; Georgia Tech.	NDIL0046; NDIL0157; RevILs	High thermal stability, no water evaporation in regeneration, no vapour pressure, tailorable	Expensive; High viscosity; High selectivity to water	Improve operating performance of ILs; Improve process chemistry; Integration of capture with manufacturing saleable goods, i.e, organic carbonates, formic acid	[84, 83, 26, 155]

Table 1.3
Large demonstration post-combustion carbon-capture (PCCC) projects - completed & operating (from Idem *et al.*, 2015 [70] - modified from Abu-Zahra *et al.*, 2013 [1]).

Large demonstration PCCC projects - completed					
Project	Feedstock	Size (MW)	Technology/solvent used	CO_2 fate	Status
Pleasant Prairie, Alstom, WI, USA	Coal	5-100 ton/day	Alstom amine & chilled ammonia	Vented	Operated 2008-2009
AEP Mountaineer, AEP, WV, USA	Coal	30-600 ton/day	Chilled ammonia	Saline	Operated 2009-2011
Karlshamn, E.ON, Sweden	Coal	5-100 ton/day	Chilled ammonia	Vented	Operated 2009-2010
Large demonstration PCCC projects - operating					
Mongstad, Statoil, Norway	Gas	0.1 Mt/yr	amines, chilled ammonia	Saline	Operational 2012
South Energy / MHI / SCS / SECARB/ EPR Plant Barry Power Station (Alabama)		500 ton/day	Chilled ammonia and KS-1 solvent (MHI technology)		Operational 2011
Burger Plant, First Energy, Shadyside, OH, USA	Coal	-	Ammonia	-	Operational 2008
Delta Electricity Munmorah Power Station, CSIRO, Munmorah, Australia	Coal	3 ton/day	Ammonia	-	Operational 2009

There are three approaches to try to minimise ammonia slip - capture, utilisation or suppression [65].

Capture approaches use water to create ammonia solutions from the lost ammonia vapours, which can be recirculated and incorporated back into the carbon-capture process. Utilisation is similar to the capture approach, since it requires capturing the excess ammonia. However, instead of the ammonia-solution being recirculated for use, utilisation involves taking the solution and producing useful end-products, such as the manufacturing of salts (such as ammonium sulphate and ammonium nitrate for fertilisers) using the excess ammonia vapour.

Suppression takes a different approach; it involves addition of chemicals or changing the operating conditions to reduce the amount of ammonia slip. The addition of chemicals suppresses ammonia slip by changing the chemistry of the system and making the ammonia less volatile. This has potential problems, such as cost of buying additives, potential chemistry changes caused by the additives, and the formation of heat stable salts which may require extra treatment. Chemical additives can be avoided by changing the operating conditions of the capture process, such as in the Chilled Ammonia Process (CAP), by reducing the temperature of the ammonia-solutions, thereby minimising the amount of ammonia-slip in the first place. This, however, comes with its own problems, since reducing operating temperatures is potentially energy intensive and therefore expensive, especially in hot climates.

There are further issues that need to be addressed, such as understanding the reaction mechanisms associated with the capturing mechanism, accurate quantification

methods to measure ammonia vapour for monitoring and controlling the reactions, and cooling the gases sufficiently for increased reaction rate without changing the absorption of CO_2 [65]. If these issues can be overcome, ammonium-based carbon-capture may become a viable and efficient method of reducing carbon emissions.

1.2.2.2 Hydrogen storage and power

Global emission of carbon dioxide remains a problem not only for industry and power use, but also for vehicular emissions. In 2010, 23 % of all emissions from fossil fuels were as a result of vehicular activity, with growth in greenhouse gas emissions continuing to rise [131]. Hydrogen power has been proposed as a solution for reducing the amount of vehicle emissions. Hydrogen power relies on fuel cells to combine oxygen and water to generate electricity, synthesising water as an end product; the idea is that this process is zero emission at the end use.

Two methods of direct storage of hydrogen are currently being investigated - physical and chemical storage [43]. Both of these methods, however, have problems in that a large amount of energy is required to store large volumes of compressed hydrogen, and hydrogen has boil-off leakage issues. Indirect storage of hydrogen in light hydrogen-containing chemicals holds a more promising potential. Methane and methanol has previously been suggested, but ammonia is the only carbon-free hydrogen carrier [86]. In terms of energy density, ammonia and hydrides are close to fossil fuels, only surpassed by nuclear technology (see Figure 1.4); however, nuclear technology is not very suitable for non-static use, such as in vehicles.

This potential for hydrogen power to reduce emissions led to a target by the U.S. Department of Energy's (DOE) for hydrogen storage materials [105]. The target set forth the minimum requirements necessary for materials to be suitable for economic use, from costs of production to the end user costs, to safety issues that need to be addressed. There have been changes since the initial targets were set in 2003, in 2005 and 2012, as the technological landscape has changed (see Table 1.4).

Ammonia meets some of the U.S. DOE targets; containing 17.6 wt% hydrogen, it is low cost basic chemical, and although it has boiling point of -33.5 °C, it can be stored as a liquid under 8 bars of pressure in stainless steel containers with no evaporation loss (unlike hydrogen) when stored in a liquid state. One problem with ammonia

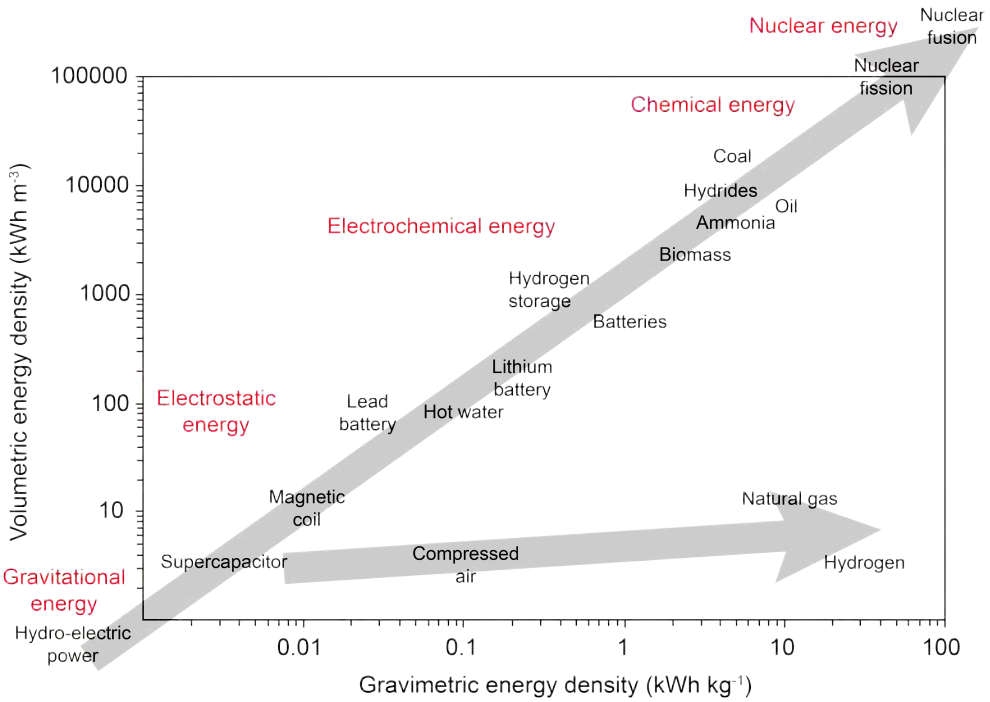

Figure 1.4
Comparison of the specific power (gravimetric energy density) against energy density (volumetric energy density) of some energy carriers. Ammonia is close to fossil fuels. Adapted from Zuttel *et al.*, 2010 [160].

is the toxicity; this can be overcome by storing the ammonia in a solid, such as ammonium carbonate or urea, with which there are no onboard storage issues for transport applications. It is actually easier to store ammonia-based chemicals than gasoline.

Ammonia-based chemicals in transport applications involves the use of fuel cells. Fuel cells are electrochemical devices, generating electricity by converting chemical energy via electrochemical reactions from fuels such as hydrogen, ammonia and hydrazine [86, 118]. There are several types of developed fuel cells, with a few using ammonium carbonates.

Ammonia-based fuel cells require the breakdown of ammonia into hydrogen. To synthesise pure hydrogen, ammonia is decomposed into nitrogen and hydrogen at high temperature; catalytic decomposition has reduced the minimum temperature for efficient release from ~500 °C to ~300 °C. Decomposition of ammonia is a mildly endothermic process, yielding hydrogen and nitrogen:

$$2\,NH_{3(g)} \longrightarrow N_{2(g)} + 3\,H_{2(g)}$$

This process produces no CO or CO_2, only nitrogen, which is benign to a fuel cell as a co-product. Commercial ammonia is 99.5 % purity; the impurity is mainly water

Table 1.4
Revisions of the U.S. Department of Energy's (DOE's) minimum requirements for hydrogen storage materials for economic use [105]. The first document was published in 2003, with two subsequent revisions in 2005 and 2012; the latter being significantly revised to reflect scientific advancements and the changing technological landscape. A final revision has been made to some aspects, such as classifying different requirements for hydrogen storage for different uses.

Storage Parameter	Units	2007	2010	2015	2020	Ultimate
System Gravimetric Capacity						
Usable, specific-energy from H_2 (net H_2useful energy/max system mass)	kWh/kg (kg H_2/kg system)	1.5 (0.045)	2 (0.06)	3 (0.09)	1.8 (0.055)	2.5 (0.075)
System Volumetric Capacity						
Usable energy density from H_2 (net useful energy/max system volume)	kWh/L (kg H_2/L system)	1.2 (0.036)	1.5 (0.045)	2.7 (0.081)	1.3 (0.040)	2.3 (0.070)
Storage System Cost						
Fuel cost	\$/kWh net (\$/kg H_2 stored)	6 (200)	4 (133)	2 (67)	10 (333)	8 (266)
	\$/gge at pump	-	2-3	2-3	2-4	2-4
Durability/Operability						
Operating ambient temperature	°C	-20/50 (sun)	-30/50 (sun)	-40/60 (sun)	-40/60 (sun)	-40/60 (sun)
Min/max delivery temperature	°C	-30/85	-40/85	-40/85	-40/85	-40/85
Operational cycle life (1/4 tank to full)	Cycles	500	1000	1500	1500	1500
Min delivery pressure from storage system	bar (abs)	8	4	3	5	3
Max delivery pressure from storage system	bar (abs)	100	100	100	12	12
Onboard efficiency	%				90	90
'Well' to power plant efficiency	%				60	60
Charging/Discharging Rates						
System fill time (5 kg)	min (kg H_2/min)	10	3	2.5	3.3 (1.5)	2.5 (1.5)
Minimum full flow rate	(g/s)/kW	0.02	0.02	0.02	0.02	0.02
Start time to full flow (20 C)	s	15	5	5	5	5
Start time to full flow (-20 C)	s	30	15	15	15	15
Transient response at operating temperature 10-90 % and 90-0 %	s	1.75	0.75	0.75	0.75	0.75
Fuel Quality (H_2 from storage)	% H_2	99.99 % (dry basis)			SAE J2719 and ISO/PDTS 14687-2 (99.97 % dry basis)	
Environmental Health & Safety						
Permeation & leakage	-	Meets applicable standards			Meets or exceeds applicable standards, e.g. SAE J2579	
Toxicity	-					
Safety	-					
Loss of usable H_2	(g/hr)/kg H_2 stored	1	0.1	0.05	0.05	0.5

and would not damage a fuel cell. The main issue facing this method is the temperature needed to decompose the ammonia into nitrogen and hydrogen. If suitable catalysts could be found, it may be possible to lower the temperature further, and this method may become more feasible. Otherwise, fuel cells which are directly fed by ammonia may be more useful as they are much more efficient.

The solids in the NH_3 + CO_2 $\pm$ H_2O system, in particular ammonium carbonate, ammonium bicarbonate and urea, contain a large percentage of hydrogen by weight, enabling them to be used as potential hydrogen carriers. Ammonium carbonate monohydrate, ammonium carbamate and stoichiometric urea-water solution are all above the DOE targets for hydrogen storage in vehicular use, based on the content of hydrogen, having 8.8 wt%, 7.7 wt% and 7.7 wt% hydrogen respectively. The two stable phases at ambient pressures and temperatures are ammonium bicarbonate, having $\sim$6.4 wt% hydrogen, and urea, having 6.7 wt% hydrogen. These are both short of the targets, but

urea is a promising fuel for use in a fuel cell if additional water (i.e. urea in solution) is present, with the value for urea becoming 7.7 wt%, which is just above the DOE target (Table 1.4). One of the main advantages of using urea over direct ammonia fuel cells is due to the stability of urea at ambient temperature and pressure, in particular as it is in solid form up to 133 °C, and can be easily stored in sealed containers for long periods of time. Other advantages are its low price and availability; it has little toxicity to the environment [121]; and there is already an existing distribution infrastructure for urea since it is readily used in many applications.

Further investment is required into researching ammonia-based fuel cells for electricity production. The ammonium carbonates offers a potential alternative to overcome the issues associated with direct storage of hydrogen. Although they do contain CO_2, issues with emission depend on the sources of carbon; the CO_2 saving would be significant if the carbon for the synthesis of these materials is sourced from biomass or carbon-capture.

1.2.2.3 Industrial processing and synthesis

The use of the ammonium carbonates in industry is mainly concerned with synthesis of novel phases and processing of materials. Most of the elements vital for use in modern technology, from catalysts to smart materials, are extracted from ores that need to be refined to be suitable for end-use.

Of particular interest are the group of elements collectively known as the rare-earths - so called due to the scarcity of these elements. Rare-earths are of particular interest for renewable energy technologies such as wind turbines, batteries, catalysts and electric cars [66], hence separation and purification of rare earths ore deposits is still a matter of utmost concern.

There are various methods for processing the ores, depending on the mineralogy of the REE-containing phases and reactivity of gangue phases. The method of monazite ore processing involves soaking the rare earth ore at 400 - 500 °C in concentrated sulphuric acid, with the resulting ore washed and filtered or decanted to remove fine impurities. The ore is further leached using extraction agents and precipitating agents; it is in the precipitating agents that the ammonium carbonates are used, typically either ammonium bicarbonate or urea. Since the solubility of REE varies progressively from

element to element with the addition of ammonium carbonates, with the heavy rare-earths more soluble than the light rare-earths, this behaviour opens up a new way of separating these elements. The resulting precipitate is then heated to form rare-earth peroxicarbonates, some of which can directly be used in industrial applications, such as didymium carbonate, $Nd_2Pr_2(CO_3)_6$, neodymium carbonate, $Nd_2(CO_3)_3$, and yttrium carbonate, $Y_2(CO_3)_3$.

For example, using ammonium hydroxide and ammonium bicarbonate can help to make yttria nanopowders Y_2O_3 (e.g. [75]). Yttria is popular because of its range of applications; it is corrosion resistant, thermally stable, optically isotropic, and has the advantage of being optically transparent over a wide range of radiation wavelengths, unlike most other ceramics, which tend to be opaque in the visible part of the spectrum. It has been suggested that yttria could be used for high temperature windows and lenses, and in solid-state lasers since it has higher thermal conductivity and lower thermal expansion than widely used yttrium aluminum garnet, which is critical for thermal management as laser power increases and produces more heat during operation.

Not only can ammonium bicarbonate be used for synthesis of materials, urea has increasingly been used to synthesise novel phases and fine particulate materials by employing homogeneous precipitation methods [24, 40]. Urea is simple, cost-effective, does not require high-temperatures, and upon heating above 60 °C, gradually raises the pH of a reaction mixture due to release of CO_3^{2-} and OH^-. Syntheses of rare-earth compounds through urea decomposition have received considerable attention (*cf.* [134]). A quick search reveals extensive literature reports of using urea to synthesise materials, both for rare earth purposes and for novel phases (highly cited examples include [29, 133, 96])

Further uses of ammonium carbonates comes from doping solutions of glycine to preferentially crystallise γ-glycine. The addition of low concentration ammonium carbonates into solutions with glycine will inhibit the growth of α-glycine and leave phase-pure γ-glycine, which has potential use for optoelectronic applications due to a wide transparency window suitable for second harmonic generation [10].

1.2.2.4 Other uses

The main use of ammonium bicarbonate is in the food industry as a raising agent. It has advantages over baking soda or baking powder in flat baked goods as it produces more gas for the same amount of agent and leaves no taste in the finished product. It cannot, however, be used in moist, bulky based goods since some ammonia will be trapped and cause an unpleasant taste. Other uses include: use in fertilisers as an inexpensive nitrogen replacement; as a component in the production of fire extinguishing compounds; in pharmaceuticals; dyes; pigments; in the plastic and rubber industry; in the manufacture of ceramics; in chrome leather tanning; and for the synthesis of catalysts.

1.2.2.5 Towards an ammonia economy

All of these uses for ammonia and ammonium carbonates suggest that a move could be made away from an oil-driven economy, towards an ammonia economy. A diagrammatic representation of an energy system based on ammonia is given in Figure 1.5.

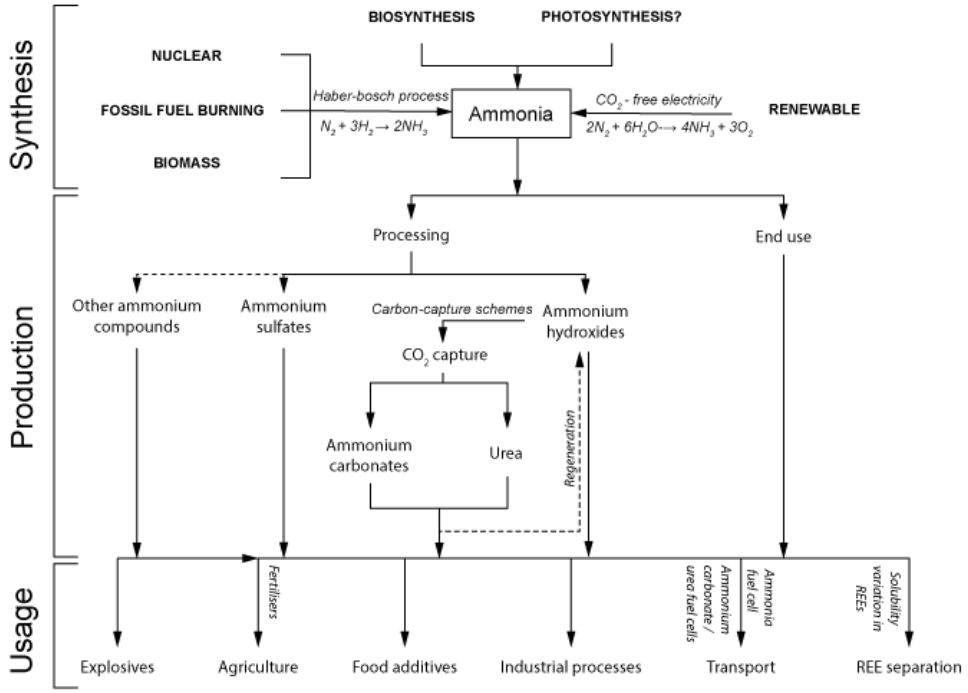

Figure 1.5
Diagram of a basic energy system using ammonia and its derivates as an energy vector. Uses discussed in the previous sections are shown at the bottom of the diagram.

The advantage of creating an ammonia economy over a hydrogen economy is that there is already an existing infrastructure for ammonia production and delivery. Storage of ammonia suffers less of the boil-off leakage issues associated with hydrogen,

and has more favourable conditions, such as low pressures and ambient temperatures of storage vessels. Ammonia is commonly produced using the Haber-Bosch process, but this could be extended in the future using other methods, such as synthesis from renewable sources of electricity, or perhaps more promisingly using biological methods for synthesis of carbon free-ammonia. Ammonia is widely used in agriculture, and hence is distributed around the world. Whilst this would likely introduce some economical costs, these could be offset by selling products based on ammonia technologies to offset the increased costs of production.

It could also be warranted that use of ammonia could be used to help remove carbon dioxide produced in other energy generation processes. By forming ammonium hydroxide solution, carbon-capture processes could be implemented into creating ammonium compounds for end use, such as synthesis of urea. In this case, ammonium carbonates could become an important constituent of an ammonia economy by reducing global CO_2 emissions. However, there is still much investment needed to minimise issues associated with ammonia-based technologies before an ammonia economy could be partially or fully implemented.

1.2.3 Ammonium carbonates in planetary science

Over the last few decades, visits by spacecraft to the outer solar system have showed a plethora of unexpected interesting features and processes occurring on the planets and moons across the solar system. As the missions have developed in capability and complexity, the range and complexity of these features and processes have increased, and with each new body investigated, yet more unexpected features are found.

Many of the most interesting bodies are moons around the Gas Giants and past the orbit of Neptune, which includes Pluto. Many of these bodies are still geologically active, but this presents a problem. Since these bodies have surface temperatures below 120 K, how can a body composed mainly of water ice be able to show features and processes and not be frozen solid? There must be some other compounds present that change the chemistry of these bodies to account for some of the features observed. One of the compounds suggested has been ammonia.

Ammonia is thought to play an important role in the outer solar system, especially in satellites and objects past the Jovian system. Ammonia plays three important roles;

it depresses the freezing point of water by ∼100 K, acting as an antifreeze; it lowers the thermal conductivity of its host ice to a small degree [38]; it can drastically lower the viscosity of water ice when ammonia is present in low concentrations [38]. Radionuclide heating of rocky cores, latent heat of crystallisation, and tidal heating may keep an icy body warm, but without depressing the freezing point, the energy budget is not large enough for liquid water to exist. Lowering the viscosity of ice enables differentiation of rock and ice, allowing bodies to reconfigure to potentially host a liquid layer under a solid crust. Ammonia is considered, theoretically, to be broadly distributed and abundant in the outer solar system, but detection of ammonia remains an issue [92].

What follows next are some details on the presence of ammonia, carbon dioxide and water in planetary environments, how they interact to form the ammonium carbonates, and how they may play an important role in icy bodies.

1.2.3.1 Volatiles in the solar system

Volatiles in the solar system are found past the orbit of Mars beyond the 'snow line' - postulated to exist around 5 A.U. - where temperatures are sufficiently cool for volatile compounds to form. Ammonia, water and carbon dioxide are considered to be amongst these volatile compounds in the solar system, because of their low melting and boiling points. The abundances of the elements relevant to these compounds, H, C, N and O, are well known in the primitive solar nebula, since solar abundances are well known (e.g., [5, 89, 109]). However, determining the way in which these elements combined, and hence determining the primordial abundances of NH_3, CO_2 and H_2O is difficult; this is important since this will affect the bulk compositions of planetary bodies.

The dominant form of nitrogen, either as N or N_2, is not known in the solar nebula, which is important since the dominant form of nitrogen on planetary bodies is dependent on the the chemical composition of the solar nebula; this composition depends on the initial abundance of N and N_2 [127]. Theoretical models predict that N_2 is efficiently dissociated into atomic N in molecular clouds, and pathways to return back to N_2 are inhibited by a lack of oxygen [38, 127]. On average, 10-20 % nitrogen is contained in NH_3, NH_4^+, and OCN^- as the solar system forms [125], which largely agrees with theoretical modelling (e.g. [25]). These ammonia and ammonia-related molecules are therefore likely to be present in icy bodies in the outer solar system past the 'snow

line', at least to a few percent. The first detection of ammonia in a protoplanetary disk has been made, around the star *TW Hya*, supporting this hypothesis [125].

Observations of solar system objects, however, lack signals for the presence of such values of ammonia. Comets and meteorites provide a snapshot of the early chemistry of the solar system, and can provide evidence for amounts of ammonia pre- and post- solar system formation. Many comets emit 0.1-0.3 % NH_3 and 3-10 % CO_2 relative to H_2O [92]. Spectral measurements taken from satellite or ground based systems only probe the top millimetres of a body's surface and cannot provide reliable estimates for the global values of ammonia; cryovolcanism and/or radiation damage may drastically alter values. The only definitive observations of extra-terrestrial ammonia occur at Pluto's largest moon, Charon [37], and at the dwarf planet Ceres, with probable observations in the atmospheres of the gas giant planets, the plumes of Enceladus, on large Kuiper Belt Objects such as Quaoar [71, 36] and Orcus [12]. Theoretical interest remains in possible ammonia-water volcanism on Titan and other icy satellites. Substantial quantities of ammonia are unlikely to have condensed in the relatively warm Jovian nebula [51].

The main contribution of ammonium carbonates involves their role in the melting of water, and storage of CO_2 in the NH_3-CO_2±H_2O ternary system in planetary and cometary ices. The next section will explore some of the evidence for the presence of ammonia in planetary environments, and in particular focus on potential interaction with carbon dioxide that could lead to the formation of ammonium carbonates.

1.2.3.2 Spectroscopic evidence

When the New Horizons probe flew past the Pluto system in 2015, it revealed the complex geology of both Pluto and Charon. One of the most interesting results in terms of this project was the detection of ammonia; this is the best evidence for the presence of ammonia and ammonia hydrates in the solar system, found on the surface of Pluto's largest moon, Charon. Strong evidence exists for the presence of ammonia hydrates based on an absorption feature at 2.22 μm from spectral observations (Figure 1.6) [37]. Further investigations suggest that ammonia may be present across Charon's encounter hemisphere at low concentrations, with local spots of intense concentrations; for example, in the crater Organa located in the northern hemisphere (Figure 1.7). Since

ammonia ice is readily destroyed by radiation, estimates of the age of these deposits place them at around 10^7 years; this suggests Charon is still active, and that these deposits must be relatively recent. It is possible that the impactor struck deep enough in Charon to reveal a possible large internal reservoir of ammonia and ammonia hydrates.

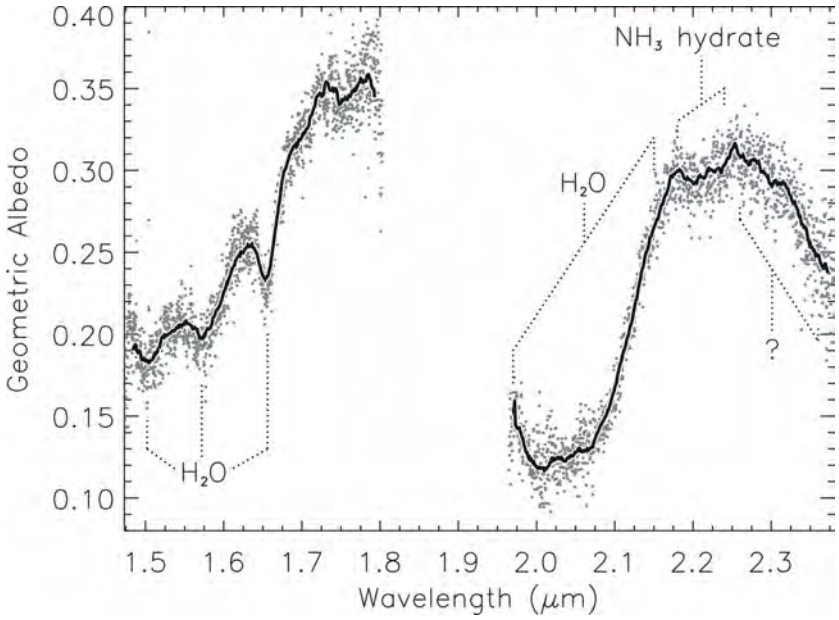

Figure 1.6
Measurement of the grand average spectrum of Charon from the New Horizons spacecraft, showing strong absorption features corresponding to water ice and a weaker absorption feature of ammonia hydrate. From Holler *et al.*, 2017 [69].

With water ice confirmed by New Horizons as the dominant surface composition of Charon, confirming Earth-based observations from the mid-1980s, ammonium carbonates have the potential to be present on Charon. However, a lack of detection thus far of CO_2 on both Pluto and Charon suggests that ammonium carbonates may not be able to form on the surface, where it is more likely that ammonium sulfate carbonates will form due to the presence of methane as the dominant carbon-bearing ice. The presence of CO_2 in the interiors of these bodies will depend on the internal oxidation states - if the interior contains some source of of free oxygen, CO_2 may form, otherwise the likely form will be CH_4.

Another body in the solar system with the presence of ammonia, water and carbon dioxide observed is Ceres. Ceres is the largest body and only dwarf planet in the main asteroid belt. It is a partially differentiated ice-rich body with low density (2.162 g/cm^3), and a rocky core surrounded by a shell composed of volatiles mixed

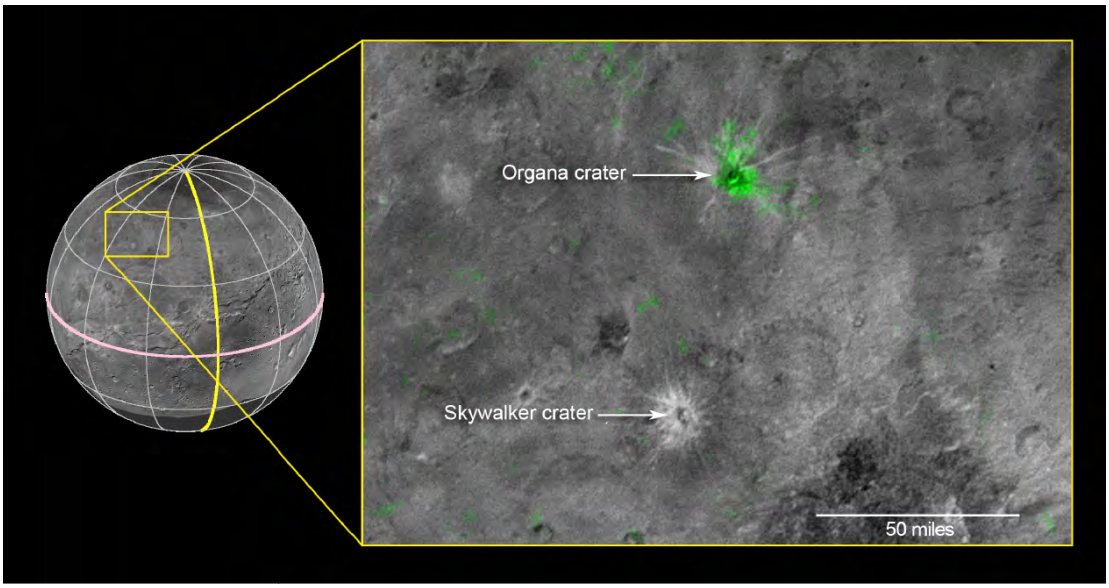

Figure 1.7
Composite image from the New Horizons spacecraft, from 50,000 miles (81,000 km) from Charon. Ammonia absorption map from LEISA shown in green. 2.22 μm ammonia-ice based absorption. Unique to Charon. Skywalker crater dominated by ordinary water ice. Right image taken at resolution of 0.6 miles (0.9 km) per pixel. Left image as 3 miles per pixel.
Credits: NASA/JHUAPL/SwRI

with denser materials such as silicates and salts. The surface is generally dark, composed of an assemblage of Mg phyllosilicates, ammoniated species, dark materials, and Mg-Ca carbonates [34].

One of the most interesting features discovered by the Dawn spacecraft was the presence of regions with a high albedo, seen as bright spots on the surface. Once such example is the 92 km-wide complex crater Occator, where two prominent spots are located, Cerealia Facula and Vinalia Faculae (Figure 1.8). These bright spots contain sodium carbonate, Na_2CO_3, along with small amounts of ammonium chloride [119] (Figure 1.9). Ammonium bicarbonate was previously also suggested to be present in small quantities [35], but the fits of Raponi *et al.* 2018 suggests that if it is present, it is less than 1 % of the volume. There are two groups of hypotheses for the emplacement of these bright materials onto the surface at Occator.

One group of hypotheses invokes an endogenic emplacement, where upwelling of subsurface liquids by diapirism or cryovolcanism results in brines accumulating on the surface. On the other hand, impact-induced heating may have caused ices in the outer shell to melt into liquid brines, which, upon refreezing, formed the species in Ceres' bright spots [35]. These two sets of hypotheses are not necessarily exclusive, however,

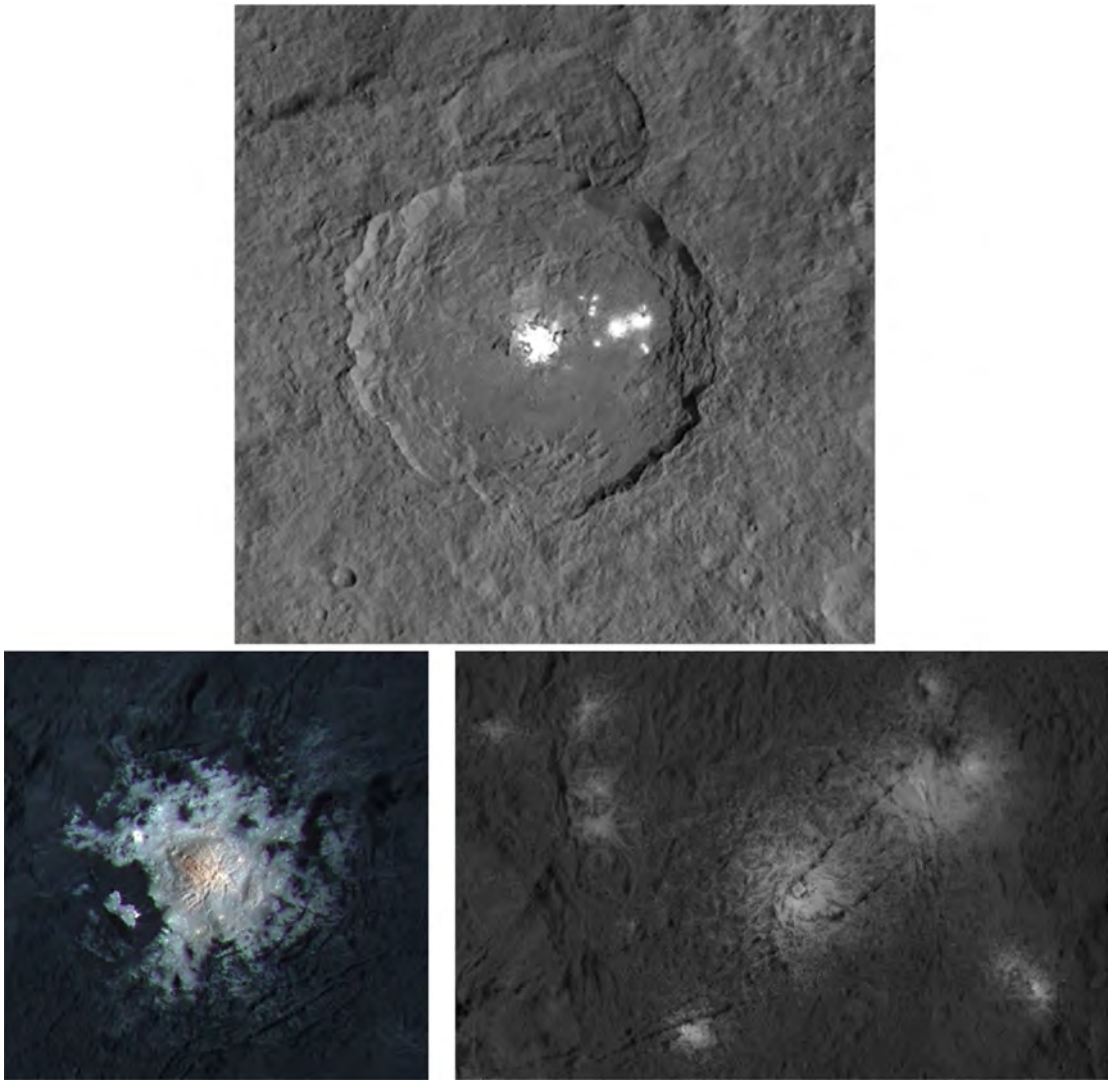

Figure 1.8
Upper panel: Occator crater at 35m/pixel, showing the prominent bright spots . Lower left: Cerealia Facula bright spot. Lower right: Vinalia Faculae bright spot. From Raponi *et al.* 2018 [119].

as upwelling may have brought the bright spot source material near the surface for final excavation by the Occator impact.

The detection of NH_4Cl on the surface could impose a number of important constraints on the composition of a subsurface liquid reservoir, and its cooling history on the surface. Due to its high solubility in water and the preferential formation of the sodium salts in the brine mixtures, it is generally difficult to form NH_4Cl unless the fluid is either rich in ammonium or rich in chloride (or both) [137]. Ammonia-rich magmas could interact with CO_2 and H_2O to yield ammonium carbonates.

Briny cryolavas can be brought to the surface by propagating through fractures

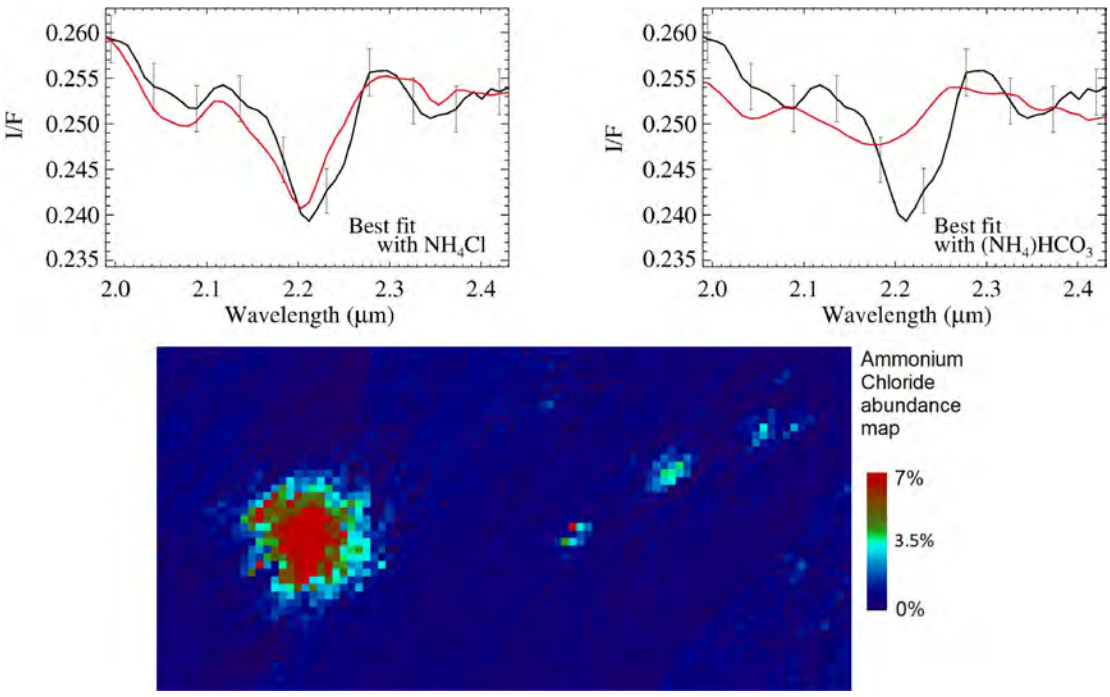

Figure 1.9
Upper panels: Measured absorption bands at 2.2 μm on Cerealia Facula (black line), and model (red line) performed with ammonium chloride (upper left), and ammonium bicarbonate (upper right). Bottom panel: abundance map of ammonium chloride. The modelling indicates the presence of this mineral on the rest of Occator crater is negligible. From Raponi *et al.* 2018 [119].

from the reservoirs to the surface while maintaining a warm enough temperature to prevent freezing. The relatively high density of Ceres' crust compared to the cryovolcanic fluids means pure H_2O and brines containing one species of a hydrated chloride salt or hydrated ammonia as their primary contaminant would be positively buoyant with respect to the crust. However, the presence of sodium-rich magmas has to exist at shallower levels to be brought to the surface by pressure driven-ascent [116]. A large Bouguer anomaly beneath Occator has been detected, suggesting a low density region that could be a cryomagma chamber feeding chloride-rich and NH_3-rich magmas to the surface [116].

There is also hypothesised to be ammonia on Titan; due to the warmer subnebula around Saturn during formation, there is expected to be a greater abundance of NH_3 to N_2 ices in icy bodies in the Saturnian system [48]. Although the origin of Titan's rich atmosphere is still uncertain [104], possible explanations include: conversion of ammonia into nitrogen by photolysis [9]; shock chemistry [95]; and thermal decomposition of the interior [56]. With the presence of liquid hydrocarbons on the surface,

and oxidised carbon, in the form of CO and CO_2 (e.g. [33, 49]) in the atmosphere, interaction with ammonia may lead to formation of ammonium carbonates.

Ammonia hydrates may also be present on Quaoar [71, 36], although this has also been interpreted to be absorption by methane [126]. On Miranda, H_2O has been found on the surface, and hints of ammonium hydrate absorption have also been reported [14], but there is a lack of CO_2 on the surface [57]. On Enceladus, there is evidence for ammonia [44, 142], carbon dioxide [22] and abundant water ice. Plume activity measured by the Cassini spacecraft suggests ammonia is present in low abundances [144], so ammonia may be present within the interior of Enceladus. A recent quantitative compositional estimate [145] puts H_2O at between 96 - 99%, with the remaining few percent including CO_2 (0.3 - 0.8%) and NH_3 (0.4 - 1.3%). H_2O and CO_2 are readily apparent in the spectra of Neptune's largest moon, Triton [30, 31, 62], with N_2 ice showing large temporal variation [62].

There is plenty of evidence that the raw constituents necessary for the formation of ammonium carbonates are present on many bodies in the outer solar system; however, the interaction of these raw components in planetary bodies is not fully understood.

1.2.3.3 Surface features

Most of the surface features related to possible presence of ammonia, ammonia hydrates and ammonium carbonates originate from cryovolcanism, cratering processes, and outgassing in the form of plumes. Internal oceans in icy bodies are thought to allow for cryovolcanic processes to take place as the liquid acts as the 'magma'. Heating from radionuclides in rocky cores has been modelled to keep an icy body sufficiently warm over billions of years to stop liquid freezing completely. Once freezing starts to take place, latent heat of crystallisation is sufficient to stop the whole liquid ocean from completely freezing. As water freezes to ice, the volume expands, creating pressure on the overlying crust. Cracks may start to appear in the crust at depth, and is plausible that these cracks could propagate to the surface over a short timescale (i.e. a day). Since the remaining liquid not freezing will become concentrated in ammonia, as the liquid is forced to rise to the surface from the pressure of freezing ice, the timescale for freezing is longer than the ascent time, so liquid cryovolcanism could occur on icy bodies.

The surface of Pluto is more than 98 % nitrogen ice, with traces of methane and carbon monoxide [63]. Nitrogen and carbon monoxide are most abundant on the anti-Charon face of Pluto, where Sputnik Planum is located. Sputnik Planum is the active, lighter coloured heart-shaped feature on Pluto, is rich in volatiles, and has glaciers flowing into and out of the plain (see Figure 1.10). There are thoughts that this could be formed from cryovolcanism from an interaction with a subsurface ocean. This is apparent due to the appearance of polygonal cells which are interpreted as convection cells carrying floating blocks of water ice crust and sublimation pits. The lack of impact craters suggests that this feature must be less than 10 million years old [100, 139], so it is thought that Pluto is still geologically active to this day. Charon is also most likely still geologically active due to its few impact craters; the southern hemisphere has fewer craters than the north, suggesting a massive resurfacing event - perhaps prompted by the partial or complete freezing of an internal ocean.

On Titan, cryovolcanism from water-ammonia mixtures has been proposed, and along with cratering processes, can lead to liquid interaction on the surface with aerosols in Titan's dense atmosphere, such as small amounts of CO_2. Urea is a main compound of Titan's tholins hydrolysed in ammonia, but may take a long period of time to form. Since urea is related to ammonium carbonates by the addition of H_2O, it seems plausible that water from depth could be interacting with aerosol deposits forming urea to produce carbonates at or near the surface. This may then be processed by tectonic processes that are thought to occur on Titan, maybe leading to ammonium carbonates at depth within Titan, or near the surface. A lack of free oxygen on Titan would to some seem to inhibit any formation of astrobiological life. However, oxygen is trapped within water which is considered to be abundant on Titan, and so reactions involving water could yield products containing large amounts of oxygen which could be a pathway for organic substances to form.

Cryovolcanic plains have also been observed on Miranda and Ariel that are most consistent with water-ammonia slurries [38].

1.2.3.4 Summary of evidence

Water, carbon dioxide and ammonia possibly occur together on planetary bodies, and so there is a possibility of mixing these parts into the NH_3 - $CO_2 \pm H_2O$ ternary system.

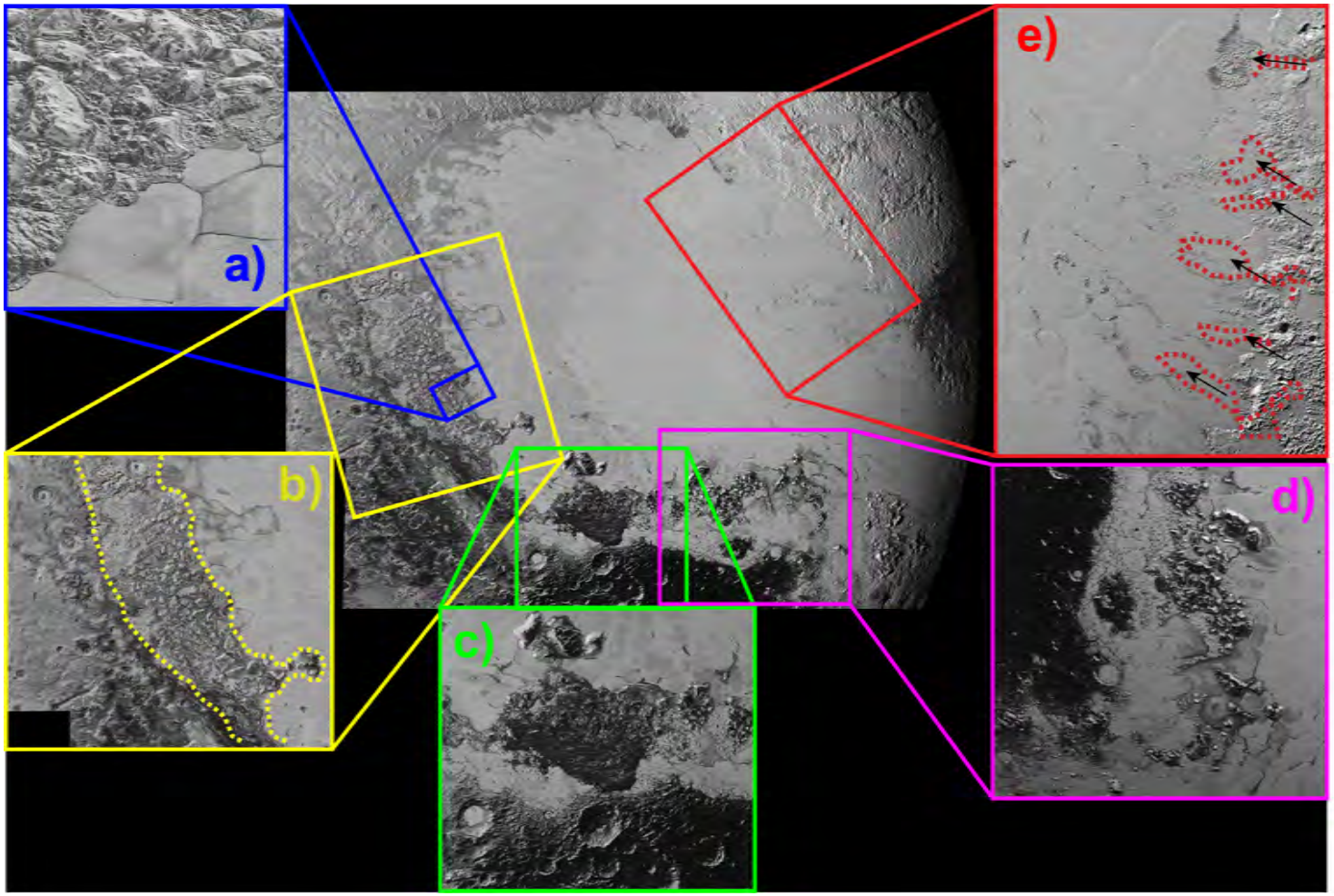

Figure 1.10
Terrains and features around Sputnik Planum on Pluto. **a)** Mountainous shoreline of Sputnik Planum. Large water-ice mountains, standing as much as 1.5 miles high, abruptly ending at Sputnik Planum, a flat plain which is composed of nitrogen-rich ices. The view is about 50 miles wide. **b)** The icy plain of Sputnik Planum to the right, against broken terrain to the centre of the image, and the typical surface of Pluto furthest left. Here the polygonal features of Sputnik Planum can clearly be seen. This image is 300 miles wide. **c)** Cratering can be seen in the ancient plains adjacent to Sputnik Planum, but is not visible (at least down to the scale of the highest resolution images) on the smooth surface of Sputnik Planum itself. This image is 220 miles across. **d)** Dark mountainous region on the southwestern margin of Sputnik Planum. There is a complex relation between the dark material in the mountains and the relatively bright and smooth surface of Sputnik Planum. **e)** Nitrogen glaciers (the extent shown by the dashed red lines) flow from water-ice mountains into the plain below, carrying huge boulders of presumed water ice blocks.

The temperature stability of this system is largely similar to the water-ammonia system, and so liquid interactions at depth could occur as ammonium carbonates, or on the surface as cryovolcanism interacts with surface CO_2 ices.

With potentially large reserves of ammonia inside Ceres, combined with the presence of CO_2 and H_2O, there is strong evidence that ammonium carbonates may form on Ceres. The possible detection of ammonium bicarbonate in some of the bright spots on Ceres further backs this evidence that the ammonium carbonates could be a major constituent of Ceres.

The discovery of ammonium hydrates in a crater on Charon suggests it may be possible that the cryovolcanism seen is derived from an internal ocean kept liquid by the presence of ammonia. With the detection of carbon monoxide, it seems plausible that the three components ($NH_3 - CO_2 - H_2O$) will interact with one another. Indeed, in the experience in this project in the handling of these components, even a brief interaction will cause ammonium carbonates to form. The lack of detection so far may not be due to the lack of ammonium carbonates on Pluto or Charon, but could be due to the poor understanding of the spectroscopic signatures and material behaviour of these icy compounds.

Low concentrations of ammonia are likely to produce ammonium carbonate monohydrate, ammonium sesquicarbonate, and ammonium bicarbonate. The controlling factor in the formation of carbonates is unlikely to be abundance of water, which is common in the outer solar system. Sufficient ammonia would have to be present to melt the water at low temperatures, and there is typically more CO_2 present than ammonia in many bodies.

Much of the previous work has focused on the presence of ammonia occurring in or on icy bodies in the solar system, or on water-ammonia solutions in subsurface oceans. Little work has been conducted directly on ammonium carbonates, and what has been done is mainly qualitative, focusing more on the possible existence as opposed to detailed structural and spectroscopic information. The problem is having both ammonia and carbon dioxide free and abundant at the same time to form the carbonates in icy bodies.

Understanding how a body so far from the Sun, and with presumably a mainly icy composition, can generate sufficient interior heat to create some of the features, is

now the focus of investigation, challenging views on how bodies form and evolve in the outer solar system.

1.3 Work in this project

As discussed, understanding of ammonium carbonates is important from earthly matters of climate change to planetary applications, but knowledge under non-ambient pressure and temperature conditions is entirely absent, especially towards higher pressures extant in the interiors of large icy bodies. This severely limits modelling of NH_3 + CO_2 $\pm$ H_2O behaviour in solids and fluids in planetary bodies. The problem is the lack of structural and stability data that could be used in planetary modelling, and spectroscopic information to help identify the associated compounds on planetary surfaces. On Earth, structural data could be important for helping to understand how best to use this material for carbon-capture schemes and hydrogen storage.

In order to determine bulk properties of the ammonium carbonates, two methods have been used - *ab initio* calculations using density functional theory, and diffraction techniques involving neutrons and X-rays (see Chapter 2). The first piece of work in this project was to replicate the *ab initio* calculations by Tse & Klug, 1998 and Fortes, 2004 [140, 51] for water ice, specifically in its high-pressure, low temperature proton-ordered phase, ice VIII, to ensure the methodology and simulations are working accurately and so could then be applied to the ammonium carbonates (see Chapter 2).

Chapter 3 presents the results of the *ab initio* simulations of ammonium carbonate monohydrate, $(NH_4)_2CO_3 \cdot H_2O$, and ammonium sesquicarbonate monohydrate, $(NH_4)_4[H_2(CO_3)_3] \cdot H_2O$, reporting the structural behaviour of each of these two compounds under pressure.

In Chapter 4 the results of the *ab initio* simulations of the ambient phase and high-pressure phases of urea, phases I, III, and IV, are presented. This work has determined athermal equations of state for each phase, the pressure dependence of the structure of each phase, and relative stability of these compounds.

Chapters 5 & 6 reports the work on the two reported phases of ammonium carbamate - α and β - and of ammonium bicarbonate respectively. The work started with *ab initio* simulations of these compounds under high-pressure; these results were used and compared with follow-up experimental work, to show validity and accuracy of com-

putational methods on the ammonium carbonates. Experiments were carried out at the *ISIS* neutron spallation source, determining the thermal expansion of both compounds, and their behaviour under pressure.

Chapter 5 reports the results of two neutron diffraction experiments at *ISIS* completed on ammonium carbamate: the first from *HRPD* looking at a refined structure at 4.2 K and subsequent thermal expansion measurements from 4.2 K to 180 K; the second being a high-pressure single crystal Laue diffraction experiment on *SXD*.

Chapter 6 reports the results of experiments on ammonium bicarbonate, with a thermal expansion study measured on *HRPD*, and high-pressure studies on the behaviour and polymorphism measured on *PEARL*.

The final chapter, Chapter 7, presents the conclusions from the *ab initio* simulations and the experimental data obtained during this work.

Chapter 2

Experimental methods and *ab initio* simulations

The work in this project falls into two categories: calculations based upon density functional theory (DFT), and experimental work. Advances in the calculations have increased the reliability and efficiency of the output, but the outputs are not always a true reflection of material properties and only experimental work provide the true answer. The DFT calculations, however, still complement experimental work and have provided reliable results. The experimental work also has the advantage of having extra information, such as phase changes, and other properties that can be measured in situ - such as Raman spectra - that cannot thus far be calculated easily (or at all) using DFT.

This chapter focuses on the theory and methods behind material science experiments. It is by no means an exhaustive review of all experimental techniques that can be applied, but rather focuses on the experiments and simulations relevant to this project. The next section gives a brief explanation behind the theory of all diffraction techniques, followed by details of diffraction techniques used throughout this project.

2.1 Experimental methods

2.1.1 Theory of diffraction

Diffraction, as originally discovered, is the process by which a system of waves of the same wavelength interacts with small apertures in a barrier, creating a secondary set of waves at each hole. In certain directions, through a process of *interference*, this secondary set of waves either gain amplitude by *constructively* interfering when ‘in

phase', or cancel out completely by *destructively* interfering when 'out of phase'. A barrier with more apertures will produce a sharper diffraction pattern.

A crystal can act as a three dimensional diffraction grating due to the long range order of atoms at regular spacings. The wavelengths required for diffraction to occur from crystals is in the same order as the interatomic spacing of atoms in the structure. The incoming electromagnetic radiation interacts and forces the electronic cloud around an atom to move. This movement of charges creates waves with the same frequency as the incoming waves (i.e. creates secondary sources of radiation), which are then radiated in all directions away from the atom. In this project, only elastic scattering is used, in which the assumption made is that no energy is lost in this process.

This process, however, is hard to visualise, so instead the incoming waves can be thought of *reflecting* from a family of planes (*hkl*) in a crystal. This 'mirror' will only work if the reflected waves from successive planes are in phase. To obtain diffraction therefore, a given set of planes must obey the condition

$$\lambda = 2d\ sin\theta \tag{2.1}$$

with the angle of incidence and angle of 'reflection' both equal to θ. This simple equation, known as Bragg's Law, allows us to determine spaces between layers of atoms in a material, and ultimately determine where the atoms are located in the crystal. By knowing where the atoms are placed, models can be applied to determine how the material in question behaves. The wavelengths required for diffraction from crystals means only certain radiation can be used. There are typically two different sources of radiation for crystallographic studies; neutrons and X-rays, discussed next.

2.1.2 X-ray diffraction

X-rays have wavelengths on the order of interatomic spacing in crystals; for crystallography wavelengths are typically around 0.5 - 2.0 Å (1 Å $= 10^{-10}$ m).

2.1.2.1 X-ray production

X-rays are produced by passing a high current through a metal filament, freeing electrons from the metal. A high voltage is applied to accelerate the electrons away from the filament and towards a target material (such as tungsten). It is important for the X-ray

tube to be under a high vacuum to achieve the greatest efficiency. There are two types of X-ray generated using this method; characteristic radiation and Bremsstrahlung radiation.

Bremsstrahlung radiation (or 'braking' radiation) is produced when electrons approach an atom in the target material and are slowed or completely stopped, due to the like charge of the high speed electron from the filament and the electrons surrounding the target atom. As the electron is slowed down, it exits the material with less energy and thus, due to the conservation of momentum, the excessive energy is radiated away. If the electron is stopped by the positive force of the nucleus, the radiated X-ray energy is equal to the total kinetic energy of the electron; this occurs with very large and heavy nuclei materials. Approximately 80 % of X-rays produced are generated in this way.

Characteristic radiation is produced when the high energy electron from the cathode collides with an innermost shell (K shell) electron of the target; both of these electrons are ejected from the atom. An outer shell (L or M shell) electron falls down to the K shell by losing energy; this energy is discrete and in the form of an X-ray photon. This gives rise to spectral lines. The strongest spectral line is called the Kα line, and is actually a closely spaced doublet visible at high Bragg angles in an X-ray diffraction pattern, which needs to be reduced to the stronger of the two signals using a monochromator, stripped in software after measurement, or included in the calculation of the diffraction pattern.

2.1.3 Neutron diffraction

Unless the atom has a magnetic moment, neutrons are scattered by the nuclei of atoms rather than the electron cloud, so have a number of advantages and over X-rays, which will be discussed in the next section. The basic properties of the neutron makes them extremely useful for studying condensed matter. The mass of a neutron means the de Broglie wavelength,

$$\lambda = \frac{h}{mv} \tag{2.2}$$

can be in the order of interatomic distances in solids and liquids, so (much like X-rays) interference effects give us information on the structure of the system.

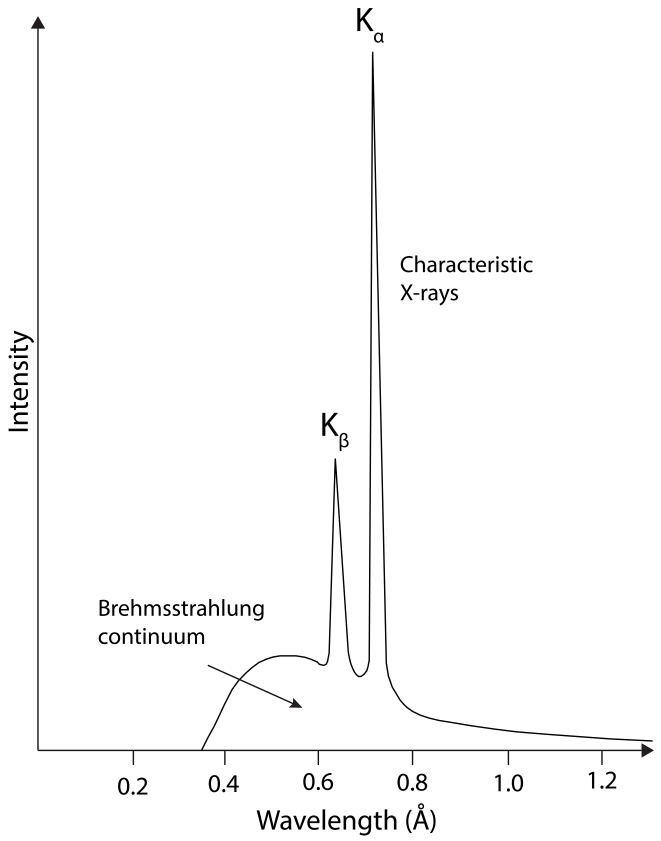

Figure 2.1
Graph of the spectrum of radiation producing from a molybdenum target at 35 kV. The background radiation is from the Bremsstrahlung process, and the two peaks are from spectral line processes.

2.1.4 Neutron production

There are two main methods for producing neutrons; from reactor sources, and by spallation. Both methods produce neutrons with extremely high energy, far higher than is useful for crystallographic analysis. The source neutrons must have their energies reduced to a useful range by 'bouncing' inside a material. The choice of material for use as this moderator is important as it will control the wavelengths of neutrons that an instrument or group of instruments receives.

Reactor sources have 'hot neutrons' ejected as a by-product of a nuclear reaction, either as a waste product if the reaction is used for energy generation, or intentionally as in a scientific research facility. The neutrons in either case can be directed away from the reaction and into a material for moderation before being guided into specific target stations, where instruments are placed to measure samples. An example of a neutron reactor source is the 'Institut Laue-Langevin' (ILL) located in Grenoble. At the

ILL, the moderation is controlled by a large tank of D_2O surrounding the reactor core, which reduces the thermal neutrons to the same kinetic temperature as the D_2O itself; most of the neutron ports and guides view this moderator. To make longer wavelength neutrons there are tanks of liquid hydrogen, and for higher energy neutrons there is a large graphite block at 2500 K.

A spallation source is caused by firing protons at very high speeds and energies at a heavy metal target. As the protons hit the target, they knock out - or 'spall' - neutrons, which are then guided into target stations. Spallation sources usually use a pulsed beam of neutrons for increased precision in measurements, but at the cost of flux. An example of a spallation source is the Rutherford Appleton Laboratory at the ISIS neutron spallation source. Here, there are similar moderators arranged above and below the target, inside a block of beryllium rods. *SXD* views a moderator filled with warm water, whilst *HRPD* and *PEARL* view a liquid methane moderator. By virtue of being colder, the methane produces 'cooler' neutrons and so *HRPD* and *PEARL* have a spectral peak at longer wavelength.

2.1.5 X-ray diffraction vs. neutron diffraction

There is considerable work showing the advantages of neutrons over X-rays for hydrogen bonded materials, so this work will not dwell upon this too much. The reader is pointed to the work by Von-Dreele (1990) [143]; this gives an in-depth review of the processes of X-ray and neutron diffraction and how they compare with each other.

Neutrons interact weakly with atoms and so neutrons can travel a long distance before being scattered or absorbed in a material. Therefore, neutrons measure the bulk of a sample so sample texture is not much of an issue, unlike X-rays which measure the surface of a sample and are more susceptible to artefacts from sample texture. It also means larger sample sizes in neutron diffraction experiments, which allows for the bulk sample to be measured, rather than the surface.

In X-ray diffraction, the atomic scattering factor, f, increases with atomic number. For neutrons however, the scattering length does not simply increase with atomic number, but varies for neighbouring elements and even isotopes in the periodic table. This means that, in a sample containing both heavy and light elements, neutrons will 'see' scattering from both kinds of atoms, whereas in X-rays the lighter elements barely scat-

ter any X-rays. In practice, this means you obtain more uniform precision on positional and displacement parameters than in an X-ray diffraction experiment. It also allows for an experiment to be tuned by isotopic substitution to better determine site occupancies by elements with similar atomic number .

Furthermore, the scattering length does not decrease as $\sin\theta/\lambda$ increases for neutron diffraction unlike X-ray diffraction. This means that Bragg reflections with small *d*-spacings are relatively stronger in neutron diffraction than X-ray diffraction. This is particularly useful for powder diffraction experiments, since the reflections revealing details in the structure are not as weak and so these details can be better constrained.

For this work, neutron diffraction is much more suited than X-ray diffraction. Since there are a large number of hydrogen atoms in the compounds of this ternary system, X-rays present a much weaker signal than that of neutrons for hydrogen atoms, which is particularly important since the majority of bonding and therefore the behaviour of the system is determined by the network of hydrogen bonds. In order to characterise the behaviour of these extensively hydrogen bonded compounds, it is important to understand the measure the properties of these hydrogen bonds.

In order, however, to accurately and precisely measure the position of these protons in these structures when using neutrons requires the compounds to be perdeuterated. This is because hydrogen (^{1}H) has a very large incoherent scattering length, resulting in a very large diffuse background and therefore a much weaker diffraction pattern, unlike deuterium (^{2}H or D) which does not suffer this issue. Therefore, an assumption has to be made that samples that are perdeuterated have the same behaviour as their protonated counterparts. This is a reasonable assumption to make, since the differences are usually very small, and the drawbacks of a slight difference is less than the benefit of measuring very precise proton positions. Also, since there are a range of lighter and heavier elements, hydrogen up to oxygen, if measured using X-rays, the majority of the scattered radiation is from oxygen and the least is from hydrogen. For neutrons, this does not apply, since the scattering length does not vary systematically with atomic number.

However, limited access due to the large cost of running a facility, requiring many people to run the instruments and the large energy consumption required, means only the most scientifically interesting of the ternary compounds will be studied using neu-

trons.

2.1.6 Time-of-flight (TOF) diffraction

Combining the de Broglie relation (eq. 2.2) with Bragg's Law (eq. 2.1) gives:

$$\lambda = \frac{h}{mv} = 2d\ sin\theta \tag{2.3}$$

where h is Planck's constant and m is the mass of the neutron. Since it will take time t to for a neutron to travel length L from the source to the detector, this gives Bragg's Law as:

$$t = \frac{2mL\ sin\theta}{h} d \tag{2.4}$$

This technique is called the time-of-flight method, which is an energy dispersive method. Unlike energy dispersive diffraction in which the Bragg angle is varied, the time-of-flight method has fixed Bragg angles, and can achieve a very high resolution. The high resolution is derived principally from the high precision with which the travel time of neutrons from their source to the detector may be measured, a quantity whose error is minimised by making the primary flightpath (L) longer and by placing detectors at the highest possible backscattering angles (θ). It requires the beam to be pulsed so the start time of the neutrons is known precisely. Although a long flight path gives high resolution, the beam intensity decreases with increasing flight path. The loss of flux can be minimised by using neutron guide tubes, but this comes at the expense of beam divergency.

TOF diffraction can have very small errors in the crystallographic measurements of cell parameters due to:

$$\frac{\Delta t}{t} = \frac{\Delta d}{d} \tag{2.5}$$

If the pulses of neutrons are of a short duration, Δt can be very small.

Now the theory behind the diffraction experiments has been covered, the next section will give some details about the specifics of the instruments used, and the sample environments in which the samples were run - high-pressure and/or low temperature.

2.1.7 Sample environments

In this project, two experiments were carried out on α-ammonium carbamate (Chapter 5) and two sets of experiments on ammonium bicarbonate (Chapter 6). These experiments were done at the ISIS neutron spallation source at the Rutherford Appleton Laboratory, a pulsed spallation source that allows for high precision measurements using the time-of-flight diffraction technique. In these experiments, equipment was used that allowed for *in situ* measurements of the properties of materials in relevant conditions to those that exist in the outer solar system. Here follows a description and explanation of the sample environments used in this thesis.

2.1.7.1 Low temperature

The compounds in this ternary system are, on the most part, only stable below 273 K due to the volatility of ammonia[1]. In the outer solar system, temperatures are below ∼120 K, so to understand material properties for planetary models, there is a need to measure the ammonium carbonates at these relevant temperatures. In industrial processes, the temperatures will not be this cold since it requires large amounts of energy to cool industrial scale processes below room temperature. Therefore, to be applicable to both areas, the ammonium carbonates need to be measured at both these ranges.

To achieve this, the sample environment of choice is a cryostat or a closed-cycle refrigerator (CCR). The difference between a cryostat and a CCR is the use of refrigerant - cryostats require cryogenic fluid (such as liquid helium), which is becoming increasingly expensive, whereas CCRs are cryogen-free (hence sometimes called 'dry cryostats').

A continuous-flow cryostat uses cryogens to cool the sample. In the experiment to determine the thermal expansion of α-ammonium carbamate, a helium-filled cryostat was used and was capable of reaching ∼1.5 K by pumping to reduce the helium vapour pressure (generated with an extra vacuum pump, which brings the boiling point down from 4.2 K to 1.2 - 1.6 K) around the sample environment. The temperature is controlled in the sample environment by altering the rate of flow of the cryogen, with a higher flow rate having faster cooling rates; once at a given temperature the flow is backed off to prevent condensing liquid around the sample. Boil-off leakage issues are

[1] Ammonium bicarbonate and urea are the exceptions to this, stable to ∼330 K and ∼400 K respectively

the main problem with this type of cryostat, since it requires greater volumes of cryogens than other cryostats. Due to the scarcity of some liquid cryogens (namely liquid helium), this type of refrigeration method is expensive to run, and so is not typical, and ideally requires an expensive form of cryogen capture and recovery system.

On the other hand, a closed-cycle cryostat, or closed-cycle refrigerator, also uses cryogens to cool the sample, but the cryogen is instead recycled around the system, with the cooling power being derived from compression and expansion of the gas. In principle, the system requires no refills; this means that this type of cryostat can be run indefinitely - although systems do leak mean and require occasional top-ups - and it consumes a large amount of electricity. The process of recycling the cryogens follows the Gifford-McMahon thermodynamic cycle - a description of this cycle is given in Figure 2.2. Additional stages can be added to the system, which feeds low temperature gas from previous larger volumes. There are further technologies that can be used to cool the sample, such as thermoacoustic technology.

In this project, there were two different CCRs used. At ISIS, for the low temperature sample environment, a top loading CCR was used, capable of temperatures of 10 K - 400 K. The top loading allows samples to be lowered into the sample environment from above, and therefore the sample environment remains in the beam line and the sample tank's cryogenic vacuum (order 10^{-5} mbar) remains unbroken so the sample can be loaded and changed easily. On the in-house X-ray diffractometer at UCL, a PheniX-FL CCR was used, capable of measuring powder samples from 40 K to 290 K, and designed to allow front loading for easy sample changes and sample loadings at liquid nitrogen temperatures [151].

2.1.7.2 High-pressure

Since the prospect of detecting ammonium carbonates in the outer solar system is likely to occur at depth within a body[2], it is important to understand how these compounds behave as a function of pressure and temperature. In this project, two pieces of equipment were used to re-create the conditions found in the interior of a planetary body.

The equipment required to reach high-pressures usually consists of large pieces

[2]Due to radiation breaking down ammonium carbonates, it is unlikely that they would be found on the surface. Furthermore, they are likely to account for the anti-freeze component in a body to allow an internal ocean to form.

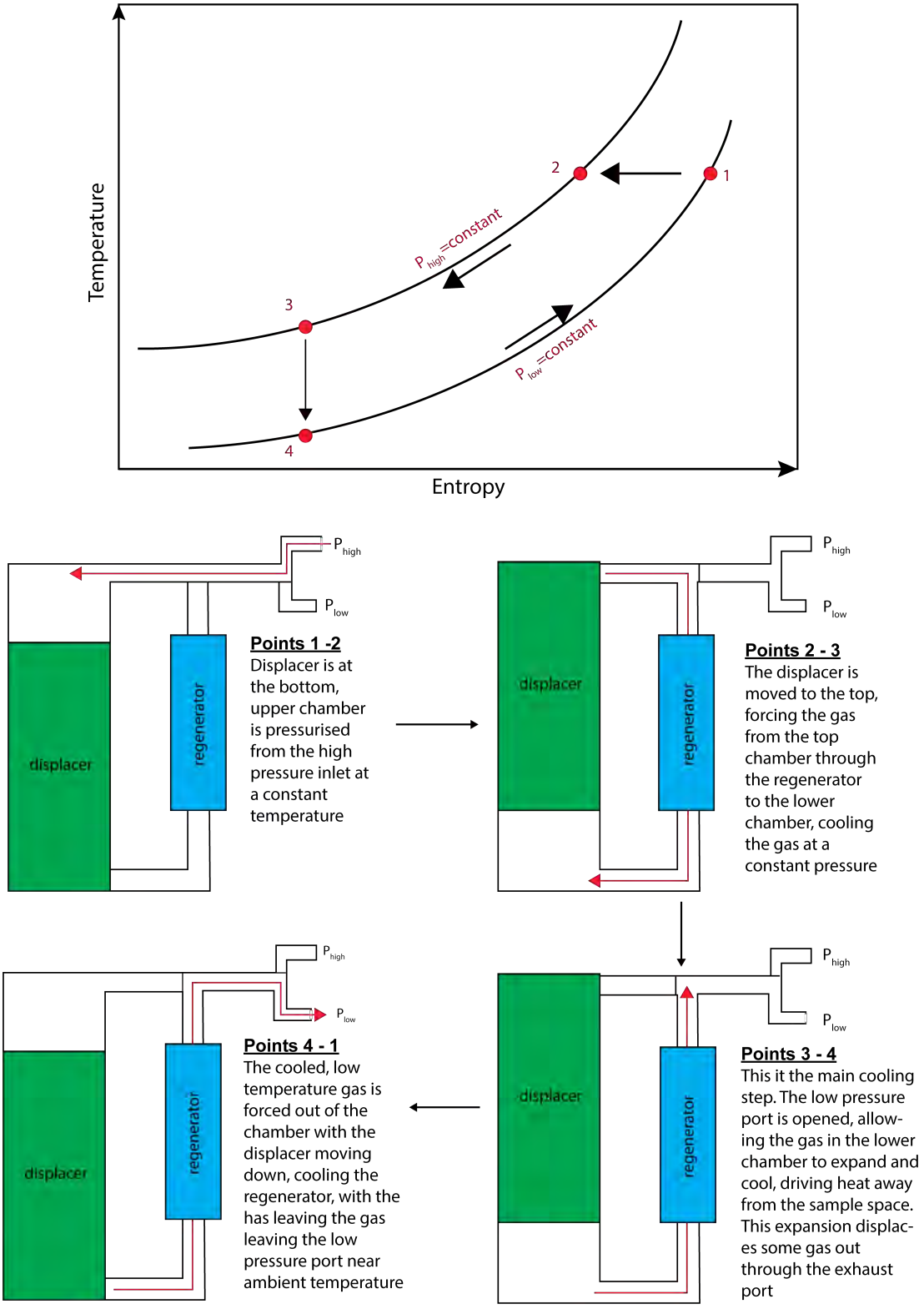

Figure 2.2
Configuration of the Gifford-McMahon thermo-dynamic system during a cycle. The system follows the graph at the top, with each point explained below. A CCR uses this process, which requires no refills of cryogens, but consumes a large amount of electricity.

of metal, with small gaps to allow the incoming beam to reach the sample and the diffracted beam to exit from the sample to the detector, and so data often has signals coming from the sample and the sample environment. An example of this is given in Figure 2.4, in which ammonium bicarbonate was measured on *PEARL*, but also contains additional peaks from the sample environment.

One such example of this is the Paris-Edinburgh press (Figure 2.3). Collaboration between the Universities of Paris and Edinburgh led to the development of the press. Equipped with Bridgman-type opposed anvils, with a toroidal profile, and based upon an existing anvil design by Khvostantsev, this high-pressure device allows for samples to be squeezed to pressures up to ca. 30 GPa, with temperatures up to 1400 K. Multi-anvil presses have the advantage over other high-pressure devices in that they have larger sample volumes - larger sample sizes are needed for neutron diffraction experiments due to the lower flux.

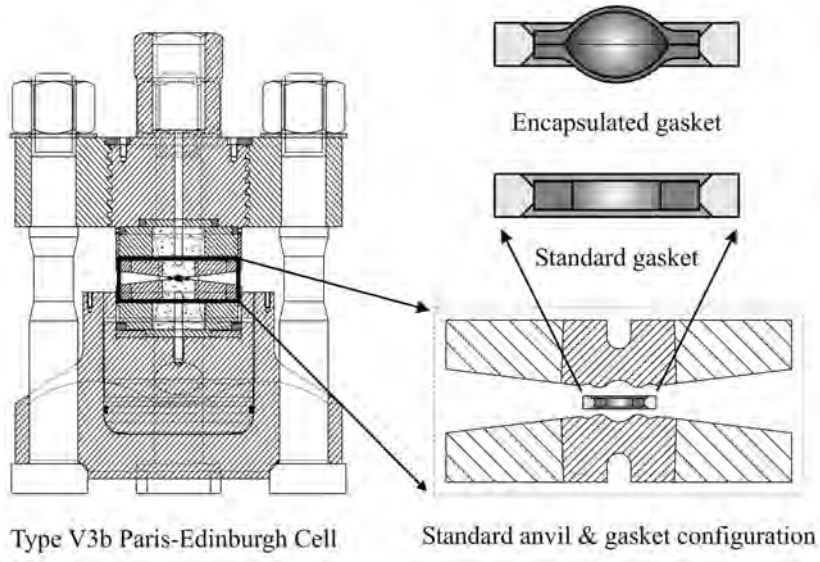

Figure 2.3
The V3b variant of the Paris-Edinburgh pressure cell (left), the standard anvil and gasket configuration (right, lower), and the standard and encapsulated gasket designs (right, upper). Drawing from Marshall & Francis, 2002 [94].

Another type of high-pressure device is a gas cell. High-pressure gas is used to squeeze the sample uniformly in all directions. The advantage of this method is that the sample is isotropically stressed, but due to the pressure of the gas, pressures are limited to be much smaller than in multi-anvil presses. This style of pressure device was used in the α-ammonium carbamate high-pressure experiment on *SXD*.

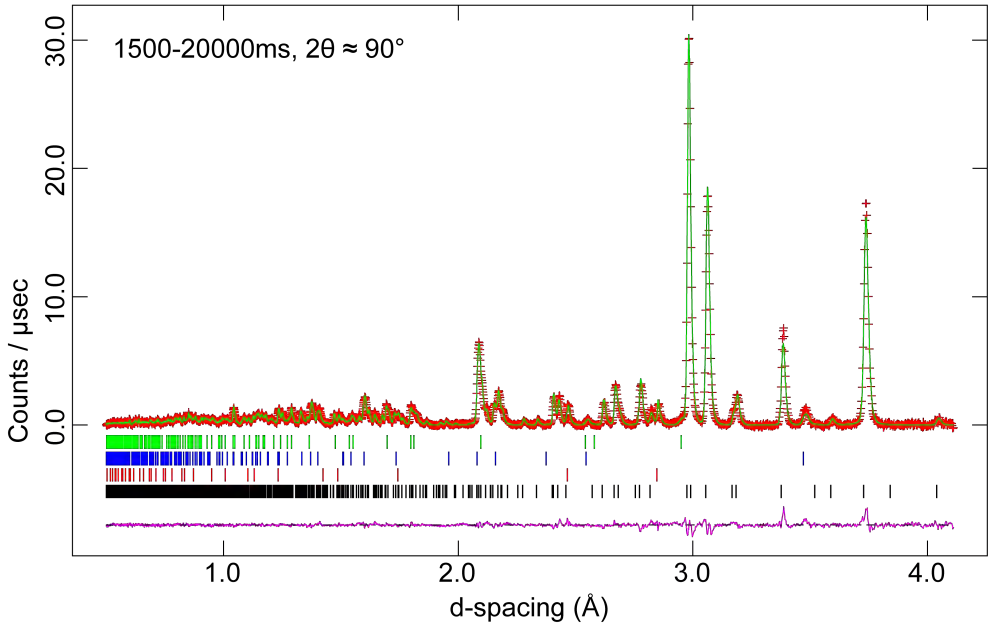

Figure 2.4
Rietveld refinement of ammonium bicarbonate at room temperature and 0.372 GPa (equivalent to a load of 60 bar). The ambient unit cell matches well with this pressure, with axes shortened (see other figure). Black tick marks correspond to ammonium bicarbonate, and the green tick marks to lead (used as a pressure determinant). The remaining tick marks are from the anvils and pressure cell - alumina (blue) and zirconia (red).

2.1.8 Instruments

Three instruments were used at the ISIS neutron spallation source, known as *HRPD* (section 2.1.8.2), *PEARL* (section 2.1.8.3), and *SXD* (section 2.1.8.4). Proposals were submitted and accepted to measure α-ammonium carbamate and ammonium bicarbonate on these instruments, to determine material behaviour under changing temperature and pressure conditions. Before travelling for these experiments, samples were prepared at UCL and checked on the in-house X-ray diffractometer.

2.1.8.1 PANalytical X-ray Powder Diffractometer

The laboratory at UCL houses a *PANalytical X'Pert Pro* multipurpose powder diffractometer. This uses germanium-monochromated Co $K\alpha_1$ radiation (λ= 1.788996 Å) and an X'Celerator multi-strip detector. Data is collected with variable divergence and receiving slits, converted to fixed-slit geometry with the proprietary *X'Pert Pro HighScore Plus* software package, and exported in an appropriate format for analysis in the *GSAS/Expgui* package. Samples were either loaded on to a back-loaded spinner stage if the sample was stable in air at room temperature (namely ammonium bicarbonate),

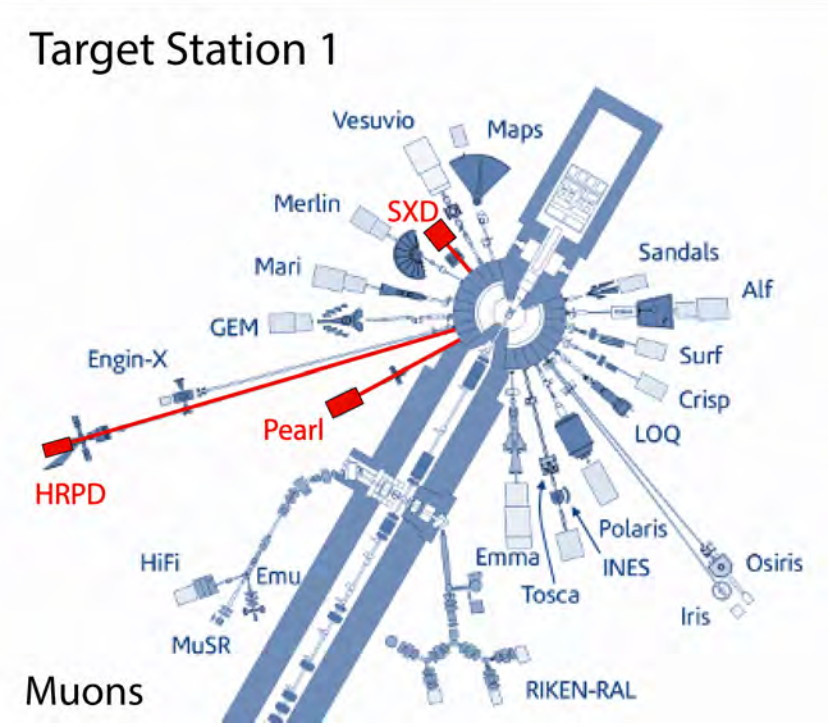

Figure 2.5
Schematic view of the instruments in Target Station 1 (TS1) at the ISIS neutron spallation source. There are 24 instruments in TS1 specialising in neutron imaging, muon spectroscopy, neutron spectroscopy, reflectometry, small angle scattering, and the technique used in this work, neutron diffraction The instruments coloured in red are those that have been used during this work

or using the modified PheniX-FL CCR if the sample needed to be loaded cold (namely α-ammonium carbamate). This piece of equipment was used to determine the purity and phase of the samples before travelling to the neutron spallation source.

2.1.8.2 HRPD

This instrument is known as the 'high resolution powder diffractometer', with a resolution $\approx \Delta d/d\ 4 \times 10^{-4}$ in the backscattering bank (see Figure 2.5).

On *HRPD*, the sample is located 95.0 m from the liquid methane moderator, making it one of the longest flightpath instruments in the world. However, this creates two problems, the biggest of which is overcoming the loss of beam intensity due to the inverse square law. In order to transport a reasonable flux of neutrons over almost 100 m, it is necessary to use a specially coated guide tube with particular geometric characteristics. *HRPD* uses a glass guide coated with a nickel multilayer (a so-called supermirror) that has an elliptical profile lengthwise - it has narrow entrance and exit apertures but is fatter in the middle - and is also curved in the horizontal plane; the first

60 m of the guide has a radius of curvature of 38 km and the final 33 m are straight. Thanks to this guide, the neutron flux on the sample is several orders of magnitude higher than it would be otherwise.

The long flightpath's other problem emerges due to the finite velocity of the neutrons. *HRPD*'s moderator produces neutrons with wavelengths between about 0.3 and 12 Å. The short wavelength neutrons travel very fast and the long wavelength neutrons travel very slowly. Over a 100 m flightpath, the fast neutrons from one pulse catch up with the slow neutrons of the previous pulse, producing a continuum that destroys the time structure that underpins the time-of-flight measurement method. Effectively, the pulses have to be trimmed in order to avoid overlap, and this is done with rotating disc choppers that block the beam for part of the time and admit it at others. Using a pair of choppers, one at 6.3 m and the other 10.3 m from the moderator, *HRPD* can tune both the bandwidth and the band centre of the wavelength range it sees, whilst avoiding pulse overlap.

This so-called 'time window' is normally set to allow neutrons with flight times that differ by 100 ms onto the sample, with the starting offset being adjusted depending on the needs of the sample and the measurement. The standard range is 30 - 130 ms, although 100 - 200 ms is often used as well (giving d-spacings between 0.3 Å to 5-6 Å in the highest resolution backscattering bank). However, with the orthogonal and low angle banks, diffraction data can be collected right out to 20 Å, albeit with a lower resolution.

Samples are powdered and loaded into an aluminium-framed slab-geometry can, with vanadium foil windows indium-sealed to the front and back faces of the slab-can, with exposed components (such as screws) on the incident-beam side masked by gadolinium foil to prevent additional peaks from the sample environment. A heater is attached to the slab-can with a RhFe resistance thermometer to accurately record the temperature across the sample.

In this work, this instrument was used to measure the thermal expansivity of α-ammonium carbamate (details of this experiment is given in Chapter 5), and to measure the thermal expansivity of ammonium bicarbonate (details of which is given in Chapter 6).

2.1.8.3 PEARL

This is a medium resolution high-flux diffractometer (see Figure 2.5) optimised for use with Paris-Edinburgh presses, designed for *in situ* studies of materials at high-pressures and varying temperatures. The maximum pressure that can be achieved is ∼28 GPa, but typically it goes no higher than around 12 GPa. A recent review paper of the instrument is provided in Bull *et al*., 2016 [23][3].

The sample is loaded into a small Ti-Zr gasket, composed of 67.6 mol% titanium and 32.4 mol% zirconium - since these elements have positive and negative neutron scattering lengths respectively, the gasket effectively has no *coherent* contribution to the diffraction pattern. A pressure marker is added to determine the pressure at the sample. To allow for hydrostatic compression, a pressure-transmitting fluid is also added; most commonly used is perdeuterated methanol/ethanol mixture in a 4:1 volume ratio. This allows for hydrostatic compression at room temperature up to ca. 10.5 GPa (and beyond if heated above the freezing point of the mixture). Also available are pentane/isopentane mixtures and Fluorinert, but these are limited to hydrostatic pressures of 6 GPa and 2.5 GPa respectively.

The gasket is loaded into the cell, and placed between high strength toroidal anvils. There is a choice of anvil materials available for use: tungsten carbide (WC); sintered diamond (SD); zirconia-toughened alumina (ZTA). Ceramic ZTA anvils are used for the majority of experiments due to their all-round suitability between 0 GPa and 7 GPa, and over the temperature range 80 K to 500 K - mainly due to their high neutron transparency. The anvils are shielded using a boron carbide epoxy mixture to reduce unwanted scattering.

PEARL was used to determine the high-pressure behaviour of ammonium bicarbonate, in which new high-pressure phases were discovered. The details of this experiment is given in Chapter 6.

2.1.8.4 SXD

Named the single crystal diffractometer, this instrument can measure in large three dimensional volumes of reciprocal space in a single measurement using the time-of-

[3]This paper contains data collected from this work. Figure 6(b) is ammonium bicarbonate as measured on PEARL in the second experiment, utilising the long *d*-spacing frame (see Chapter 8 for details on the experiment). Section 6.3. Planetary bodies contains details relevant to the work in this project.

flight Laue technique (see Figure 2.5). A review of the *SXD* instrument is given in Keen *et al.*, 2006 [74]. *SXD* is used to determine high precision structural properties of crystals, particularly useful for locating missing protons in structures, and to measure thermal parameters (librations) on single or groups of atoms.

The instrument also has the advantage of being able to simultaneously collect data from multiple crystals - crystals are placed in different orientations, and the time-sorted Laue method can be used to distinguish Bragg reflections from the different crystals. This allows for quicker data collection, significantly greater over-determination of intensities, or can overcome issues from sample apparatus with reduced flexibility.

SXD has a number of sample environments designed specifically for use on the diffractometer. This includes a CCR capable of temperatures between 10 K and 300 K (which can be used in conjunction with a helium gas pressure cell with pressures up to 0.2 GPa and 0.5 GPa), and a helium cryostat capable between 1.6 K and 300 K.

textitSXD was used in a single crystal neutron diffraction measurement of the structure of α-ammonium carbamate under pressure, the details of which are given in Chapter 5.

2.2 Summary

In Section 2.1, a brief explanation of the experimental methods used throughout this work was given. It started by explaining X-ray diffraction and neutron diffraction, followed by explaining why neutron diffraction is most suited to the compounds forming in this ternary system. This then moved on to giving descriptions of the sample environments used to replicate the conditions that would be found in the outer solar system, and the instruments that would be used to measure the behaviour of the samples. The next section gives details on the theory behind the density functional theory calculations used in this project.

2.3 *Ab initio* simulations

The simulation of matter has come to the forefront of modern science. There is a growing need to understand the properties of materials and processes on an atomic

level to develop modern materials science. The laws governing the interactions at the atomic level are quantum mechanics. Detailed understanding of the equations covered by quantum mechanics is an absolute requirement for modelling materials with many atoms. However, quantum mechanics is a complex area to study, requiring computations on powerful machines which have only become feasible in recent times.

'First principles calculations' require in principle little more than fundamental equations containing fundamental physical constraints such as the Planck constant, the mass of an electron, the nuclear mass, and inputted into systems with the atomic coordinates and species. The calculations are complex and can be computationally intensive, but with the advance in computational power, and a series of assumptions and approximations, this approach is becoming ever more relied upon and accurate.

In this study, *ab initio* calculations are employed to simulate the material properties of ammonium carbonates. Before the results, however, it is worth considering the theory behind the quantum mechanical methods, including the assumptions and approximations made to simplify and increase efficiency of the calculations but still maintain accurate results. One of the first approximations we can make is known as the Born-Oppenheimer approximation.

2.3.1 Born-Oppenheimer approximation

To simulate materials, we need to know how the atoms move inside solids and liquids. How these atoms move depends both on the nucleus and the electron cloud surrounding the atom. Knowing how these move however is complicated; and since we typically have many atoms inside solids and liquids, knowing how the nucleus and electrons of each atom move with respect to each other is a huge problem. To simplify this, we make two assumptions: 1) compared to electrons, nuclei are massive and slow, and 2) that the electrons are always found in the lowest energy state, or ground-state. These two assumptions are known as the Born-Oppenheimer approximation.

The first approximation is based on the fact that, compared to electrons, nuclei are massive and slow. Electrons will react almost instantaneously to nuclear motion whereas moving one nucleus would have very slow effects on other nuclei; we therefore assume that the nuclei are static, and hence only need to know how electrons move.

Secondly, since the electrons are assumed to be in the ground-state, we do not need

to worry about excited states. Most materials will have electrons in the lowest energy configuration, so for most systems this is a good assumption to make.

These two assumptions simplify the problem of calculating material properties hugely. We now only have to use quantum mechanics for electrons, and we only need the time-independent (rather than time-dependent) Schrödinger equation.

2.3.2 Time-independent Schrödinger Equation

The theory behind modern *ab initio* simulations using quantum mechanics stems from this time-independent Schrödinger equation:

$$\hat{H}\psi_n = \hat{E}_n\psi_n \tag{2.6}$$

There is a probability of finding an electron within a specific space, which will be referred to as the 'particle in a box' idea. This is where an electron can be considered trapped within a box surrounded by hard walls. There are only certain quantised waves that can be used to show the motion within the box. To describe these waves, we need a wavefunction, ψ_x. However, this wavefunction does not tell us where the particle is within the box - the only way to find it is a probability of the wavefunction to find the particle at position x, $|\psi(x)|^2$.

The position and spin of an electron is important. An electron has internal angular momentum i.e. effectively spinning on its own axis, which is quantised and fixed, and can be either up $\uparrow$ or down $\downarrow$. This means that the wavefunction given to an atom depends on the position and spin of an electron.

The simplest case is to solve this equation for a hydrogen atom, which has one proton and one electron. Since we have only one proton and one electron, these equations are easy to compute. We can solve the Schrödinger equation exactly for a hydrogen atom to determine the allowed energies. This is a relatively simple calculation to compute. So what about a system with more than one electron?

2.3.3 Many electron problem

Up until now, everything seems relatively straightforward - calculate the kinetic energy of electrons and the energy due to interaction of nuclei and electrons, solve the Schrödinger equation, out comes the answer. Easy, right? Well electrons repel each

other due to both having like charge, meaning that their motions are correlated with one another. If electrons did not repel each other, then we would simply have a single electron bodied like equation, which as we have already seen, is easy to solve. However, since they interact we would need to be able to compute the positions of electrons, which is impossible to find exactly.

2.3.3.1 Antisymmetry and Pauli exclusion principle

A second issue is that the wave-function for a system of two electrons is not simple. Take one electron occupying the ground-state, x_1, and the other in the first excited state, x_2, and it should give,

$$\psi(x_1,x_2) = \psi_a(x_1)\psi_b(x_2) \tag{2.7}$$

However, this is not correct for electrons; fermions have spin $\pm\, 1/2$ and hence the two wave-functions *must* exactly change sign, since they would not be distinguishable between each other. This antisymmetry forms part of the Pauli exclusion principle. Therefore, if we swap electrons, the following equation

$$\psi(x_1,x_2) = \psi_a(x_2)\psi_b(x_1) \tag{2.8}$$

can clearly be seen not having a change of sign, and hence is not antisymmetric. Instead, in order to obey antisymmetry the wave-functions of the two electrons need to be in this form:

$$\psi(x_1,x_2) = \psi_a(x_1)\psi_b(x_2) - \psi_a(x_2)\psi_b(x_1) \tag{2.9}$$

In this case, the exchange of electrons would result in an exact change of sign. If the electrons were in the same state, $a = b$:

$$\psi(x_1,x_2) = 0 \tag{2.10}$$

This is the basis of the Pauli exclusion principle; that we cannot have more than one electron in any given quantum state, such as position and spin. The change in sign of the wavefunction when two electrons are changed is known as exchange symmetry, and the energy difference is called the exchange energy.

So herein lies the problem with doing first principle calculations; how do we calculate the ground-state wavefunction of a many electron system? The answer is not a simple one. So how do we get around this problem?

2.3.4 Variational Principle

One of the main challenges in computational science of materials is to calculate the ground-state energy of a system of atoms with nuclei in specific positions. We would like to get a good approximation to the ground-state energy to solve Schrödinger's equation accurately. A system only depends on the number of electrons and the external potential, N and V_{ext} respectively. Since the solution of the equation is an eigenvalue problem, we need to determine the eigenfunctions and eigenvalues of the Hamiltonian; in this case, the eigenfunctions are the wavefunctions, ψ_i. One idea was that we could guess the ground-state wavefunction and vary it.

The trial wavefunction, ψ_T, will always have a greater value than the true ground-state energy, E_0, according to the variational principle. We vary the trial wavefunction until we get the lowest possible value, which will be closest to the ground-state energy and so the best approximation. The problem is that we don't know how many trial wavefunctions are needed to get to the actual wavefunction, and hence the true ground-state energy of the system.

2.3.5 Hartree theory

The repulsion between electrons cannot be ignored, since the energy between two electrons is great enough for us to get the wrong results. But instead of ignoring the correlation between electrons, we can instead ignore the correlation between multiple electrons. Ignoring correlation is the essence of Hartree theory. All electrons are free to move inside an average potential, and since all the electrons are acted on by this average potential, they are behaving like independent electrons, but also feel each other's repulsion in an average sense. This simplifies the many-electron problem, but it is at the expense of correlation.

2.3.6 Hartree-Fock theory

The Hartree-Fock approximation was the first partially useful method of calculating the ground-state energy of a system. Although this is not as accurate as Density Functional

Theory, it can still be useful, and contains some good ideas that are partly used by DFT (Density Functional Theory). The idea is simple: we take a trial wavefunction for a many electron system and allow the orbitals to be varied since we don't know them using the variational principle; we then minimise the expectation value which will give the best approximation to the ground-state energy.

By replacing the wavefunctions from Hartree theory with the correct antisymmetry product, this reduces the energy of the system because of the exchange energy. The exchange energy is very important, because it explains that if one electron is found on one side of the atom, there is a greater probability of finding the other on the other side of the atom, meaning that the electrons are kept away from each other and so feel less repulsive energy, reducing the energy of the system. Hartree-Fock theory is not all that accurate however, as it does not include electron correlation.

2.3.7 Thomas-Fermi theory

One scheme for solving the many electron body was proposed by Thomas and Fermi. In this model it is the electron density that is the variable rather than the wavefunction; it is obvious that in a real solid, the density distribution of electrons is not uniform, because there is a potential field V($\mathbf{r}$) acting on the electrons. This field comes from the electrostatic interaction of the electrons with the nuclei.

By writing expressions for parts of the total energy, this can then be minimised with respect to the density distribution to find the ground-state energy. The kinetic energy, E_{kin} = sum of all the individual kinetic energies of the electrons. The crucial approximation made here is that the total kinetic energy can be obtained by integrating kinetic energy density over the volume of a non-uniform system. The outcome, the Thomas-Fermi equation,

$$\frac{\alpha\hbar^2}{m}\frac{5}{3}\rho(\mathbf{r})^{\frac{2}{3}} + V_{ext}(\mathbf{r}) + \frac{e^2}{4\pi\varepsilon_0}\int d(\mathbf{r})\frac{\rho(\mathbf{r})}{|\mathbf{r}-\mathbf{r}'|} - \frac{\beta e^2}{4\pi\varepsilon_0}\frac{4}{3}\rho(\mathbf{r})^{\frac{1}{3}} = 0 = \mu \qquad (2.11)$$

is a remarkable equation, because it tells us that the ground-state density distribution $\rho(\mathbf{r})$ of the system of interacting electrons in the presence of the field $V(\mathbf{r})$ is exactly the same as that of a non-interacting system in an effective potential, and therefore can be solved directly to obtain the groundstate density. There is, however, a

problem with this; it is not very accurate in practice. The kinetic energy expression is not very accurate as it does not attempt to represent the exchange energy of an atom, and is incapable of accounting for the binding energy of molecules, so molecules and solids cannot form in this theory. But it does point the way to density functional theory.

2.3.8 Density Functional Theory

The Hartree and Hartree-Fock theories ignored the repulsive interaction between electrons by ignoring correlation. The idea behind density functional theory (DFT) is that we can include correlation by modifying the static potential used in both Hartree and HF theories, which in principle can be done exactly.

The many-electron wave function Ψ is complicated, and nobody knows how to solve Schrödinger's equation to determine it exactly (apart from the hydrogen atom). Density functional theory gets around this by avoiding the need to compute the many-electron wave function, instead following Thomas-Fermi strategy of expressing the total energy as a functional of the electron density.

2.3.9 Hohenberg and Kohn

Thomas-Fermi theory assumes that specifying the electron density is by itself enough to uniquely determine the ground-state properties, including the ground-state energy. The first Hohenberg-Kohn theorem justifies this assumption:

- **Theorem 1**: It is impossible for two *essentially* different external potentials to give the same ground-state density distribution, $\rho(\mathbf{r})$

Essentially different means they differ by more than an additive constant. Hence, the density distribution determines ground-state energy:

$$E_g = \int V_{ext}(\mathbf{r})\rho(\mathbf{r})d\mathbf{r} + F[\rho(\mathbf{r})] \tag{2.12}$$

where $F[\rho(\mathbf{r})]$ is a universal functional of the density $\rho(\mathbf{r})$ representing the expectation value of $H_0 = \hat{T} + \hat{U}$ when the ground-state density is $\rho(\mathbf{r})$. This is an important theorem, because specifying the ground-state density $\rho(\mathbf{r})$ uniquely determines the value of F and hence the total ground-state energy

The second Hohenberg-Kohn theorem justifies finding the ground-state by minimising the total energy with respect to $\rho(\mathbf{r})$, subject to fixed total number of electrons

N.

- **Theorem 2**: The true ground state density distribution, $\rho(\mathbf{r})$ for given $V_{ext}(\mathbf{r})$ is obtained by minimising E_{tot} $[\rho(\mathbf{r})]$ with respect to $\rho(\mathbf{r})$ at constant number of electrons

What do we need to do in practice for F$[\rho(\mathbf{r})]$?

$$F[\rho(\mathbf{r})] = E_{kin}[\rho(\mathbf{r})] + E_{Har}[\rho(\mathbf{r})] + E_{xc}[\rho(\mathbf{r})] \tag{2.13}$$

with the final term, $E_{xc}[\rho(\mathbf{r})]$ = exchange and correlation, containing everything we don't know:

$$E_{xc}[\rho(\mathbf{r})] = \int dr \varepsilon^0_{xc}(\rho(\mathbf{r}))\rho(\mathbf{r}) \tag{2.14}$$

2.3.10 Kohn-Sham equations

The first term, $E_{kin}[\rho(\mathbf{r})]$ is defined as the kinetic energy of a non-interacting electron gas with density $\rho(\mathbf{r})$; the second term, $E_{Har}[\rho(\mathbf{r})]$, is the Hartree energy (electrostatic energy); the final term is an implicit definition of the exchange-correlation energy. The aim of this separation is the first two terms can be dealt with easily, and the last term - containing the effects of the complex behaviour - is only a small fraction of the total energy and can be approximated well. F$[\rho(\mathbf{r})]$ is dealt with by Kohn and Sham by calculating as much as possible of F$[\rho(\mathbf{r})]$, and then calculating what is left separately in a smaller term.

The ground-state is now determined by minimising the total energy with respect to $\rho(\mathbf{r})$, while holding N constant. This is done exactly as in Thomas-Fermi theory; at the ground state, the energy must be stationary with respect to variations of $\rho(\mathbf{r})$. We write the total energy as:

$$E = \int d\mathbf{r}\rho(\mathbf{r})V(\mathbf{r}) + \hat{T}[\rho(\mathbf{r})] + G[\rho(\mathbf{r})] \tag{2.15}$$

where G = $E_{Har} + Exc$, then:

$$\partial E = 0 = \int d\mathbf{r} \left[V(\mathbf{r}) + \frac{\partial \hat{T}}{\partial \rho(\mathbf{r})} + \frac{\partial G}{\partial \rho(\mathbf{r})} \right] \partial\rho(\mathbf{r}) \tag{2.16}$$

subject to the constraint:

$$\int d\mathbf{r}\, \partial\rho(\mathbf{r}) = 0 \tag{2.17}$$

The ground state condition is:

$$\frac{\partial \hat{T}}{\partial\rho(\mathbf{r})} + V(\mathbf{r}) + \frac{\partial G}{\partial\rho(\mathbf{r})} = \mu \tag{2.18}$$

where μ is the Lagrange undetermined multiplier. It is more convenient to write this as:

$$\frac{\partial \hat{T}}{\partial\rho(\mathbf{r})} + v_{eff}(\mathbf{r}) = \mu \tag{2.19}$$

where μ is the Lagrange undetermined multiplier, the 'effective' potential $v_{eff}(\mathbf{r})$ is $v(\mathbf{r}) + \partial G/\partial\rho(\mathbf{r})$.

There is a way of re-interpreting this equation, which makes it easy to deal with. For non-interacting electrons, G = 0, since G is the sum of Hartree and exchange-correlation energies, and both of these vanish for non-interacting electrons. In this case, the minimum condition becomes:

$$\frac{\partial \hat{T}}{\partial\rho(\mathbf{r})} + v(\mathbf{r}) = \mu \tag{2.20}$$

This means that the ground-state density of the interacting system with the external potential $v(\mathbf{r})$ is identical to the ground-state density of the non-interacting system with the external potential $v_{eff}(\mathbf{r})$. But we know perfectly well how to find the ground-state density of a system of non-interacting electrons in potential $v_{eff}(\mathbf{r})$. All we have to do is to solve the Schrödinger equation.

Since the Kohm-Sham potential $V_{KS}(r)$ depends upon the density, it is necessary to solve these equations self-consistently. Direct solution of the Schrödinger equation for the extended non-interacting orbitals requires a computational effort that scales as N^3, where N is the system-size.

2.3.11 Local density Approximation

We don't have an exact formula for $E_{xc}[\rho(\mathbf{r})]$, but there is a very simple approximation which works surprisingly well. This makes use of the fact that we know E_{xc} al-

most exactly for a uniform electron gas. There are extremely accurate formulas for its exchange-correlation energy per electron ${\varepsilon_{xc}}^0(\rho)$ as a function of ρ. Following Thomas-Fermi ideas, for a non-uniform system, every point $\mathbf{r}$ there is a density of exchange-correlation energy given by $\rho(\mathbf{r}){\varepsilon_{xc}}^0(\rho(\mathbf{r}))$. The total exchange-correlation energy in the whole system is:

$$E_{xc}[\rho(\mathbf{r})] = \int d\mathbf{r}\rho(\mathbf{r})\varepsilon_{xc}^0(\rho(\mathbf{r})) \tag{2.21}$$

This is called the Local Density Approximation (LDA), containing one of the very accurate formulas for ε_{xc}^0 in the uniform electron gas for evaluating E_{xc}. While the works quite well for bulk metals, the LDA has a few principal failings for other systems:

1. The binding energies are frequently overestimated. This means that in solid-state calculations the unit-cell parameters are underestimated, leading to an error in the calculated bulk modulus.

2. The wrong groundstate is predicted to be stable, such as for iron, which is predicted to be non-magnetic-hcp under ambient conditions

3. Insulating systems exhibiting strong correlation effects are predicted to be metallic

4. It contains a poor description of weak bonding, such as van der Waals forces, which are not accounted for at all

2.3.12 Generalised Gradient Approximation, GGA

While the LDA approximates the energy of the true density by the energy of a local constant density, it fails in situations where the density undergoes rapid changes such as in molecules. The Generalised Gradient Approximation improves on this by considering the gradient of the electron density. This can be written as:

$$E_{xc} = E_{xc}\left[\rho(\mathbf{r}), \nabla\rho(\mathbf{r})\right] \tag{2.22}$$

This leads to a large improvement over the LDA with good accuracy. There are many GGA functionals that deal with the unknown exchange-correlation energy, each

one built to reproduce specific properties of a system (such as elastic properties); therefore it is necessary to consider which functional is of best use for a specific property.

2.3.13 Plane wave basis set

How do we represent wave functions on a computer? Computers work by storing and manipulating lists of numbers, so we need to represent wave functions as a list of numbers. A way of doing this is called the plane-wave method. In this method, electrons are considered to be like free particles in condensed matter. The wave function for a free electron is $e^{i\mathbf{k}\cdot\mathbf{r}}$, where $\mathbf{k}$ is the momentum of the electron divided by $\hbar$. The idea is to use these plane-waves as basis functions:

$$\psi_i(\mathbf{r}) = \sum_k c_{i\mathbf{k}} e^{i\mathbf{k}\cdot\mathbf{r}} \tag{2.23}$$

and the coefficients $c_{i\mathbf{k}}$ are the list of numbers to be varied. For large numbers of atoms, this method is very successful, since we can use the symmetry in crystals. By exploiting the periodicity in crystals, the need for wavefunctions to be calculated for each electron in a system is reduced down to one unit-cell repeated infinitely in all directions. The theorem of Bloch shows the wavefunction in a periodic system can be written as the product of a periodic term and a wave-like term in terms of a plane-wave basis set. In principle, an infinite number of plane waves is required in the basis set. However, since this is not possible the expansion is truncated at a cut-off value because plane waves with small kinetic energies are more important than those with large energies.

The truncation of the basis set at a cut-off energy leads to an error in the total energy of the system; therefore the cutoff energy is increased until the total energy of the system converges to within a chosen value, thereby minimising this error. The wave functions can be made as accurate as necessary by increasing the number of plane waves, so that the method is systematically improvable.

2.3.13.1 Projector Augmented Waves method, PAW

The drawback of the plane-wave method is that all the information on the full wave function close to the nuclei is lost; in the bonding region it is smooth, but the near the nuclei it displays rapid oscillations, which are very demanding on the numerical repre-

sentation of the wave functions. This can influence the calculation of certain properties, such as hyperfine parameters, and electric field gradients.

A different approach is the augmented-plane-wave method (APW), in which space is divided into atom-centred augmentation spheres inside which the wave functions are taken as some atom-like partial waves, and a bonding region outside the spheres, where some envelope functions are defined. The partial waves and envelope functions are then matched at the boundaries of the spheres.

The projector augmented wave method (PAW), proposed by Blöchl in 1994 [17], offers APW as a special case, and the pseudopotential method as a well defined approximation. This is the generalisation of the pseudopotential and plane-wave methods, and allows for the DFT calculations to be performed with greater efficiency. To address the problem with the features of wavefunctions in different regions of space, we seek a linear transformation which takes us from an auxiliary smooth wave function to the true all electron Kohn-Sham single particle wave function. The trouble of the original Kohn-Sham wave functions was that they displayed rapid oscillations in some parts of space, and smooth behaviour in other parts of space.

Separation of the original wave functions is done by splitting them into auxiliary wave functions which are smooth everywhere, and a contribution which contains rapid oscillations, only contributing in certain small areas of space. The transformation is expressed in terms of the three components; the partial waves $\phi_i^a(\mathbf{r})$; the smooth partial waves $\tilde{\phi}_i^a(\mathbf{r})$; and the smooth projector functions $\tilde{p}_i^a(\mathbf{r})$. The PAW method is typically combined with the frozen core approximation. For this approximation, it is assumed that the core states are naturally localised within the augmentation spheres, and that the core states of the isolated atoms are not changed by the formation of molecules or solids.

The PAW method has exceptional precision, even for strong magnetic moments and large electronegative differences; typical bond length errors are smaller than 0.5 %. Although the ultra-soft pseudopotential method offers similar precision, the PAW method is much more reliable for magnetic systems.

2.3.14 Pseudopotentials

Pseudopotentials were thought of as a way to approximate the change in electron density close to atomic cores as opposed to between atoms. It can be thought of as a weaker effective potential. The idea behind pseudopotentials is to choose a core radius, $\mathbf{r}_c$, and pseudise the atomic wave functions in the channel of interest. Once this is achieved, inverting the Schrödinger equation finds the pseudopotential. The resulting pseudopotential will reproduce reference eigenstates that can be used to solve the Schrödinger equation.

Norm-conserving pseudopotentials are built on a given reference atomic configuration, meeting a set of conditions:

- orbital energy is equal to atomic orbital energy
- radial part of the pseudopotential valence wave function is node-less

The core radius is approximately at the outermost maximum of the wave function. Norm conserving pseudopotentials are split into a local and a non-local part, the latter however, is very expensive to compute. It is very convenient to recast norm conserving pseudopotentials into a separable, full nonlocal form. The separable form usually yields good results, but may badly fail in some cases.

Employing a plane-wave basis set and the pseudopotential approximation has proved to be very successful for computational material science, owing to its simplicity. However, this comes at a cost: first-row elements, transition metals, and rare-earth elements are computationally demanding to treat with standard norm-conserving pseudopotentials. Various attempts to rectify this were made, with the most successful the concept of ultrasoft pseudopotentials.

2.3.14.1 Ultrasoft pseudopotentials, US

Ultrasoft (Vanderbilt) pseudopotentials can be soft because norm conservation is not required, giving the freedom to choose core radii. In this scheme the pseudowavefunctions are allowed to be as soft as possible within the core region, so that the cutoff energy can be reduced dramatically. The electron density is subdivided into: i) a smooth part that extends throughout the unit cell, and ii) a hard part localised in the core regions. The augmented part appears in the density only, not in the wave func-

tions; this differs from methods like local-PAW, where a similar approach is applied to wave functions.

Ultrasoft pseudopotentials allow the use of much smaller plane wave basis, but: there are additional terms in the charge density and in the forces; electronic states are orthonormal with an overly matrix; the charge which has been removed has to be put back to compute the density functional; the wave functions are smoother, but the charge density is not smoothed at all.

We want pseudopotentials to make calculations faster; we introduced norm-conserving pseudopotentials to make them transferrable, the semi-local formulation to make them faster; and ultrasoft to make them softer at the price of orthogonality.

2.3.15 $\vec{k}$-point sampling

$\vec{k}$-points are sampling points in the first Brillouin zone of the material. The need for $\vec{k}$-points arises from Bloch's theorem, and can be exploited so that the symmetry of the crystal being simulated reduces the number of these sampling points; symmetry operators in the crystal will reproduce the whole of the unit-cell from the irreducible Brillouin zone. There is no variational principle governing the convergence of the $\vec{k}$-point mesh, meaning the total energy does not simply increase or decrease, instead fluctuating with an increased $\vec{k}$-points mesh.

The number of $\vec{k}$-points required for accurate calculations depends upon:

1. The size of the simulation. Large unit cells are smaller in reciprocal space, and so require fewer $\vec{k}$-points.

2. The periodicity of the system i.e. if it is a liquid or gas only a single $\vec{k}$-point is required since the periodicity of the simulation is itself an approximation.

3. The band-gap. More $\vec{k}$-points are required for metals because it becomes difficult to compute the Fermi surface.

There are different methods used to create a mesh of $\vec{k}$-points - a popular method (used in this thesis) is the Monkhorst-Pack mesh. In this, the $\vec{k}$-points are distributed homogeneously in the Brillouin zone, with rows or columns of $\vec{k}$-points running parallel to the reciprocal lattice vectors. This approach allows for the errors in the sampling to be easily reduced simply by increasing the $\vec{k}$-point density.

2.3.16 Dispersion correction in DFT

Popular local and semi-local density functionals do not describe van der Waals interactions resulting from dynamical correlations between fluctuating charge distributions. The dispersion energy is a long-ranged (C_6/R^6) electron correlation effect that becomes part of the normal correlation energy; merging this long-range behaviour with the short regions already calculated by DFT requires careful attention.

One of the methods used is the DFT-D3 method [59]. DFT-D3 is a refined form of DFT-D2 with higher accuracy, broader range of applicability and less empricism [59]. The total DFT-D3 energy is given by

$$E_{DFT-D3} = E_{KS-DFT} + E_{disp} \tag{2.24}$$

where E_{KS-DFT} is the usual self-consistent Kohn-Sham energy and E_{disp} is the dispersion correction. The correction E_{disp} is computed using approximations.

The advantages of the DFT-D3 method are: computationally very efficient, particularly in geometry optimisations and harmonic frequency calculations; can be coupled with any standard functional without significant loss of accuracy; allows for calculation of energy gradients for efficient geometry optimisation. Under rare and special circumstances, the DFT-D3 method with zero damping may lead atoms to experience a small repulsive force that may lead to longer interatomic distances with dispersion correction than without dispersion correction [59].

The inclusion of dispersion into DFT adds London forces and therefore weak intermolecular forces are more accurately represented. Care needs to be taken not to let the system overbind, which is the converse of what is usually seen (the forces are overestimated). For hydrogen bonded systems, this can help to correct for the underbinding of the unit-cell that is common without the dispersion correction.

2.3.17 Summary of Density Functional Theory

To summarise, a complete outline of a calculation of the ground-state energy of an assembly of atoms using DFT will be given. Since the terms v_{Har} and v_{xc} in the Kohn-Sham potential depend on $\rho(\mathbf{r})$, which is what we want to determine, there is a requirement of self-consistency. A DFT calculation proceeds thus:

Assume an initial density distribution $\rho_{in}(\mathbf{r})$ - this is sometimes chosen to be a

superposition of atomic electron densities.

- Use this $\rho_{in}(\mathbf{r})$ to compute $v_{Har}(\mathbf{r})$ and $v_{xc}(\mathbf{r})$, and hence $v_{KS}(\mathbf{r})$.
- Solve the Kohn-Sham equation to obtain the Kohn-Sham orbitals $\psi_n(\mathbf{r})$ and the Kohn-Sham orbital energies ε_n
- Fill up the lowest 1N states and compute the "output" density $\rho_{out}(\mathbf{r})$.
- In general, $\rho_{out}(\mathbf{r})$ will not agree with $\rho_{in}(\mathbf{r})$, so we have to iterate the process to self-consistency, i.e. until $\rho_{out}(\mathbf{r}) = \rho_{in}(\mathbf{r})$ to within a specified tolerance
- Finally, use the self-consistent ground-state density to compute the ground-state energy

---

2.4 Applying DFT

The greatest achievement of all this theory is that computing properties of materials can be simple, accurate and reliable, in principle only requiring the relative positions and type of atoms. However, this is still a job for large, powerful computers running a series of steps in the form of algorithms.

One program used for performing quantum mechanical *ab initio* calculations is a complex package known as *VASP* (*Vienna Ab Initio Simulation Package*) [80], used during this study. *VASP* uses the PAW method or ultrasoft pseudopotentials, implementing a self-consistency cycle to calculate the electronic ground state.

This self-consistency cycle tries to guess the wavefunction and then tests whether the next answer is best or worse: if the answer is worse, it tries another; if it is better, it adopts that answer and takes another guess. By using this self-consistency cycle, it minimises the energy to get to the right answer; you can choose how it gets to this minimum by choosing either the LDA or GGA approximations. This method requires many calculations to be run quickly at the same time.

2.4.1 Parallelisation on modern multi-core machines

The problem of trying to solve the Schrödinger equation on modern computers is basically how to break down the huge amount of calculations needed into manageable

parts. There has been a huge progress in the power of modern computers, which has stemmed from Moore's Law - the observation that the number of transistors in a dense integrated circuit doubles approximately every two years. This has driven computer chip manufacturers to develop smaller and smaller CPU chips, and these have become increasingly powerful. One way thought to improve the efficiency in modern computers was the invention of the multi-core processor. This optimises the way modern machines have developed, in which many processes can be run at the same time by different applications.

The problem, however, lies in the fact that the average speed at which a CPU operates is currently around 4 GHz. The speed in which a core can compute is actually of more value to the problem of computational material science than the use of many cores. The problem of a many core system is one of dividing the job up. Whilst this division seems sensible - to distribute the load evenly across many cores - the reality is that all cores have to be able to share information quickly between themselves. It is in this data transfer wherein the problem lies. The speed of large data transfer across cores is a slow process, especially when all cores require information from all other cores.

There are systems that are designed to take advantage of multi-core systems, in particular the Message Passing Interface (MPI). This distributes the load across many cores and processors and gathers all the information together. To maximise performance, many *ab initio* codes (*VASP*, *CASTEP*, *ABINIT* etc.) have implemented codes to make use of large national supercomputers that rely on this method.

The best way to split up a DFT calculation is to parallelise depending on the number of $\vec{k}$-points. Since the $\vec{k}$-points can be thought of as a sampling size, it is most efficient on modern multi-core machines to have groups of cores working on an individual $\vec{k}$-point, and then the groups of cores put all the data together to solve the problem; this is known as *$\vec{k}$-point parallelisation*. This is one of the most efficient methods of speeding up the time taken to calculate a problem using DFT.

For example, during this investigation the national supercomputer *ARCHER* has been used to run the *VASP* code. This supercomputer boasts 118,080 processing cores - this is split between 4920 nodes, with each node containing two 12-core processors (essentially 24 cores per node). It could be assumed that running all 118,080 cores

to solve a DFT calculation would make it run very quickly, but the reality is not that simple (plus getting access to all the cores at once would make quite a few people very unhappy). If a job submitted to this supercomputer was a relatively small one, lets say with 4 $\vec{k}$-points, then if split between 118,080 cores, each core would have 1/118,080th of 1 $\vec{k}$-point to calculate, that needs to be done four times. In theory this sounds great; in practice, it takes so much more time than using a small number of cores, because it takes a long time to split the job up into 118,080 pieces, send that information to each core, and then gather all 118,080 separate calculations into something that makes sense.

The best way is tell the program how to split the job into manageable sizes. A 4 $\vec{k}$-point job is best to be split between 4 nodes, so that each node, comprising of 24 cores (total number of cores used therefore is $24 \times 4 = 96$ cores), is focussed on calculating one $\vec{k}$-point, and then only 4 calculations have to be collated together. This has been shown to be a very efficient method, and implemented in this thesis to ensure that calculations take as little time as possible.

2.4.2 Running VASP

In order to run the calculations, *VASP* requires four input files; these are the POSCAR, POTCAR, KPOINTS, and INCAR files. To calculate material properties, all we need in principle are the positions of atoms and the species of atoms. The POSCAR file tells *VASP* where the positions of the atoms are within the unit cell (or rather the simulation box) of the body investigated. The positions of atoms can be given in direct (fractional) or cartesian coordinates, with the lattice vectors given in matrix form, where each vector is scaled by a universal scaling factor. The atomic positions must be known to some degree of certainty, so are typically taken from experimental diffraction data.

The species of the atoms is then given in the POTCAR file; this consists of the pseudopotentials for each atomic species relevant to the calculation, concatenated together. The file also contains information about the atoms, such as their mass and valence. There are a series of different pseudopotentials distributed in *VASP*, and it is up to the user to select which of these is the most applicable. Since the POSCAR and POTCAR files contain all the atomic information *separately*, the order in which they appear in the final POTCAR file must correspond to the order in which the coordinates

of those species appear in the POSCAR file.

These input files contain only the atomic information, and do not require any convergence tests. The next two files contain values that we must run convergence tests to specify a degree of accuracy which we define for a particular problem.

The KPOINTS file determines how densely the irreducible Brillouin zone is to be sampled to calculate the total energy. The number of $\vec{k}$-points required depends on the size of the box (a larger box in real space has a small area in reciprocal space and hence fewer points are generally required). Generally, more $\vec{k}$-points will give the most accurate results, but increases the total time and cost of computing the total energy. Therefore a trade-off is used by running preliminary simulations to determine where an increase in density of sampling gives no real-time improvements in the accuracy. The dimensions of the $\vec{k}$-points grid is suggested to be scaled according to unit cell dimensions, so a unit cell with axes *a*-, *b*-, and *c*- in a ratio 4:2:1 would have $\vec{k}$-points in the ratio 1:2:4 (since a longer unit cell axis is smaller in reciprocal space it hence requires fewer $\vec{k}$-points, so the $\vec{k}$-point ratio is inverted). The advantage of this method is that fewer $\vec{k}$-points are generally required to achieve the same accuracy compared to using an equidimensional grid.

The final input file, the INCAR file, gathers all the other inputs and tells *VASP* how to implement them. The file consists of a series of tags to which user-defined values can be attached. The ENCUT tag is of particular interest in this file, since a higher number should give a better accuracy, but at the expense of calculation time. We therefore also run convergence tests to find a value in which the increase in energy is below a threshold given in the EDIFF tag, and usually EDIFF=10^{-5} eV. Both the $\vec{k}$-points and energy cutoff are independent of each other, so once one is converged changing the other value will have no effect on the other.

2.4.3 Determining material properties

Once all the inputs are ready and the convergence tests are completed, the calculation can be started, giving an output in terms of internal energy for a chosen volume. The internal energy of the solid under investigation is calculated and outputted by *VASP*, with all physical properties of the system contained within the quantum mechanical description given by the Schrödinger equation. An external force, which can be a strain

applied, a change in temperature, pressure etc., then in turn affects the internal energy of the system. This change in energy can be converted into useful physical quantities; in this work, this is done by fitting an equation of state (EoS) to the outputted energy and pressure.

An EoS is a relation between functions of state, such as pressure (P), volume (V), temperature (T), internal heat, and specific heat. It is used to describe the behaviour of a solid under a set of physical conditions. In mineral physics, an EoS is used to determine the stability of a solid at a given pressure, temperature and/or volume, which depends upon the atomic structure.

VASP is used to calculate the total energy for a range of molar volumes, which can be used to determine an EoS. From the First and Second Laws of Thermodynamics, pressure under a set temperature is related to the energy via

$$-P = \left(\frac{\partial E}{\partial V}\right) \tag{2.25}$$

The value for the internal energy is given by the integral of the pressure with respect to volume at a constant temperature,

$$E = -\int P\,\partial V \tag{2.26}$$

This can be related to an isothermal equation state via the pressure as a function of volume.

There are several equations of state to choose from (Vinet, natural strain, Murnaghan etc...), each with their strong and weak points. This work has used the Birch-Murnaghan equation of state, as this provides a good fit with sensible parameters over an intermediate pressure range. To 4th order (BMEOS4) the Birch-Murnagha EoS takes the form,

$$P = 3K_{0,T} f_E (1+2f_E)^{5/2} \left[1 + \frac{3}{2}(K'_{0,T} - 4) f_E + \frac{3}{2}\left(K_{0,T}K''_{0,T} + (K'_{0,T} - 4)(K'_{0,T} - 3) + \frac{35}{9}\right) f_E^2\right] \tag{2.27}$$

which gives a four parameter EoS, $V_{0,T}$, $K_{0,T}$, $K'_{0,T}$ and $K''_{0,T}$. The normalised

pressure is:

$$F_E = \frac{P}{3f_E(1+2f_E)^{5/2}} \tag{2.28}$$

and the Eulerian strain is:

$$f_E = \frac{1}{2}\left[\left(\frac{V_0}{V}\right)^{2/3} - 1\right] \tag{2.29}$$

If the EoS is truncated to second-order (BMEOS2), the coefficient of $f_E = 0$, requiring that $K'_{0,T} = 4$, giving a two parameter EoS, $V_{0,T}$, $K_{0,T}$. To third-order (BMEOS3), $f_E^2 = 0$, which gives a three parameter EoS, $V_{0,T}$, $K_{0,T}$ and $K'_{0,T}$, with an implied value of $K''_{0,T}$ given by

$$K''_{0,T} = \frac{-1}{K_{0,T}}\left((3-K'_{0,T})(4-K'_{0,T}) + \frac{35}{9}\right) \tag{2.30}$$

To determine which order EoS is to be fitted to the data, the Eulerian strain can be plotted against the normalised pressure, called a *f-F* plot. This is a visual diagnostic tool to determine which higher order term is significant in an EoS. In this plot, data points showing a trend can indicate which order EoS can be fitted, with:

i. Data points plot on a horizontal line of constant F_E; $K' = 4$; data can be fitted with BMEOS2.

ii. Data points plot on an inclined straight line; slope is equal to $3K_0(K'-4)/2$; data can be fitted with BMEOS3.

iii. Data points plot on a parabolic curve; K'' differs from implied value; $f_E^2 \neq 0$; data can be fitted with BMEOS4.

In this work, materials are found to have a $K'_{0,T} \neq 4$, with a *f-F* plot showing an inclined straight line, or a curved line, so a third- and fourth order EoS is used to fit the data.

The BMEOS3 can be fitted to *P(V)* data via:

$$P_{V,T} = \frac{3}{2}K_{0,T}\left(x^{\frac{7}{3}} - x^{\frac{5}{3}}\right)\left[1 + \frac{3}{4}(K'_{0,T}-4)(x^{\frac{2}{3}}-1)\right] \tag{2.31}$$

where $x = V_{0,T}/V_{P,T}$ and $V_{0,T}$, $K_{0,T}$, and $K'_{0,T}$ are the zero-pressure molar volume, bulk modulus and first derivative of the bulk modulus respectively.

The output from *VASP* is given in terms of the total energy of the system; this is related to the pressure by the integrated form of the BMEOS3 (Eq. 2.31):

$$E = \left(\frac{9}{4}\right) K_0 V_0(x) \left[\frac{1}{2}(x)^{\frac{1}{3}} - \left(\frac{1}{x}\right)^{\frac{1}{3}}\right] + \left(\frac{9}{16}\right) K_0(K'_0 - 4)V_0(x) \left[x - 3\,(x)^{\frac{1}{3}} + 3\left(\frac{1}{x}\right)^{\frac{1}{3}}\right] + E_0 - \left(\frac{9}{16}\right) K_0(K'_0 - 6)V_0 \quad (2.32)$$

By taking the unit-cell volume, and the dimensions of the axes, an estimate of the bulk modulus on the system can be determined, either in a particular direction or on the whole. By plotting the pressure against the calculated bulk modulus, it can be seen how the system changes its stiffness under load, and the zero pressure bulk moduli can be determined by extracting back.

The next section focusses on the preliminary work done at the beginning of the PhD to ensure that the calculations using *VASP* were running as intended.

2.4.4 Testing *VASP*: ice VIII

To begin, the goal is to reproduce the calculations by Fortes, 2004 [51] and Tse, 1998 [140] of the high-pressure phase of H_2O ice, ice VIII. There is plenty of theoretical literature and experimental work related to this phase, which lends itself well for testing the calculations are working as intended before moving on to ammonium carbonate ices. To begin therefore, the results from the work on ice VIII and comparison to previously published work will be presented.

Ice VIII is the high-pressure, low temperature phase of water ice, transforming above ∼2.1 GPa and below ∼263 K from either ice VI or ice IV phases into this tetragonal phase (space group $I4_1/amd$, with origin at inversion centre $2/m$). The reader is pointed to the work by Fortes, 2004 [51] and other work for more information on the stability and structures of phases of high-pressure water ice, which easily in itself could be an extensive project.

The hydrogen bonded nature of these water ice systems are analogous to the am-

monium carbonate ices in this work by virtue of the treatment of hydrogen bonding in DFT calculations, which are difficult to calculate, and as mentioned previously, the extensive works, both experimental and theoretical, make this an ideal starting point.

2.4.5 Computational details

To determine bulk properties of ice VIII, first-principles calculations using DFT [68, 78], as implemented in *VASP* [80], were used. As a comparison to the ultra-soft pseudopotentials used in previous studies, the plane-wave expansion was treated using the Projected Augmented-Wave method, PAW [17], using the PAW pseudopotentials distributed with *VASP* [81]. The exchange-correlation was accommodated using the PBE generalised gradient corrected functional [110]; despite not correctly representing dispersion forces, this form of the generalised gradient approximation (GGA) yields results of comparable accuracy to higher-level quantum chemical methods in hydrogen bonded systems.

Convergence tests were carried out to optimise the $\vec{k}$-point sampling of the Brillouin zone within the Monkhorst-Pack scheme [98] and the kinetic energy cut-off of the plane-wave basis set. A total energy convergence better than 10^{-3} eV was achieved when using a 6x6x4 $\vec{k}$-point mesh and kinetic energy cut-off of 860 eV.

What is interesting to note is the convergence of the $\vec{k}$-point sampling of the Brillouin zone. In previous studies, equidimensional grids were used, e.g. 5x5x5 $\vec{k}$-point grid [51]. Whilst this is a reliable method, the $\vec{k}$-point sampling is done over reciprocal space, so long unit-cell axes require fewer points to achieve equal sampling. Therefore in this study, grids follow the unit-cell axes ratios of a:b:c of $\sim$1.45: $\sim$1.45: 1.00. Therefore instead of needing over 30 $\vec{k}$-points, this study has reduced this down to 12 $\vec{k}$-points with the same accuracy.

A series of fixed volume calculations were performed in which the ions were allowed to move according to the Hellman-Feynman forces and the unit cell shape allowed to vary, starting from the structural parameters given in Fortes, 2004 [51]. At each specified volume, the structure was relaxed via the conjugate-gradient technique in order to optimise the lattice parameters and internal coordinates.

Given next are the results of the fits of isothermal EoS to the E(V) points obtained, so as to yield useful thermodynamic parameters such as the isothermal bulk modulus

and its pressure derivatives.

2.4.6 Equation of state of ice VIII

A series of constant volume relaxations were run over a volume range of 100 - 350 Å^3. The values of total energy and pressure were plotted against cell volume, producing E(V) and P(V) curves respectively; both curves correspond well with previous work [51, 140]. The PAW pseudopotentials cannot be directly compared with the previous work since the energy output is greater, but the overall shape matches well, and should yield the same answer.

The third order Birch-Murnaghan equations of state (BMEOS3) were used to fit the *ab initio* results to the E(V) and P(V) values. The E(V) and P(V) plots between 0 - 32 GPa are given in Figures 2.6, and the parameters of these fits are given in Table 2.1

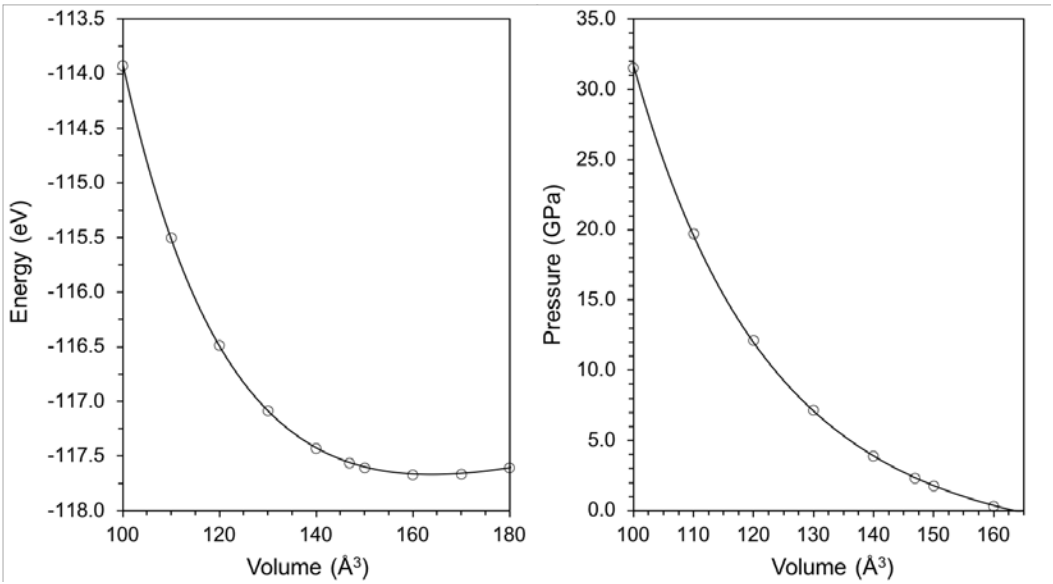

Figure 2.6
Calculated E(V) curve and P(V) curve of ice VIII using PAW pseudopotentials. The solid line shows the best fit BMEOS3.

2.4.7 Results

The experimental and calculated values for the bulk modulus are quite varied due to the range of experimental conditions (see Table 2.2). The zero-pressure unit-cell volume at 4 K is 159.59 Å^3, which was measured by Klotz *et al.*, 1999 [77] on D_2O ice VIII recovered to ambient pressure. The value of V_0 calculated here is a $\sim$2.6 % overestimation of the measured value. The differences between the calculated and experimental

values of K_0 and K_0' can be attributed to the correlation between the two when fitting an EoS.

Table 2.1
Fitted EoS parameters of ice VIII, using the PAW method and PBE pseudopotentials. The equation of state used is the BMEOS3 for direct comparison with the work by Fortes, 2004 [51]. The bottom two rows contains fits to the calculated E(V) curve when K_0' is fixed at 4.5 and 4.0.

	V_0 (Å^3)	K_0 (GPa)	K_0'	K"$_0$ (GPa^{-1})	E_0 (eV molecule^{-1})
BMEOS3, E(V)	163.8(1)	15.82(6)	5.83(1)	-	-14.7089(2)
BMEOS3, P(V)	163.7(3)	16.0(2)	5.66(4)	-	-
BMEOS3, E(V)	161.8(2)	21.0(1)	4.5*	-0.221	-14.7113(4)
BMEOS2, E(V)	161.0(2)	23.6(1)	4.0*	-0.165	-14.7125(4)

* indicates the value is fixed

However, by setting $K_0' = 4.5$ and $K_0' = 4.0$, although the actual quality of fit decreases slightly, the values are a better match to those in comparison in Table 2.2, specifically those of Besson *et al.*, 1997 [16], in which the sample was measured after decompression to zero-pressure. The zero-pressure volume is now overestimated by $\sim$1.4 % and $<$ 1 % respectively, and the bulk modulus, K_0, is now much closer to the measured value with $K_0' = 4.5$, and is within errors for $K_0' = 4$. The problem shown here is from the correlation between K_0 and K_0' when fitting the equation of state.

Interestingly, the values for the bulk modulus its pressure derivatives in this work do vary from the previous work. When compared with literature data, the values do not seem so unreasonable. The difference is likely due to the difference in the way the pseudopotentials are constructed - the PAW method and pseudopotentials are 'harder' than the ultrasoft pseudopotentials and perhaps are not able to fully calculate hydrogen bonding properties in ice.

These results do show, however, that the DFT calculations using *VASP* have successfully been applied to ice VIII, with parameters similar to those found previously. Therefore, there can be reasonable assurance that, for ammonium carbonates, the properties calculated will be how the material behaves; experimental work should be able to prove the properties calculated.

Table 2.2
Comparison of fitted parameters from previous experimental and computational studies of ice VIII, given from lowest temperature (top of the table) to the highest temperature (bottom of the table). There is excellent agreement between fitted parameters from the literature and the work in this thesis. In the method column, NPD denotes neutron powder diffraction and XPD X-ray powder diffraction.

	Method	$V_{0,T}$ (Å^3)	$K_{0,T}$ (GPa)	$K'_{0,T}$	T (K)	P range (GPa)
BMEOS3 [51]	DFT	159.8(3)	16.8(7)	6.0(2)	0	
LNEOS4 [51]	DFT	160.2(3)	17.5(8)	4.3(8)	0	
BMEOS3 [16]	NPD	159.95	23.8(1.4)	4.5(1.5)	85	0 - 4
BMEOS3 [152]	XPD	159.95$^+$	24.3	4.5$^+$	87	5 - 50
BMEOS3 [76]	NPD	160.35*	18.7(2)	5.7(1)	93	2.75(2) - 11.63(7)
BMEOS3 [76]	NPD	164.05	15.6(3)	6.2(1)	196	2.75(2) - 11.63(7)
Vinet [114]	XPD	166(2)	19(4)	5.0(6)	220	3 - 28
BMEOS3 [152]	XPD	164.46	15.5	6.9	266	5 - 17

* value fixed based on a measurement on the sample recovered from high-pressure at 93 K

$^+$ value fixed based on the values of Besson *et al.*, 1997 [16]

2.5 Summary

This section has focused on the theory behind solving the time independent Schrödinger equation to calculate material properties, starting from Hartree-Fock through to the widely used density functional theory.

This was followed by how these theories are used in practice to simulate the material - in particular how *VASP* is used to calculate material properties. Some of the shortcomings of modern-day computers were discussed, including how to ensure calculations remain efficient on multi-core machines, through to the details of the inputs and outputs used by *VASP*.

The final section moved on to how the information given in the output of *VASP* can be turned into something meaningful for material science, such as the bulk modulus and changes in structure as a function of pressure. This was then applied to the water ice system, specifically the high-pressure phase ice VIII. There has been plenty of both computational and experimental work to compare against, and this showed that the calculations are indeed running as intended, ready for calculations now to begin on the ammonium carbonates.

The next few chapters will now focus on the work on materials in the $NH_3 + CO_2 \pm H_2O$ ternary system, starting with the hydrated compounds - namely ammonium

carbonate monohydrate and ammonium sesquicarbonate monohydrate.

Chapter 3

Ab initio simulations of ammonium carbonate hydrates

This chapter presents the results of the *ab initio* work for ammonium carbonate monohydrate, $(NH_4)_2CO_3 \cdot H_2O$, and ammonium sesquicarbonate monohydrate, $(NH_4)_4[H_2(CO_3)_3] \cdot H_2O$. The aim is to simulate the behaviour under compression of the hydrous compounds in the NH_3 - $CO_2 \pm H_2O$ ternary system; namely ammonium carbonate monohydrate and ammonium sesquicarbonate monohydrate. The sparseness of literature data presents a difficulty in assessing the veracity of the calculated compressibility.

3.1 Ammonium carbonate monohydrate

Ammonium carbonate monohydrate crystals, $(NH_4)_2CO_3 \cdot H_2O$, are stable at temperatures below 273 K, transforming to ammonium bicarbonate by loss of ammonia above this temperature. Ammonium carbonate monohydrate can be identified from the other carbonates by the morphology of the crystals. The first crystallographic description can be found in Divers, 1870 [39], in which the morphology of the crystals is described; distinct herringbone pattern and hollowed-out terminating faces can be seen. And yet it took over 140 years for the first crystal structure to be reported [53], in which it was shown that ammonium carbonate monohydrate crystallises in the orthorhombic crystal system, space group *Pnma*, Z = 4, with $a = 12.047(3)$ Å, $b = 4.453(1)$ Å, $c = 11.023(3)$ Å, and $V = 591.3(3)$ Å^3 at 10 K (see Figure 3.1).

The structure is composed of CO_3^{2-} anions, with each of the O atoms accepting three hydrogen bonds from a NH_4^+ tetrahedron. The $N(1)H_4^+$ tetrahedra form chains

with the CO_3^{2-} anions along the *a*-axis, with the $N(2)H_4^+$ tetrahedra 'decorating' this chain by donating a single out-of-plane hydrogen bond to a water molecule. Chains in adjacent sheets are related to one another by the 2_1 symmetry operation along *b*, the result being a fully three-dimensional hydrogen-bonded framework, albeit with a strongly layered character [53].

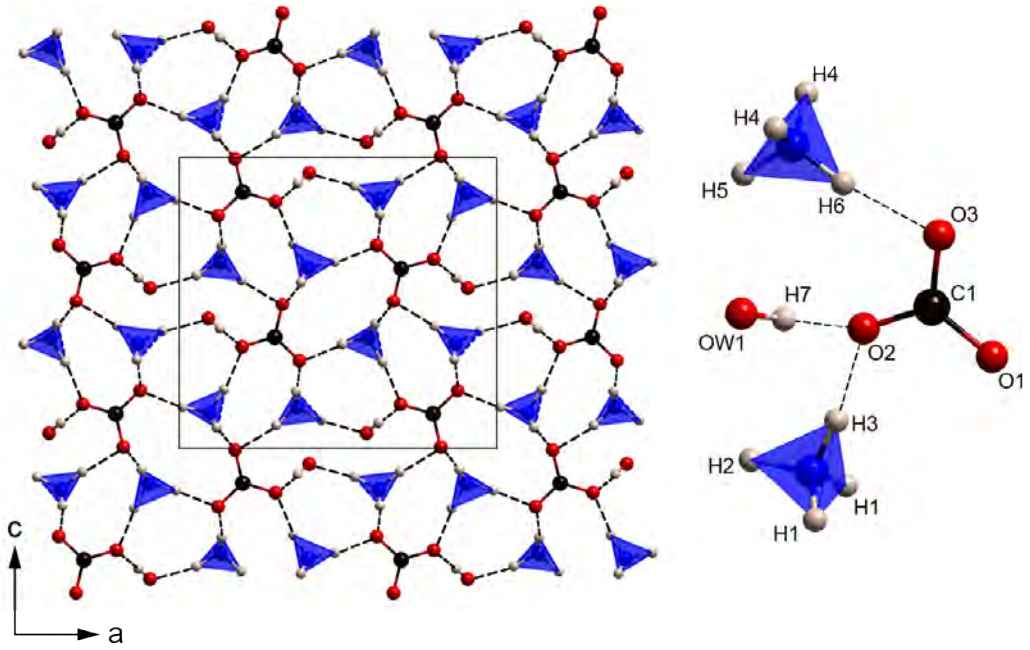

Figure 3.1
(left) The crystal structure of ammonium carbonate monohydrate viewed in the *ac* plane. The solid black box marks the outline of the unit-cell, and the dark dashed lines are hydrogen bonds. (right) The asymmetric unit of ammonium carbonate monohydrate with labelled atoms. The structure is composed of carbonate ions (CO_3^{2-}), ammonium tetrahedra (NH_4^+) and water molecules. Atomic labels are the same used by Fortes *et al*., 2014 [53].

3.1.1 Computational details

In order to determine bulk properties of ammonium carbonate monohydrate, first-principles calculations using dispersion-corrected DFT [68, 78] as implemented in *VASP* [80] were used. The plane-wave expansion was treated using the Projected Augmented-Wave method, PAW [17], using the PAW potentials distributed with *VASP* [81]. The exchange-correlation was accommodated using the PBE generalised gradient corrected functional [110] augmented by the D3-correction of Grimme and co-workers together with Becke-Johnson damping [60]. This method arrived at the closest $V_{0,0}$ value to that measured experimentally at 10 K.

Convergence tests were carried out to optimise the $\vec{k}$-point sampling of the Bril-

Table 3.1
Structural parameters of ammonium carbonate monohydrate, measured by a single crystal neutron diffraction experiment on SXD at 10 K by Fortes *et al.*, 2014 [53]. This structure was used as the starting point for the DFT calculations.

d_8-ammonium carbonate monohydrate

Formula	$(NH_4)_2CO_2 \cdot H_2O$	Lattice parameters	
Space group	*Pnma*	*a*-axis (Å)	12.048(2)
Z	4	*b*-axis (Å)	4.461(2)
ρ (kg m^{-3})	1272	*c*-axis (Å)	11.090(2)
Temperature (K)	10	Volume (Å^3)	596.0(3)

Label	Fractional coordinates			U_{iso}	Site
	x	y	z	(x10^2)	
C1	0.3000(2)	0.7500	0.38125(15)	0.17(3)	4c
N1	0.09629(16)	0.7500	0.12198(12)	0.42(3)	4c
N2	0.12951(16)	0.7500	0.64120(12)	0.44(2)	4c
O1	0.3777(2)	0.7500	0.30102(19)	0.35(3)	4c
O2	0.1975(2)	0.7500	0.34848(19)	0.39(3)	4c
O3	0.3244(2)	0.7500	0.49516(18)	0.35(4)	4c
OW1	0.0913(3)	0.2500	0.4467(2)	0.57(4)	4c
H1	0.1176(4)	0.5610(8)	0.0716(3)	1.77(8)	8d
H2	0.0111(6)	0.7500	0.1420(5)	1.74(10)	4c
H3	0.1417(6)	0.7500	0.2031(5)	1.72(10)	4c
H4	0.1333(4)	0.5597(7)	0.6955(3)	1.77(7)	8d
H5	0.0534(6)	0.7500	0.5965(5)	1.73(10)	4c
H6	0.1953(6)	0.7500	0.5798(5)	1.67(10)	4c
H7	0.1285(4)	0.4248(7)	0.4125(4)	1.87(8)	8d

louin zone within the Monkhorst-Pack scheme [98] and the kinetic energy cut-off of the plane-wave basis set. A total energy convergence better than 10^{-3} eV per unit-cell and pressure converged better than 0.2 GPa was achieved when using a $\vec{k}$-point mesh and kinetic energy cut-off of 2x5x2 (16 irreducible $\vec{k}$-points, $\sim$0.04 Å^{-1} reciprocal lattice spacing) and 960 eV.

A series of fixed volume calculations were performed in which the ions were allowed to move according to the Hellman-Feynman forces and the unit-cell shape allowed to vary, starting from the structural parameters given in Fortes *et al.*, 2014 [53] (Table 3.1). At each specified volume, the structure was relaxed via the conjugate-gradient technique in order to optimise the lattice parameters and internal coordinates.

3.1.2 Structure and bonding

A comparison of a zero-pressure relaxation of ammonium carbonate monohydrate and the experimentally measured values of the crystal structure at 10 K is given in Fortes

et al., 2014 [53], showing very good agreement between the DFT calculations and the experimentally measured values.

The experimentally measured volume of the unit-cell at 10 K is 591.3(3) Å^3 [53]; the zero-pressure athermal relaxation in this work gives $V_0 = 589.43$ Å^3, which is an approximately 0.3 % under-estimation of the measured volume (Table 3.2). As noted in Fortes *et al.*, 2014 [53], the only substantial difference between the experimental and computational structures is the length and linearity of the hydrogen bonds donated by and accepted by the water molecule, which is still the case in this study (see Table 3.3).

Table 3.2
Comparison of unit-cell cell parameters of ammonium carbonate monohydrate between experiments and a zero-pressure calculation.

	Calculated[a]	Experimental[b]		
		10 K	100 K	245 K
a-axis (Å)	12.0518	12.047(3)	12.056(3)	12.160 (7)
b-axis (Å)	4.3939	4.453(1)	4.452(1)	4.486(2)
c-axis (Å)	11.1309	11.023(3)	11.016(3)	11.011(7)
volume (Å^3)	589.4262	591.3(3)	591.2(3)	600.7(6)

[a] This work
[b] from Fortes *et al.*, 2014 [53]

Table 3.3
Comparison of hydrogen bond lengths in ammonium carbonate monohydrate between the values determined by DFT simulations in this work, and a previous study involving a zero-pressure DFT relaxation and a single crystal neutron diffraction experiment [53].

	This work			Fortes *et al.*, 2014 [53]					
	ab initio (0 K)			*ab initio* (0 K)			10 K		
	H···Y (Å)	X···Y (Å)	X-H···Y (°)	H···Y (Å)	X···Y (Å)	X-H···Y (°)	H···Y (Å)	X···Y (Å)	X-H···Y (°)
N1-H1···O3	1.7391	2.7764	169.92	1.7640	2.8027	170.44	1.766(4)	2.797(2)	170.6(4)
N1-H2···O1	1.7108	2.7611	171.53	1.7308	2.7819	171.89	1.721(6)	2.766(3)	171.1(5)
N1-H3···O2	1.7239	2.7719	171.66	1.7436	2.7935	172.75	1.740(5)	2.778(2)	171.6(6)
N2-H4···O1	1.7959	2.8325	171.08	1.8224	2.8604	171.58	1.808(3)	2.840(1)	171.7(4)
N2-H5···Ow1	1.7136	2.7614	170.45	1.7255	2.7745	171.32	1.807(7)	2.831(3)	167.0(5)
N2-H6···O3	1.7951	2.8345	170.82	1.8130	2.8534	170.68	1.814(6)	2.847(3)	170.2(5)
Ow1-H7···O2	1.7666	2.7597	179.26	1.7937	2.7843	178.99	1.813(4)	2.788(2)	179.6(5)

3.1.3 Thermal expansion

In Fortes *et al.*, 2014 [53], the authors offer an estimate of the thermal expansion of ammonium carbonate monohydrate (given here in Figure 3.2). In the thermal expansion data given, it is suggested that the *c*-axis may show negative thermal expansion (NTE) at all temperatures, although to a very small degree ($\alpha_c \approx -1 \times 10^{-6}$ K^{-1}). From this,

the authors also predict that "the *a*-axis will prove to be the most compressible direction in the crystal whilst the *c*-axis will be the least compressible".

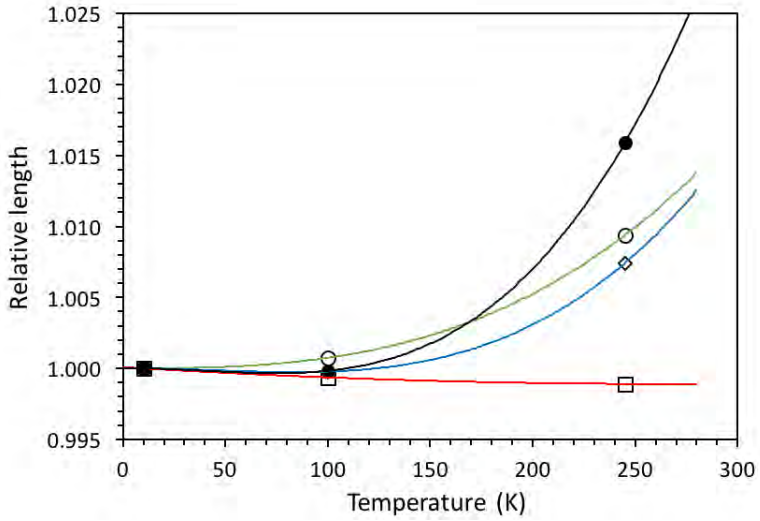

Figure 3.2
Thermal expansion of ammonium carbonate monohydrate, measured by Fortes et al., 2014 [53] at 10 K (neutron), 100 K (neutron) and 245 K (X-ray). The symbols correspond to: *a*-axis (open circle, green line); *b*-axis (open diamond, blue line); *c*-axis (open square, red line); unit-cell volume (black circle, black line). The lines are qualitative interpolations to guide the eye.

The same thermal expansion behaviour is seen in an experiment conducted using UCL Earth Science's modified Phenix-FL CCR, in which the thermal expansion of ammonium carbonate monohydrate from 40 K to 160 K was determined (details of this experiment are given in Appendix B). Although the data quality in that experiment is not great, it does confirm the thermal expansion behaviour predicted. In Figure B.1, it can be seen that the *c*-axis does indeed show negative thermal expansion (NTE) across the whole temperature range measured, but the volumetric expansion remains positive at all temperatures due to the similar positive expansion along *a* and *b*. The prediction offered for the linear compressibility of each axis has proved, as can be seen next, to be accurate.

3.1.4 Equation of state

A series of constant volume relaxations were performed over a volume range of 365 - 675 Å^3 (corresponding to a pressure range between 25 GPa and -3 GPa). Inspection of the unit-cell parameters as a function of pressure reveals a subtle change at pressures higher than 3 GPa which is not immediately obvious from cursory analysis of the unit-cell volume (Figure 3.4).

A plot of total energy against volume, *E(V)*, and pressure against volume, *P(V)*, with a fitted third-order and fourth-order Birch-Murnaghan equation of state are given in Figure 3.3; a BMEOS3 and BMEOS4 was fitted to the E(V) and P(V) curves across all of the data. In the lower panel of Figure 3.3, two equations are fitted around an inflection point at 5 GPa, indicative of a second-order phase transition. Fitted equation of state parameters for ammonium carbonate monohydrate are given in Table 3.4.

The bulk modulus is rather high in this case, around 25 - 35 GPa depending on the equation of state fitted to the data. It seems apparent that the negative linear compressibility along *c* amplifies the anisotropy in the crystal and results in a higher bulk stiffness - similar behaviour is seen in ammonium oxalate monohydrate [115].

Table 3.4
Fitted parameters to the E(V) and P(V) curves of ammonium carbonate monohydrate, using a BMEOS3 and BMEOS4 equation of state. The bottom two rows are BMEOS3 fits to the lower panel of Figure 3.3).

	V_0 (Å^3)	K_0 (GPa)	K_0'	K_0'' (GPa^{-1})	E_0 (eV)
BMEOS3, E(V)	593(2)	26.1(9)	2.8(1)	-0.159(2)	-378.23(2)
BMEOS3, E(V)	589.4*	28.0(6)	2.65(9)	-0.156(3)	-378.23(3)
BMEOS4, P(V)	595(2)	29.8(9)	1.1(2)	-0.032(8)	-
BMEOS4, P(V)	589.4*	34.9(8)	0.3(1)	-0.069(9)	-
BMEOS3, P(V)$^+$	590.3(6)	29.4(4)	3.7(2)	-0.126(4)	-
BMEOS3, P(V)$^\#$	681(9)	9.3(5)	4.5*	-0.50(3)	-

* Value was fixed

$^+$ Fitted to the data below <5 GPa (see lower panel of Figure 3.3)

$^\#$ Fitted to the data at pressures >5 GPa (see lower panel of Figure 3.3)

3.1.5 High-pressure structure

As can be seen in Figure 3.4, the structure compresses with no step changes up to ∼3 GPa, and is highly anisotropic. The compression is greatest along the *b*-axis, and least along the *c*-axis; in the crystal structure, this corresponds to chains of rigid NH_4^+ and CO_3^{2-} molecules running in the *ac* plane, as seen in Figure 3.1, with limited bonding connecting chains along *b*. The medium-range H-bonds, in the form N-H$\cdots$O, are the most compressible in the structure, with the NH_4^+, CO_3^{2-} and H_2O molecules compressing at a much slower rate.

The anisotropic compressibility seen in Figure 3.4 corresponds with the limited thermal expansion data available, in which the *b*-axis and *a*-axis expand more than

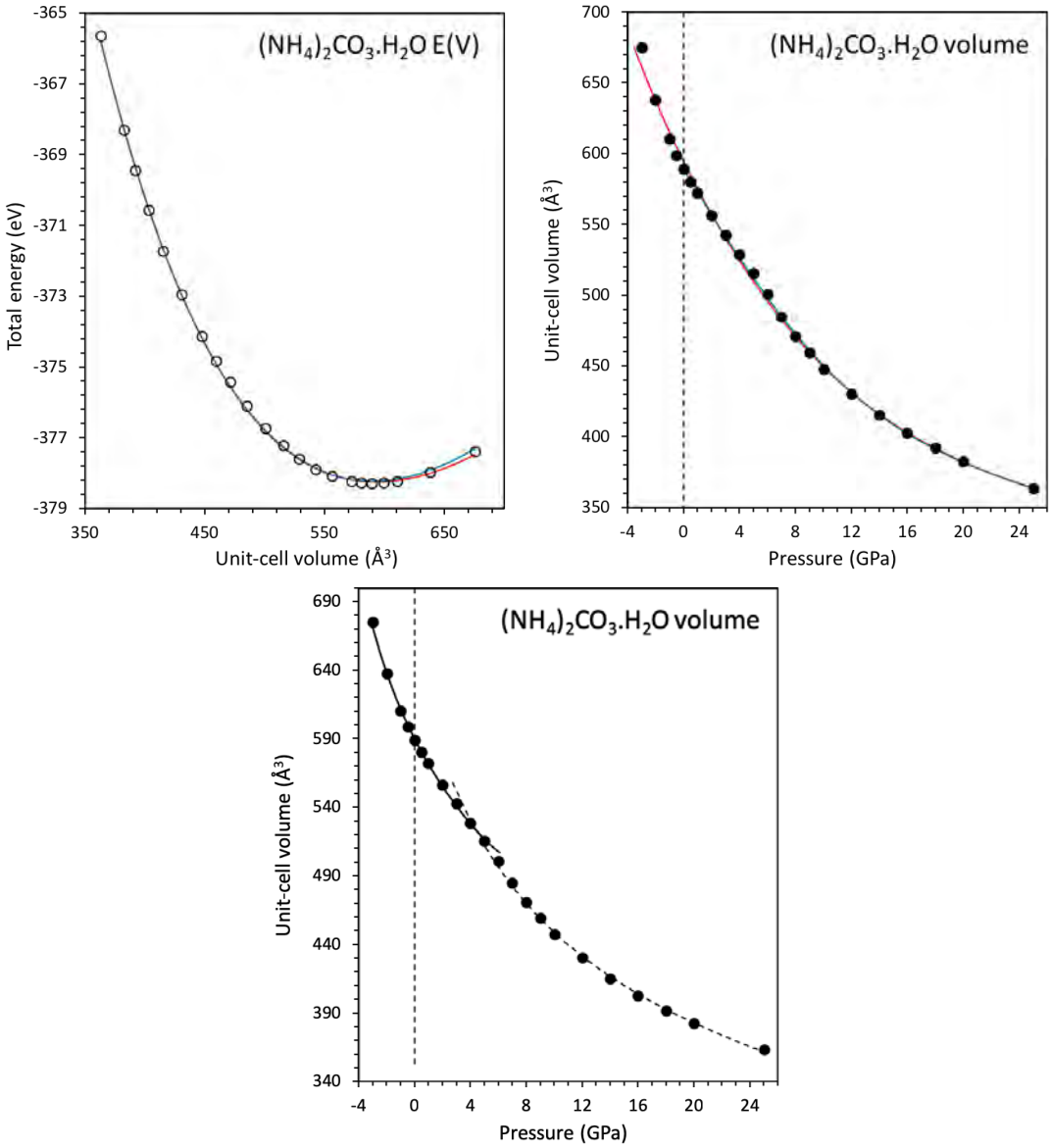

Figure 3.3
Calculated E(V) curve (left), P(V) curve (right), and P(V) curve with two fitted equations (bottom) of ammonium carbonate monohydrate. The circles are calculated points, and the solid lines show the best fit BMEOS4 with (red) no fixed values (blue) fit with values fixed (see Table 3.4 for more information). The solid black line in the lower panel is a BMEOS3 fit to the data below 5 GPa, and the dashed line is a fitted BMEOS3 to the data above 5 GPa. The dotted line on the right-hand panel and lower panel is the zero-pressure line for clarity between negative and positive pressures.

the *c*-axis (Figure 3.2). This behaviour, in which there is lesser area expansivity (or compressibility) formed by chains in one plane and greater linear expansivity (or compressibility) perpendicular to these sheets is common in the ammonium carbonates, as will be seen in the following chapters.

Above ∼6 GPa, the structure begins to deform in a different manner to before. Al-

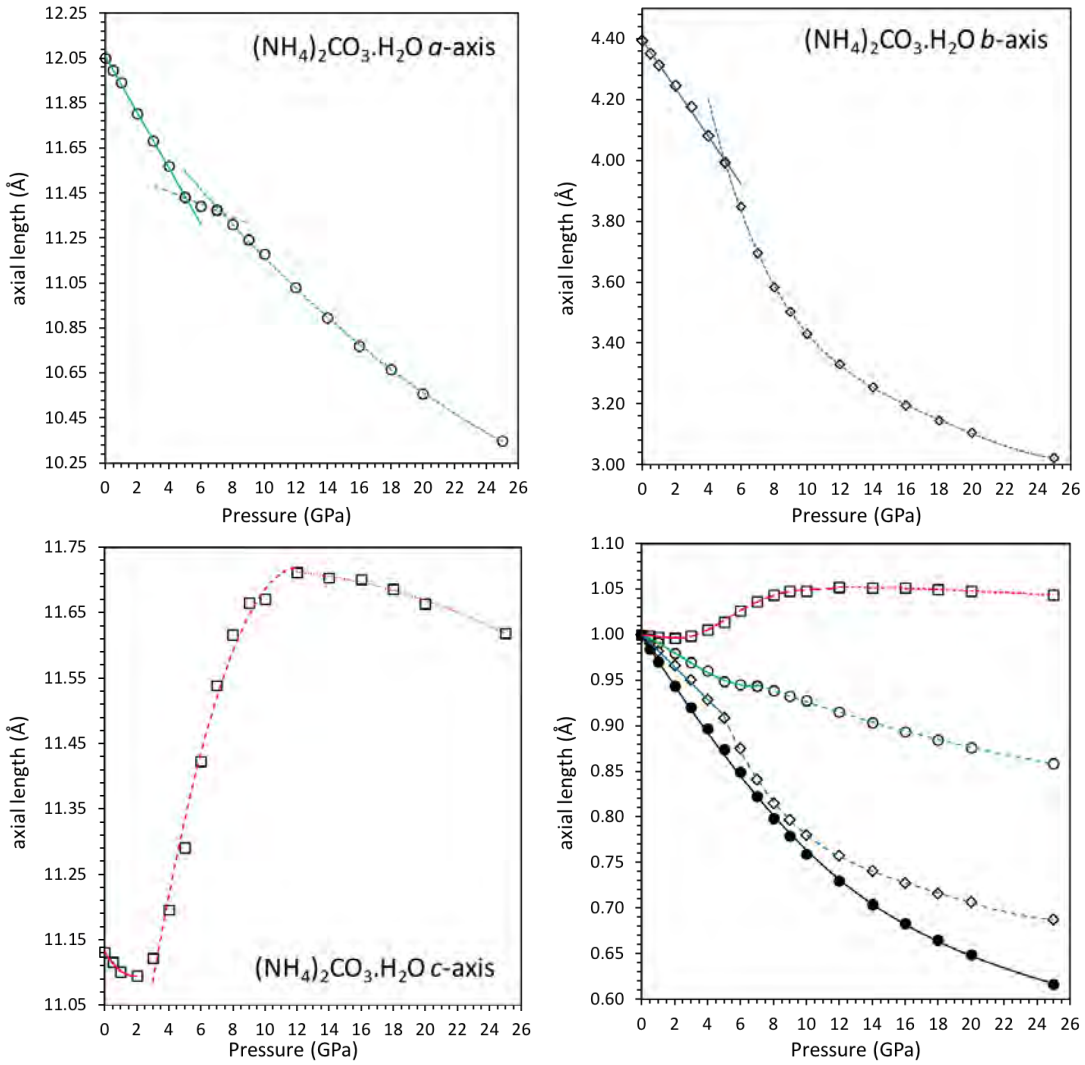

Figure 3.4
Calculated change in size of the unit-cell dimensions of ammonium carbonate monohydrate. The solid lines are fitted polynomials, and the dashed lines are polynomials after the structural change, corresponding to; (green) a-axis (blue) b-axis (red) c-axis (black) unit-cell volume.

though this is not immediately obvious in looking at the unit-cell volume as a function of pressure - which only shows a very small deviation - it is obvious when looking at how the lattice parameters of ammonium carbonate monohydrate change as a function of pressure. In Figure 3.4, this change in the deformation is shown by the dashed lines - it can be seen that the *c*-axis shows negative linear compressibility (NLC) at pressures higher than $\sim$2 GPa, increasing dramatically in size up to $\sim$11 GPa and then returning to positive linear compressibility (PLC) (also see Figure 3.5).

The presence of NLC is quite uncommon - most materials compress in all directions when hydrostatically stressed. NLC is a rare but highly attractive mechanical

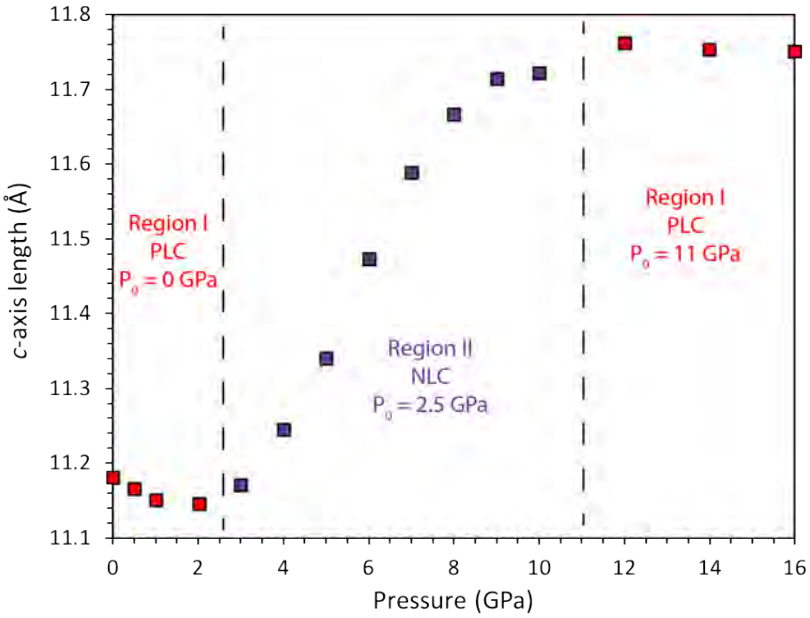

Figure 3.5
Calculated *c*-axis length of ammonium carbonate monohydrate up to 17 GPa. Points coloured red are positive linear compressibility (PLC), points in purple are negative linear compressibility (NLC).

property, having various applications, such as in the design of pressure sensors, artificial muscles and actuators [15] (see [46] for some ideas for uses of NLC). When comparing ammonium carbonate monohydrate to the similar ammonium oxalate monohydrate, a remarkable similarity of the behaviour of the lattice parameters as a function of pressure can be seen [115]. In ammonium oxalate monohydrate, it is the *b*-axis that shows NLC, persistent above 5.1 GPa and returning the PLC above 11.5 GPa, having a near constant negative compressibility of -2.3(7)TPa^{-1}. In this work, ammonium carbonate monohydrate has NLC along the *c*-axis, persistent above 2 GPa and returning to PLC at 12 GPa, but the negative compressibility varies with pressure, ranging from -8 TPa^{-1} at 2 GPa to -5 TPa^{-1} at 12 GPa, averaging over the pressure range at -6(1) TPa^{-1} (there are quite large errors associated with these values). The persistence of the NLC and the structural stability, ranging over several GPa, is similar to ammonium oxalate monohydrate.

The NLC is most likely caused by very 'soft' N-H···O bonds that easily compress over the low pressure range, but slowly stiffen as the CO_3^{2-} and NH_4^+ molecules get closer. At the critical pressure (2.5 GPa), the N-H···O have become 'rigid' and the H-bonds motifs allow for NLC along *c* due to a mechanical response to pressure (Figure

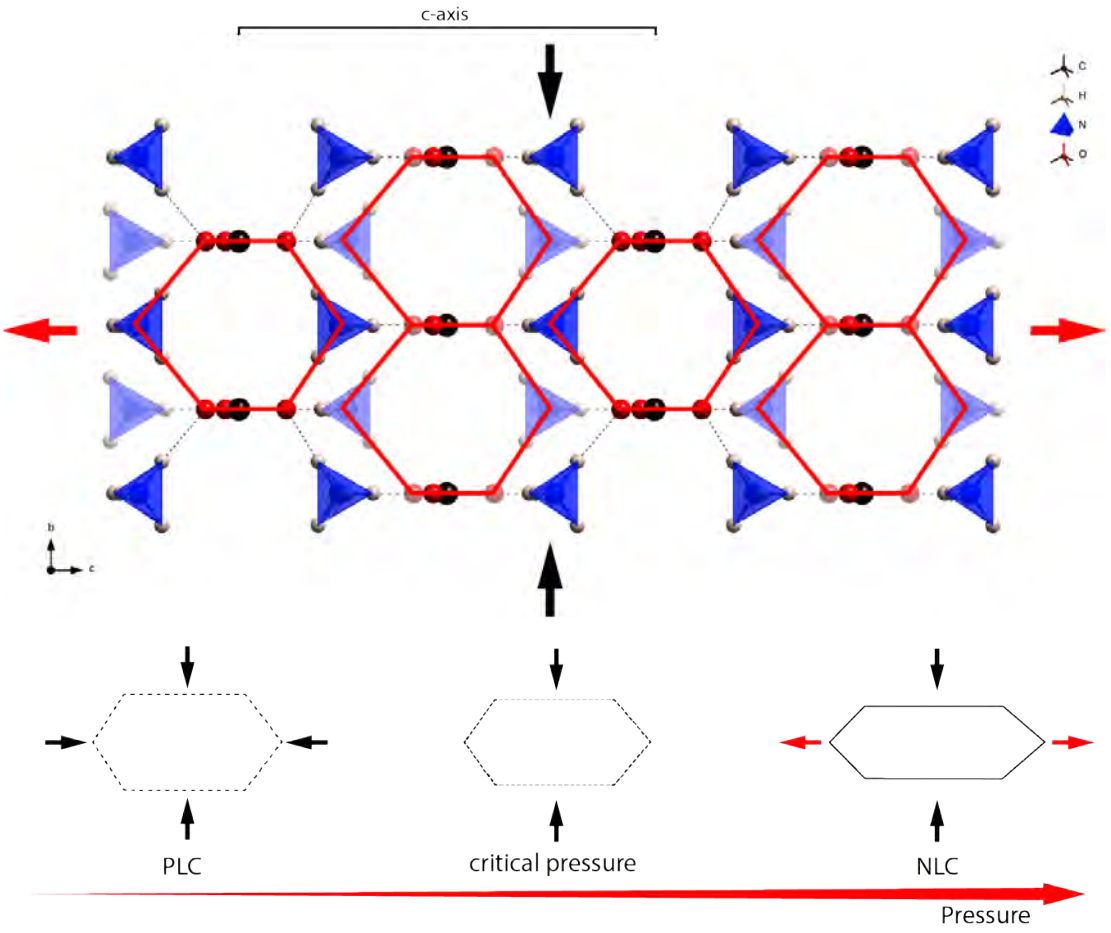

Figure 3.6
Structure of ammonium carbonate monohydrate viewed along the *a*-axis direction at ambient pressure. The red hexagons extend along *b*, compressing vertically and expand laterally. At the bottom is the schematic representation of the hydrogen bonding NLC mechanism.

3.6). Eventually, the hydrogen bonds become sufficiently 'soft' once more so as to allow the structure to compress in all directions once more.

In the NLC region, rotation and translation of the molecules in the structure can be seen. The two $N(1)H_4^+$ ions in the centre of the structure rotate around their central atom, forcing the CO_3^{2-} ions to move along *c*, increasing the axial length in this orientation and shrinking slightly along *a* due to the reshuffling of the atoms inside the structure. This change in the structure continues up to 12 GPa; this can be seen as the flattening of the *c*-axis size in Figure 3.4.

Ammonium oxalate monohydrate has been suggested to have a phase change after the NLC, at pressures between 12.3 and 13.3 GPa. With the remarkable similarity seen in the behaviour of the structure as a function of pressure between ammonium oxalate monohydrate and ammonium carbonate monohydrate, it is highly likely that

ammonium carbonate monohydrate will undergo a phase change at similar pressures based upon these DFT calculations, although no phase change was evident in the DFT simulations. Experimental work will be able to prove this hypothesis.

3.1.6 Planetary parameters

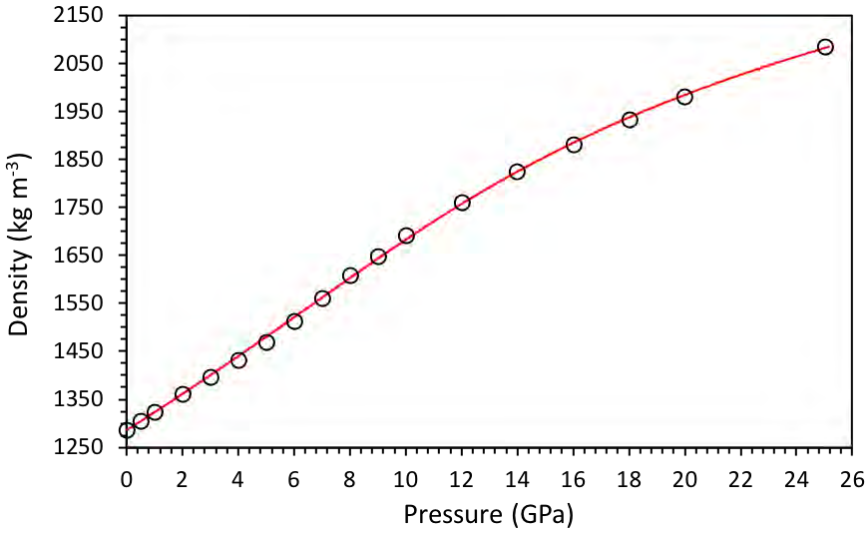

Figure 3.7
Calculated density as a function of pressure of ammonium carbonate monohydrate. The solid line is a from a BMEOS4 fit.

Without knowing something as simple as the density as a function of pressure, modelling of the ammonium carbonates as planetary-forming materials is severely limited. Therefore, in this section in each chapter, the density as a function of pressure will be reported, calculated either from the DFT simulations or from experimentally measured unit-cell volumes. To fit the density, a 4^{th}-order Birch-Murnaghan equation of state is used where, instead of $x = V/V_0$, it is $x = \rho/\rho_0$. Using this can fit the density with the equation of state to understand how the density varies with depth inside a planetary body. Figure 3.7 shows how the density varies as a function of pressure, assuming a single EoS across the whole of the simulated pressure range. The equation of state parameters are $\rho_{0,0} = 1285.8$ kg m^{-3}, $K_0 = 34.9(8)$ GPa, $K_0' = 0.3(1)$ GPa^{-1}, and $K_0'' = -0.069(9)$.

3.2 Ammonium sesquicarbonate monohydrate

The second hydrous compound in the ternary system has been known since at least 1854, when Sainte-Claire Deville [123] reported a morphological analysis of ammonium sesquicarbonate monohydrate crystals. Divers, 1870 [39] gives details of the compound, including stability, synthesis methodology, and a determination of the chemical formulae. However, as with ammonium carbonate monohydrate, it took many years before a crystal structure was published. The structure of ammonium sesquicarbonate monohydrate, $(NH_4)_4[H_2(CO_3)_3]\cdot H_2O$, is orthorhombic, space group *Fmm2*, Z = 4, with $a = 7.1916(6)$ Å, $b = 15.8913(14)$ Å, $c = 10.4912(12)$ Å, and $V = 1199.0(2)$ Å^3 at 173(2) K [91].

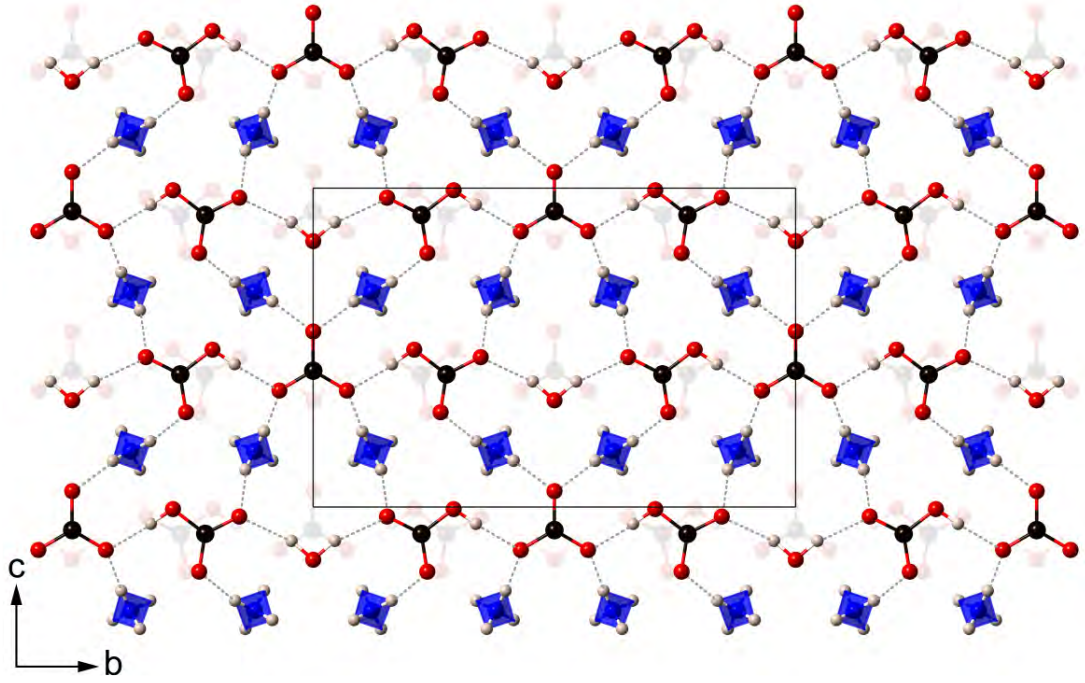

Figure 3.8
The crystal structure of ammonium sesquicarbonate monohydrate viewed in the *bc* plane. The solid black line is the outline of the unit-cell, and the grey dashed lines are long-range hydrogen bonds. The structure is made up of carbonate ions (CO_3^{2-}) and bicarbonate ions (HCO_3^-), coordinated via water molecules and ammonium tetrahedra (NH_4^+). The faded atoms are in the plane below, *a*/2.

The structure consists of units of carbonate anions (CO_3^{2-}), bicarbonate anions (HCO_3^-) and water molecules, hydrogen bonded together in planar chains running parallel to *b* along mirror planes (Figures 3.8 & 3.9). These units consist of a CO_3^{2-} anion, with the central C atom lying on a mirror plane, and two of the O atoms accepting hydrogen bonds from the HCO_3^- anion H atom, on either side of the mirror;

Table 3.5
Structural parameters of ammonium sesquicarbonate monohydrate, measured in a single crystal X-ray diffraction experiment by Margraf *et al.*, 2003 [91]. This structure was used as the starting point for the DFT calculations.

Ammonium sesquicarbonate monohydrate

Formula	$(NH_4)_4[H_2(CO_3)_3]\cdot H_2O$	Lattice parameters	
Space group	*Fmm2*	*a*-axis (Å)	7.1916(6)
Z	4	*b*-axis (Å)	15.8913(14)
ρ (kg m^{-3})	1508.1	*c*-axis (Å)	10.4912(12)
Temp. (K)	173(2)	Volume (Å^3)	1199.0(2)

Label	Fractional coordinates			U_{iso}	Site
	x	y	z	(x100)	
C1	0.5000	0.0000	0.42763(16)	1.38(3)	4a
C2	0.0000	0.22408(7)	0.41613(13)	1.51(2)	8c
N1	0.74620(11)	0.12128(4)	0.67537(10)	1.82(2)	16e
O1	0.0000	0.0000	0.33490(18)	3.72(5)	4a
O11	0.5000	0.06990(6)	0.36567(9)	1.88(2)	8c
O12	0.5000	0.0000	0.55065(12)	1.69(3)	4a
O21	0.0000	0.29081(7)	0.49366(10)	2.55(3)	8c
O22	0.0000	0.15308(7)	0.47048(10)	2.11(2)	8c
O23	0.0000	0.23633(6)	0.29708(10)	2.08(2)	8c
H1	0.0000	0.045(2)	0.394(4)	6.5(11)	8c
H1A	0.817(2)	0.1405(9)	0.618(2)	2.5(4)	16e
H1B	0.672(2)	0.1620(10)	0.7064(18)	2.5(4)	16e
H1C	0.815(3)	0.1018(11)	0.7374(18)	2.8(4)	16e
H1D	0.674(2)	0.0848(11)	0.6458(17)	2.8(4)	16e
H21	0.0000	0.3368(19)	0.448(4)	4.3(7)	8c

this unit of three repeats via a water molecule, with the O atom of the water also on a mirror plane. Between each layer of chains is a translation by half a unit-cell along *b*. Ammonium tetrahedra, NH_4^+, lie between the sesquicarbonate chains, with each bonded to four separate anions - two carbonate and two bicarbonate anions - creating a three-dimensional structure.

3.2.1 Computational details

Static DFT calculations (see section 3.1.1) were carried out to determine an equation of state. Convergence tests were carried out to optimise the $\vec{k}$-point sampling of the Brillouin zone within the Monkhorst-Pack scheme and the kinetic energy cut-off of the plane-wave basis set. A converged 4x2x3 grid (4 irreducible $\vec{k}$-points, and $\sim$0.03 Å^{-1} reciprocal lattice spacing) with energy cut-off 1075 eV yielded total energy convergence better than 10^{-3} eV per unit-cell.

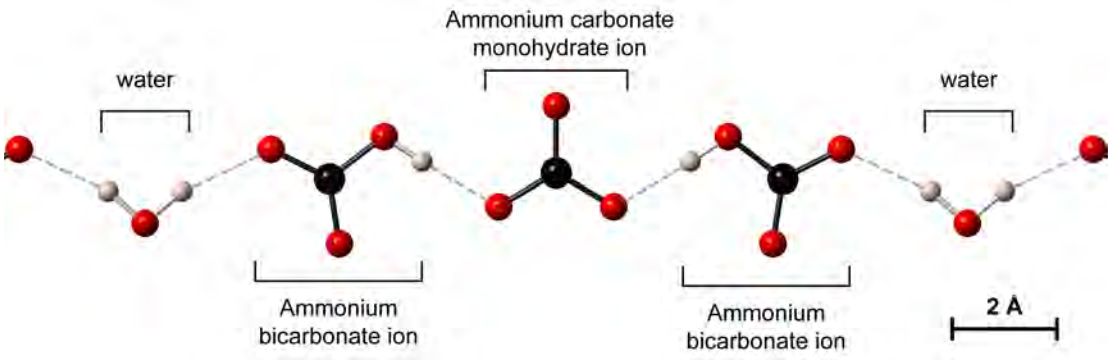

Figure 3.9
Chain motif in ammonium sesquicarbonate monohydrate, running parallel to *b*, consisting of a carbonate ion bonded to bicarbonate ion, repeated via a water molecule. The grey dashed lines are O-H···O bonds.

A series of fixed volume calculations were performed in which the ions were allowed to move according to the Hellman-Feynman forces and the unit-cell shape allowed to vary, starting from the structural parameters given by Margraf *et al.*, 2003 [91] (Table 3.5). At each specified volume, the structure was relaxed via the conjugate-gradient technique in order to optimise the lattice parameters and internal coordinates.

3.2.2 Structure and bonding

The experimental value for the unit-cell volume, measured at 173(2) K is 1199.0(2) Å^3 [91] (Table 3.6). The difference between this and the calculated zero-pressure athermal relaxation is a ∼0.4 % under-estimation for the calculated value. This under-estimation is likely due to the effect of temperature on the structure; the only experimental value of the unit-cell was measured at 173 K, whereas the DFT simulations in this work are athermal. Intuitively, it would be expected that the unit-cell would decrease in volume under cooling, so a smaller estimated unit-cell volume is not too problematic.

The experiment to determine the thermal expansion of ammonium carbonate monohydrate, the details of which are given in Appendix B, did provide the evidence for a smaller unit-cell volume of ammonium sesquicarbonate monohydrate at a lower temperature than 173 K; at 40 K, the unit-cell volume of 1179.9(1) Å^3 . Using this value, the zero-pressure unit-cell volume is ∼1.2 % overestimated compared to the only previous experimental value. A thermal expansion study to determine the behaviour of this compound is need to provide an accurate low temperature structure and structural behaviour as a function of temperature.

Table 3.6
Comparison of unit-cell cell parameters of ammonium sesquicarbonate monohydrate between experimental value and the zero-pressure calculation in this work.

	Calculated[a]	Experimental[b] 173(2) K
a-axis (Å)	7.1331	7.1916(6)
b-axis (Å)	15.8657	15.8913(14)
c-axis (Å)	10.5539	10.4912(12)
volume (Å^3)	1194.40	1199.0(2)

[a] This work
[b] from Margraf *et al.*, 2003 [91]

Table 3.7
Zero-pressure atomic coordinates of ammonium sesquicarbonate monohydrate determined from the DFT simulations.

Label	Fractional coordinates			Site
	x	y	z	
C1	0.50000	0.00000	0.42886	4a
C2	0.00000	0.22239	0.41779	8c
N1	0.74663	0.11981	0.67611	16e
O12	0.50000	0.00000	0.55215	4a
O11	0.50000	0.07052	0.36658	8c
O1	0.00000	0.00000	0.33942	4a
O22	0.00000	0.15139	0.47572	8c
O23	0.00000	0.23224	0.29802	8c
O21	0.00000	0.29094	0.49291	8c
H1A	0.83333	0.14377	0.60505	16e
H1C	0.82919	0.09366	0.74766	16e
H1B	0.66278	0.16702	0.71607	16e
H1D	0.65900	0.07452	0.63641	16e
H1	0.00000	0.05047	0.39432	8c
H21	0.00000	0.34533	0.43939	8c

The greatest error between the calculated and experimental values is along *a* (see Table 3.6), which is $\sim$1 % underestimated; this direction is perpendicular to a mirror plane, in which the chains of HCO_3, H_2O and CO_3 molecules lie. The difference can easily be seen when looking at the distance between the NH_4^+ tetrahedra that are halfway between these chains - the zero-pressure relaxation gives a distance of 3.5185 Å compared to the measured value at 173(2) K of 3.650 Å.

Comparing the structural units in this compound - CO_3 from ammonium carbonate monohydrate, HCO_3 from ammonium bicarbonate, and H_2O - they are entirely unremarkable in bond lengths and angles, albeit with a caveat. The H-bond lengths given in

Margraf *et al.*, 2003 are typically short due to the use of X-ray diffraction to measure the sample (see Tables 3.8 & 3.9). The ammonium tetrahedra have an average bond length of 0.86 Å and volume 0.33 Å^3; compare this to the zero-pressure relaxation, with average bond length 1.04 Å and polyhedral volume 0.584 Å^3. This difference in the bond length then causes the H···O distance between the CO_3 and HCO_3 molecules to become overestimated. The same under- and over-estimation of H-bonding can also be seen in the chain structure, in which the H of the HCO_3 molecule has a bond distance of 0.87 Å from the X-ray diffraction experiment compared to the relaxed bond distance of 1.028 Å, again leading to an overestimation of the H···O bond distance. The bond distance between the H and O in the water molecule is not that different between the experimental and computational values, but the H1-O1-H1 angle is 98.1° compared to 107.99°. The relaxed bond lengths are much closer to typical values seen in ammonium bicarbonate and α-ammonium carbamate and are quite closely matched.

Table 3.8
Comparison of bond lengths, polyhedral volumes and various distortion metrics in ammonium sesquicarbonate monohydrate between the values determined by DFT simulations and a single crystal X-ray diffraction experiment by Margraf *et al.*, 2003 [91].

	DFT athermal	[91] X-ray 173(2) K
C1 - O11	1.300 Å	1.269(3) Å
C1 - O12	1.361 Å	1.340(3) Å
C2 - O21	1.300 Å	1.3365(16) Å
C2 - O22	1.285 Å	1.2642(14) Å
O21 - H21	1.03141 Å	0.87(4) Å
O1 - H1	0.98836 Å	0.95(4) Å
H1-O1-H1	107.99 °	98.1(11) °
N1 - H1A	1.04378 Å	0.845(19) Å
N1 - H1B	1.04711 Å	0.900(16) Å
N1 - H1C	1.04360 Å	0.87(2) Å
N1 - H1D	1.04044 Å	0.838(17) Å
$NH(D)_4$ volume	0.5831 Å^3	0.3304 Å^3
Distortion index	0.00164	0.0262
Quadratic elongation	1.0005	1.0026
Bond-angle variance	1.9590	6.3700

Table 3.9
Comparison of hydrogen bond lengths in ammonium sesquicarbonate monohydrate between the values determined by DFT simulations and a single crystal X-ray diffraction experiment by Margraf *et al.*, 2003 [91].

	This work			Margraf *et al.*, 2003 [91].		
	ab initio (0 K)			X-ray (173(2) K)		
	H···Y (Å)	X···Y (Å)	X-H···Y (°)	H···Y (Å)	X···Y (Å)	X-H···Y (°)
N1-H1A···O22	1.81415	2.82674	162.3971	2.041(19)	2.8648(13)	164.4(8)
N1-H1B···O23	1.77966	2.81638	169.8268	1.957(17)	2.8475(12)	170.0(8)
N1-H1C···O11	1.78729	2.81397	167.0068	1.96(3)	2.8256(12)	170.9(8)
N1-H1D···O12	1.86417	2.90169	174.6394	2.092(17)	2.9260(10)	173.2(8)
O21-H21···O11	1.54037	2.57078	176.7728	1.72(4)	2.5889(15)	177.0(12)
O1-H1···O22	1.81702	2.79965	172.3265	1.90(4)	2.1880(15)	164.1(11)

3.2.3 High-pressure structure

A series of constant volume relaxations were performed over a volume range of 915 - 1300 $Å^3$ (corresponding to a pressure range between 14 GPa and -2 GPa). Plots of total energy against volume, *E(V)*, and pressure against volume, *P(V)*, with fitted third order Birch-Murnaghan (BMEOS3) equations of state, are given in Figure 3.10. Fitted equation of state parameters for ammonium sesquicarbonate monohydrate are given in Table 3.10.

Looking at Figures 3.10 & 3.11, there are no step changes, indicating the structure is stable over the pressure range, and there is no evidence of NLC as calculated for ammonium carbonate monohydrate. The relative change in size of the unit cell dimensions shows this compound to have large compressional anisotropy, with the *a*-axis having a higher compressibility than either the *b*- or *c*-axes. In terms of the structure, this is due to limited bonding between chains of carbonate ions running parallel to the *b*-axis. The carbonate chains are linked via ammonium tetrahedra, running in chains between the carbonate ions.

Unsurprisingly, most of the compression in the structure arises from the X-H···Y bonding rather than the stronger individual molecules of HCO_3, CO_3 and H_2O. Shortening along *a* is due to the N-H···O bonding between the planar layers of the carbonate and bicarbonate ions and the ammonium tetrahedra. While the N-H bond shortens by $\sim$1 % over the 14 GPa pressure range simulated here, the longer H···O interaction shortens by $\sim$15 % between the CO_3 molecule and the ammonium tetrahedra. Likewise, the N-H bonding between the HCO_3 molecule and the NH_4 tetrahedra shortens

only by ∼1 %, compared with the H···O shortening by ∼8 %. The lesser shortening in this second instance is due to the HCO_3 molecule having a longer range interaction with H_2O (see Figure 3.9), with the oxygen sharing a longer range H···O interaction between two ammonium tetrahedra and a water molecule.

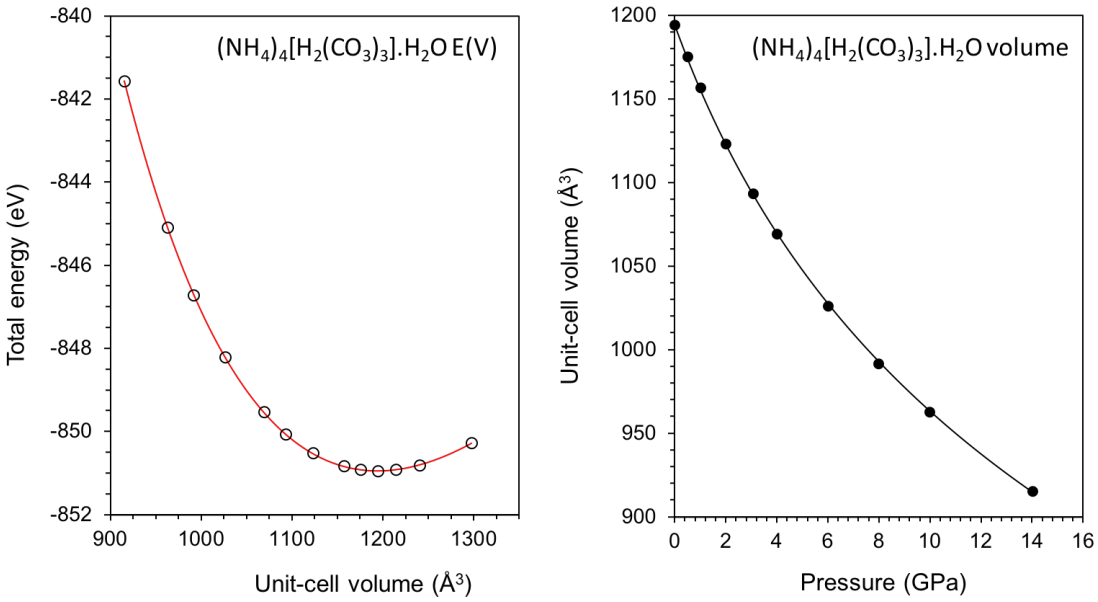

Figure 3.10
Calculated E(V) curve (*left*) and P(V) curve (*right*) of ammonium sesquicarbonate monohydrate. The open circles are calculated points, and the solid lines show the best fit BMEOS3.

Table 3.10
Fitted parameters to the E(V) and P(V) curves of ammonium sesquicarbonate monohydrate, using the BMEOS3 equation of state.

	V_0 (Å^3)	K_0 (GPa)	K_0'	K_0'' (GPa^{-1})	E_0 (eV)
BMEOS3, E(V)	1194.4(2)	27.7(2)	4.71(5)	-0.184(5)	-850.942(3)
BMEOS3, P(V)	1193.6(8)	28.1(3)	4.67(8)	-0.178(9)	-

There is less shortening along *b*, as there is a H···O interaction between the water and the bicarbonate molecule. In this instance, there is a ∼16 % shortening of this longer range interaction over the same pressure range, but the rest of the chain structure remains rigid and resists compression. The least compressibility along *c* is due to the lack of these H···O interactions between the chains in this orientation, so the shortening is between the chains themselves. There is no evidence in the calculated compressibility that any negative linear thermal expansion will occur in this compound.

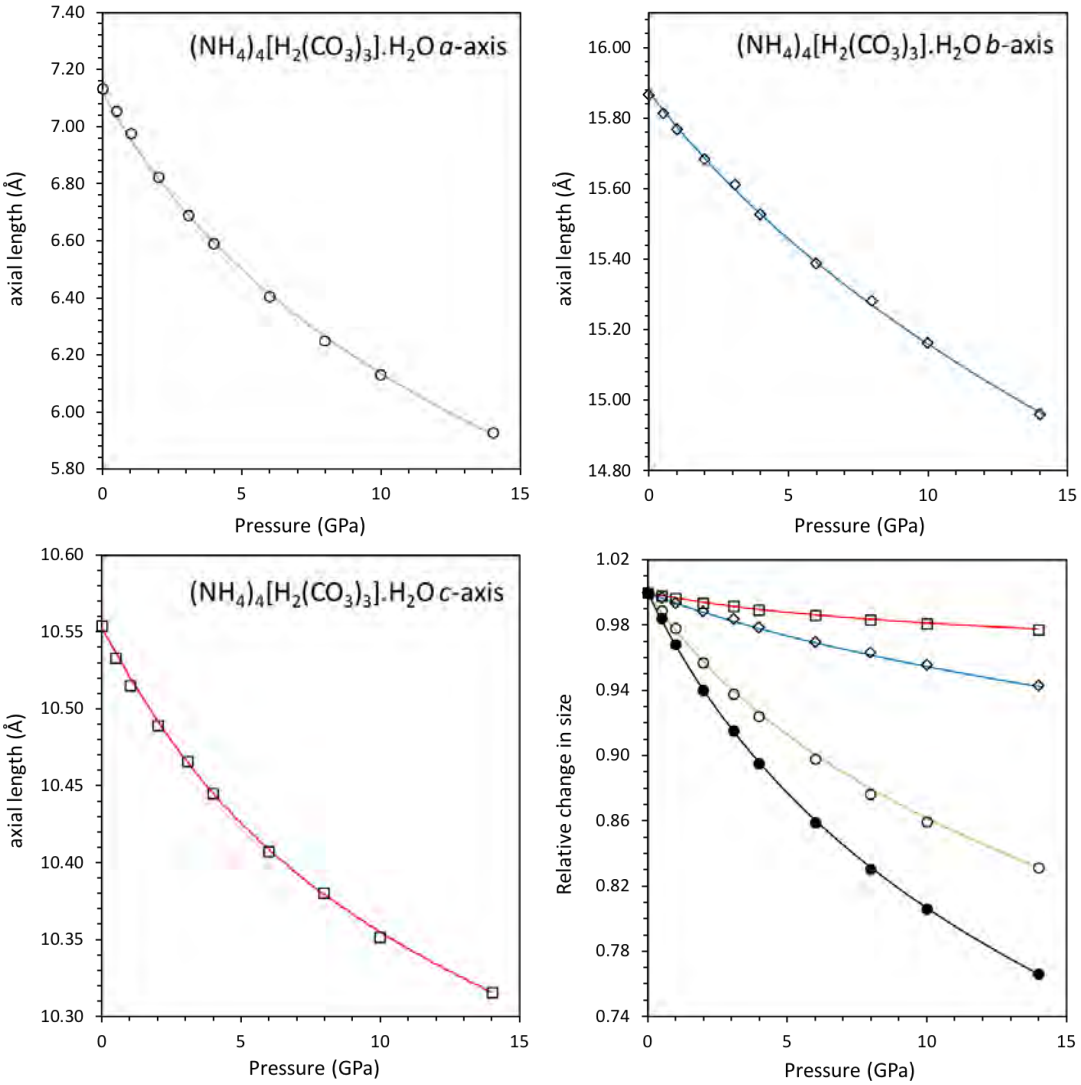

Figure 3.11
Relative change of unit-cell dimensions as a function of pressure of ammonium sesquicarbonate monohydrate. The lines correspond to BMEOS3 fits to: (green) *a*-axis, (blue) *b*-axis, (red) *c*-axis (black) unit-cell volume.

3.2.4 Planetary parameters

A 3^{rd}-order Birch-Murnaghan equation of state was used to fit the density,

$$P_{V,T} = \frac{3}{2} K_{0,T} \left(x^{\frac{7}{3}} - x^{\frac{5}{3}} \right) \left[1 + \frac{3}{4} (K'_{0,T} - 4)(x^{\frac{2}{3}} - 1) \right] \tag{3.1}$$

where $x = \rho/\rho_0$. Figure 3.12 shows how the density varies as a function of pressure. The equation of state parameters are $\rho_{0,0} = 1514.33$ kg m^{-3}, $K_0 = 27.70$ GPa, and $K'_0 = 4.77$ GPa^{-1}.

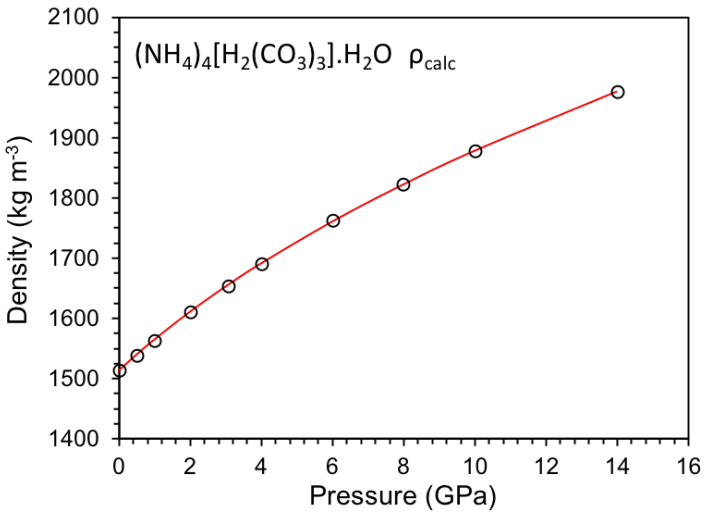

Figure 3.12
Calculated density as a function of pressure of ammonium sesquicarbonate monohydrate. The solid line is from a BMEO3 fit.

3.3 Chapter summary

This chapter has presented the results of *ab initio* simulations of ammonium carbonate monohydrate and ammonium sesquicarbonate monohydrate. A series of static calculations at fixed volumes were performed, and an equation of state was fitted to E(V) and P(V) curves to yield useful elastic parameters. Ammonium carbonate monohydrate showed some interesting behaviour, with one axis having negative thermal expansivity and above 2 GPa having a large region of negative linear compression, stable over a large pressure range.

This behaviour is quite rare in materials, and could have important affects in planetary environments and in earthly matters. In planetary environments, having a material that expands in one direction as a function of pressure or contracts on increasing temperature will dramatically change the evolution and stability of such a body. On Earth, negative linear thermal expansion could be used to make composite materials with specific thermal expansion properties, such as having a composite with no thermal expansion. Negative linear compressibility has been suggested to have a range of applications, such as in the design of pressure sensors, artificial muscles and actuators [15]. Ammonium sesquicarbonate monohydrate on the other hand shows no sign of negative linear compression, and is stable over a large pressure range. The compressibility is highly anisotropic, a feature that is common in these ammonium carbonates.

Chapter 4

Ab initio simulations of urea: phases I, III & IV

This chapter presents the results of the *ab initio* simulations of three phases of urea, phases I, III, and IV. Urea is related to the NH_3 - $CO_2 \pm H_2O$ ternary system by loss of water from ammonium carbonate monohydrate via ammonium carbamate. Urea, also known as carbamide, is commonly produced as a by-product of life. For this reason, urea is typically thought of as a biomarker in the solar system.

4.0.1 Phases and Structures

The pressure-temperature phase diagram of urea was first established in 1916 by Bridgman [19], reporting three solid phases and a liquidus below 1 GPa. The three solid phases reported were phases I, II and III. Since then, various studies have pinpointed two other high-pressure polymorphs of urea at room temperature, phases IV and V [106, 94, 148].

Phase I crystallises in the tetragonal system, $P\bar{4}2_1m$, under ambient conditions. At high temperatures and pressure, phase II crystallises, but so far the structure of this polymorph is unknown. It has been suggested that urea II may be the same phase as urea IV [42]. Phases III and IV both form under ambient conditions of temperature and at high-pressure, crystallising in the lower symmetry orthorhombic space groups $P2_12_12_1$ and $P2_12_12$ respectively. Phase III has also been suggested to be consistent with space group $Pna2_1$ [85][1]. There is evidence for a fifth polymorph to form, phase

[1]Note that in the work by Lamelas et al., 2005 [85], they report phases I, III, IV, V in their work as phases I, II, III, IV. Also note the values for the a-axis and b-axis for phase III are the opposite way around to that in this work

V (space group *Pmcn*), as can be seen in [94, 148], but there are no published structural parameters.

The phase diagram from Bridgman suggested that phase I would be stable down to about 90 K, below which phase III would become the thermodynamically stable phase. However, Andersson *et al.*, 1984 [6] give a phase diagram suggesting that urea III is the thermodynamically stable phase below 218 K. From the experiment conducted on *HRPD* (see Appendix A), the transition in deuterated urea from phase III → I occurs between 180 K and 190 K. See Figure 4.1 for an attempt to make a pressure-temperature phase diagram from the data known so far.

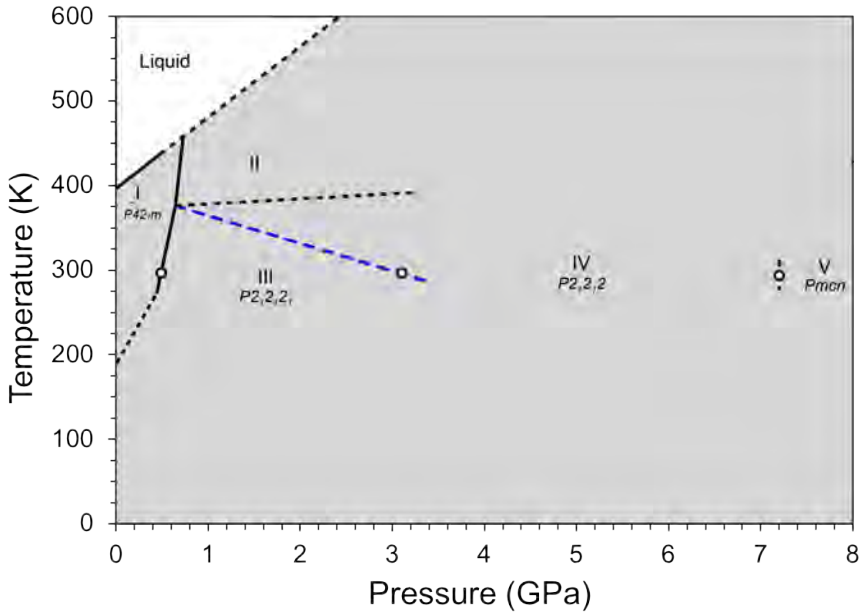

Figure 4.1
Pressure-temperature phase diagram of urea. The solid lines are values given in Bridgman, 1916 [19], and the liquidus is a linear extension as determined by Bridgman, 1916. The circles are phase transitions observed in high-pressure neutron diffraction experiments [94, 148]. The blue dashed line based on work by Dziubek *et al.*, 2017 [42], where they report that urea II may be the same phase as urea IV. The black dashed line above that is an extension of the phase boundary from Bridgman, 1916. The I → III phase boundary at ambient pressure occurs between 180 K and 190 K.

Transformation from phase I → III occurs at 0.48 GPa at room temperature. The transition is reported to be quite slow, occurring over several hours over a broad pressure range [85]. Hydrogen bonding changes extensively, in particular, breaking of some bonds and changing dimensions of others; in phase I each molecule forms eight hydrogen bonds, but only six in phase III.

At room temperature, at 2.8 GPa, the phase transition from III → IV occurs.

Phases I and IV have very similar hydrogen bonding characteristics, whereas phase III has extensive changes to the hydrogen bonding [106]. Phase V is similar to previous phases of I and IV, forming above 7.2 GPa. As the pressure increases, each new phase is a progressively more distorted version of phase I [148].

Although five phases of urea are known, the knowledge of these high-pressure phases is limited to ambient temperatures; therefore the phase diagram is incomplete. The problem for this work is the temperatures are limited to these ambient conditions, which are not analogous to those found in the outer solar system. The aim here is to provide details on the three phases of urea with published crystal structures, namely phases I, III, and IV, such as equations of state for each phase, the pressure dependence of the structure of each phase, and relative stability of these compounds.

Table 4.1
Structural parameters for urea I, from a single crystal neutron diffraction experiment at 12 K and ambient pressure by Swaminathan & Craven, 1980 [135]. This crystal structure was used for the DFT calculations.

Urea I

Formula	$CO(NH_2)_2$	Lattice parameters	
Space group	$P\bar{4}2_1m$	a-axis (Å)	5.565(1)
Z	2	c-axis (Å)	4.685(1)
ρ (kg m^{-3})	1375	Volume (Å^3)	145.09(4)
Temperature	12 K		

Atom	Fractional coordinates			Site
	x	y	z	
C1	0.0000	0.5000	0.3260	2c
O1	0.0000	0.5000	0.5953	2c
N1	0.1459	0.6459	0.1766	4e
N1B	-0.1459	0.3541	0.1766	4e
H1	0.2575	0.7575	0.2827	4e
H2	0.1441	0.6441	-0.0380	4e
H1B	-0.2575	0.2425	0.2827	4e
H2B	-0.1441	0.3559	-0.0380	4e

4.0.2 Computational details

Static DFT calculations (as described in Chapter 3) were carried out to determine an equation of state for urea I, III and IV. The starting structural parameters can be found in Tables 4.1, 4.2 & 4.3. The exchange-correlation was accommodated using the PBE generalised gradient corrected functional [110], and the plane-wave expansion was treated using the Projected Augmented-Wave method, PAW [17].

Table 4.2
Structural parameters for urea III, from a Diamond Anvil Cell (DAC) single crystal experiment at 296 K and 0.8 GPa, by Olejniczak *et al.*, 2009 [106]. This structure was used for the DFT calculations.

Urea III

Formula	$CO(NH_2)_2$	Lattice parameters	
Space group	$P2_12_12_1$	*a*-axis (Å)	3.6235(11)
Z	4	*b*-axis (Å)	8.272(4)
ρ (kg m^{-3})	1505	*c*-axis (Å)	8.844(4)
Temperature	296(2) K	Volume (Å^3)	265.09(18)
Pressure	0.8 GPa		

Label	Fractional coordinates			U_{iso}	Site
	x	y	z	(x10^2)	
C1	0.1608(1)	0.4811(6)	0.0591(6)	2.91(12)	4a
O1	0.0768(7)	0.4456(4)	-0.0736(3)	3.82(11)	4a
N1	0.3248(9)	0.3759(6)	0.1518(4)	3.72(12)	4a
N2	0.0976(8)	0.6314(5)	0.1147(4)	3.95(12)	4a
H1A	0.3760	0.2800	0.1206	4.5	4a
H1B	0.3793	0.4040	0.2427	4.5	4a
H2A	-0.0018	0.7040	0.0582	4.7	4a
H2B	0.1570	0.6542	0.2064	4.7	4a

Table 4.3
Structural parameters for urea IV, from a Diamond Anvil Cell (DAC) single crystal experiment at 296 K and 0.8 GPa, by Olejniczak *et al.*, 2009 [106]. This structure was used for the DFT calculations.

Urea IV

Formula	$CO(NH_2)_2$	Lattice parameters	
Space group	$P2_12_12$	*a*-axis (Å)	3.414(3)
Z	2	*b*-axis (Å)	7.360(8)
ρ (kg m^{-3})	1723	*c*-axis (Å)	4.606(10)
Temperature	296(2) K	Volume (Å^3)	115.7(3)
Pressure	3.1 GPa		

Label	Fractional coordinates			U_{iso}	Site
	x	y	z	(x10^2)	
C1	0.0000	0.5000	0.870(4)	2.3(8)	2b
O1	0.0000	0.5000	1.136(3)	4.6(6)	2b
N1	0.1270(9)	0.6429(4)	0.7181(19)	4.4(2)	4c
H1A	0.2115	0.7379	0.8070	5.3	4c
H1B	0.1244	0.6399	0.5315	5.3	4c

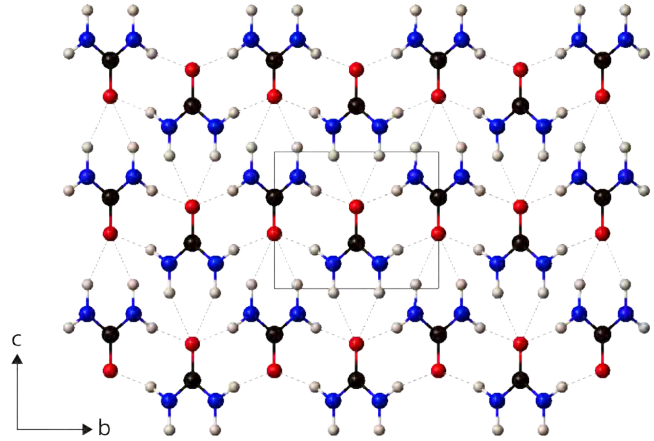

Urea I

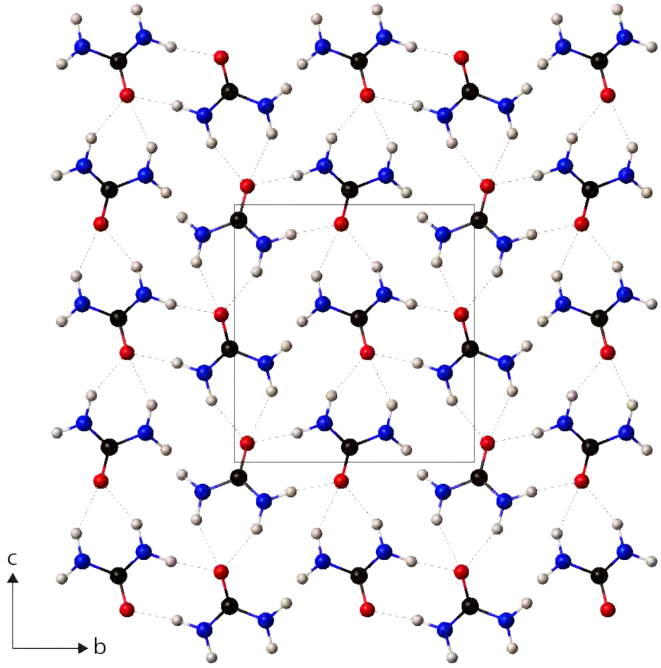

Urea III

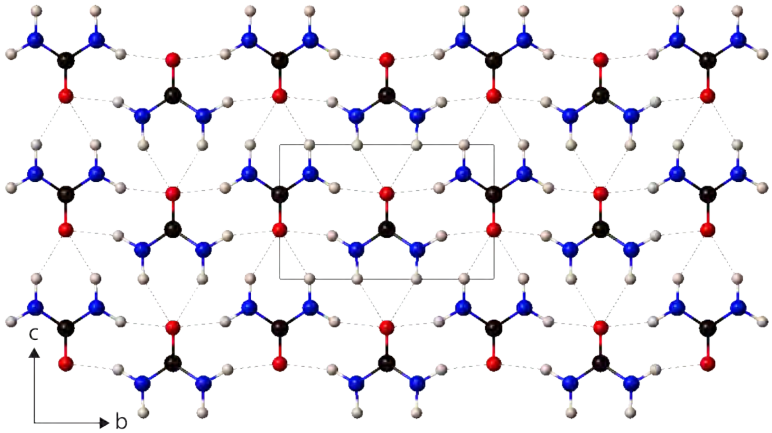

Urea IV

Figure 4.2
The crystal structures in the *bc* plane of urea I (top), III (middle), and IV (bottom), to scale. The solid black line is the outline of the unit-cell, and the dotted lines represent N-H···O bonding.

The DFT-D3 method of Grimme *et al.*, 2010 [59] gave the closest match the to unit-cell values measured experimentally. Convergence tests were carried out to optimise the $\vec{k}$-point sampling of the Brillouin zone within the Monkhorst-Pack scheme and the kinetic energy cut-off of the plane-wave basis set. The $\vec{k}$-point meshes and kinetic energy cut-off of each polymorph of urea: **urea I**, 3x3x4 (6 points), 990 eV; **urea III**, 5x2x2 (3 points), 1100 eV; **urea IV**, 4x2x3 (4 points), 1800 eV. These values yielded total energy convergence better than 10^{-4} eV per unit cell.

4.1 Results

4.1.1 Equation of state

Static calculations were performed for urea I, III and IV. Calculations on the urea I structure were performed at unit cell volumes from 110 Å^3 to 160 Å^3 (corresponding to a pressure range between 12.0 GPa and -1 GPa), urea III from 190 Å^3 to 318 Å^3 (corresponding to a range between 12 GPa and -1 GPa), and urea IV from 90 Å^3 to 160 Å^3 (corresponding to a pressure range between 18 GPa and -1 GPa). Plots of total energy against volume, *E(V)*, and pressure against volume, *P(V)*, for these phases are given in Figure 4.3.

When fitting an equation of state to the E(V) and P(V) curves of urea, the curves are quite flat; hydrogen bonded crystals, such as urea, have very low binding energies, and hence the change in energy is small. This makes it challenging when fitting an EoS to accurately determine the values of the zero-pressure parameters.

Table 4.4
Fitted equation of state parameters for urea I. Phase I has literature values for comparison, and show reasonable agreement.

	V_0 (Å^3)	K_0 (GPa)	K_0'	K_0'' (GPa^{-1})	E_0 (eV)
BMEOS3, E(V)	144.26(1)	15.03(3)	7.80(3)	-1.47(2)	-98.2529(1)
BMEOS3, P(V)	144.5(2)	14.5(5)	7.9(3)	-1.6(2)	-
BMEOS1*, 296 K	150	8.3	18	-	-
BMEOS3*, 296 K	150	8.0	24	-	-
#	-	10.7	9.1		
BMEOS3 (DFT)	127.3(1)	27.8(8)	7.0(3)	-0.56(8)	

* is from Lamelas *et al.*, 2005 [85], # is from Lundin *et al.*, 1994 [90]. Independent fitting of the values by Lamelas *et al.*, 2005 [85] give values of K_0, ≈8 GPa, but is only achieved by fixing certain values. The DFT is from Miao *et al.*, 2000 [97], with the values given here fitted by the author using their data.

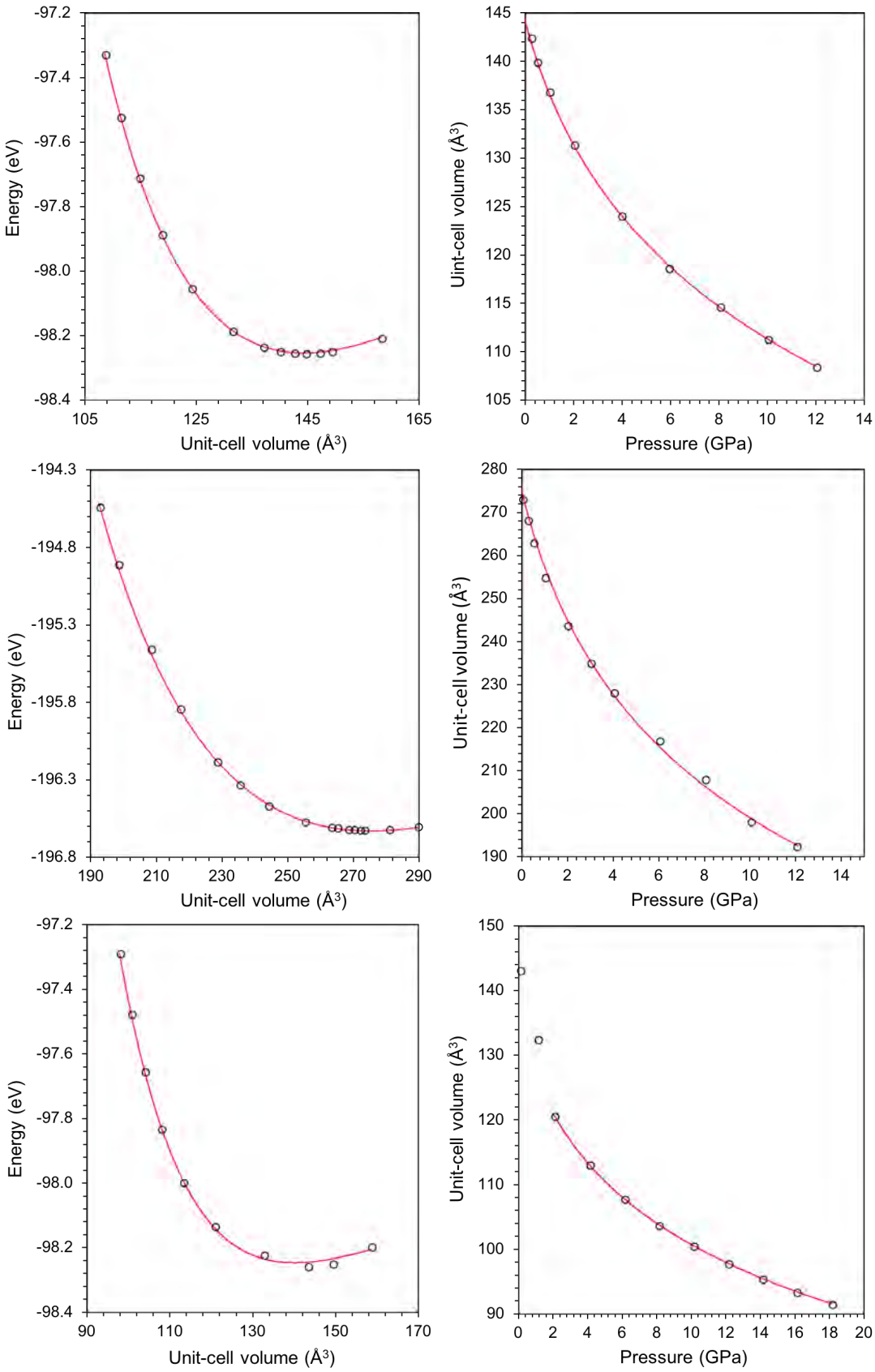

Figure 4.3
Calculated (left) E(V) curves and (right) P(V) curves for urea phases: (top) phase I; (middle) phase III; (bottom) phase IV. The open circles are calculated points, and the solid lines show the best fit BMEOS3.

Table 4.5
Fitted equation of state parameters for urea III. Phase III has literature values for comparison, and show reasonable agreement.

	V_0 (Å^3)	K_0 (GPa)	K_0'	K_0'' (GPa^{-1})	E_0 (eV)
BMEOS3, E(V)	275.4(5)	11.5(4)	6.3(3)	-1.0(2)	-196.628(5)
BMEOS3, P(V)	275(1)	12.5(9)	5.6(4)	-0.6(2)	-
BMEOS1*, 296 K	277.6	11.7	6	-	-
BMEOS3*, 296 K	278	10.8	7	-	-
#	-	9.4	6.7	-	-

* is from Lamelas *et al.*, 2005 [85], # is from Lundin *et al.*, 1994 [90]. Independent fitting of the values by Lamelas *et al.*, 2005 [85] give values of $K_0 \approx$10 GPa, but is only achieved by fixing certain values

Table 4.6
Fitted equation of state parameters for urea IV. The Vinet equation of state is from the work of Dziubek *et al.*, 2017 [42].

	V_0 (Å^3)	K_0 (GPa)	K_0'	K_0'' (GPa^{-1})	E_0 (eV)
BMEOS3, E(V)	140(1)	8(2)	8(1)	-4(2)	-98.246(7)
BMEOS3, P(V)*	134.1(4)	13.0(5)	7.2(2)	-1.3(2)	-
Vinet , 296 K	132.5	19.4	4.5		

* Fitted to the P(V) curve at calculated pressure points above and including 2 GPa

4.1.2 Phase I

A previous DFT calculation of the structure of urea under high-pressure [97] computed the structure of phase I up to 10 GPa. Independent EoS fitting of their data gives values that are greatly overestimated due to a unit-cell volume that is greatly under-estimated; the zero pressure unit-cell volume is 127.255 Å^3, a 12 % difference (Table 4.4).

The values in this work for the bulk modulus are a much better match, although still not in agreement with experimental results [85, 90]. This could be due to the temperature difference - the only high-pressure experiments have been conducted at room temperature. Since, intuitively, it is expected in most cases the bulk modulus of the material would increase as the temperature drops, it could be that the stiffness of urea I is highly temperature dependent.

It could also be due to the relatively small stability region of urea I at room temperature, transitioning to phase III at 0.48 GPa. In the literature, there are only a few points in the high-pressure measurements to constrain the value of K_0 and K_0', whereas in the

ab initio simulations undertaken here, the structure is computed to a much higher pressure than is stable at room temperature. This can be seen in the fitting of the EoS in the calculations; a good fit can be achieved over the same stability range that is measured experimentally (0 - 0.5 GPa) by setting $K_0 = 10$ GPa, giving a $K_0' = 33$. Conversely, fixing $K_0' = 20$ (between the two values available [85]) gives $K_0 = 11.8(7)$ GPa.

Table 4.7
Comparison of previous DFT calculations of urea I using different methods compared against this work and experimental data

	Literature				This work	Experiments	
	PZ [97] (LDA)	PBE [27] (GGA)	PW91 [27]	PBE+D3M(BJ) [55] (dispersion)	PBE + D3 (dispersion)	[135] 12 K	Fortes, pers comms 1.710(7) K
a-axis	5.299	5.604	5.598	5.485	5.567	5.565(1)	5.560840(8)
c-axis	4.532	4.669	4.659	4.664	4.678	4.684(1)	4.67888(2)
c/*a*	0.855	0.833	0.832	0.850	0.840	0.8417(2)	0.841398(3)
Volume	127.26	146.6	146.00	140.32	144.97	145.06(5)	144.685(1)

Table 4.8
Comparison of DFT calculated bond lengths and angles of urea I between this work, that of Miao *et al.*, 2000, against the results of the neutron diffraction experiment measured at 12 K by Swaminathan, 1984 [135].

	[97] DFT	[27] DFT	This work DFT (dispersion)	[135] Neutron
Bond lengths				
C = O (Å)	1.284	1.283	1.278	1.262(1)
C - N (Å)	1.336	1.354	1.349	1.345(1)
N - H1 (Å)	1.040	1.024	1.021	1.009(2)
N - H2 (Å)	1.034	1.023	1.020	1.005(2)
Bond angles				
O=C-N (°)	120.07	121.3	121.21	121.4(1)
N-C-N (°)	118.60	117.3	117.57	117.2(1)
C-N-H1 (°)	120.53	120.0	120.05	119.1(1)
C-N-H2 (°)	119.17	120.3	120.46	120.6(1)
H-bond lengths				
H1···O (Å)	1.773	1.982	2.032	1.992(2)
H2···O (Å)	1.899	2.012	1.962	2.058(2)

There is excellent agreement between the zero-pressure unit-cell dimensions of the ambient phase with that measured experimentally. d_4-urea phase I has a unit-cell volume at 1.710(7) K of 144.685(1) Å^3 (per comms, Fortes); the athermal, zero-pressure volume from the DFT is 144.971 Å^3. Compared against previous DFT calculations (Table 4.7), the dispersion correction used in this study has done an excellent job of

replicating the measured lattice parameters, much improved over not including a dispersion correction (see Chapter 7). The H-bond characteristics also agree well with the single crystal neutron diffraction work at 12 K by [135] for phase I (Table 4.8).

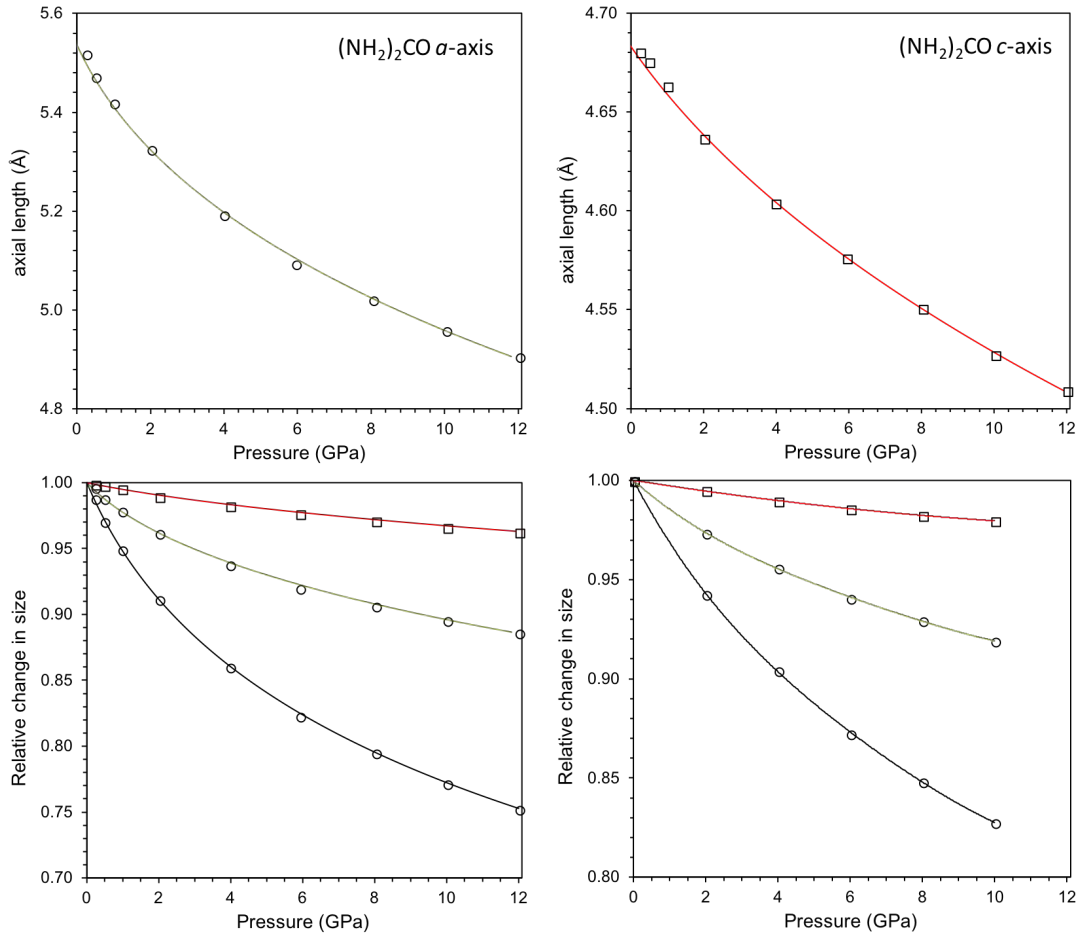

Figure 4.4
Compression curves of urea phase I along the *a*-axis, *c*-axis, unit-cell volume, and the relative axial compression. The solid lines are BMEOS3 fits through the points over this relaxation. Bottom left panel: the relative compression curve along the unit-cell axes normalised to the values at 0 GPa from this work. Bottom right panel: the relative compression of urea I, by Miao *et al.*, 2000 [97].

As can be seen in Figure 4.4, there is a high degree of anisotropy present in the ambient phase of urea. This behaviour is in excellent agreement with the relative compression of phase I as calculated by Miao et al., 2000; however the values are quite different because of their very small zero-pressure unit-cell volume. The least compression is along the *c*-axis, which corresponds to the molecular units of urea stacked on top of each other, which are linked by the C=O bond accepting four N-H···O bonds, with two of these hydrogen bonds parallel the *c*-axis. The greatest compression is due to the distance between perpendicular urea molecules reducing, due to the shortening

of the O···H bonds.

4.1.3 Phase III

Urea III has an excellent match between the *ab initio* simulations here and the experimental values available (Table 4.9). An experiment was conducted on deuterated urea III recovered from 1 GPa under liquid nitrogen to ambient pressure, measuring the thermal expansion from 10 K to 300 K on *HRPD*. This work provided a low temperature structure that can be used for comparison with the DFT simulations. Further details of this experiment and the results are given in Appendix A.

There is good agreement between the unit-cell dimensions from the DFT simulations and from the experiment on *HRPD*. d_4-urea phase III has a unit-cell volume at 9.99(2) K of 268.717(4) Å^3. The DFT simulated zero-pressure unit-cell volume is 273.220 Å^3, an overestimate of 1.7 % (Table 4.9). However, the individual lattice parameters are not such an excellent match to the experimental values. The *b* and *c* axes are both underestimated by 1.4% and 0.7 % respectively, with the *a*-axis overestimated by 3.8 %.

Table 4.9
Comparison of urea III lattice parameters between the DFT calculations and the experimental value at 10 K from the work on *HRPD*.

	a-axis	*b*-axis	*c*-axis	Volume
PBE+D3	3.79675	8.22767	8.7462	273.220
HRPD	3.65620(4)	8.34391(9)	8.8084(1)	268.717(4)

Although the individual lattice parameters are not in excellent agreement with the experimental values, there is excellent agreement between the linear compressibility measured by Lamelas *et al.*, 2005 [85] and the simulations in this work. The relative compression of phase III is a very good match; only the *b*-axis is not matched very well (see Figure 4.5). Therefore, even though the zero-pressure values are not as good a match to experimental values as was seen in phase I, the high-pressure behaviour is still an excellent match.

The experimental bulk modulus at room temperature is between 9 GPa and 11 GPa [85, 90]; the fitted EoS give a bulk modulus ∼12 GPa (Table 4.5). The excellent match is also seen in the the pressure derivatives K_0' and K_0''. The high-pressure experiment by Lamelas *et al.*, 2005 [85] suggests that urea III has a greater bulk modulus than urea

I at room temperature. On the basis of this work, urea III is stiffer than urea I; this observation is also backed up by the work of Lundin *et al.*, 1994 [90], in which they show urea III as stiffer than urea I. It could be that urea III has a bulk modulus that changes greatly with temperature, becoming stiffer as the temperature is decreased.

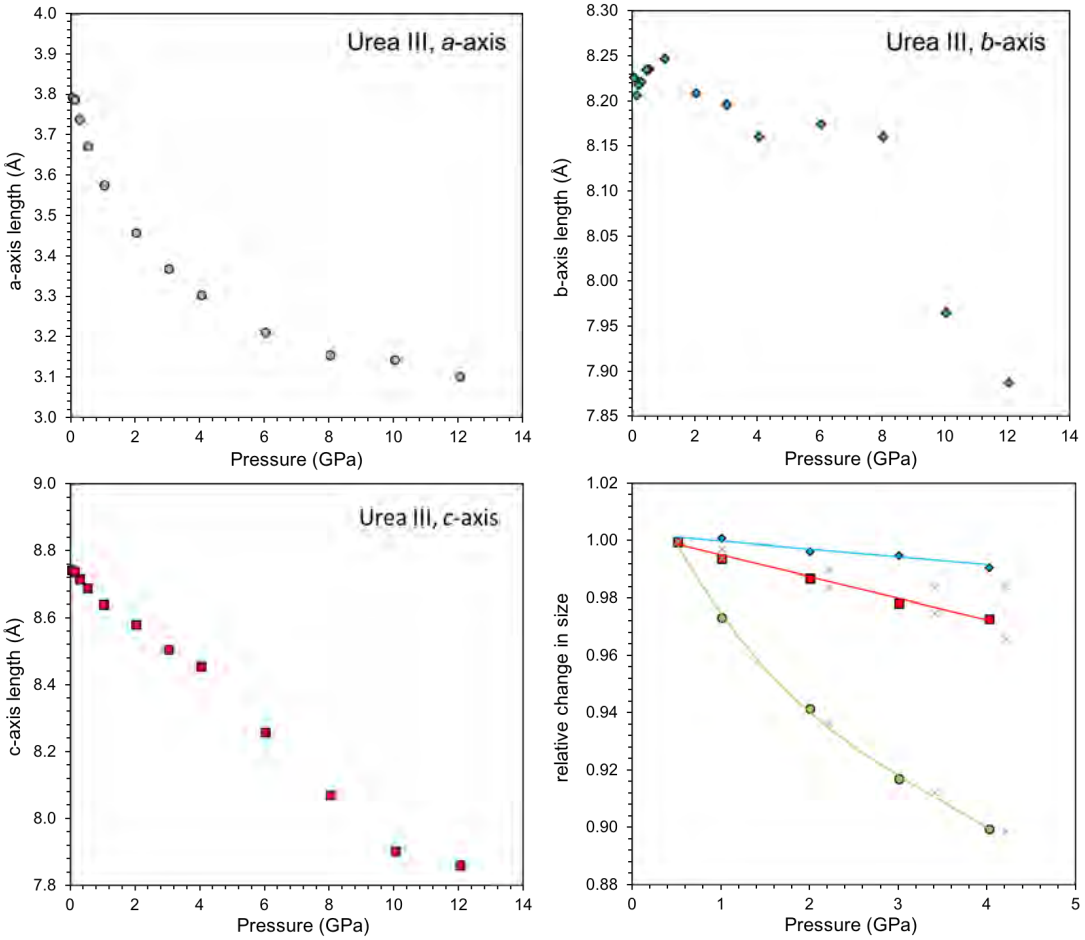

Figure 4.5
Compression curves of urea phase III along the *a*-axis, *b*-axis, *c*-axis, unit-cell volume, and the relative axial compression. The grey crosses on the bottom right show the relative compression from the work by Lamelas *et al.*, 2005 [85].

The structure here also shows a high degree of anisotropy as a function of temperature and pressure. In the thermal expansion experiment, the *b*-axis exhibits negative linear expansivity over the full temperature range measured before it back-transformed to phase I. The volumetric expansivity remains positive at all temperatures, due almost entirely to the expansion of the *a*-axis, with the *c*-axis also having positive expansivity but is much smaller in magnitude.

This behaviour matches extremely well to the DFT simulations, with the *a*-axis the most compressible direction; this is normal to the hydrogen bonded sheets form-

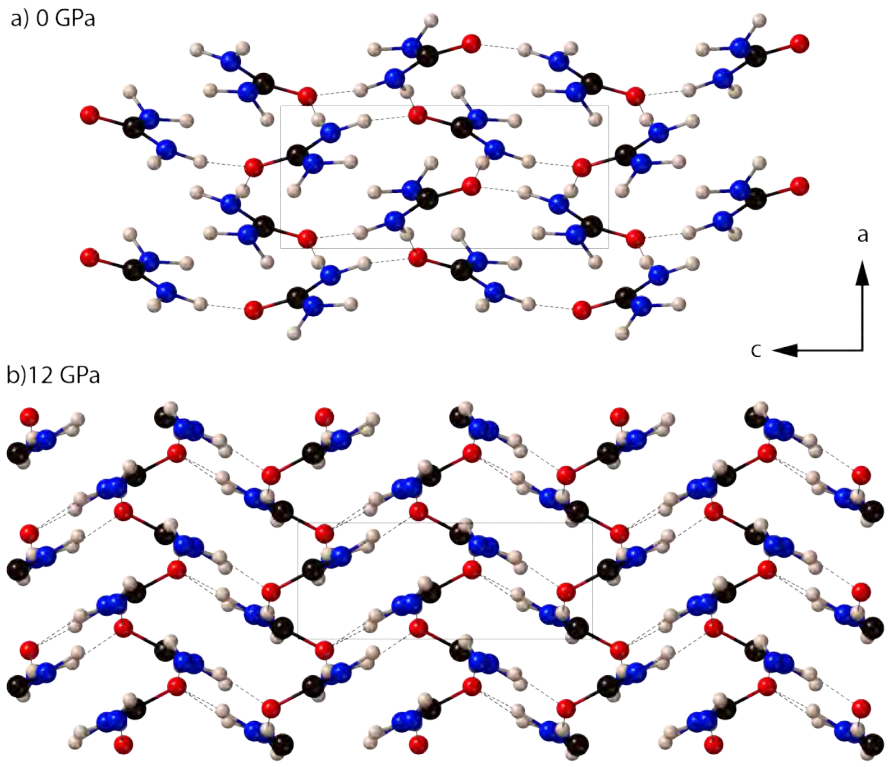

Figure 4.6
Structural change in urea III in the *ac* plane from a) 0 GPa to b) 12 GPa. The change in the motif structure is towards what is seen in phase IV (see Figure 4.8) and may suggest how the phase transition from III $\rightarrow$ IV may occur.

ing along *c*. The *b*-axis, interestingly, does exhibit a small degree of negative linear compressibility below 1 GPa, before returning to positive linear compressibility. The unusual behaviour that can be seen along *b* can be attributed to the arrangement of the molecular framework. In Figure 4.6, it is quite clear that the $CO(NH_2)_2$ molecules are moving in the structure between 0 GPa and 12 GPa to form a similar arrangement to that seen in phases I and IV. The step changes are due to the changes in the structure - the structure changes and becomes less compressible for a small pressure change, until the molecules once again move and eventually end up in the arrangement seen at 12 GPa.

Looking at the hydrogen bonding in this high-pressure phase in comparison with the work by Olejniczak et al., 2009 [106], the lengths of the N - H bond are much closer to a typical value of $\sim$1 Å (see [53]). The large difference between calculated and experimental H-bond dimensions can be attributed to the use of X-ray diffraction by Olejniczak *et al.*, 2009 [106], which typically give H-bonds lengths as 20% shorter than seen in neutron diffraction experiments. The shortened N-H bond measured by X-

Table 4.10
Comparison of DFT calculated H-bond lengths and angles in urea III under external pressures similar to that of Olejniczak et al., 2009.

	[106] 0.80 GPa	[106] 1.48 GPa	This work 0.5 GPa	This work 1 GPa	This work 2 GPa
Bond lengths					
C = O (Å)	1.248(6)	1.260(7)	1.26734	1.26759	1.26801
C - N(1) (Å)	1.335(6)	1.333(7)	1.34187	1.34081	1.33851
C - N(2) (Å)	1.357(7)	1.349(8)	1.37589	1.37479	1.37288
Bond angles					
O=C-N(1) (°)	122.2(5)	122.2(5)	122.9894	122.9851	122.9753
O=C-N(2) (°)	121.0(4)	120.7(4)	119.9431	119.9180	119.8377
N(1)-C-N(2) (°)	116.8(6)	117.1(6)	117.0523	117.0818	117.1732
C-N(1)-H(1A) (°)	120.0	120.0	119.4307	119.4235	119.4586
C-N(1)-H(1B) (°)	120.0	120.0	118.1985	118.0422	117.8732
C-N(2)-H(2A) (°)	120.0	120.0	115.1135	115.0494	114.8322
C-N(2)-H(2B) (°)	120.0	120.0	117.5191	117.4330	117.2528
Hydrogen bond distances					
N(1) - H(1A) (Å)	0.86	0.86	1.03066	1.03113	1.03193
N(1) - H(1B) (Å)	0.86	0.86	1.02976	1.02993	1.03011
N(2) - H(2B) (Å)	0.86	0.86	1.01988	1.01967	1.01938
H(1A)···O (Å)	2.05	2.02	1.80326	1.78939	1.76404
H(1B)···O (Å)	2.05	2.04	1.81756	1.80692	1.78836
H(2B)···O (Å)	2.32	2.30	2.28546	2.26875	2.22759
Hydrogen bond angles					
N(1)-H(1A)···O °	169.47	169.04	170.6686	170.5659	170.3130
N(1)-H(1B)···O °	157.18	156.5	159.7450	159.5395	158.6352
N(2)-H(2B)···O °	144.69	144.38	135.8313	135.5995	135.5234

rays subsequently lengthens the H···O length, so there is a systematic underestimate of the N-H bond length and overestimate of the H···O length in the experimental values.

Comparing the bond lengths in phase III to those in phase I shows the similarity between the rigid urea molecules (Table 4.10). The main difference between these two phases is in shortening of the medium-range hydrogen bonds; H···O distances are shorter than in phase I, due to the change in the O atom coordination - the 4-fold coordination in phase I drops to 3-fold, with the two bonds in the plane of the *c*-axis shorter and therefore strengthening the structure along this direction.

4.1.4 Phase IV

The DFT simulated zero-pressure values for urea IV give the unit-cell volume as 143.2695 Å^3 (Table 4.11). The literature values for the lattice parameters of urea IV

are measured at room temperature and high-pressure, so comparing the values to this work is difficult. The V_0 value of Dziubek *et al.*, 2017, taken from their Vinet equation of state fit to the data, places a zero-pressure value at room temperature to be 132.5 Å^3.

Urea IV, by virtue of the similarity in the structures between urea I and IV, has a volumetric bulk modulus similar to that of urea I (Table 4.6). The bulk modulus from the BMEOS3 fit here is lower than measured by Dziubek *et al.*, 2017 [42]. This may be due to the correlation between fitting K_0 and K_0'. If the reported values had a higher K_0', as the DFT calculations suggest, then the bulk modulus has to decrease. There could also be a temperature factor at play here: the values reported are from room temperature experiments whereas the calculations are athermal - it is expected in most cases that the bulk modulus of the material increases as the temperature drops. The difference could also be due to the fitting of V_0; fitting V_0 is difficult due to some interesting structural features (see Figure 4.7). By setting V_0 to that of Dziubek *et al.*, 2017, the value of $K_0 = 15.1(2)$ GPa, with $K_0' = 6.60(8)$.

Table 4.11
Comparison of urea III lattice parameters between the DFT calculations in this work (top three rows) and the high-pressure experimental value of Olejniczak *et al.*, 2009 [106], determined from single crystal X-ray diffraction, and the $V_{0,T}$ value from the Vinet equation of state fitted by Dziubek *et al.*, 2017 [42].

	Pressure (GPa)	Temp (K)	*a*-axis (Å)	*b*-axis (Å)	*c*-axis (Å)	Volume (Å^3)
PBE+D3	0	0	5.05365	6.04058	4.69321	143.2695
PBE+D3	1.961	0	3.60457	7.16668	4.67454	120.7562
PBE+D3	4.002	0	3.41484	7.15944	4.63063	113.2110
[42]*	0	296				132.5
[106]	3.10(5)	296(1)	3.414(3)	7.360(8)	4.606(10)	115.7(3)

* Value is taken from their $V_{0,T}$ fit to a Vinet equation of state

Looking at Figure 4.7, there is some interesting behaviour below 2 GPa. Phase IV shows some relaxation, with the *a*-axis and *b*-axis increasing and decreasing in size respectively, both becoming closer to 6 Å; this move towards a similar value for the *a* and *b* axes suggests a transition back towards the structurally similar ambient pressure phase, with the *c*-axis size also similar to that seen in the ambient phase. The behaviour in the arrangement of the urea motifs that can be seen in the *ab* plane shows a large change in the angle (Figures 4.7 & 4.8).

Above 2 GPa, the angle between the two motifs changes at a much slower rate due to a stiffening of the structure. This behaviour of the unit-cell matches the experimental

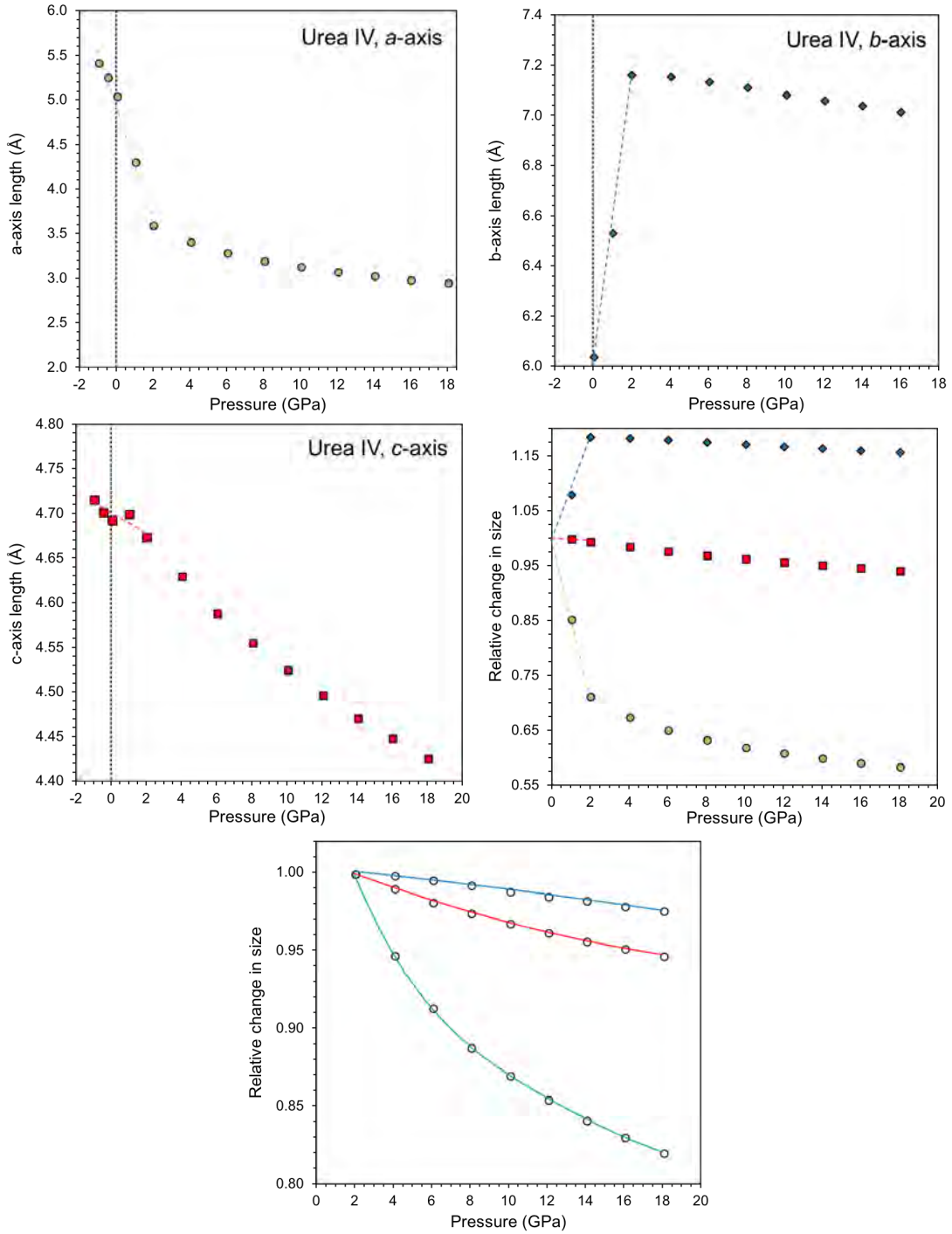

Figure 4.7
Compression curves of urea phase IV along the *a*-axis, *b*-axis, *c*-axis, unit-cell volume, the relative axial compression, and the relative axial compression normalised by their 2 GPa values. The fitted lines are BMEOS3 fits through the points.

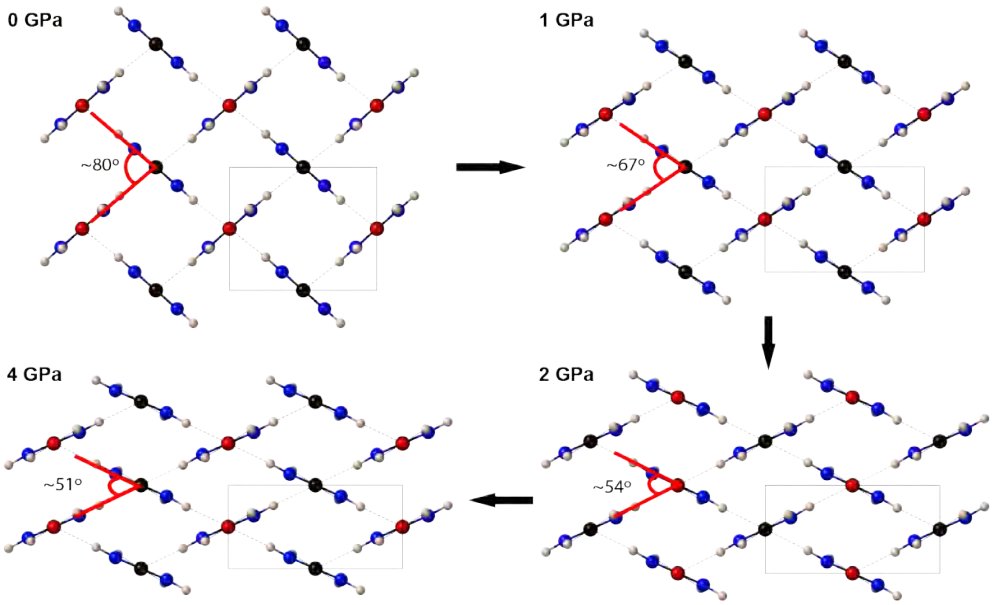

Figure 4.8
Compression of urea IV in the *ab* plane, showing how the structure deforms from zero pressure up to 4 GPa. To scale. Below 2 GPa, there is a systematic increase in the angle between the two perpendicular molecular motifs towards 90°, which is seen in the ambient phase of urea.

work by Dziubek et al., 2017 [42]. In this case, the compression is due to the shortening of the intermolecular bonds, with the intramolecular bonds remaining much the same; the O···H bonds in the structure shorten by ∼9 % from 0 GPa to 14 GPa, compared with the N-H bonds which shorten by less than 1 % over the same pressure range.

The compression calculated here is not so similar to phase I, due to the structure and the symmetry. In phase I, the molecular framework is forced to be at 90° to each other because of the symmetry, which also forces the compression in the *ab* plane to be the same. However, there are no such symmetry restrictions in phase IV, so the framework can compress in a different manner. Most of the shortening along the *a*-axis is due to the deformation of the framework, whereas for the *b* and *c*-axes it is due to the shortening of the H-bonds. The least compression along *c* is due to the two-centred interaction in the *c* plane, and the rigidity of the C - O and C - N bonding.

Looking at the bonding in this high-pressure phase in comparison with the work by Olejniczak et al., 2009 [106], the H-bonding lengths and angles are much improved in this work once again. Comparing the bond lengths between phases I and IV shows the remarkable similarity between the two structures (Table 4.12); the H···O distances are almost the same in phase I as in phase IV, as seen in experimental work (Table 4.8) [42] . The difference between the two structures is due to the angle of the molecular

Table 4.12
Comparison of DFT calculated bond lengths and angles in urea IV under external pressures between this work and that of Olejniczak et al., 2000

	[106] 3.10 GPa	This work 2.964 GPa
Bond lengths		
C = O (Å)	1.225(17)	1.27266
C - N (Å)	1.336(13)	1.34703
Bond angles		
O=C-N (°)	121.7(8)	121.7798
N-C-N (°)	116.6(16)	116.4405
C-N-H1 (°)	120.0	121.1574
C-N-H2 (°)	120.0	119.1869
H-bond lengths		
N - H1 (Å)	0.86	1.01943
N - H2 (Å)	0.86	1.02019
H1···O (Å)	2.997	1.94300
H2···O (Å)	2.913	2.01205
Hydrogen bond angles		
N(1)-H(1A)···O °	158.07	161.4336
N(1)-H(1B)···O °	150.15	145.5426

motif, as seen in Figure 4.8.

4.1.5 Relative stability and planetary parameters

To determine which phase of urea is the thermodynamically stable phase, Figure 4.9 plots the calculated enthalpy of each phase of urea per molecule. In this figure, it can be seen that urea III has the lowest enthalpy and is indeed the stable phase of urea in the athermal limit, as was also suggested by Andersson & Ross, 1994 [6]. Urea III remains stable over the pressure range simulated here, but without any reported structures for phase V, which is stable above 7.2 GPa at room temperature, the stability of this polymorph at base temperature cannot be determined.

To fit the density, the same equation of state as given in Chapter 3 has been used (eq. 3.1). Figure 4.10 shows the fitted density profiles as a function of pressure. The fitted parameters are: *I*, $\rho_0 = 1343.5$ kg m^{-3}, $K_0 = 15.27$ GPa and $K_0' = 8.95$: *III*, $\rho_0 = 1450.5.5$ kg m^{-3}, $K_0 = 12.37$ GPa and $K_0' = 7.12$: *IV*, $\rho_0 = 1487.0$ kg m^{-3}, $K_0 = 12.93$ GPa and $K_0' = 8.56$.

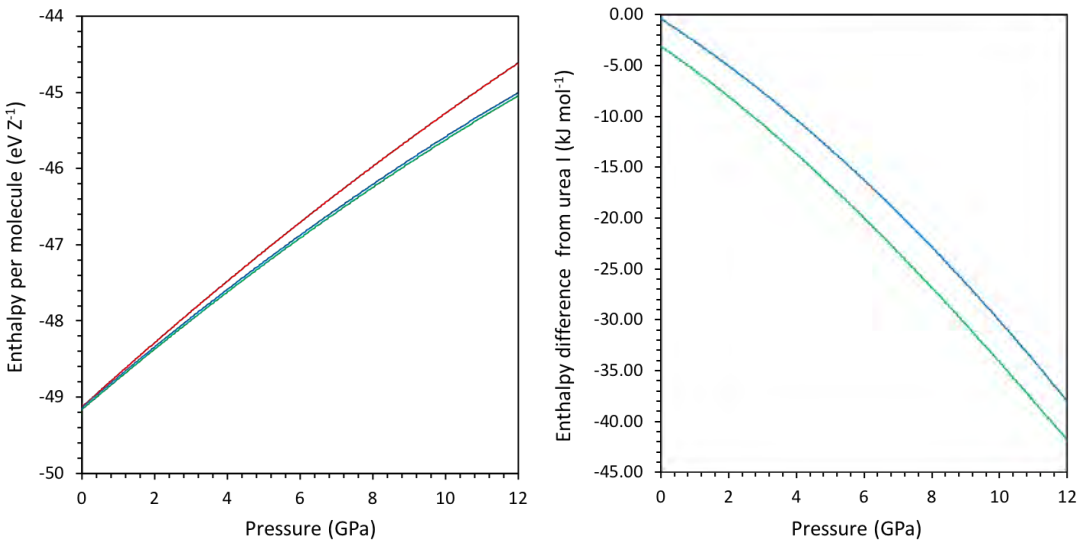

Figure 4.9
Calculated enthalpies of urea phases I (*red*), III (*green*), and IV (*blue*) in the athermal limit. The enthalpy of urea III is the lowest, as can be seen clearly in the right hand panel, which plots the enthalpy difference from urea I.

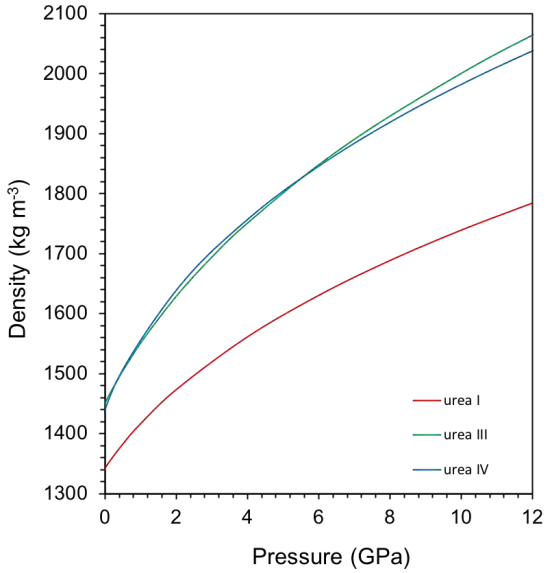

Figure 4.10
Calculated density as a function of pressure of urea phases I, III and IV, based upon the DFT calculations. The red line is phase I, the green line is phase III and the blue line is phase IV. Phases III and IV have similar densities as a function of pressure, with phase III slightly more dense than phase IV at pressure greater than $\sim$ 6 GPa in the athermal limit.

4.2 Chapter summary

Static DFT calculations have been performed on three phases of urea, phases I, III and IV. On the basis of these simulations, urea III is the stable phase as a function of pressure up to $\sim$ 12 GPa under athermal conditions. The lack of a reported structure for phase V restricts the investigation of the stability field of phase III at higher pres-

sures. There is no evidence of phase V in these simulations. An equation of state has been determined to derive bulk elastic properties, and examined structural behaviour as a function of pressure. The sparse literature data on elastic properties shows good agreement with the results presented. The data here yields the parameters necessary for incorporation into structural models of icy planetary bodies.

Future experimental work is badly needed to determine the phase stability, and values for the bulk properties of each phase of urea are required below room temperatures, preferably at temperatures applicable to the icy bodies in the solar system, so that urea can be accurately modelled in planetary interiors. The phase behaviour could also be important for matters on Earth, since urea is used in a variety of industrial processes, and since each phase will have its own unique properties, it is crucial to understand the behaviour of urea at a range of pressures and temperatures.

Chapter 5

Ammonium carbamate: *ab initio* simulations & experiments

This chapter presents the work on ammonium carbamate, $[NH_4]^+[NH_2CO_2]^-$: the *ab initio* calculations of the two phases of ammonium carbamate, α and β; and measurements of the thermal expansion and high-pressure behaviour of α-ammonium carbamate. The experimental work was conducted at the ISIS pulsed neutron spallation source of the Rutherford Appleton Laboratory on two instruments: the high resolution powder diffractometer, *HRPD*, and the single crystal diffractometer, *SXD*. Details of the experiments follow.

5.1 Ammonium carbamate, α and β

Ammonium carbamate is interesting because of the similarity of the carbamate ion and the primary amide group [2]. The compound is unstable when exposed to air, losing ammonia and carbon dioxide; this breakdown takes place over a matter of minutes at room temperature, but is slowed substantially by working in a dry, cold environment (i.e. below 0 °C) or when enclosed in a vessel. When exposed to moisture from the air, the compound transforms to ammonium bicarbonate. The crystals are platelet-shaped and usually very small in size, and can sometimes form either a fibrous mass (similar to cotton wool) when in solution or a white paste (similar to toothpaste) when forming on the top edge of a beaker as the ammonia leaks out of the liquid.

5.1.1 Phases and structures

There are two crystal structure published of α-ammonium carbamate. In 1973, the first crystal structure was published from a single crystal X-ray diffraction study (using monochromatic Cu-$K\alpha$ radiation) at 295 K [2] (Table 5.1), and in 2006 a second single crystal X-ray diffraction study (using monochromatic MoKα radiation) presents the crystal structure and an infra-red (IR) spectrum [11]. The identity of a second (β) phase of ammonium carbamate was reported in 2006 [82], measured by single crystal X-ray diffraction using monochromatic Cu-$K\alpha$ radiation (Table 5.2). Both phases are orthorhombic, α-ammonium carbamate crystallises in space group *Pbca* with Z = 8, while β-ammonium carbamate crystallises in space group *Ibam* with Z = 8. Both phases can co-exist [82], but data are lacking on which phase is thermodynamically more stable.

Table 5.1
The starting structural parameters of α-ammonium carbamate, from the single crystal X-ray diffraction study of Adams & Small, 1973 [2].

α-ammonium carbamate

Formula	$[NH_4]^+[NH_2CO_2]^-$	Lattice parameters	
Space group	*Pbca*	*a*-axis	17.121(6) Å
Z	8	*b*-axis	6.531(2) Å
ρ (kg m^3)	1375.5	*c*-axis	6.742(3) Å
Temperature	295 K	Volume	753.8(5) Å^3

Atom	Fractional coordinates			Site
	x	y	z	
C1	0.1063(2)	0.0765(5)	0.8463(5)	8c
O1	0.1046(1)	-0.0543(4)	0.9855(4)	8c
O2	0.1669(1)	0.1131(4)	0.7410(4)	8c
N1	0.3190(2)	0.0795(5)	0.8684(5)	8c
N2	0.0412(2)	0.1851(6)	0.8075(5)	8c
H1	-0.001(3)	0.360(8)	0.362(8)	8c
H2	0.043(3)	0.218(10)	0.229(9)	8c
H3	0.265(3)	0.431(7)	0.318(7)	8c
H4	0.328(3)	0.527(8)	0.436(7)	8c
H5	0.339(3)	0.298(8)	0.406(7)	8c
H6	0.341(3)	0.457(8)	0.279(8)	8c

The structure of α-ammonium carbamate is formed of pairs of planar carbamate ions running parallel to the *b*-axis, which are linked via ammonium tetrahedra (see Figure 5.1). Hydrogen-bonding between centrosymmetric pairs of carbamate ions creates a hexagonal ring-like structure 4.295 Å in width between centrosymmetric pairs of car-

Table 5.2
The starting structural parameters of β-ammonium carbamate, from the single crystal X-ray diffraction study of Kuhn *et al.*, 2006 [82].

β-ammonium carbamate

Formula	$[NH_4]^+[NH_2CO_2]^-$			Lattice parameters	
Space group	*Ibam*			*a*-axis	10.1428(1) Å
Z	8			*b*-axis	9.1579(1) Å
ρ (kg m^3)	1499.1			*c*-axis	7.4485(1) Å
Temperature	298 K			Volume	691.87(1) Å^3
Atom	Fractional coordinates			U_{iso}	Site
	x	y	z	x10^2 Å^2	
C1	0.2707(8)	0.0388(9)	0.5000	4.3(2)	8j
N1	0.0000	0.1976(7)	0.2500	2.8(2)	8g
N2	0.3403(6)	0.0796(6)	0.5000	3.7(2)	8j
O1	0.1443(4)	0.0275(4)	0.5000	3.0(1)	8j
O2	0.3262(4)	0.1692(5)	0.5000	4.3(2)	8j
H1	0.054(3)	0.126(3)	0.318(5)	14(1)	16k
H2	0.056(3)	0.275(4)	0.162(4)	14(1)	16k
H3	0.409(5)	0.020(8)	0.500	14(1)	8j
H4	0.173(6)	0.669(6)	0.500	14(1)	8j

bon atoms (Figure 5.2); these rings are typically seen in primary amide structures, with amide molecules, R-$CONH_2$, forming the rings.

These hydrogen-bond ring motifs are described by the graph-set approach, $X_d^a(n)$, where $X = D, C, R$, or S is the type of motif (discrete, infinite chain, ring or intramolecular ring motifs respectively), d is the number of donor atoms, a is the number of acceptor atoms, and n is the total number of atoms comprising the motif [45]. These rings can therefore be described as ring $R_2^2(6)$ H-bonded motifs.

There are many different arrangements of these rings possible within a crystal structure, including various ring, tape, and sheet-like motifs (*cf.* [88]). In ammonium carbamate, layers of these hexagonal rings are alternately arranged perpendicular to one another, known as a herring-bone motif arrangement (Figure 5.3). Indeed the space group of ammonium carbamate, *Pbca*, can[1] generate an interlayer herring-bone motif between the terminal atoms of the amide residue groups, R, which lie on the outside of the bilayer, due to the *b* glide plane [88]. The form of the ammonium carbamate motifs in α-ammonium carbamate is therefore similar to the shallow glide motif in primary

[1]The space group *Pbca* does not always form the same interlayer herring-bone motif seen in α-ammonium carbamate, as can be seen in thienylacrylamide, and in isohydroxyurea where the amide does not form H-bonded rings.

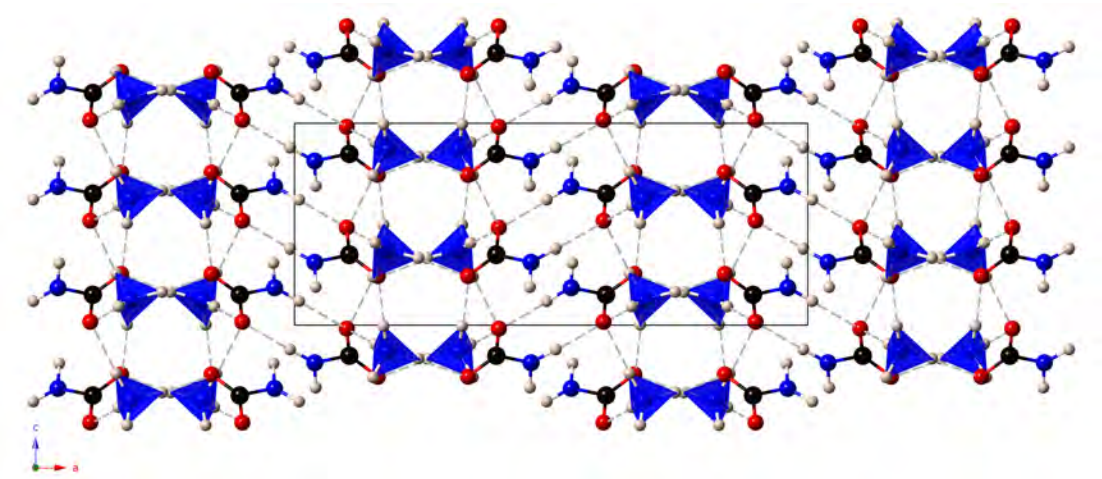

α-ammonium carbamate.

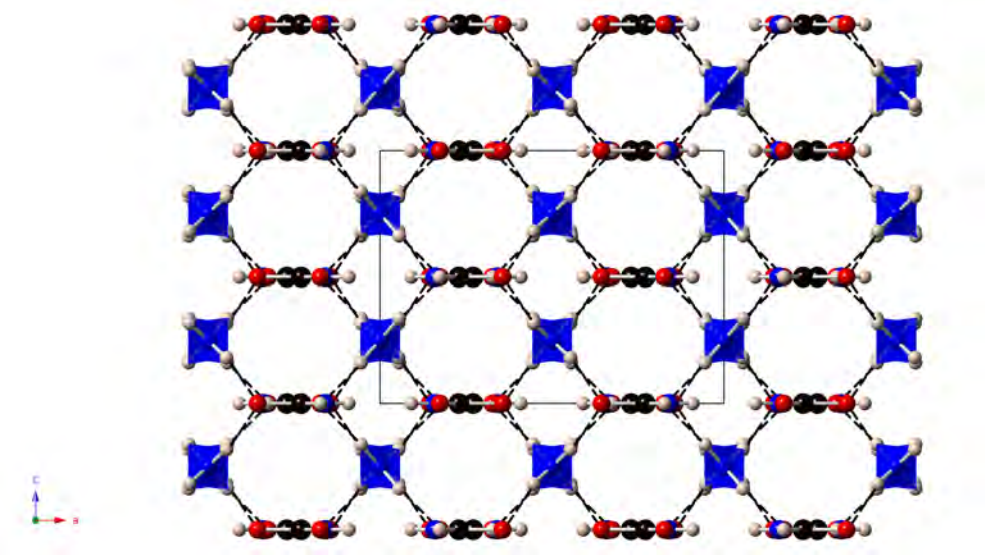

β-ammonium carbamate.

Figure 5.1
Crystal structure of (top) α-ammonium carbamate and (bottom) β-ammonium carbamate, viewed down the *b*-axis. The solid black line is the outline of one unit-cell, and the dashed lines are hydrogen bonds in the form N-H(D)···O.

amide structures.

In the shallow glide motif, the spacing between layers of the same orientation is typically 3.4 Å; in ammonium carbamate, this spacing is almost doubled in length, at 6.436 Å or 6.681 Å, (equivalent to the *b*- and *c*-axis dimensions respectively), due to the interlayer motif acting as an additional layer. Three carbon atoms of separate hexagonal ring structures usually have a spatial separation of ∼10 Å, but here make a distance of 9.27 Å. This is accommodated by the tilt angle of the ring structures being ∼68 ° rather than a typical 61 ° [88].

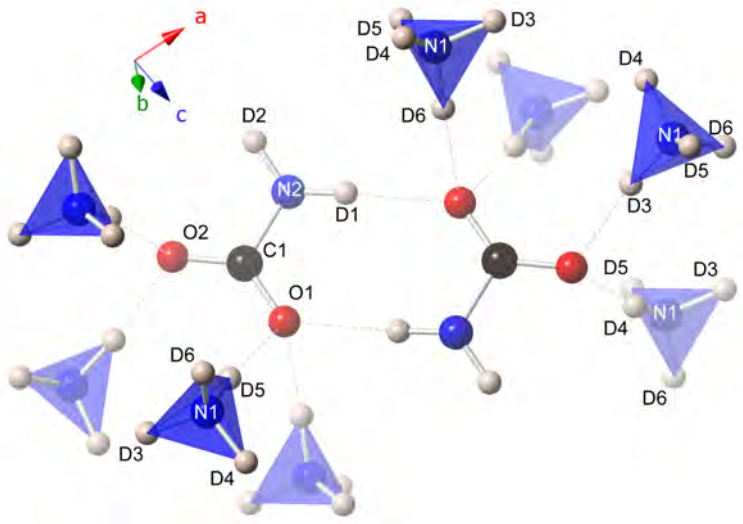

Figure 5.2
The $R_2^2(8)$ ring carbamate ions seen in the structure of α-amonium carbamate. Faded tetrahedra are below the plane of the centrosymmetric ring structure, and the dotted lines represent H(D)-bonding.

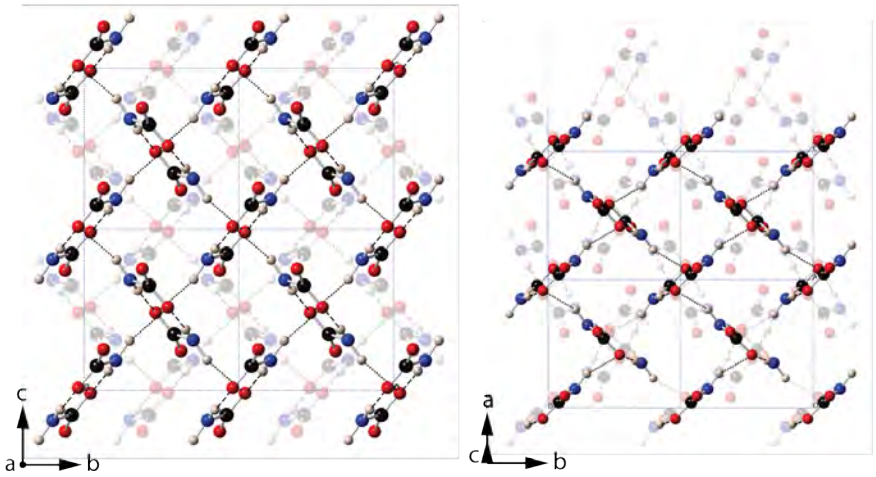

Figure 5.3
View of the motif of carbamate ions in the α-ammonium carbamate structure (left) as viewed down the *a*-axis and (right) as viewed on the diagonal $(10\bar{1})$. The faded atoms are from the next layer along the *a*-axis - this is the interlayer shallow glide herringbone motif structure found in the primary amide group.

β-ammonium carbamate however, does not form the centrosymmetric dimer ring motifs seen in α-ammonium carbamate. Instead it forms 2-dimensional chains halfway along the *b*-axis that link by hydrogen-bonding one of the carbonyl oxygens, with the other carbonyl oxygen hydrogen-bonded to an ammonium tetrahedron midway between these 2-dimensional chains.

5.2 Methods

5.2.1 Computational details

Static DFT calculations (see section 3.1.1) were carried using *CASTEP* out to determine an equation of state. Calculations were carried out using the PBE pseudopotential with Tkatchenko-Scheffler (TS) dispersion correction. Convergence tests were carried out to optimise the $\vec{k}$-point sampling of the Brillouin zone within the Monkhorst-Pack scheme and the kinetic energy cut-off of the plane-wave basis set. For α-ammonium carbamate, a converged grid of 2x6x5 with energy cut-off 1000 eV yielded total energy convergence better than 10^{-3} eV per unit cell. For β-ammonium carbamate, a converged grid of 2x2x3 with energy cut-off 980 eV yielded total energy convergence better than 10^{-3} eV per unit cell.

5.2.2 Experiment I: *HRPD*

Neutron powder diffraction data were collected using *HRPD* at the ISIS neutron spallation source of the Rutherford-Appleton Laboratory. The *HRPD* instrument was chosen due to its high resolution (Δd/d 4 x 10^{-4} in the backscattering bank), allowing the highest precision in refined lattice parameters and accurate partitioning of intensity in well-resolved high-Q Bragg beaks.

5.2.2.1 Sample Preparation

A 25 wt% ND_3 solution[2] (Sigma Aldrich 176702, 99 % purity) was exposed to CO_2 from sublimating dry ice in a partially sealed container, forming a slurry of white material. The resulting white compound was stored in a freezer. The sample was taken out of the freezer and allowed to warm and soften, after which the partially molten slurry was transferred into a liquid nitrogen cooled cryo-mortar and ground to a fine powder using a nitrogen cooled pestle. Once fully ground, the material was loaded into a an aluminium-framed slab-geometry can of inner dimensions 23 x 18 x 15 mm (h x w x d, relative to the incident neutron beam), also pre-cooled in liquid N_2. Vanadium foil windows were indium-sealed to the front and back faces of the slab-can, the exposed components on the incident-beam side being masked with Gd foil. The sample holder was wired with a RhFe resistance thermometer and a 30 mm cartridge heater, after

[2]Note the deuteration of the sample, which is much preferred over a protonated sample using neutron diffraction (see Chapter 2).

which it was immersed in liquid nitrogen for transfer into a He cryostat operating at 100 K. Once oriented in the beam, the cryostat temperature was reduced to 4.2 K for measurements to commence.

5.2.2.2 Data Acquisition

Time-of-flight data on *HRPD* are measured routinely in a range of 100 ms bandwidth 'windows' where disc choppers act as bandwidth selectors, these being 30-130 ms or 100-200 ms. In the instrument's backscattering detector bank, these time-of-flight ranges provide access to *d*-spacings from 0.65 - 2.60 Å (30-130 ms) and 2.15 - 4.00 Å (100-200 ms) at the highest resolution. Intermediate resolution data are simultaneously measured in the 90-degree detector banks (0.85-3.90 Å in 30-130 ms, 2.82-6.00 Å in 100-200 ms). Since *HRPD* has an essentially Q-independent resolution function, high-precision lattice parameters can be obtained from data measured only in the 100-200 ms window whilst avoiding the peak overlap from the additional peaks at shorter *d*-spacings. For the purpose of accurate structure refinement, however, it is more desirable to measure the shorter *d*-spacing peaks in the 30-130 ms window.

Consequently, a low-noise structural dataset was collected at 4.2 K in the 30-130 ms window, counting for 6.5 hr (corresponding to an integrated proton beam current of 250 μA hr) and then measured on warming using only the 100-200 ms window. These thermal expansion data were collected in 5 K increments from 10 - 150 K and (due to a lack of time) in 10 K increments up to 180 K. Counting times were 15 minutes, corresponding to an integrated proton beam current of 15 μA hr. The diffraction data were focussed, normalised to the incident beam spectrum and corrected for detector efficiency by reference to a vanadium standard using Mantid [7] and then exported in a format suitable for analysis with *GSAS/Expgui* [87, 138].

5.2.2.3 Structural refinement

Time-of-flight neutron powder diffraction data were refined by the Rietveld method using *GSAS/Expgui* [87, 138] starting from previously published atomic coordinates based upon a single crystal X-ray investigation [2] (Table 5.1).

In the 4.2 K dataset, two phases were identified - deuterated water ice and α-ammonium carbamate - by inspection of peak positions. Data were fitted by refinement of unit-cell of α-ammonium carbamate, scale factors and phase fractions, peak-profile

coefficients (*GSAS* profile function 3), and a ten term Chebyschev polynomial background. Atomic coordinates were refined independently, without restraints, whilst the isotropic displacement parameters (U_{iso}) were constrained to shift equally for all deuterium atoms and equally for all non-deteurium atoms. It was found necessary to refine a wavelength-dependent absorption/reflectivity correction (*GSAS* model #1), and for D_2O a sample texture correction (using a 6^{th} order spherical harmonic model). The refined phase fractions were ~63 % $[ND_4]^+[ND_2CO_2]^-$ and ~37 % D_2O. The final fit to the data is excellent, R_{wp} being better than 2 %; graphical depictions of the fit to the neutron powder data are given in Figure 5.4.

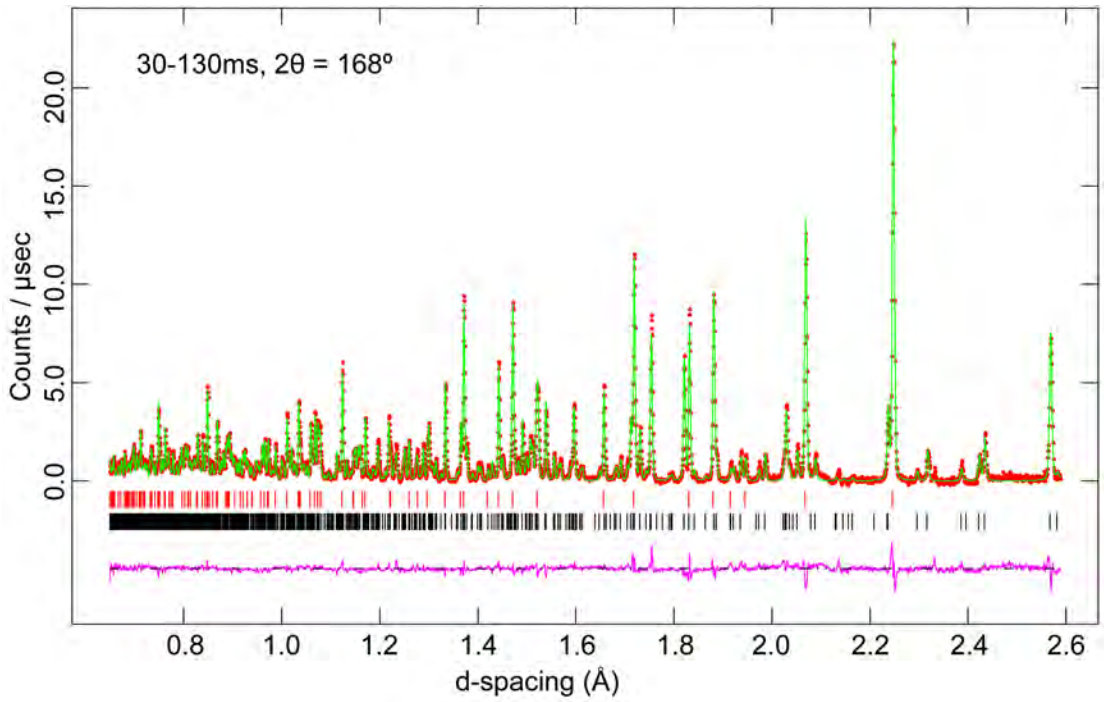

Figure 5.4
Neutron powder diffraction pattern of α-ammonium carbamate acquired at 4.2 K in the highest resolution backscattering banks (30 -130 ms window, $2\theta = 168°$) of *HRPD*. Red symbols represent the measured data and the green line the result of Rietveld refinement; the tick marks the expected positions of each Bragg reflection for $ND_4ND_2CO_2$ (black) and D_2O (red); and the pink line is the difference profile.

Refinements at each temperature step included changes to the unit-cell parameters and peak profile parameters. Since the sample had residual D_2O as a contaminant, the lattice parameters of D_2O at 180 K were fixed to those measured in a previous experiment with a silicon standard [52]. When comparing D_2O ice *Ih* lattice parameters to literature values, a significant difference was observed in the ice cell parameters compared with pure ice at low temperatures (Figure 5.5). Although the unit-cell volumes

at 180 K agree well, there is a growing divergence at lower temperatures, such that the cell volume is smaller than that of pure D_2O ice at 10 K by 0.11 %. Furthermore, the deviation is associated almost entirely with the behaviour of the crystal's *a*-axis; this is most apparent from a plot of *c/a* ratio against temperature (Figure 5.5). From 180 K down to 135 K, the *c/a* ratio is in excellent agreement with both the absolute values and the temperature dependence found in pure D_2O; below 135 K, the *c/a* ratio increases systematically.

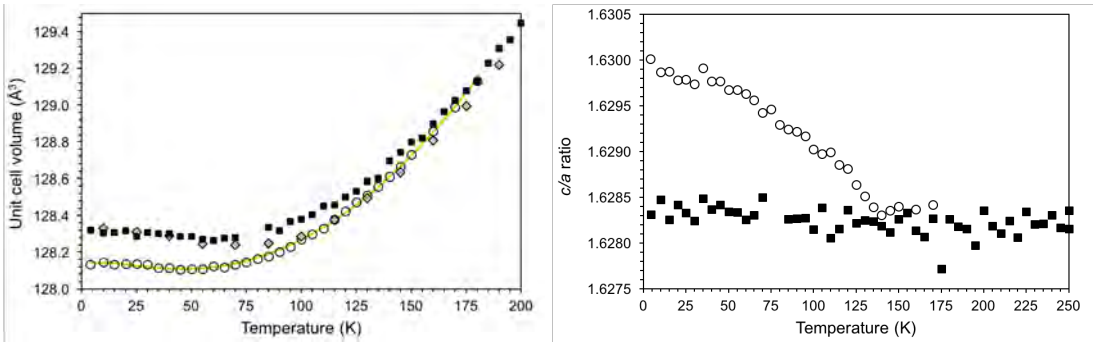

Figure 5.5
Refined unit-cell parameters of D_2O ice *Ih* compared against literature values. Solid symbols are from Rietveld refinements at each temperature step; black symbols are from [50]; diamond symbols are from [122].
Comparison of axial ratios in pure D_2O ice *Ih* and ice with ammonium carbamate. The change in thermal expansion behaviour - principally of the *a*-axis - is clear to *ca.* 135 K

Small concentrations of ammonia appear to have been present in the D_2O ice I*h*, creating a subtle change in the structure of the ice, shown in this case as having a smaller unit-cell volume than seen in pure ice. Once the sample had warmed sufficiently, the small amounts of trapped ammonia present in the ice became volatile and reacted with the ice, and were seen in the diffraction patterns - this became apparent at 150 K as new impurity phase had appeared. Peaks from this phase became larger at 160 K, and were joined by peaks from another accessory phase at 170 K (see Figure 6.2). During the final measurement at 180 K all impurity peaks had disappeared completely.

Peaks were matched from both accessory phases; the first to appear being ammonia monohydrate ($ND_3 \cdot D_2O$) and the second being ammonia dihydrate ($ND_3 \cdot 2D_2O$). The appearance and disappearance of the two ammonia hydrate phases between 150 K and 180 K could be an indication that the sample was losing ammonia, which then reacted with available water ice to form the ammonia hydrates. Since these are both known to melt between 170 K and 180 K, it is not surprising that they are absent from

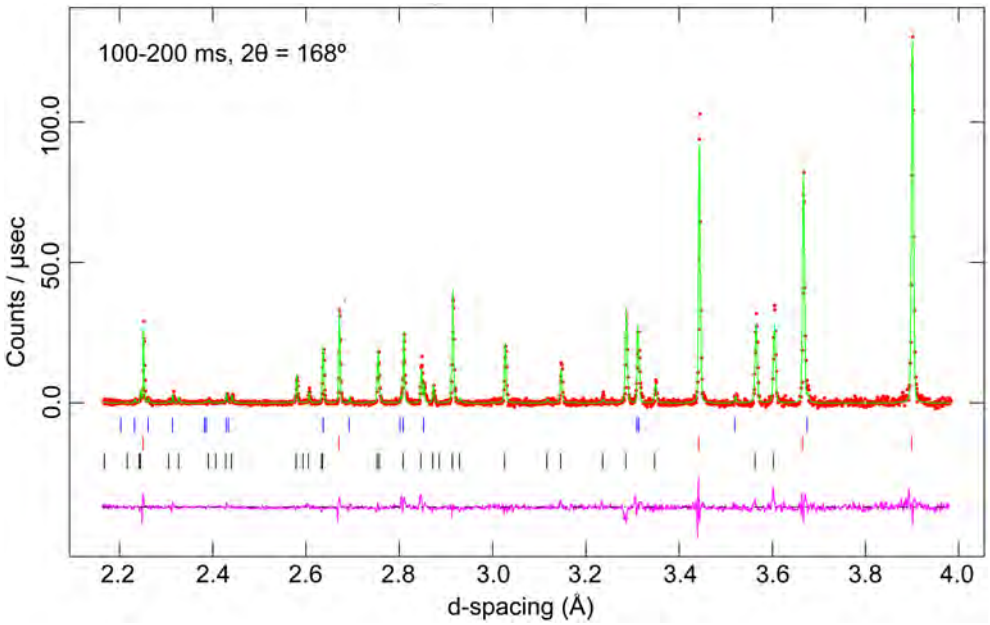

At 160 K, peaks of $ND_3 \cdot D_2O$ appear (blue ticks).

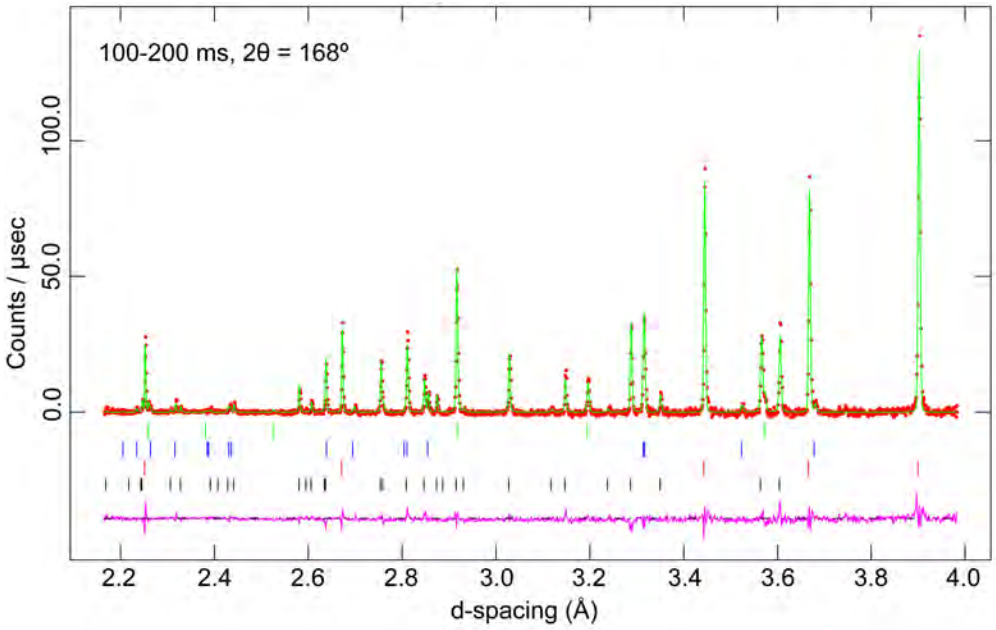

At 170 K peaks of $ND_3 \cdot 2D_2O$ also appear (green ticks).

Figure 5.6
Neutron powder diffraction patterns acquired at 160 K (top) and 170 K (bottom) in the highest resolution backscattering banks (100 -200 ms window, $2\theta = 168°$). Red symbols represent the measured data, green lines the result of Rietveld refinement, pink lines the difference profile, and the tick marks the expected positions of each Bragg reflection for; $ND_4ND_2CO_2$ (black); D_2O (red); $ND_3 \cdot D_2O$ (blue); $ND_3 \cdot 2D_2O$ (green). By 180 K, the extra peaks have disappeared.

the 180 K diffraction data. However, it could also signify the devitrification of glassy ammonia-water phases upon warming. Since the changes in the background would be too small to be detectable, there is no way of knowing if the sample is losing ammonia or crystallising as an amorphous precursor.

5.2.3 Experiment II: *SXD*

Single crystal time-of-flight neutron diffraction data were collected using *SXD* at the ISIS neutron spallation source of the Rutherford-Appleton Laboratory to obtain an accurate and precise crystal structure of α-ammonium carbamate.

5.2.3.1 Sample Preparation

A 25 wt% NH_3 solution[3] was exposed to CO_2 from sublimating dry ice in a partially sealed container, forming a slurry of white material. The slurry was extracted from the mother liquor and dried, allowing individual crystals to be picked out from the mass; individual crystals were very thin and plate-like, measuring up to two millimetres in length. Three crystals, each of approximate dimension 1.5 x 1 x 0.1 mm, were placed in different orientations side-by-side in an aluminium foil pouch suspended inside a TiZr alloy pressure cell, which was mounted onto a pre-cooled CCR on a vertical (ω) rotation device [74]. The pressure was applied using helium gas, with a maximum pressure available of up to 0.5 GPa. The pressure cell has an internal diameter of ∼1.7 mm, which limits the size of crystals that it is possible to use. Since mounting of the pressure cell is restricted to a vertical geometry, a multiple crystal sample technique was employed using three single crystals to obtain representative three-dimensional single-crystal data.

5.2.3.2 Data Acquisition

Time-of-flight Laue diffraction data were collected as the sample cooled to 200 K, revealing reflections from all three crystals, and indexed with the unit-cell obtained at 180 K in the previous powder experiment on *HRPD*. Once at 200 K, data were collected with the crystals in four discrete orientations with respect to the incident beam, optimising the coverage of reciprocal space, with integration times of 300 μA hr each (roughly 2 hr per frame at typical ISIS beam intensity) to obtain an accurate crystal

[3]Note the protonated nature of this sample.

structure. For comparison with the high-pressure behaviour seen in the DFT simulations, data were subsequently collected as the pressure was increased using an off-line intensifier from 0.1 - 0.5 GPa in 0.13 GPa steps using the same measurement strategy. The peaks were indexed and integrated using the instrument software, *SXD2001* [64] and exported in a format suitable for analysis using *SHELX2014* [129, 61].

5.2.3.3 Structural refinement

A summary of the structure refinement details are summarised in Table 5.3. Structure refinement with *SHELXL* were carried out starting from the atomic coordinates obtained at 180 K for deuterated ammonium carbamate. For all datasets, no restraints were used all and anisotropic displacement parameters were refined independently.

Table 5.3
Unit-cell parameters and refinement statistics of α-ammonium carbamate, as measured on SXD between 0 GPa and 0.5 GPa at 200 K.

Pressure	Ambient	0.10 GPa	0.23 GPa	0.36 GPa	0.50 GPa
a-axis (Å)	17.080(9)	17.041(9)	16.992(9)	16.953(9)	16.905(9)
b-axis (Å)	6.495(3)	6.477(3)	6.454(3)	6.431(3)	6.412(3)
c-axis (Å)	6.702(4)	6.687(4)	6.679(4)	6.663(4)	6.689(4)
Volume (Å^3)	743.4(7)	738.1(7)	732.5(7)	726.4(7)	720.7(7)
Radiation	Neutron, λ= 0.48 -7.0 Å				
Diffractometer	*SXD*				
Refinement					
R_σ	0.053	0.0527	0.0511	0.1429	0.0517
No. of reflections	1650	1667	1621	1829	1700
No. of parameters	109	109	109	110	110
No. of restraints	0	0	0	0	0
Extinction coefficient	0.0037(6)	0.0027(4)	0.0026(3)	0.0030(7)	0.0026(4)

5.3 Results

In this section, the results of the DFT simulations will be presented, along with the experiments based on the high-pressure and thermal expansion behaviour of α-ammonium carbamate. Firstly, the results of the DFT simulations of the β-phase will be presented, including a zero-pressure relaxation, followed by the high-pressure behaviour to characterise elastic parameters.

5.3.1 β-ammonium carbamate

5.3.1.1 DFT zero-pressure structure

The zero-pressure relaxation on the β-phase has given a unit-cell volume of 711.6(2) $Å^3$, which equates to an approximately 3 % overestimation from the measured value at 298 K of Kuhn *et al.*, 2006 (Table 5.4). This can largely be attributed to the differences in the bond lengths between the relaxed structure and experimental structure; DFT calculated bond lengths for β-ammonium carbamate are compared to the experimental values in Table 5.6.

Table 5.4
Unit-cell parameters of β-ammonium carbamate from experimental work and literature values. The methods correspond to: (*DFT*) the zero-pressure relaxation in *CASTEP*; (*XPD*) X-ray powder diffraction.

β-ammonium carbamate		
Formula	$[NH_4]^+[NH_2CO_2]^-$	
Crystal system	Orthorhombic	
Space group	*Ibam*	
Z	8	
Reference	This work	[82]
Method	DFT	XPD
Temperature (K)	athermal	298
a-axis (Å)	9.8718	10.1428(1)
b-axis (Å)	9.5064	9.1579(1)
c-axis (Å)	7.6071	7.4485(1)
Volume ($Å^3$)	713.89	691.87(1)

The N-H bond lengths given in Kuhn *et al.*, 2007 [82] are typically short due to the use of X-ray diffraction, varying from 0.75-0.99 Å (average ≈ 0.86 Å); compare this to the work here using DFT, with N-H bond lengths varying from 1.019-1.064 Å (average ≈ 1.04 Å), much closer to typical values between 1.03 Å and 1.06 Å (see Fortes *et al.*, 2014 [53] for comparison of N-H bond lengths in experimental and computational studies). The results of this work improve on the accuracy and the uncertainty on the H atomic coordinates (Table 5.5) and are thus a much better determination of the H-bond lengths in the structure (see Table 5.6). This allows for more definitive statements regarding the structure and bonding in (both phases of) ammonium carbamate to be made.

The H3···O2 bond as given by Kuhn *et al.*, 2006 [82], has a small angle (155°)

Table 5.5
Fractional coordinates of β-ammonium carbamate from the zero-pressure DFT simulation

Atom	Fractional coordinates			Occupancy	Site
	x	y	z		
C1	0.27824	0.03997	0.50000	1.0	8j
O1	0.14827	0.04527	0.50000	1.0	8j
O2	0.35511	0.15050	0.50000	1.0	8j
N1	0.00000	0.18847	0.25000	1.0	8g
N2	0.33719	-0.08921	0.50000	1.0	8j
H1	0.05856	0.12647	0.33657	1.0	16k
H2	0.06402	0.25203	0.17439	1.0	16k
H3	0.44072	-0.09915	0.50000	1.0	8j
H4	0.22297	-0.67756	0.50000	1.0	8j

Table 5.6
Comparison of bond lengths, polyhedral volumes and various distortion metrics in β-ammonium carbamate. The β-ammonium carbamate values are from the DFT simulations and a X-ray powder diffraction experiment [82].

β-ammonium carbamate					
	DFT athermal	[82] X-ray 298 K		DFT athermal	[82] X-ray 298 K
C1 - O1	1.300	1.287(9)	H1···O1	1.710	1.87(4)
C1 - O2	1.285	1.320(9)	H2···O2	1.804	1.77(4)
C1 - N2	1.361	1.294(9)	H3···O2	2.074	3.01(6)
N2 - H1	1.034	0.89(6)	H4···O2	2.091	2.15(6)
N2 - H2	1.019	0.83(6)			
N1 - H1	1.044	0.99(4)	N1-H1···O1	171.31	100.5(6)
N1 - H2	1.055	1.12(4)	N1-H2···O2	165.40	157.2(8)
N2 - H3	1.051	0.89(7)	N2-H3···O2	171.67	115.0(6)
N2 - H4	1.064	0.83(6)	N2-H4···O2	176.67	143(2)
NH_4 volume	0.5987	0.5883			
Distortion index	0.0057	0.0600			
Quadratic elongation	1.001	1.0231			
Bond-angle variance	3.4483	65.0215			

and long length (∼3 Å) and, in this instance, is unlikely to form a hydrogen bond. However, in the DFT relaxed structure, the hydrogen atoms have relaxed and the carbamate molecules have rotated. The H3···O2 bond has become quite linear, with an angle ∼172 ° and is much shorter, at 2.074 Å. The relaxing of the hydrogen atoms has altered the bonding geometry so that, now, β-ammonium carbamate forms the same hexagonal ring motif, a double two-centre H-bonded $R_2^2(8)$ ring, that is seen in the α-phase, albeit with a different motif layout to the latter (see Figure 5.7). This motif layout is not herringbone arrangement as seen in the α-phase. It is instead the same centrosymmetric H-bonded rings, which, in this phase lie on a mirror plane, but are offset by the two glide planes in the structure; therefore, it is still in the glide motif arrangement as in the α-phase. These planar $R_2^2(8)$ rings are joined via ammonium ions (at 1/4 and 3/4).

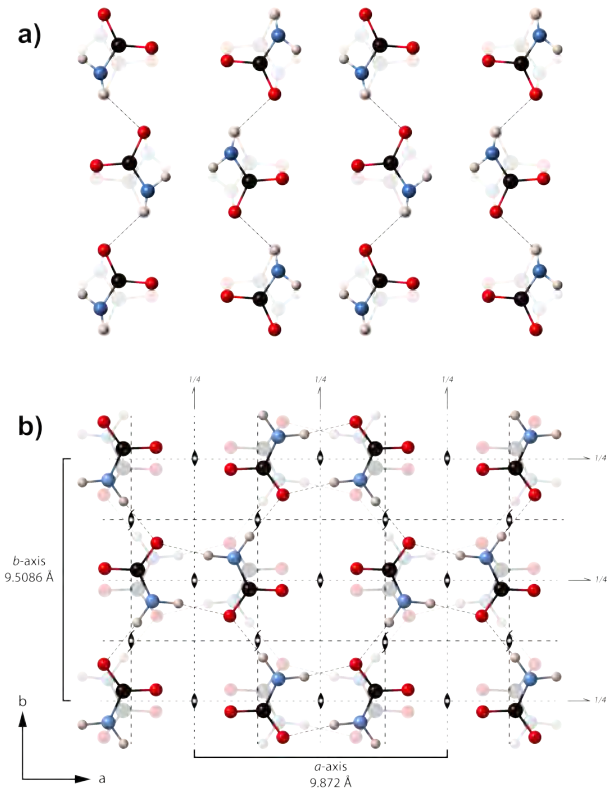

Figure 5.7
Comparison of the hydrogen bond motif of β-ammonium carbamate in the *ab* plane between (**a**) a X-ray diffraction experiment [82] (**b**) the zero-pressure structure outputted from *CASTEP* with symmetry operators overlain. The relaxed structure shows the same hexagonal-ring motif present in the α-phase. Not to scale.

It can also be seen in the experimental values that the ammonium tetrahedra are extremely distorted (Table 5.6). In the relaxed structure, the NH_4 tetrahedra have a lower

distortion, with each of the H atoms donating a hydrogen bond to different carbamate O atoms. The length of the H1···O1 and H2···O2 bonds, which form the out-of-plane bonds between the NH_4 tetrahedra and planar $NH_2CO_2^-$ ions, are shorter than the remaining two hydrogen bonds that form along the planes.

5.3.1.2 High-pressure behaviour

A series of constant-volume relaxations were performed for β-ammonium carbamate. Calculations were performed over a pressure range of -2 GPa to 10 GPa. Plots of energy against volume, and pressure against volume, were fitted with a BMEOS3 equation of state, with the plots given in Figure 5.8 and values of the fit in Table 5.7.

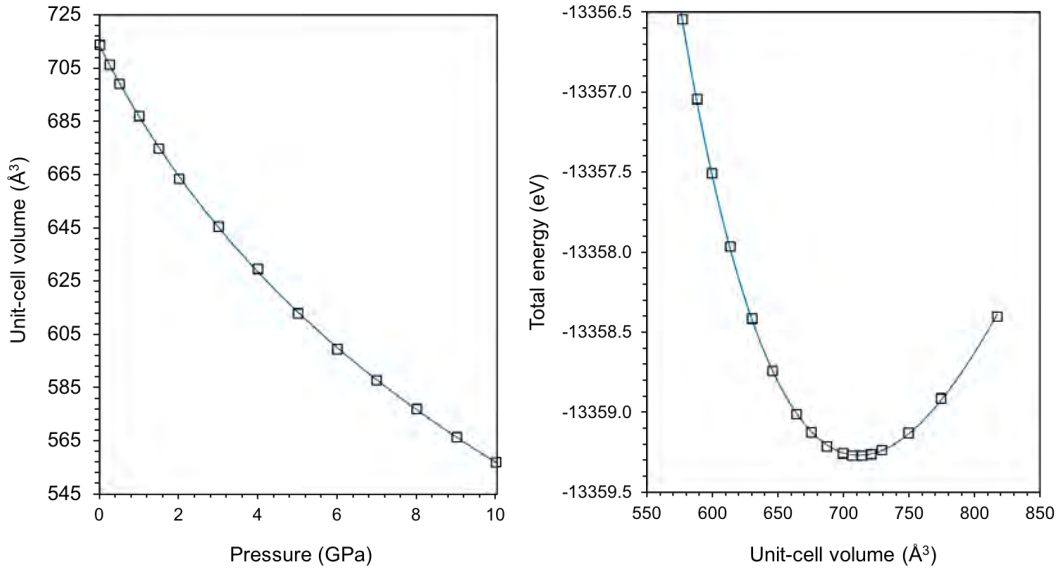

Figure 5.8
Dispersion corrected (*left*) E(V) curve and (*right*) P(V) curve of β-ammonium carbamate. The open squares are the calculated points, and the solid blue line is the best fit BMEOS3.

Table 5.7
Fitted EoS parameters to the E(V) and P(V) curves of β-ammonium carbamate, using a best fit BMEOS3

	V_0 (Å^3)	K_0 (GPa)	K_0'	K_0'' (GPa^{-1})	E_0 (eV molecule^{-1})
BMEOS3, E(V)	711.6(2)	23.3(2)	4.51(8)	-0.200(8)	-1669.9084(3)
BMEOS3, P(V)	714.5(4)	23.5(2)	4.30(8)	-0.182(7)	-

The behaviour of the β-phase shows no step changes in the lattice parameters, E(V) or P(V) curves as a function of pressure, indicating the structure is stable over the simulated 10 GPa pressure range in the athermal limit.

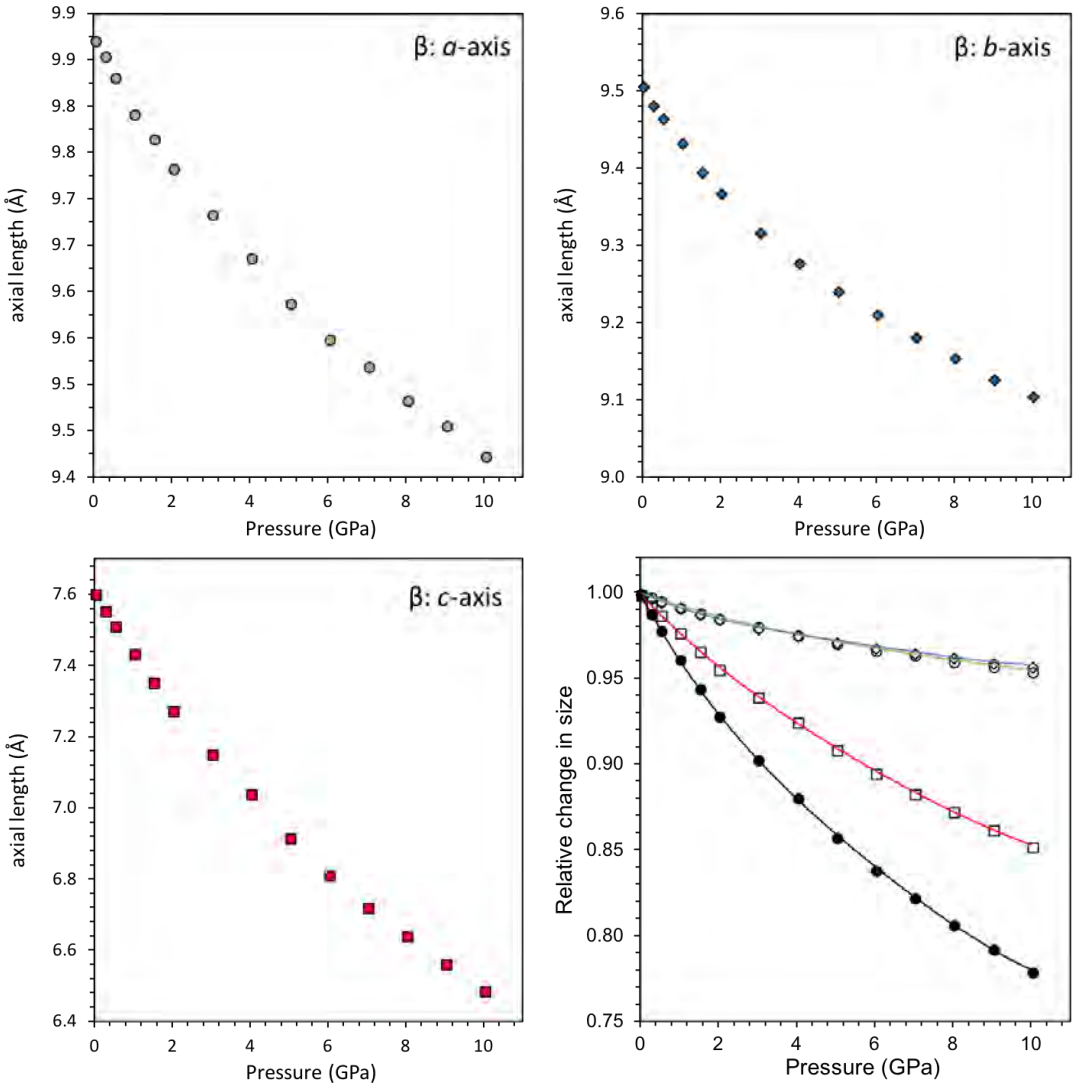

Figure 5.9
Lattice parameters and unit-cell volume of β-ammonium carbamate as a function of pressure from the *CASTEP* simulations. This phase does not exhibit the same behaviour as seen in the α-phase.

In β-ammonium carbamate, the *a* and *b* axes compress at a much slower rate than the *c*-axis (Figure 5.9). The compression seen along the *a* and *b* axes is caused by the similar hydrogen bond geometry in both directions from the $R_2^2(8)$ ring motifs of the carbamate ions. The structure is much less stiff perpendicular to the planar layers, in which the planar layer of carbamate ions are linked by ammonium tetrahedra halfway between. This can be seen in the compression of the medium range hydrogen bonds that connect the layers of carbamate ions via ammonium tetrahedra halfway between; the O1···H1 and O2···H2 bonds compress by 5.32 % and 6.65 % respectively over a pressure range of 0 GPa to 10 GPa.

5.3.2 α-ammonium carbamate

The zero-pressure relaxation on the α-ammonium carbamate output a unit-cell volume of and 743.7(6) Å^3, which equates to an approximately 1.5 % overestimation from the value determined at 4.2 K and ambient pressure on *HRPD* (Table 5.8).

Table 5.8
Structural parameters of α-ammonium carbamate, measured on *HRPD* at 4.2 K and ambient pressure using neutron powder diffraction.

d$_8$-α-ammonium carbamate

Formula	$ND_4ND_2CO_2$	Lattice parameters	
Space group	*Pbca*	*a*-axis (Å)	17.0523(2)
Z	8	*b*-axis (Å)	6.43571(7)
ρ (kg m^{-3})	1524.0	*c*-axis (Å)	6.68124(8)
Temp. (K)	4.2	Volume (Å^3)	733.225(9)

Atom	Fractional coordinates			Occupancy	U$_{iso}$	Site
	x	y	z			
C1	0.1060(5)	0.0820(10)	0.8515(12)	1.0	0.00379	8c
O1	0.1044(6)	-0.0534(11)	0.9778(14)	1.0	0.00379	8c
O2	0.1653(5)	0.1200(11)	0.7414(10)	1.0	0.00379	8c
N1	0.31973(35)	0.0840(9)	0.8762(9)	1.0	0.00379	8c
N2	0.0391(4)	0.2042(8)	0.8146(9)	1.0	0.00379	8c
D1	-0.0117(5)	0.3510(12)	0.3788(13)	1.0	0.01974	8c
D2	0.0417(5)	0.2186(13)	0.1927(14)	1.0	0.01974	8c
D3	0.2565(5)	0.4068(12)	0.3360(15)	1.0	0.01974	8c
D4	0.3281(5)	0.5167(14)	0.5033(13)	1.0	0.01974	8c
D5	0.3446(5)	0.2762(16)	0.4055(11)	1.0	0.01974	8c
D6	0.3458(5)	0.4789(13)	0.2474(13)	1.0	0.01974	8c

The difference for the α-phase can largely be attributed to the angle between the two herringbone motif carbamate ions - the calculated value has this close to 90°, whereas the refined 4 K structure has an angle greater than 90°. This means that the *b*-axis has become longer and the *c*-axis shorter in the relaxed lattice parameters, resulting in the over- and under-estimation of the individual lattice parameters. The bond lengths in the structure are slightly different, but pretty much cancel each other out, i.e. the length of the carbamate ion is very similar, and between centrosymmetric pairs of ions is 4.254 Å for relaxed and 4.304(5) Å for measured. The result of relaxing α-ammonium carbamate made no significant changes to the structure.

As with β-ammonium carbamate, the results of this work improve on the accuracy and the uncertainty on the H(D) atomic coordinates (Tables 5.8 & 5.10), and are thus a much better determination of the H(D)-bond lengths in the structure (see Table 5.9). The bond distances between the α-phase and β-phase (Tables 5.9 & 5.6) are unremarkable, almost identical to each other.

Table 5.9
Comparison of bond lengths, polyhedral volumes and various distortion metrics in α-ammonium carbamate and β-ammonium carbamate. The α-ammonium carbamate values are from the DFT simulations, measurements on *HRPD*, *SXD*, and a single crystal X-ray diffraction experiment [2] (note the *HRPD* sample was deuterated).

α-ammonium carbamate					
	DFT athermal	*HRPD* neutron 4.2 K	*SXD* neutron 200 K	[11] X-ray 293(2) K	[2] X-ray 295 K
C1 - O1	1.300	1.231(6)	1.277(18)	1.269(3)	1.270(5)
C1 - O2	1.285	1.237(6)	1.270(15)	1.266(2)	1.279(4)
C1 - N2	1.361	1.400(5)	1.358(11)	1.340(3)	1.348(5)
N2 - H(D)1	1.034	1.018(6)	1.00(3)	0.84(3)	0.85(6)
N2 - H(D)2	1.019	0.994(6)	0.98(4)	0.81(3)	0.83(7)
N1 - H(D)3	1.044	1.093(5)	1.04(3)	0.94(4)	1.00(5)
N1 - H(D)4	1.055	1.031(6)	1.02(4)	0.93(3)	0.85(6)
N1 - H(D)5	1.051	1.028(5)	1.02(4)	0.93(3)	0.91(6)
N1 - H(D)6	1.064	1.045(6)	1.05(3)	0.93(3)	0.75(6)
$NH(D)_4$ volume	0.5987	0.5904	0.5615	0.4166	0.3205
Distortion index	0.0057	0.0210	0.0116	0.0028	0.08704
Quadratic elongation	1.001	1.0028	1.0006	1.0026	1.0615
Bond-angle variance	3.4483	9.0163	1.4430	9.7185	114.3099
H(D)1···O1	1.86322	1.935(7)	1.96(3)	2.16(3)	2.12(5)
H(D)2···O1*	2.51504	2.397(7)	2.4 8(4)	2.70(3)	2.64(6)
H(D)3···O2	1.67391	1.757(6)	1.72(3)	1.82(3)	1.77(5)
H(D)4···O2	1.76183	1.762(7)	1.84(4)	1.93(3)	2.13(5)
H(D)5···O1	1.76712	1.812(6)	1.80(3)	1.93(3)	1.93(6)
H(D)6···O1	1.86180	1.930(7)	1.92(4)	2.03(3)	2.19(6)
N2-H(D)1···O1	177.11	177.1(4)	176.8(10)	174.7(8)	174(5)
N2-H(D)2···O1*	148.00	151.5(4)	149.6(7)	149.9(8)	158(1)
N1-H(D)3···O2	170.15	168.2(4)	169.7(9)	171.4(8)	166(4)
N1-H(D)4···O2	164.32	165.8(4)	162.0(10)	162.4(8)	138(5)
N1-H(D)5···O1	170.33	169.3(4)	170.7(7)	168.5(8)	173(4)
N1-H(D)6···O1	157.51	156.8(4)	154.3(10)	155.4(7)	158(5)

Atomic labels in Baisch *et al.*, 2006 [11], according to the labelling of Adams & Small, 1973 [2], correspond to: H11=H3, H12=H2, H22=H5, H23=H6, H24=H4 and N2=N1

* in Adams & Small, 1973 [2], this bond is suggested to not be a H-bond

The structure consists of $NH(D)_4$ tetrahedra and planar $NH(D)_2CO_2^-$ ions linked by moderately strong hydrogen bonds (H···O ranges from 1.72 - 2.19 Å). The length of the N2-H(D)1 bond is longer than N2-H(D)2 bond due to the H(D)1 atom donating a hydrogen bond (forming part of the $R_2^2(6)$ H-bonded motif).

The N2-H(D)2 bond, interestingly, was suggested not to be involved in a hydrogen bond by Adams & Small, 1973 [2]. Although the length of this bond is much longer and is more distorted than the remaining H-bonds, it appears that this H atom is sharing an interaction with two different O1 atoms, one slightly stronger than the other - one H(D)2···O1 bond length measures 2.64(6) Å, the longer and weaker interaction is 3.10(6) Å in length.

One thing to note is the distortion of the ammonium tetrahedra in the *HRPD* sample measured at 4.2 K, which is much larger than the other values in Table 5.9. Apart from the distortion of the tetrahedra, the work on *HRPD* and *SXD* shows a very good agreement with the structure bonding geometry, such as the H(D)1···O1 and H(D)6···O1 bonds being slightly longer than the remaining three bonds, and also agrees well with the work of Adams *et al.*, 1973 [2]. Although the DFT simulations do predict this bond angle to be smaller than the remaining bonds, there is an underestimate of this bond length by ∼3.5 % and overestimate of the bond angle by ∼1 %, caused by an overestimate of the N1-H5 and N1-H6 bond lengths.

Table 5.10
Structural parameters of α-ammonium carbamate at 200 K and ambient pressure from the single crystal neutron diffraction experiment on *SXD*

α-ammonium carbamate

Formula	$[NH_4]^+[NH_2CO_2]^-$	Lattice parameters			
Space group	*Pbca*	*a*-axis (Å)	17.080(9)		
Z	8	*b*-axis (Å)	6.495(3)		
ρ (kg m^{-3})	1395	*c*-axis (Å)	6.702(4)		
Temp. (K)	200(2)	Volume (Å^3)	743.4(7)		

Label	Fractional coordinates			U_{11} (x10^2)	U_{22} (x10^2)	U_{33} (x10^2)	U_{12} (x10^2)	U_{13} (x10^2)	U_{23} (x10^2)	U_{iso} (x10^2)	Site
	x	y	z								
C1	0.1063(4)	0.0790(14)	0.846(2)	1.3(5)	1.9(5)	2.1(8)	0.0(4)	-0.2(5)	-0.9(6)	1.8(3)	8c
O1	0.1043(6)	-0.0521(17)	0.988(2)	2.1(5)	1.9(5)	3.9(12)	0.2(5)	-0.2(6)	1.0(9)	2.6(4)	8c
O2	0.1668(6)	0.1167(16)	0.742(2)	1.6(5)	2.9(6)	3.3(12)	-0.2(4)	0.4(5)	-0.1(6)	2.6(4)	8c
N1	0.3191(5)	0.0799(13)	0.8678(18)	2.0(5)	2.2(4)	1.8(8)	-0.2(4)	0.0(4)	-0.6(5)	2.0(2)	8c
N2	0.0405(4)	0.1896(12)	0.8080(18)	1.9(4)	2.8(5)	3.8(9)	0.8(3)	0.4(5)	1.4(4)	2.8(3)	8c
H1	-0.0095(11)	0.352(3)	0.376(5)	1.8(9)	4.0(11)	8(2)	-0.2(8)	0.6(11)	-1.1(14)	4.4(8)	8c
H2	0.0395(14)	0.217(5)	0.193(5)	5.3(13)	7.0(17)	4(2)	-1.4(13)	0.1(14)	-2.9(16)	5.3(8)	8c
H3	0.2599(11)	0.407(3)	0.337(4)	2.3(9)	3.3(10)	5.2(19)	-0.2(9)	0.6(11)	0.3(13)	3.6(6)	8c
H4	0.3277(14)	0.516(3)	0.486(5)	4.9(13)	1.8(11)	4(2)	-0.2(9)	-1.1(14)	-0.6(12)	3.7(7)	8c
H5	0.3423(10)	0.276(3)	0.407(4)	3.5(10)	2.3(10)	4.3(19)	0.5(8)	0.2(11)	0.1(11)	3.4(6)	8c
H6	0.3477(13)	0.474(4)	0.245(5)	2.8(11)	6.0(16)	5(3)	-0.8(11)	-1.3(13)	-1.3(13)	4.7(8)	8c

The single crystal work on protonated α-ammonium carbamate has produced anisotropic displacement parameters (ADPs) at 200 K (see Figure 5.10). The zero-pressure structure shows the ADPs of the hydrogen atoms associated with the carbamate ions (H1, H2) are, in general, of a marginally greater magnitude than the hydrogen

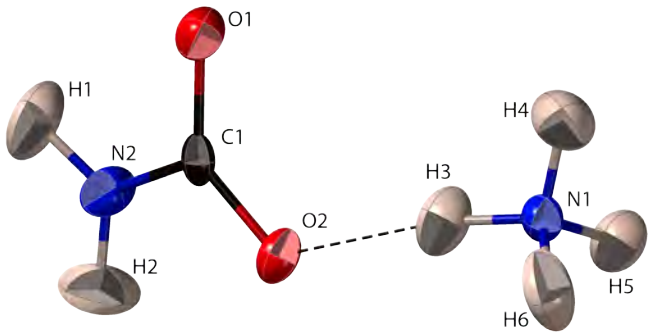

Figure 5.10
Asymmetric unit of α-ammonium carbamate with atomic thermal ellipsoids determined at 200 K from the *SXD* measurement at ambient pressure, drawn at the 50 % probability level. The dashed line corresponds to a hydrogen bond.

atoms associated with the ammonium tetrahedra (see Figure 5.10 for the ADPs at ambient pressure, and Figure 5.13 for the ADPs at 0.5 GPa). Unsurprisingly, the H2 atom, which is part of two weak hydrogen bonds, has the largest ADP.

5.3.2.1 High-pressure behaviour

A series of constant-volume relaxations were performed for α-ammonium carbamate. Calculations were performed over a pressure range of -1 GPa to 15 GPa. Plots of energy against volume, and pressure against volume, were fitted with BMEOS3 equations of state, with the plots given in Figure 5.11 and values of the fit in Table 5.11.

There is an excellent agreement between the elastic parameter values for the DFT simulations and the measured high-pressure behaviour of α-ammonium carbamate as measured on *SXD*, although the values for the pressure derivatives from *SXD* have larger errors due to the smaller pressure range (0 - 0.5 GPa) and having only 4 pressure points measured (plus a zero-pressure measurement).

Although not apparent when looking at the E(V) and P(V) curves of ammonium carbamate, there are some interesting features in how the structure deforms in response to an external pressure. There is a high degree of anisotropy in the structure when put under pressure; plots of the lattice parameters as a function of pressure are given in Figure 5.12 and Figure 5.9.

The simulated high-pressure behaviour of α-ammonium carbamate does show a slight difference to what was measured on *SXD* (Figure 5.12), in that the *a*-axis and *c*-axis are reversed i.e. the simluations suggest that the *c*-axis should compress marginally less than the *a*-axis, but this is reversed in the experimentally measured values. Al-

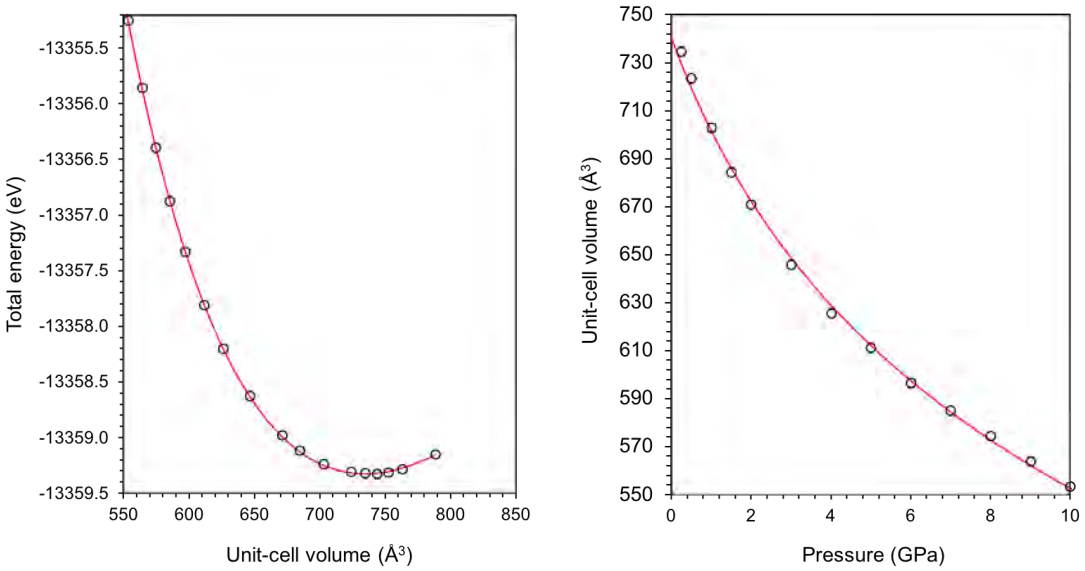

Figure 5.11
Dispersion corrected E(V) curve (left) and P(V) curve (right) of α- ammonium carbamate (red line, open circles)

Table 5.11
Comparison of the fitted EoS parameters of α-ammonium carbamate between the DFT simulations and the work on *SXD*, using the BMEOS3 equation of state.

	DFT		*SXD*
	BMEOS3, E(V)	BMEOS3, P(V)	BMEOS3, 200 K
α-ammonium carbamate			
V_0 (Å^3)	743.7(6)	741(2)	743.3(3)
K_0 (GPa)	16.0(3)	16.2(5)	14.4(9)
K_0'	5.35(9)	5.1(1)	8(4)
K_0'' (GPa^{-1})	-0.44(3)	-0.38(4)	-2(3)
E_0 (eV molecule^{-1})	-1669.9149(4)		

Table 5.12
Unit-cell parameters of α-ammonium carbamate, as per the *HRPD* deuterated α-ammonium carbamate powder experiment and the *SXD* protonated single crystal α-ammonium carbamate experiment

Crystal system	Orthorhombic			
Space group	*Pnma*			
Z	8			
Instrument	*HRPD*		*SXD*	
Formula	$ND_4ND_2CO_2$		$[NH_4]^+[NH_2CO_2]^-$	
Temperature (K)	4.2	180	200	200
Pressure (bar)	1	1	1	5000
a-axis (Å)	17.0517(3)	17.0910(4)	17.080(9)	16.905(9)
b-axis (Å)	6.4357(1)	6.4823(1)	6.494(3)	6.412(3)
c-axis (Å)	6.813(1)	6.7042(1)	6.702(4)	6.649(4)
Volume (Å^3)	733.21(2)	742.75(2)	743.4(7)	720.7(7)

Table 5.13
Structural parameters of α-ammonium carbamate at 200 K and 0.5 GPa from the single crystal neutron diffraction experiment on *SXD*

α-ammonium carbamate			
Formula	$[NH_4]^+[NH_2CO_2]^-$	Lattice parameters	
Space group	*Pbca*	*a*-axis (Å)	19.905(9)
Z	8	*b*-axis (Å)	6.412(3)
ρ (kg m^{-3})	1439	*c*-axis (Å)	6.649(4)
T (K), P (GPa)	200(2), 0.5	Volume (Å^3)	720.7(7)

Label	Fractional coordinates			U_{11}	U_{22}	U_{33}	U_{12}	U_{13}	U_{23}	U_{iso}
	x	y	z	(x10^2)	(x10^2)	(x10^2)	(x10^2)	(x10^2)	(x10^2)	(x10^2)
C1	0.1049(3)	0.0857(11)	0.8375(16)	1.6(3)	1.6(4)	1.6(7)	0.2(3)	0.3(4)	-0.1(4)	1.6(2)
O1	0.1032(5)	-0.0498(13)	0.9775(17)	2.0(4)	2.1(4)	2.5(9)	0.3(4)	-0.1(4)	0.2(6)	2.2(3)
O2	0.1655(5)	0.1222(11)	0.7317(17)	1.6(4)	2.8(5)	2.3(9)	-0.1(3)	0.5(4)	-0.3(5)	2.2(3)
N1	0.3187(3)	0.0815(11)	0.8610(16)	2.0(3)	2.0(3)	2.6(7)	0.0(3)	-0.2(3)	-0.2(4)	2.2(2)
N2	0.0386(3)	0.1989(10)	0.8048(12)	1.8(3)	2.6(4)	3.7(7)	0.8(3)	0.2(3)	0.8(3)	2.7(2)
H1	-0.0110(8)	0.342(2)	0.378(3)	2.1(7)	4.6(10)	3.4(16)	-0.6(7)	0.5(8)	-0.3(9)	3.4(5)
H2	0.0376(11)	0.207(3)	0.191(3)	4.8(9)	6.3(13)	3.1(19)	-1.6(10)	0.5(11)	-2.3(12)	4.8(6)
H3	0.2592(8)	0.406(2)	0.329(3)	2.2(7)	3.2(8)	5.2(17)	-0.1(6)	-1.1(8)	-0.4(10)	3.5(5)
H4	0.3273(11)	0.516(3)	0.476(4)	4.7(11)	2.3(9)	4.2(19)	0.3(7)	-0.6(10)	-0.8(10)	3.7(6)
H5	0.3420(8)	0.274(2)	0.398(3)	3.4(7)	3.1(9)	4.0(16)	0.5(7)	0.1(8)	0.0(9)	3.5(5)
H6	0.3472(10)	0.475(3)	0.236(3)	3.1(9)	5.7(12)	2.8(18)	-1.1(8)	0.2(9)	1.2(11)	3.8(5)

Table 5.14
Comparison of bond lengths (Å), polyhedral volumes (Å^3) and various distortion metrics in α-ammonium carbamate between the *SXD* measurements and the DFT simulations.

	SXD		DFT	
	200 K 0 GPa	200 K 0.5 GPa	0 GPa	0.5 GPa
C1 - O1	1.277(18)	1.274(14)	1.300	1.300
C1 - O2	1.270(15)	1.265(12)	1.285	1.285
C1 - N2	1.358(11)	1.353(9)	1.361	1.358
N2 - H1	1.00(3)	1.004(17)	1.034	1.033
N2 - H2	0.98(4)	0.97(3)	1.019	1.019
N1 - H3	1.04(3)	1.031(15)	1.044	1.063
N1 - H4	1.02(4)	1.00(3)	1.055	1.050
N1 - H5	1.02(4)	1.03(3)	1.051	1.055
N1 - H6	1.05(3)	1.036(16)	1.064	1.044
NH_4 volume	0.5615	0.5494	0.5987	0.5986
Distortion index	0.0116	0.01214	0.00568	0.00579
Quadratic elongation	1.0006	1.0005	1.001	1.0009
Bond-angle variance	1.443	0.6587	3.4483	3.3019

though this discrepancy between the simulations exists, the relatively small pressure region of the experimental values do not make this too problematic for simulated high-pressure structural behaviour, especially since the majority of the structural compression occurs along the *b*-axis. Much like in the high-pressure data, when looking at the thermal expansion of α-ammonium carbamate, there is a large degree of anisotropy present, so when comparing the DFT and the *SXD* values, consideration of this effect needs to be taken (see the next section). However, there is some interesting behaviour seen in the lattice parameters from the simulations.

Similar behaviour is seen in α-ammonium carbamate as was seen in ammonium carbonate monohydrate, in which along one unit-cell axis there is negative linear compressibility (NLC) at high-pressure. The α-ammonium carbamate structure has positive linear compressibility (PLC) in all directions up to a pressure of 5 GPa; between 5 GPa and 8 GPa there is a small degree of NLC and an inversion to PLC. The largest NLC region however occurs over 8 - 11 GPa, and continues up to 15 GPa but to a smaller degree. The initial loading up to 5 GPa is quite 'noisy' along the *a*-axis, but the relative change in size is quite small - smaller than the *b* and *c*-axes. There is an initial stiffening of the structure along *a* at 5 GPa before relaxing again, but the main stiffening is above 8 GPa.

In this, there does not seem to be any manifestation in the unit-cell volume, unlike ammonium carbonate monohydrate. There does also seem to be some sort of change in the *b*-axis, which occurs at the same point as the end of the major part of the NLC. The *c*-axis does show some very minor slope changes. There is no evidence present of a phase change in α-ammonium carbamate.

The change is coming from the rotation and translation of the NH_2CO_2 molecules, which is causing the NH_4^+ tetrahedron to become distorted. The $R_2^2(8)$ ring motifs do not show the same sort of behaviour, meaning the distortion and stiffening of the structure is due to the N-H$\cdots$O bonding between the molecules in the structure - indeed the quadratic elongation and bond angle variance of the ammonium tetrahedra become increasingly distorted at high-pressure, showing a noticeable sharp increase at 9 GPa, due to the change of the carbamate ions.

It seems rather curious that this behaviour is not seen in β-ammonium carbamate. If it were found in the beta structure, a 'wine-rack' motif that forms between the car-

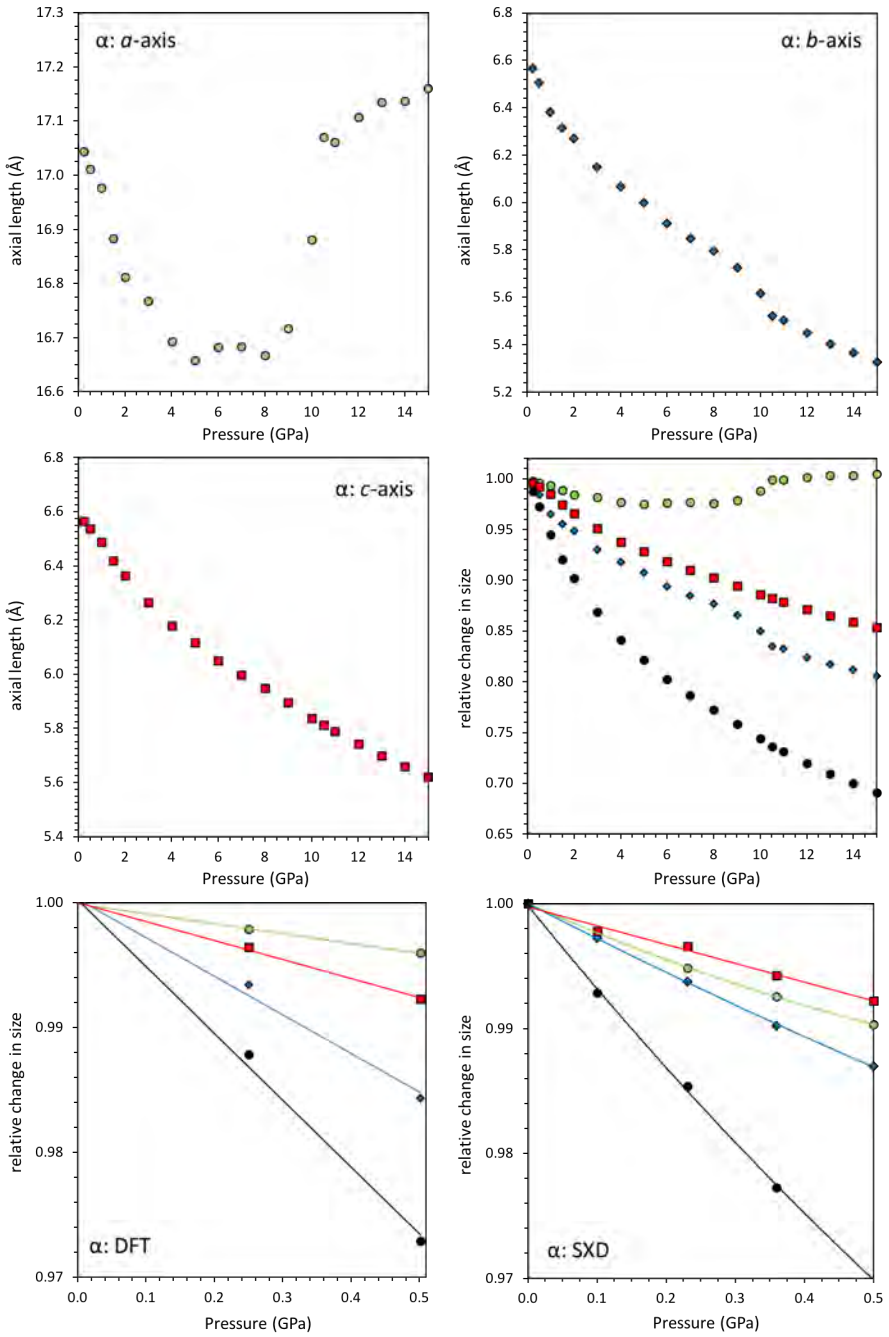

Figure 5.12
Lattice parameters of α-ammonium carbamate as a function of pressure from the CASTEP simulations are given in the top four panels. The *a*-axis and *b*-axis shows some interesting features, similar to what was seen in ammonium carbonate monohydrate. See the text for further details. The bottom two panels show a comparison of the relative change in unit cell dimensions of α-ammonium carbamate, as measured on *SXD* at 200 K and as calculated using DFT.

bamate ions on the mirror planes and the ammonium ions that form halfway between these layers would cause the carbamate ions on the mirror planes to squeeze closer together, with the ammonium ions moving further apart to accommodate this change.

5.3.2.2 Thermal expansion

The thermal expansion was determined for deuterated α-ammonium carbamate between 4.2 K and 180 K. A description of the thermal expansion begins with Grüneisen's relation between the thermoelastic parameters,

$$\gamma = \frac{\alpha_V V K_{0,T}}{C_V} \tag{5.1}$$

where γ is the Grüneisen ratio, α_V is the volume thermal expansion coefficient, $K_{0,T}$ is the isothermal bulk modulus, and C_V is the isochoric specific heat capacity.

The volumetric thermal expansion coefficient was calculated using

$$\alpha_V(T) = \frac{1}{V}\frac{dV}{dT} \tag{5.2}$$

where the value α_V is the volumetric expansion coefficient as a function of temperature.

To quantify the thermal expansion of α-ammonium carbamate, the data were fitted to an Einstein oscillator model. The thermal expansion can be expressed in terms of the internal energy of the crystal via the heat capacity, from the assumption of temperature dependence for $\gamma$and K_T,

$$V(T) = V_0 + \frac{\gamma}{K_{0,T}}\int_0^T C_V \tag{5.3}$$

If all the atoms in the solid vibrate at the same characteristic angular frequency, ω_E, then expressed in terms of an Einstein temperature, $\theta_E = \hbar\omega_E/k_B$, the isochoric specific heat capacity is

$$C_V = \frac{3R(\theta_E/T)^2 exp(\theta_E/T)}{(exp(\theta_E/T)-1)} \tag{5.4}$$

By integrating Eq. 5.3, the volume thermal expansion can be quantified via

$$V(T) = V_0 + \frac{E}{exp\left(\frac{\theta_E}{T}\right) - 1} \tag{5.5}$$

where $E = 3R\gamma\theta_E/K_T$. To get the correct asymptotic behaviour as the temperature nears 0 K, the parameter E can be allowed to vary as a function of temperature in the form of a simple polynomial

$$E = e_0 + e_1T + e_2T^2 + e_3T^3 \tag{5.6}$$

The coefficient of the thermal expansion, α_V, is

$$\alpha_X = \frac{(exp(\theta_E/T)-1)(3e_3T^2+2e_2T+e_1)+((\theta_E/T^2)(exp(\theta_E/T))(e_3T^3+e_2T^2+e_1T+e_0))}{X(exp(\theta_E/T)-1)^2} \tag{5.7}$$

Values of the polynomial were allowed to vary, and the temperature T was also allowed to vary.

Table 5.15
Parameters obtained from fitting Eqs 5.5 (and 5.6) to cell parameters of ammonium carbamate (top) and D_2O (bottom)

	Volume	a-axis	b-axis	c-axis
X_0	732.942(15)	17.0526(2)	6.4352(1)	6.6800(1)
θ_E	134(5)	172(12)	127(3)	262(6)
e_0	7.32(78)	0.07(1)	0.044(16)	0.076(43)
e_1	0.019(19)	$-7(4)\times10^{-5}$	-	-
Reduced R^2	99.9922%	99.9999%	99.9999%	99.9999%
	Volume	a-axis		c-axis
X_0	128.064(0)	4.493(0)	-	7.323(1)
θ_E	99.4(2)	85(15)	-	77(23)
e_0	$-4.385(2)\times10^{-1}$	$-4.6(15)\times10^{-1}$	-	$-8(5)\times10^{-1}$
e_1	$5.816(3)\times10^{-1}$	$7.5(2)\times10^{-1}$	-	$7(7)\times10^{-1}$
e_2	$7.85(8)\times10^{-1}$	$9(16)\times10^{-1}$	-	4(17)

At low temperatures, a Debye approximation provides a more physically correct model of the behaviour of the solid than the (mathematically simpler) modified Einstein model used in the analysis of the lattice parameters above. Eq. 5.1 assumes that K_T/γ has the Gruneisen parameter = 1 (not an unreasonable approximation) to give

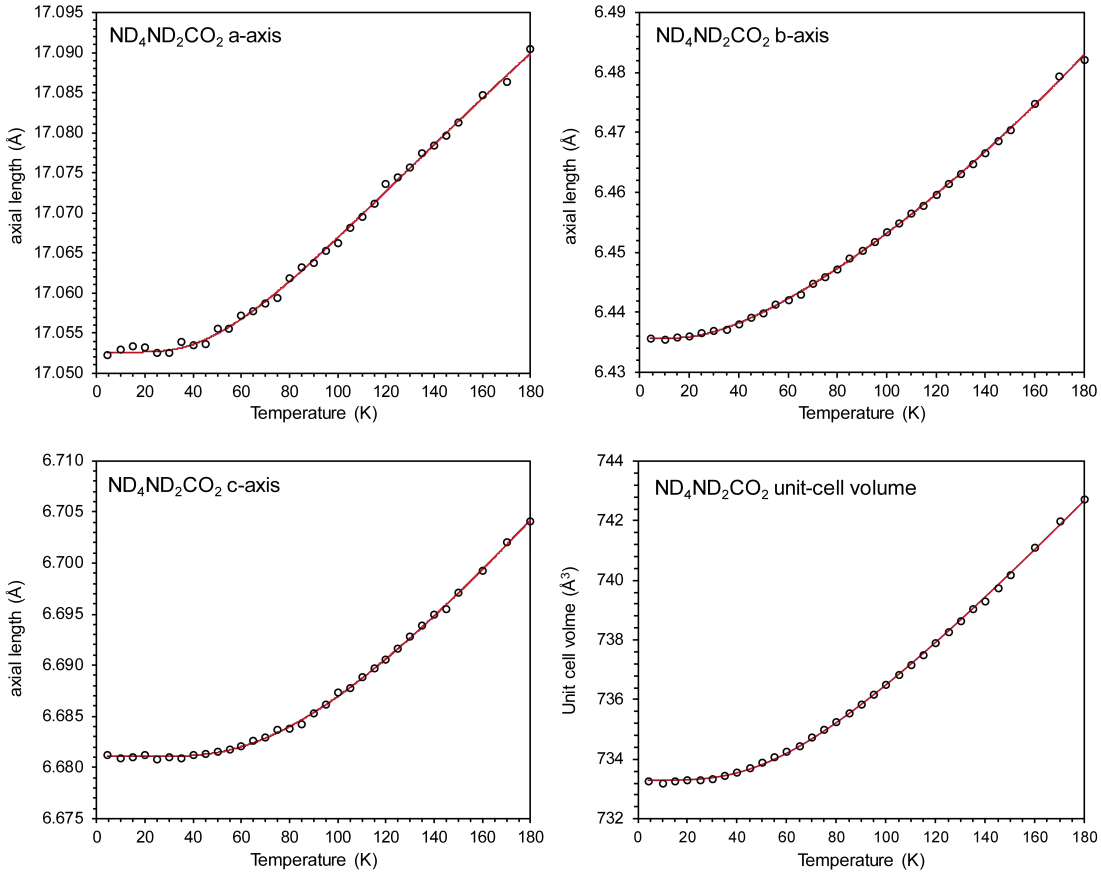

Figure 5.13
Refined cell parameters of α-ammonium carbamate and unit cell volume. Solid symbols are from Rietveld refinements, and the solid lines are the fitted Einstein model (Eqs 5.5 and 5.6).

an approximation for K_T. If γ and K_T are assumed to be independent of temperature, integration of the above equation with respect to temperature leads to the following expression for the thermal expansion in terms of the internal energy of the crystal to first order [146]:

$$V(T) = V_0 + \frac{\gamma U(T)}{K_{0,T}} \tag{5.8}$$

where V_0 is the zero temperature volume. The internal energy, U(T), may be calculated using a Debye approximation [28]:

$$U(T) = 9Nk_BT\left(\frac{T}{\theta_D}\right)^3 \int_0^{\frac{\theta_D}{T}} \frac{x^3}{e^x - 1} dx \tag{5.9}$$

where N is the number of atoms in the unit cell, k_B is Boltzmann's constant, and θ_D is the Debye temperature.

First-order Debye models were used in least-squares fitting to the to the unit-cell

volume only (since it is not dimensionally correct along each axis), with the respective values of θ_D freely refined. The results of these fits are given in Table 5.16, with the fit looking identical to that seen in Figure 5.14.

Table 5.16
Parameters obtained by fitting of a single first-order Debye model to the lattice parameters of α-ammonium carbamate between 4.2 K and 180 K at ambient pressure.

	x_0	K_T / γ(GPa)	θ_D (K)
a	17.0524(2)	119(3)	217(9)
b	6.4361(1)	106(1)	199(5)
c	6.6809(6)	134(3)	382(8)
V	733.27(2)	40.3(8)	248(3)

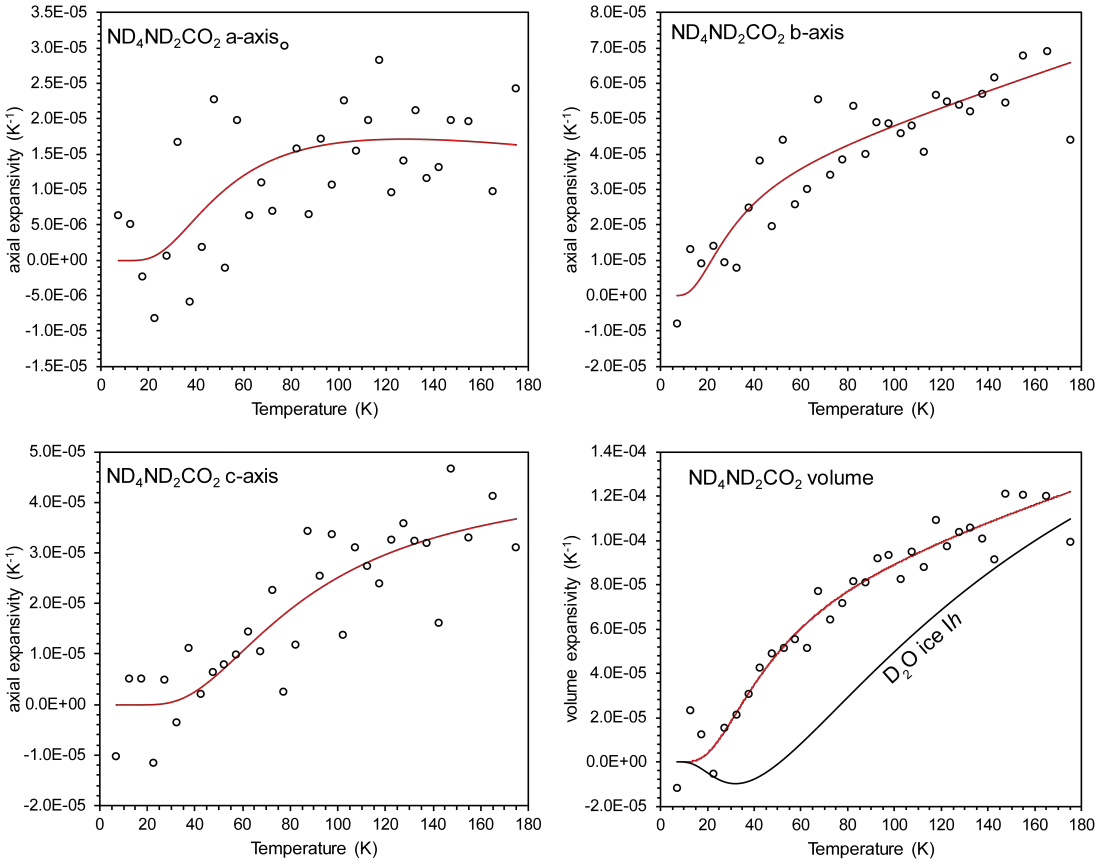

Figure 5.14
Linear and volume thermal expansion coefficients of α-$ND_4ND_2CO_2$ with D_2O ice I*h*. The white circles show values from the numerical derivative of the refined unit cell data.

Lattice parameters were obtained for α-ammonium carbamate and for D_2O ice Ih at 4.2 K, from 10 K to 140 K in 5 K increments, and from 140 K to 180 K in 10 K increments. A single-Debye model does not work accurately for D_2O due to the negative thermal expansion between 10 K and 60 K.

This process yielded Debye temperatures for the *a*-, *b*- and *c*-axes of 217(9) K, 199(5) K and 382(8) K respectively. The thermal expansion appears to be dominated by vibrational modes with characteristic temperature of about 250 K. The difference in the Debye temperatures along the three axes supports the anisotropic behaviour of the unit-cell as calculated using DFT.

A representation surface of the thermal expansion tensor coefficients at 180 K is given in Figure 5.15, and a projection along axial planes at increasing temperature is also given in Figure 5.16. The measured thermal expansion agrees well with the high-pressure behaviour of α-ammonium carbamate as calculated using DFT and as measured on *SXD*. The high degree of anisotropy under pressure in both α and β is due to details in the structure. The *b*-axis is the most compressible in α-ammonium carbamate, due to few bonds forming between layers of ammonium tetrahedra and carbamate ions, which run parallel to the *c*-axis, and hence provide little resistance to compression.

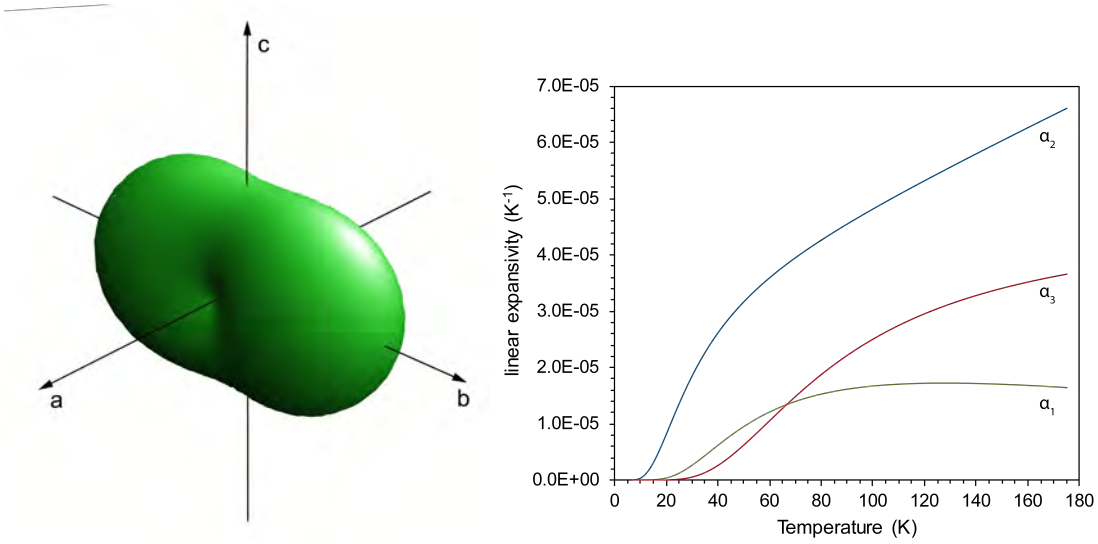

Figure 5.15
(a) Representation surface of the coefficients of thermal expansion at 180 K (drawn in WinTensor; Kaminski, 2004 [73]) (b) Magnitudes of the principal axes of the thermal expansion tensor

The direction of greatest thermal expansion is perpendicular to corrugated sheets of alternating ammonium tetrahedra and centrosymmetric carbamate ions, whereas the minimum thermal expansion is in the plane of these alternating sheets. The intermediate value is parallel to stacks of centrosymmetric carbamate ions running along *c*-,

connected by chains of ammonium tetrahedra. The limited bonding between the corrugated sheets running along *b*-axis provides little resistance to expansion, with a 3-dimensional bonding network running in the planes of these sheets resisting expansion (Figure 5.16).

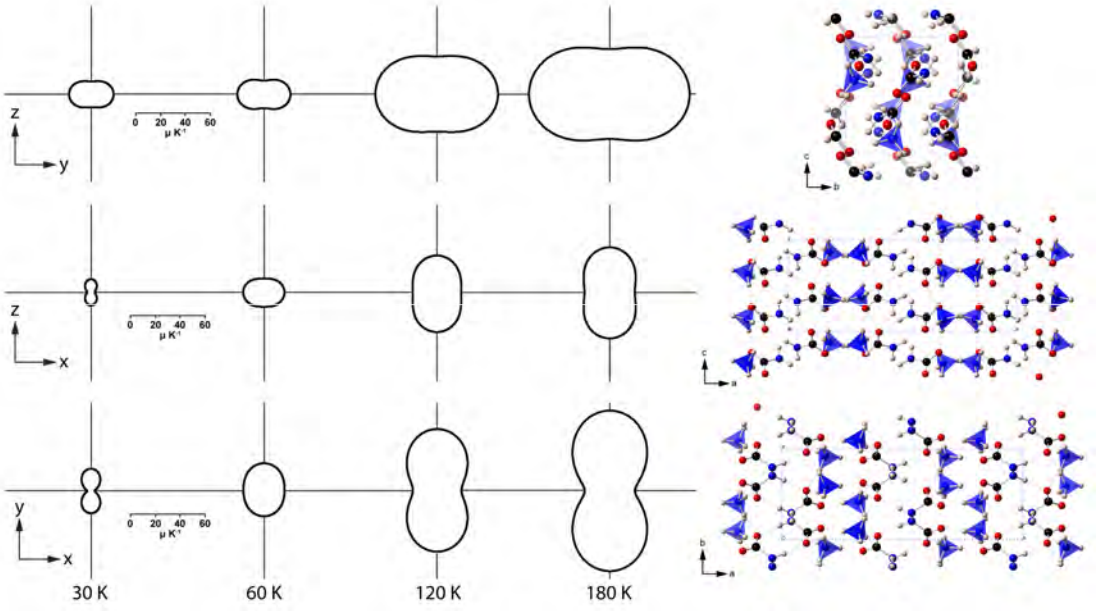

Figure 5.16
Projections of the thermal expansion coefficient representation surface from 30 K to 180 K. Solid black lines are positive values. Projections of the structure of ammonium carbamate are shown on the right.

Based on the DFT calculations, it could be expected that β-ammonium carbamate should have a smaller thermal expansivity than α-ammonium carbamate, due to a higher volumetric bulk modulus and lower compressibility.

When α- and β- ammonium carbamate are compared against thermal expansion measurements of compounds in this ternary system, the high degree of anisotropy is comparable. The ammonium carbonates are highly anisotropic, typically with one unique axis, and two axes that behave similarly, due to planar layers of interconnected ammonium tetrahedra. Indeed, in ammonium carbonate monohydrate, the *c*-axis is the stiffest and has been suggested to have negative linear thermal expansion along this direction, with *a*- and *b*- similar [53]. The next chapter shows that in ammonium bicarbonate, the *a*-axis is the softest and the *b*- and *c*-axes are similar, having negative area thermal expansion at low temperatures.

5.3.3 Relative stability and planetary parameters

To asses the relative stability between the two phases, the enthalpy has been calculated as a function of pressure for each phase, and also assessed the common tangent between the two energy-volume curves.

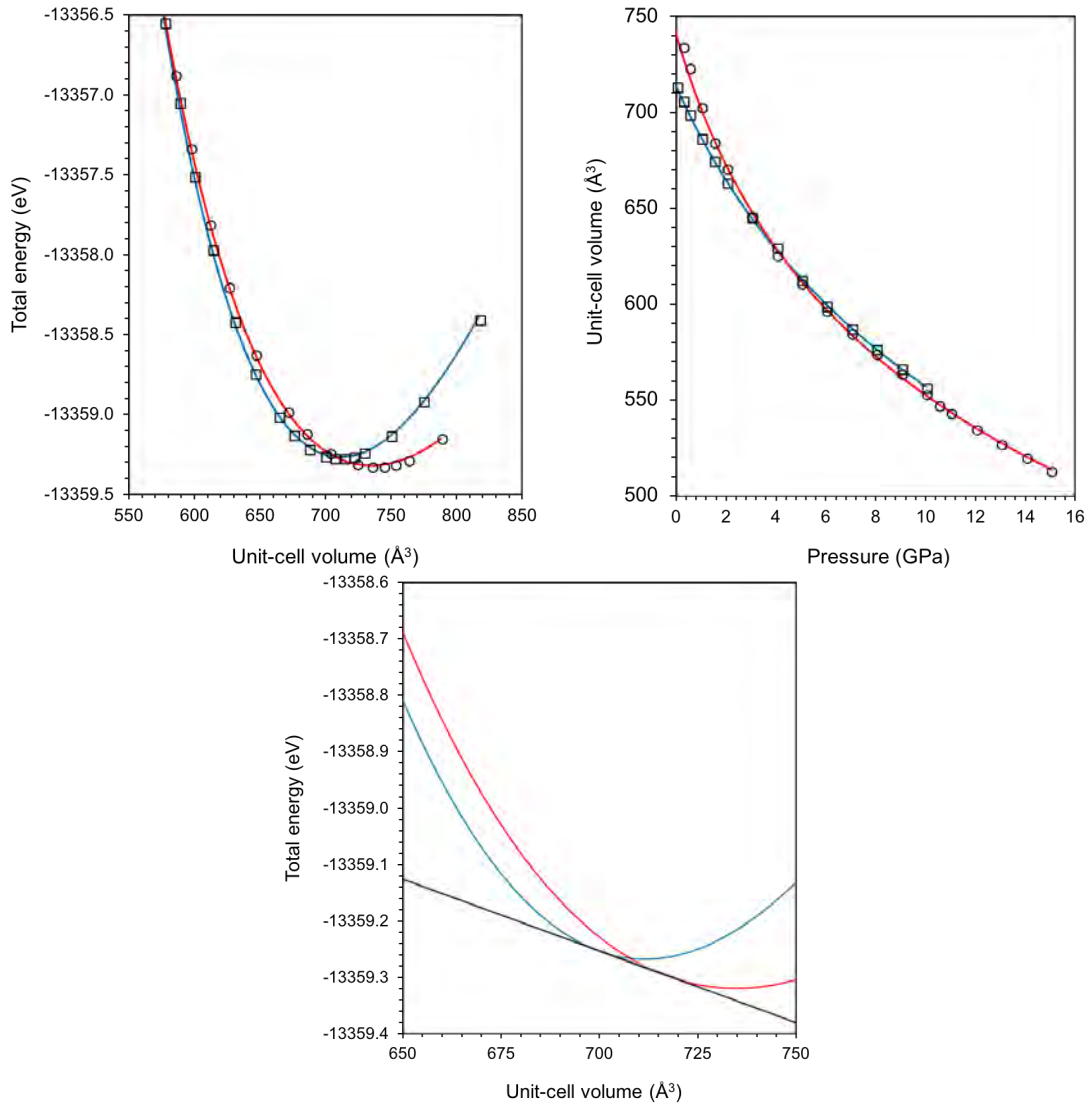

Figure 5.17
Dispersion corrected E(V) curves (left) and P(V) curves (right) of: α-ammonium carbamate (red line, open circles) and; β- ammonium carbamate (blue line, open squares).

By assessing the common tangents of the two fitted equations of state that cross (Figure 7.1), a pressure point where transition may occur can be calculated. Any straight line on an internal energy-volume graph will have a constant enthalpy H, with the common tangent of the two curves meaning both phases are in thermodynamic equilibrium. The common tangent between the α-phase and β-phase has a slope of -0.0025

eV Å^{-3}, equivalent to a transition pressure of ∼0.4 GPa.

A similar method to calculate the stability of these two compounds is to calculate the enthalpy as a function of pressure. The enthalpy has been calculated using

$$H = U + PV \tag{5.10}$$

The enthalpies are compared in Figure 5.18. α-ammonium carbamate has the lowest enthalpy of the two phases at zero-pressure in the athermal limit, with a difference of 399.33 J mol^{-1} to the β-phase. When increasing the pressure, the enthalpies of the two phases cross; the transition pressure between the two phases, where ΔH = 0, is ∼0.4 GPa, after which the β-phase has the lowest enthalpy. α-ammonium carbamate was compressed up to 0.5 GPa during the single crystal experiment on *SXD*, but no evidence was observed for this phase transition.

This trend - of α-ammonium carbamate having increasing enthalpy difference to the β-phase - continues up to pressures of ∼2 GPa. However, as the α-phase starts to undergo subtle structural changes above this pressure, the trend reverses and the enthalpy difference between the two phases begins to decrease.

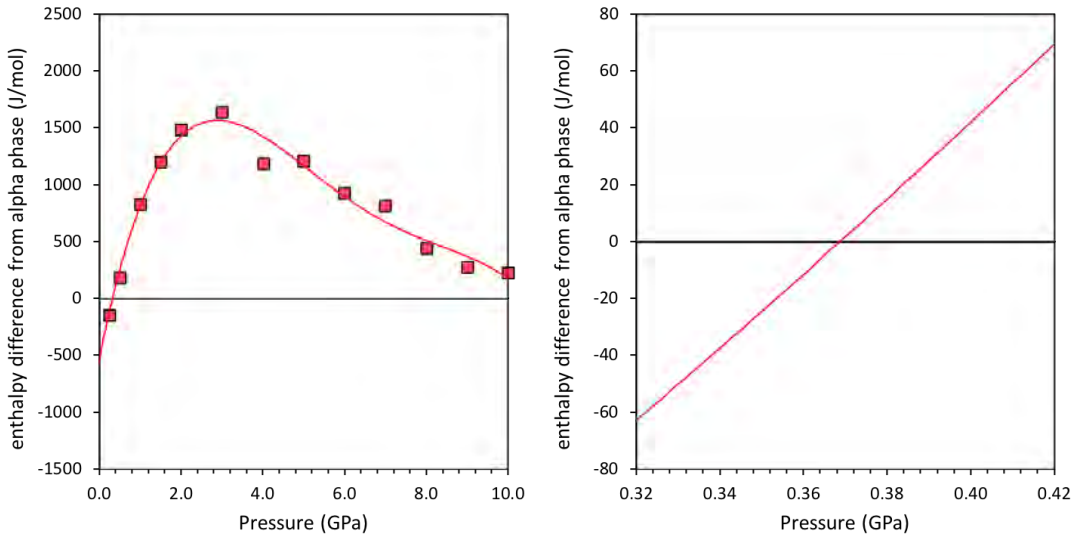

Figure 5.18
Calculated enthalpy difference between β- (normalised to zero) and α-ammonium carbamate (red squares, red polynomial line).

The work indicates that α-ammonium carbamate is the more thermodynamically stable phase at ambient pressure, but for pressures greater than ∼0.4 GPa, β-ammonium carbamate becomes the most thermodynamically stable. However, the work on *SXD* to

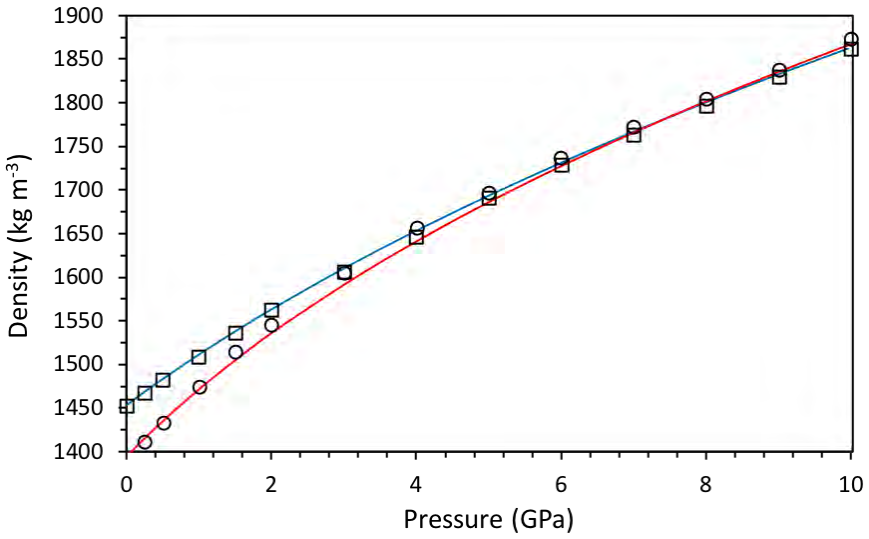

Figure 5.19
Calculated density as a function of pressure α-ammonium carbamate (red line, open circles) and; β- ammonium carbamate (blue line, open squares), based upon the DFT calculations.

measure the behaviour of α-ammonium carbamate at pressure showed no evidence of a phase transition between the α- and β-phases at pressures up to 0.5 GPa. It may be that the system requires a stimulus to induce the phase transition, such as over-pressure. It could also be due to the temperature difference between the experiment, which was conducted at 200 K, and the DFT simulations, which are athermal; the phase change could be temperature dependent, or could be kinetically inhibited at low temperatures.

The density has been fitted using the same equation of state as given in Chapter 3 (eq. 3.1). Figure 5.19 shows the fitted density profiles as a function of pressure. The fitted parameters are: α-ammonium carbamate, $\rho_0 = 1394.2$ kg m^{-3}, $K_0 = 16.2$ GPa and $K_0' = 5.1$; β-ammonium carbamate, $\rho_0 = 1452.7$ kg m^{-3}, $K_0 = 23.5$ GPa and $K_0' = 4.3$.

5.4 Chapter summary

This chapter has presented the experimental work on α-ammonium carbamate using two instruments at the ISIS neutron spallation source of the Rutherford-Appleton Laboratory. The experiment involving *HRPD* is the first neutron powder diffraction study of α-ammonium carbamate, with accurate structural refinement at 4.2 K, and the determination of the magnitudes of the thermal expansion tensor principal axes as a function

of temperature and the relationship with structural elements. The experiment involving *SXD* is the first single crystal neutron diffraction experiment of α-ammonium carbamate , and the first high-pressure experiment to determine high-pressure behaviour from 0 GPa to 0.5 GPa at 200 K. The high degree of anisotropy observed in the *HRPD* experiment was also seen here.

Also presented in this chapter, are the first *ab initio* calculations of two phases of ammonium carbamate, α and β. A series of static calculations at fixed volumes yielded energy-volume curves, E(V), and pressure-volume curves, P(V), which were analysed by fitting an equation of state to determine elastic parameters. The high-pressure structure is described, and the relative stability of the two phases is determined using thermodynamic equations. The values obtained during the experiments matches the density functional theory calculations very well.

The data presented in this chapter from the DFT simulations and the experiments yields the parameters necessary for incorporation into structural models of icy planetary bodies. Understanding the phase behaviour of this system could be important in understanding the behaviour of the ammonium carbonates in terrestrial systems.

Chapter 6

Ammonium bicarbonate: *ab initio* simulations & experiments

This chapter presents the *ab initio* calculations and the experimental work on ammonium bicarbonate, NH_4HCO_3. Ammonium bicarbonate is the only compound in the $NH_3 + CO_2 \pm H_2O$ ternary system to form naturally on Earth. Neutron powder diffraction data were collected at the ISIS pulsed neutron spallation source of the Rutherford Appleton Laboratory, on the high resolution powder diffractometer, *HRPD*, and on the high-pressure diffractometer, *PEARL*. The details of the experiments follow.

6.1 Details and structure

First discovered in 1806 by Berthollet, ammonium bicarbonate, NH_4HCO_3, is known as the mineral teschemacherite, found in layers of guano in South Africa and South America [136, 141, 112, 108] and in geothermal waters in New Zealand [21].

Crystals are clear and colourless with a prismatic habit, usually with a slight odour of ammonia. Their distinguishing feature compared to the other ammonium carbonates is that this is the only compound stable in air above 273 K. The crystal morphology was described by Gustave Rose, Hallows Miller and H. St. Claire Deville, with further details given by Divers, 1870 [39].

The lattice constants of ammonium bicarbonate were first published by Mooney, 1932 [99], in which the structure is reported as orthorhombic, space group *Pccn* and Z = 8, and a structure without protons was published by Brooks & Alcock, 1950 [20]. The last reported structure of ammonium bicarbonate was published by Pertlik, 1981 [111], which included all atomic positions based upon a single crystal investigation;

the unit-cell from this is given as a = 7.225 Å, b = 10.709 Å, c = 8.746 Å, V = 679.51 Å^3 [111].

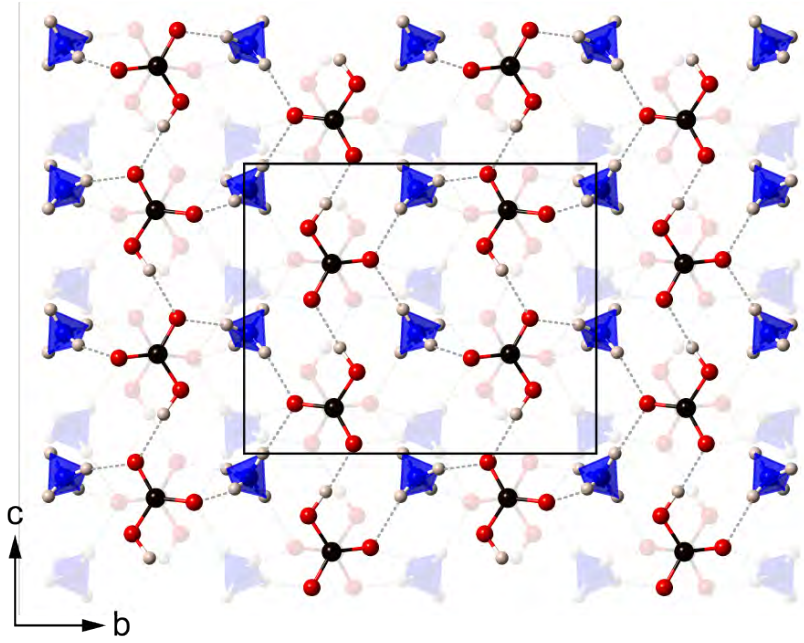

Figure 6.1
The crystal structure of ammonium bicarbonate, viewed in the *bc* plane. The solid black line is the outline of the unit-cell, the faded atoms are in the plane below, and the grey dashed lines are long-range hydrogen bonds. The structure consists of chains of bicarbonate anions (HCO_3^-) running along c, with ammonium ions (NH_4^+) connecting the chains along a and b.

The structure of ammonium bicarbonate (Figure 6.1) is made up of chains of bicarbonate anions (HCO_3^-) running parallel to [001], by which one of the bicarbonate O atoms accepts a H-bond from the O-H of the next [CO_2(OH)] anion. Ammonium tetrahedra link the bicarbonate chains along a and b, with each bicarbonate O atom accepting bonds from two ammonium tetrahedra, creating a fully 3-dimensional hydrogen bonded structure, albeit with a strongly layered character.

6.2 Methods

6.2.1 Computational details

Static DFT calculations (see section 3.1.1) were carried out to determine an equation of state. Convergence tests were carried out to optimise the $\vec{k}$-point sampling of the Brillouin zone within the Monkhorst-Pack scheme and the kinetic energy cut-off of the plane-wave basis set. A grid of 3x2x3, with 4 unique $\vec{k}$-points ($\sim$0.04 Å^{-1} reciprocal lattice spacing), and energy cut-off 1400 eV yielded total energy convergence better

Table 6.1
Structural parameters ammonium bicarbonate, measured by a single crystal X-ray diffraction experiment at ambient temperature by Pertlik, 1981 [111]. This structure was used as the starting point for the DFT calculations.

Ammonium bicarbonate

Formula	NH_4HCO_3	Lattice parameters	
Space group	*Pccn*	*a*-axis (Å)	7.255
Z	8	*b*-axis (Å)	10.709
ρ (kg m^{-3})	1545.6	*c*-axis (Å)	8.746
Temperature (K)	293	Volume (Å^3)	679.5

Label	Fractional coordinates			U_{iso}	Site
	x	y	z	(x10^2)	
C1	0.0088(2)	0.2470(1)	0.1566(2)	2.28	8e
N1	0.2456(2)	0.0120(1)	0.4152(2)	2.964	8e
O1	0.9851(1)	0.1907(1)	0.0325(1)	3.432	8e
O2	0.9649(1)	0.1812(1)	0.2811(1)	3.052	8e
O3	0.0677(1)	0.3566(1)	0.1711(1)	3.052	8e
H1	0.300(2)	0.057(2)	0.349(2)	1.393	8e
H2	0.651(3)	0.028(2)	0.125(2)	2.28	8e
H3	0.207(2)	0.051(2)	0.498(2)	1.90	8e
H4	0.824(2)	0.051(2)	0.055(2)	1.393	8e
H5	0.986(2)	0.23(2)	0.365(2)	2.153	8e

than 10^{-3} eV per unit-cell.

6.2.2 Synthesis of samples

Deuterated ammonium bicarbonate was prepared in the same way for all experiments. Dry ice pellets were placed in a container connected to a conical flask partially filled with a 25 wt% ND_3 solution (Sigma Aldrich 176702, 99 atom % D) at room temperature (Figure 6.2a). As the pellets sublimate, the CO_2 passes to the flask, causing an exothermic reaction with the solution. After a few hours, small crystals began to appear on the surface of the liquid. The container was then sealed and left for a day, after which large, well faceted clear crystals had developed. In-house X-ray powder diffraction confirmed these crystals to be phase pure ammonium bicarbonate. The crystals were transported to the ISIS neutron facility kept in solution, as in previous experience, other compounds in this ternary system are prone to readily break down once exposed to the atmosphere at room temperature.

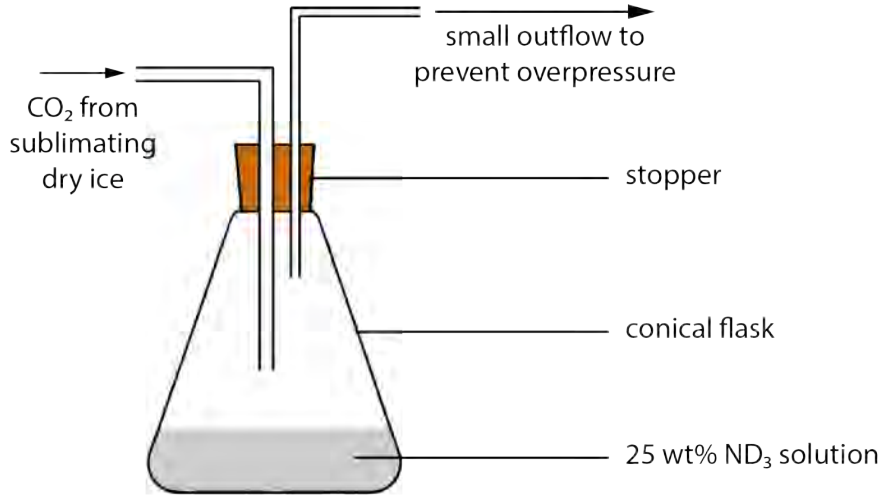

Diagram showing the method used to synthesise the deuterated ammonium bicarbonate crystals.

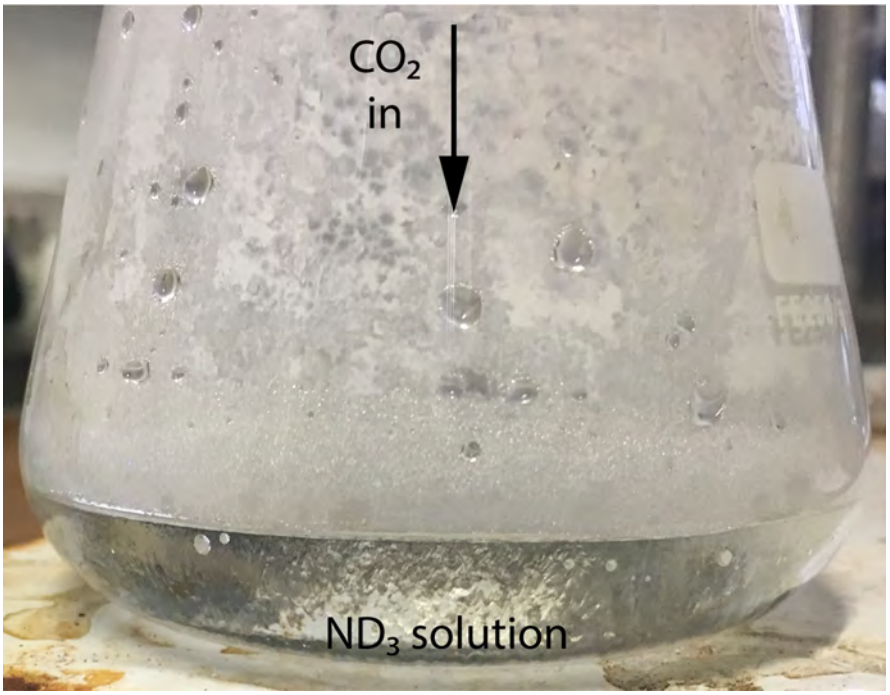

Image taken of the bottom of the conical flask during the synthesis of deuterated ammonium bicarbonate.

Figure 6.2
The method of synthesising the samples of deuterated ammonium bicarbonate for the experiments on PEARL and HRPD. As the CO_2 interacts with the ND_3 solution, heat is given off, forming the condensation on the side of the conical flask, which can be seen in the lower image. Just above the liquid, small crystals form on the surface of the flask. As the CO_2 interacts with the liquid, 'ripples' can be seen flowing in the solution. After a few hours, small crystals of ammonium bicarbonate appear on the surface of the solution, which, upon growth, sink to the bottom of the flask. These crystals are then extracted from the remaining liquor, dried and powdered ready for measurement.

6.2.3 Experiment: *HRPD*

The neutron diffraction data were collected using *HRPD* due to its high resolution, speed and accuracy to determine cell parameters for structural refinement and hence for thermal expansivity determination.

6.2.3.1 Sample Preparation

Crystals were extracted from the growth solvent, dried on filter paper and ground to a fine powder using a stainless steel pestle and mortar at room temperature. Once fully ground, the material was loaded into an aluminium-framed slab-geometry can of inner dimensions 23 × 18 × 15 mm, which was transferred to a CCR pre-cooled to 100 K. The CCR centre-stick was lowered into the CCR and the temperature reduced to 10 K for measurements to begin.

6.2.3.2 Data Acquisition

Time-of-flight powder diffraction data were collected at 10 K in the 30-130 ms window using the backscattering detector (2θ = 168°, d-spacing range 0.65 - 2.6 Å) for high resolution structural refinement, counting for ∼8 hr (corresponding to an integrated proton-beam current of 320 μA hr); this well counted dataset was used for precise structural refinement. Subsequent data were collected on warming in 10 K increments up to 300 K. Each measurement lasted for ∼1 hr (corresponding to an integrated proton-beam current of 40 μA hr per step). The diffraction data were focussed, normalised to the incident beam spectrum and corrected for detector efficiency by reference of a vanadium standard using *Mantid* [7], and exported to a format suitable for analysis with *GSAS/Expgui* [87, 138].

6.2.3.3 Structural refinement

Neutron powder diffraction data were refined at 10 K by the Rietveld method using *GSAS/Expgui* [87, 138], starting from the structure given by Pertlik, 1981 [111] (Table 6.1). Deuterated ammonium bicarbonate and deuterated water ice I*h* were identified in the initial 10 K dataset by inspection of peak positions. Data were fitted by refinement of unit-cell parameters, scale factors and phase fractions, peak-profile coefficients (*GSAS* profile function 3), and an eight term Chebyschev polynomial. Atomic coordinates were refined independently without restraints, whilst the thermal displacement

parameters were set to anisotropic to improve the fit, with values staying positive. It was found necessary to refine a sample texture correction, using a 4^{th} order spherical harmonic model for both phases. The refined phase fractions are > 99 % ammonium bicarbonate and < 1 % deuterated water ice, leading to the conclusion that the ice derives from a very small amount of mother liquor occluded inside the original crystallites or else adhering to the surfaces of grains. The final fit to the data have R_{wp} better than 3 %; a graphical depiction of the fit to the 10 K dataset is given in Figure 6.3.

The subsequent data points have been refined in different ways for comparison against each other, paying particular attention to the lattice parameters for D_2O ice, since these can be used to correct for the small change in the sample position that occurs with every loading. The data were analysed using: a LeBail method for both phases, *GSAS* F(calc); the Rietveld method for both phases; Rietveld for ND_4DCO_3 and *GSAS* F(calc) method for D_2O. Each method has its own advantages and disadvantages.

A LeBail refinement ignores the atomic structure, instead fitting only the peak intensities (assuming initially that all intensities are equal), and adjusting peak positions by refining the unit-cell. The advantage of this method is the ability to obtain more precise unit-cell parameters from a more accurate fitting of peak intensities than may be possible using a Rietveld model. However, in doing this, it is not possible to see how the crystal structure changes as a function of temperature (and/or pressure). There are two methods available in *GSAS* for a LeBail refinement, the first being a 'normal' LeBail refinement, the second is a variation of a LeBail refinement called the *GSAS* F(calc) method.

The F(calc) method initially computes peak intensities from structure factors, calculated from the inputted atomic coordinates, which are then used as a starting point for the refinement - this means peak intensities should be closer to the true value at the start and, therefore, the refinement should converge quicker. This could also be useful if there is more than one phase measured at the same time, as any peak overlap between the two phases will be easier to refine since the approximate peak intensities are known. However, once again, the atomic structure in this method is not refined and therefore no information can be given on how the structure changes as a function of an external stress.

The Rietveld method analyses the data using the crystal structure as a model, and

is able to give information on how the atomic coordinates varies, values for the thermal displacement parameters, as well as weight-fractions between phases and any texture that may be present in the sample. However, the data needed to obtain an accurate and precise crystallographic structure requires good quality data at low *d*-spacings, in particular below 1 Å to get anisotropic displacement parameters, which for some materials may require long count times per temperature step; materials with lower symmetry will require longer counting time due to the increased number of reflections at low *d*-spacings compared to higher symmetry structures. However, this is not always an option.

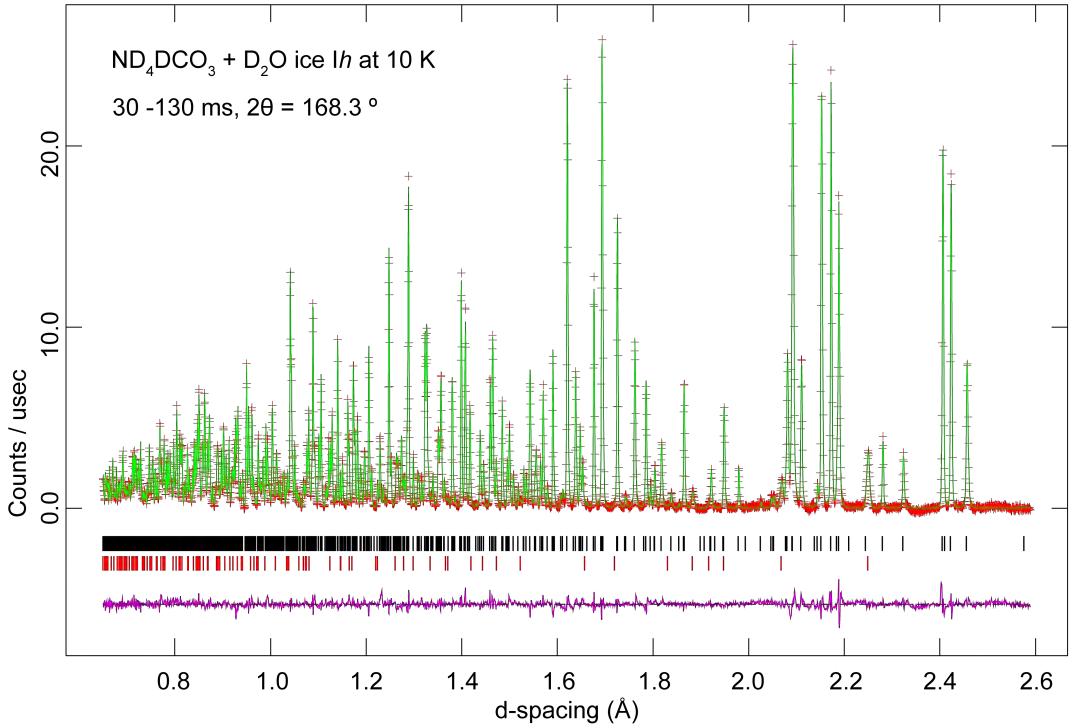

Figure 6.3
Neutron powder diffraction pattern of ND_4DCO_3 with D_2O ice I*h* acquired at 10 K in the highest resolution backscattering bank of *HRPD*. Red pluses represent the measured data, the solid green line the result of Rietveld refinement, the purple line the difference profile, and the tick marks the expected positions of each Bragg reflection for ND_4DCO_3 (black) and D_2O (red).

Comparisons between the different methods show little to no difference for the lattice parameters for ND_4DCO_3, but do show a larger difference for D_2O (presumably due to the small quantity in the sample). During the refinements of D_2O, it became apparent that the *c/a* ratio was changing as a function of temperature (Figure 6.4). Below 200 K, the *a*-axis is larger than the reported lattice parameters given by Fortes, 2018 [52], in which the ice has been refined against an internal standard of silicon, but

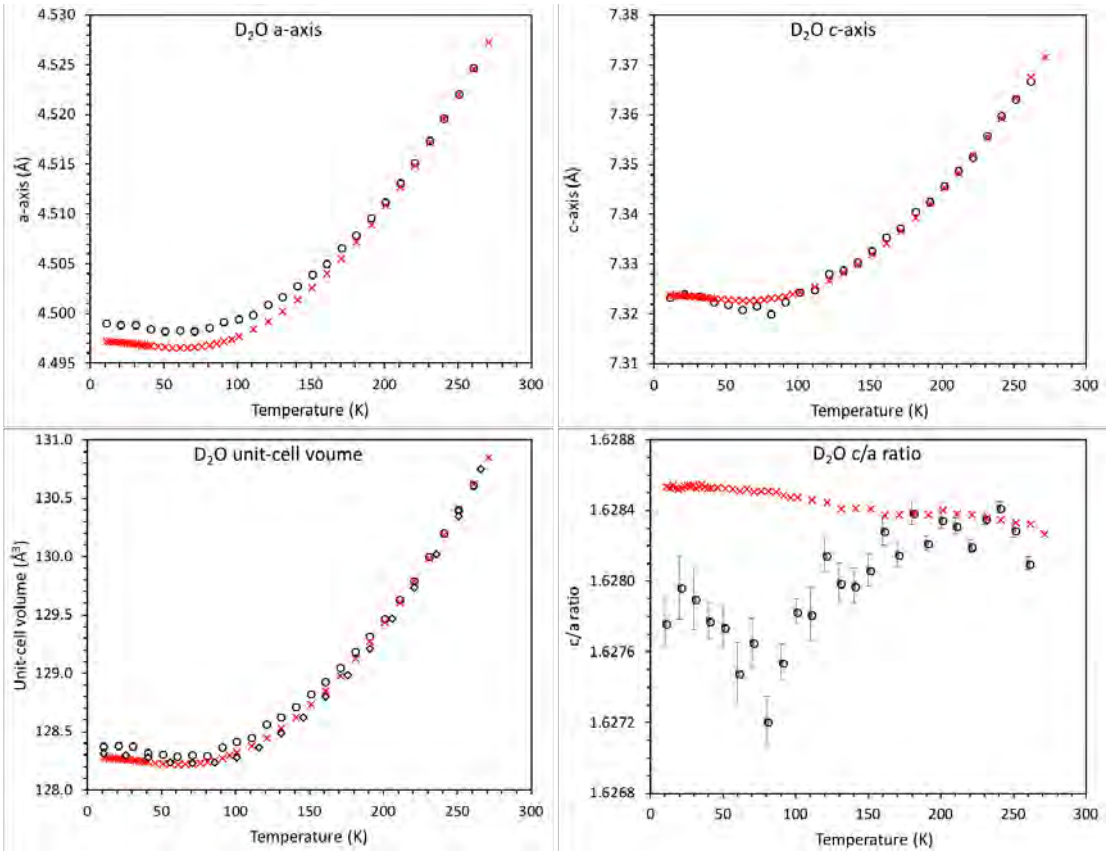

Figure 6.4
Lattice parameters of D_2O ice I*h*. The open circles are the data from this work, the red crosses are from Fortes, 2018 [52], and the open diamonds are from Röttger *et al.*, 1994 [122]. There is a systematic trend for the c/a ratio of D_2O ice I*h*, in which the lattice parameter of the *a*-axis starts to deviate below 200 K away from literature values.

the *c*-axis follows the reported values much more closely. This is apparent when the *c/a* ratio is plotted as a function of temperature. This type of behaviour seems to be as a result of the thermal history of the D_2O, in which the structure shows a stress below 100 K but then subsequently relaxes back to the reported values above this temperature. This behaviour can be seen in all three methods used to refine the data, but is most apparent in the two LeBail methods used. Therefore, the Rietveld refinement of D_2O is not the most accurate method of refining the data.

Careful attention was paid when fixing the lattice parameters of D_2O to literature values, since the structure shows some kind of strain below 200 K. The values of D_2O were fixed to the literature values between 240 K and 260 K since the structure had relaxed back to its unstrained state, and by fixing the values over these temperature points, a better average of the values of DIFA and DIFC could be attained. To do this, the values of D_2O were taken from Fortes, 2018 [52] fixed in *GSAS*, and then DIFC and

DIFA were refined to correct for the small change in the sample position that occurs with every loading. These values of DIFC and DIFA were then averaged over the three temperature points. These averaged values were then used to refine all of the data once again to get the most accurate lattice parameters for both phases.

At 270 K and above there are slightly fewer peaks due to melting of D_2O; since D_2O normally melts at ∼276 K, the disappearance of the peaks at 270 K is presumably due to the presence of small concentrations of ammonium lowering the melting point. Indeed, the presence of D_2O in the sample is most likely from very small amounts of mother liquor still present when extracting the crystals, which would most likely contain some ammonium to a small degree that did not react with CO_2 during synthesis.

Table 6.2
Unit-cell parameters of ND_4DCO_3 from this work, compared with the work by Pertlik *et al.*, 1981 [111] on NH_4HCO_3. Here, the difference between the corrected and uncorrected sample position can clearly be seen in the unit-cell values.

	This work ND_4DCO_3 10 K	This work ND_4DCO_3 300 K	[111] NH_4HCO_3 295 K*
Uncorrected sample position			
a-axis (Å)	7.13795(1)	7.25260(4)	7.255
b-axis (Å)	10.68151(2)	10.69230(5)	10.709
c-axis (Å)	8.75086(1)	8.76642(3)	8.746
Volume (Å^3)	667.201(2)	679.809(4)	679.5
Corrected sample position			
a-axis (Å)	7.14047(2)	7.25492(2)	7.255
b-axis (Å)	10.68487(2)	10.69598(2)	10.709
c-axis (Å)	8.75373(1)	8.76924(1)	8.746
Volume (Å^3)	667.866(2)	680.480(2)	679.5

* no temperature is given, so is assumed to be at room temperature

6.2.4 Experiment: *PEARL*

Several experiments were conducted on the instrument *PEARL* at the ISIS neutron spallation source of the Rutherford-Appleton Laboratory. The instrument was chosen due to its ability to measure diffraction patterns from powder specimens to at least several GPa and measure to 8 Å *d*-spacing. The aim of this was was to to fit an equation of state for comparison to the *VASP* calculations, and to measure and characterise any phase changes that might be observed.

6.2.4.1 Sample preparation

Initial preparation of the sample is described in Section 6.2.2. Single crystals were extracted from solution, which were dried and ground into a powder. The powder was left quite coarse, to reduce breakdown of the sample at room temperature. Once ground, the material was loaded into a small TiZr encapsulated gasket with a lead standard inserted for pressure determination, and a perdeuterated methanol/ethanol solution in a 4:1 volume ratio respectively. This was mounted between ceramic ZTA anvils inside a Paris-Edinburgh load-frame.

6.2.4.2 Data acquisition

A total of four loadings were carried out over three experiments: two loadings at room temperature ($\sim$295 K); one loading at 245 K; and one loading at 200 K. The room temperature loadings did not require a thermocouple or a variable-T insert. For the two loadings below room temperature, a calibrated thermocouple was taped to one of the anvils to measure the temperature close to the sample, with a variable-temperature insert to control the temperature of the sample; this allows the sample to be warmed and cooled *in situ*.

During the experiment, pressures were monitored by reading the (111) reflection of Pb from the diffraction pattern. The peak position was converted into a pressure using the Pb EoS (as parameterised by Fortes, per comms.). Subsequently, whole-pattern fitting produced a more accurate value for the lattice parameter of Pb, and the the standard error allowed calculation of the propagated uncertainty in the pressure.

Time-of-flight neutron powder diffraction data were collected in the 1500-20,000 μs window (2θ = 90°, d-spacing 0.5 - 4.1 Å), and a few data points using the long-pulse, in the 20,000-40,000 μs window (2θ = 90°, d-spacing 4 - 8 Å). Each scan was counted until an integrated proton-beam current of 150 μA hr was achieved, equivalent to $\sim$1 hour. Longer counts therefore required summing the data together; this allowed a check that the sample was not changing between runs. The diffraction data were focussed, normalised to the incident beam spectrum and corrected for detector efficiency by reference to a vanadium standard using *Mantid* [7], and exported to a format suitable for analysis with *GSAS/Expgui* [87, 138].

6.2.4.3 Loading I

An initial data set at a load of 60 bar oil pressure in the PE press (corresponding to 0.32(5) GPa) was counted for ∼2 hr (corresponding to an integrated proton-beam current of 300 μA hr); this well-counted dataset was used for a starting 'zero pressure' refinement. Subsequently, the load was increased in 25 bar increments up to 185 bar (equivalent to a pressure of 2.26(8) GPa), counting for ∼2 hr counts per step. At 185 bar it was apparent that there was a new phase present by the appearance of additional peaks. The load was increased slowly in 10 bar increments from 185 bar to 205 bar (equivalent to pressures of 2.26(8) - 2.37(8) GPa) with the same counting times, then from 215 to 235 bar with ∼1 hr counting times. At 245 bar (equivalent to 2.73(8) GPa), the original low-pressure phase had completely disappeared, and a long count of ∼7 hr was performed. Work was then done to try and characterise this newly discovered phase, beginning with indexing the diffraction pattern. Details of this are given in Section 6.3.7.

After this, the load was increased in 50 bar increments to 595 bar (equivalent to 5.7(2) GPa), the maximum load available in this experiment, with data collected for ∼2 hr at each step, and with a long count of ∼8 hr at the highest pressure data point.

6.2.4.4 Loading II

A second loading with an initial load of 100 bar (equivalent to a pressure of 0.12(3) GPa) at room temperature was then cooled to 200 K, with the intention of following the same method as during the room temperature loading. The load was increased by 25 bar up to 350 bar (up to 3.01(6) GPa equivalent), and then by 50 bar increments to 450 bar (to 3.90(8) GPa), with each step counted for ∼2 hr scans. At 500 bar (4.42(9) GPa) new peaks appeared, so a longer count was initiated lasting ∼5 hrs. The final two loads were at 550 and 600 bar (4.9(1) GPa and 5.4(1) GPa), with each scan lasting ∼4 hrs.

Once 600 bar was achieved and counted, the sample was warmed in 50 K steps from 200 K to 450 K at 600 bar load; three additional phase changes were encountered during warming, but due to time constraints it was only possible to count each point for ∼2 hrs.

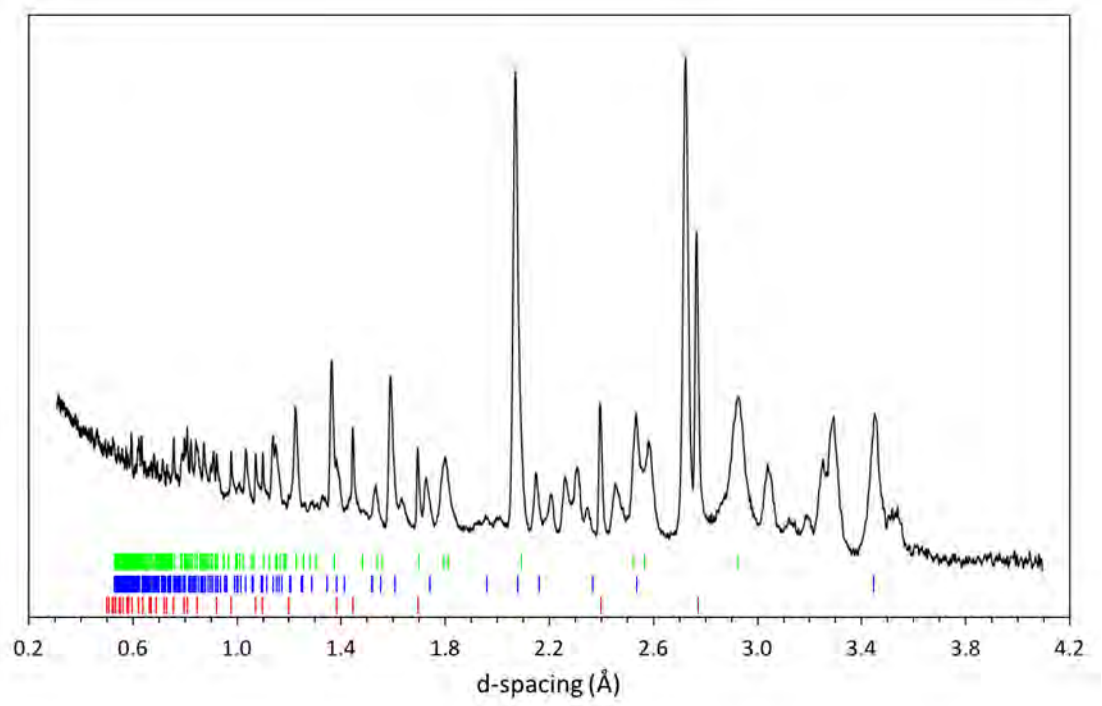

Figure 6.5
Time-of-flight neutron powder diffraction pattern of deuterated phase III ammonium bicarbonate measured at 200 K and 4.468 GPa on *PEARL*. The tick marks correspond to lead (red), alumina anvils (blue), and zirconia (green), with the unmarked peaks being from the new phase.

6.2.4.5 Loading III

During this second experiment, the long pulse (1/4 beam at the longest wavelengths) was used to aid in indexing new phases. In order to reach the first phase change encountered in the first experiment quickly to maximise counting time on the new phase, the patterns were counted for only ∼12 min per step (corresponding to 30 µA hr per step), from 100 - 350 bar of load in 50 bar steps. Upon reaching 350 bar, the same phase transition occurred as before, and hence a long count was initiated to help with indexing the new phase (equivalent to 1050 µA hr, see Figure 6.7). Once counted, the sample was then cooled to 200 K and the load increased up to 600 bar in 50 bar increments. At 200 K and 600 bar load, the sample was warmed to 225 K and 250 K respectively (repeating the previous method), where, once again, a long data count was initiated.

6.2.4.6 Loading IV

This experiment was undertaken at 245 K, in between the two previous experiments. The aim was to observe the first phase transition, phase I to phase II. It started with an

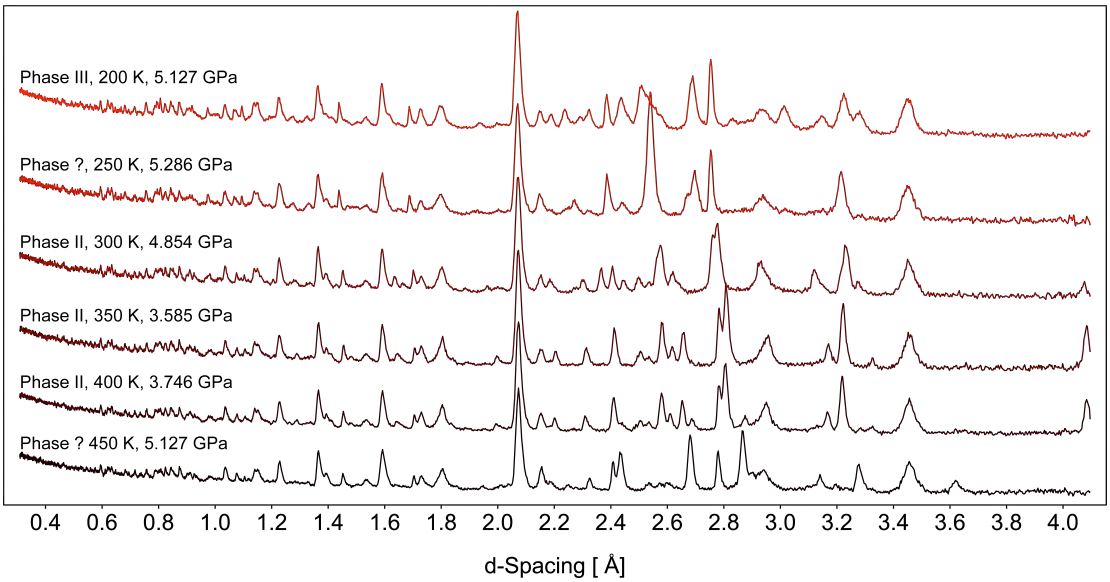

Figure 6.6
Stack plot of neutron powder diffraction data of ammonium bicarbonate. Temperature increases from 200 K (top) to 450 K (bottom). Between the 250 K and 350 K data sets, the pressure has dropped from 5.4(1) GPa to 3.8(1) GPa. This is due to transformation of phase III $\rightarrow$ II, where phase III has a higher unit-cell volume. Note that at 250 K, the diffraction pattern has changed from phase III but is not phase II.

initial load of 65 bar (0.06(4) GPa). The load was increased in 25 bar increments up to 265 bar (2.58(7) GPa), with each step counted for 1 hours. At 290 bar (2.69(7) GPa), a phase change occurred, so a longer count was initiated, lasting 9 hours. This new phase was phase II that was seen during the room temperature loadings. The pressure was then increased in 25 bar increments up to 535 bar (4.9(1) GPa). The last pressure point, at 570 bar (5.3 (1) GPa) was counted for 10 hours.

6.2.4.7 Structural refinement

The neutron powder diffraction data were analysed by the Rietveld method using *GSAS/Expgui* [87, 138], starting from previously published atomic coordinates based upon 3-dimensional X-ray data [111].

In the initial data set at $\sim$295 K and 0.32(5) GPa, ammonium bicarbonate was identified, plus peaks from the pressure calibrant (lead), and the sample environment (alumina and tetragonal zirconia). The peaks from the anvils were refined using the known structures of alumina and zirconia, which stayed constant as a function of pressure. The lead peaks were used to determine the sample pressure (based on the equation of state of lead) by refining peak positions.

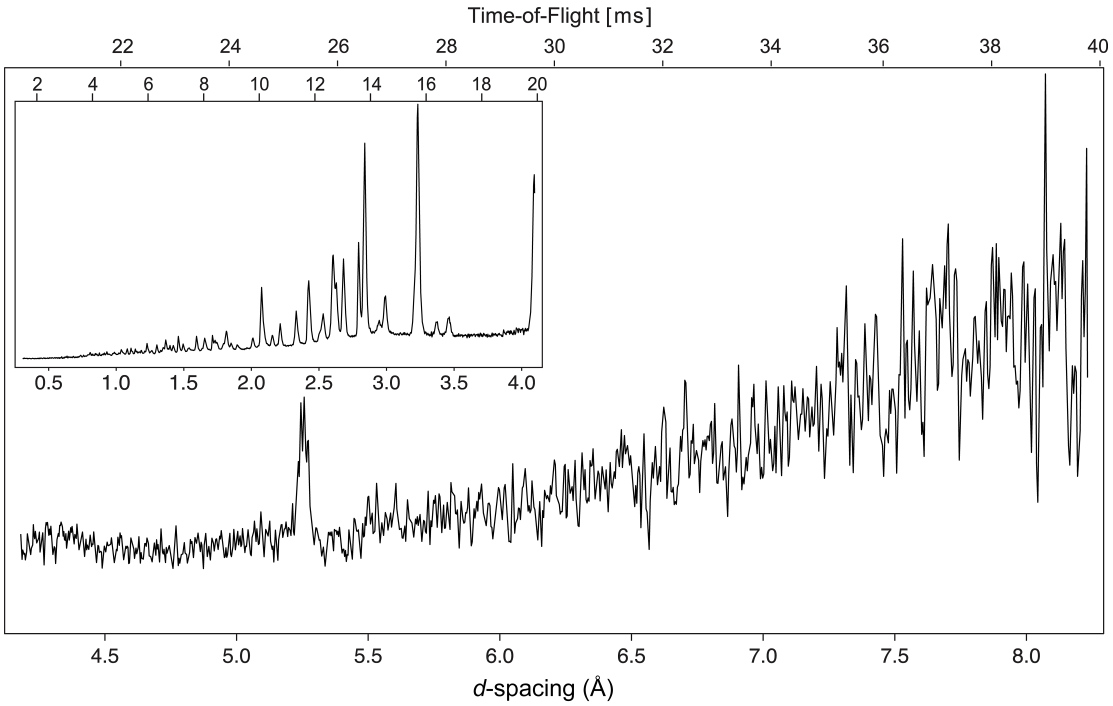

Figure 6.7
Time-of-flight neutron powder diffraction pattern of deuterated phase II ammonium bicarbonate measured at ∼295 K and 350 bar load on *PEARL* using the long time-frame window, with the 'regular' window inset.

Data were fitted by refinement of unit-cell parameters, peak-profile coefficients (*GSAS* profile function 3), and a twelve-term shifted Chebyschev polynomial to represent the background. A graphical depiction of the fit to the neutron powder data at ∼295 K and 60 bar load (equivalent to 0.32(5) GPa) is given in Figure 6.8. Refinements of each pressure step included changes to the cell parameters and peak shape profiles. It became apparent during the high-pressure work that new phases were being created at different temperatures and pressures; these were recognised by either a drop in the refinement statistics for the quality of fit, or by visual inspection due to substantial change in the diffraction patterns.

6.3 Results

This section presents the results from several experiments of d_8-ammonium bicarbonate. To begin, the results of the known, ambient P/T phase - which includes the behaviour as a function of pressure and temperature - are presented. The second section gives details of the new phases that were discovered during the work on the instrument *PEARL*, and the attempts to characterise these previously unknown crystal structures.

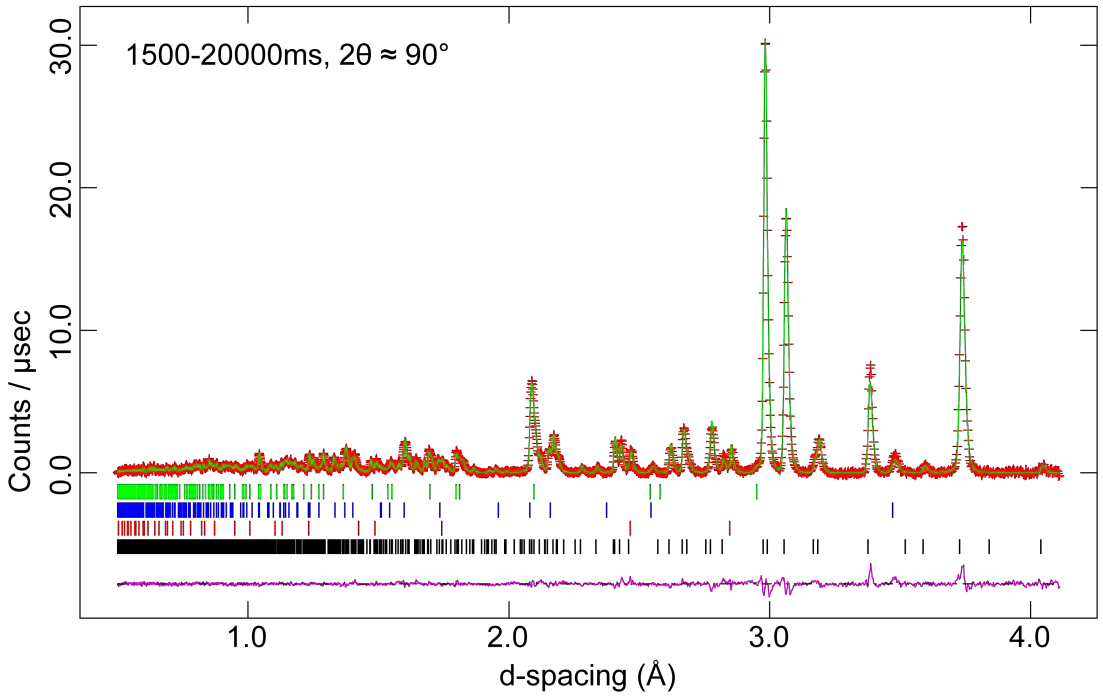

Figure 6.8
Rietveld refinement of ammonium bicarbonate at room temperature and 0.32(5) GPa (equivalent to a load of 60 bar). The ambient unit cell matches well with this pressure, with axes shortened (see other figure). Black tick marks correspond to ammonium bicarbonate, and the red tick marks to lead (used as a pressure determinant). The remaining tick marks are from the anvils and pressure cell - alumina (blue) and zirconia (green). The background has been subtracted.

6.3.1 Structure and bonding

The zero-pressure unit-cell volume from the athermal DFT simulations, 668.924 Å^3, is in very good agreement with the unit-cell volume measured at 10 K during the thermal expansion experiment on *HRPD* (see section 6.3.3) , 667.866(2) Å^3; this is a ∼0.2 % overestimation of the unit-cell volume (Table 6.3). The results of this work improve on the accuracy and the uncertainty on the H atomic coordinates (Table 6.4) and are a much better determination of the hydrogen-bond lengths in the structure (Table 6.5).

The only substantial difference between the experimental and computational structures is in the length of the H(D)···Y bonds. In the DFT relaxation, the H(D)2···O3 bond is approximately 2.8 % shorter, the H(D)4···O1 bond is approximately 3.2% shorter, and the O2···H(D)5 is approximately 5% shorter than is observed in the experiments, but the overall length, X···Y, is a much closer match, and the bond angles are within 2° of each other. The other calculated hydrogen bond lengths are less than 2% different.

Table 6.3
Comparison of the unit-cell of ammonium bicarbonate from the zero-pressure DFT simulation and from the 10 K measurement on *HRPD*.

	a-axis (Å)	*b*-axis (Å)	*c*-axis (Å)	Volume (Å^3)
10 K	7.14047(2)	10.68487(2)	8.75373(2)	667.866(2)
DFT	7.181547	10.700716	8.704559	668.924
	+0.57 %	+0.15 %	-0.56 %	0.16 %

Table 6.4
The refined structural parameters of deuterated ammonium bicarbonate, measured at room pressure and 10 K in the highest resolution backscattering banks of *HRPD* (30-130ms, $2\theta \approx 168°$). The oxygen and carbon atoms were refined with isotropic displacement parameters. This work has improved the precision of the H(D) positions by an order of magnitude.

Label	Fractional coordinates			U_{11}	U_{22}	U_{33}	U_{12}	U_{13}	U_{23}	U_{iso}
	x	y	z	(x10^2)	(x10^2)	(x10^2)	(x10^2)	(x10^2)	(x10^2)	(x10^2)
C1	0.0101(2)	0.2454(1)	0.1551(1)							0.85(3)
O1	0.9867(3)	0.1901(2)	0.0285(2)							0.82(4)
O2	0.9608(2)	0.1801(2)	0.2788(2)							0.96(4)
O3	0.0755(2)	0.3555(1)	0.1684(2)							0.82(3)
N1	0.2439(2)	0.0122(1)	0.4130(1)	1.217	0.675	1.060	-0.321	-0.184	0.108	0.98
D1	0.3087(2)	0.0698(1)	0.3347(2)	2.291	2.107	2.340	-0.012	0.101	1.072	2.25
D2	0.6286(2)	0.0283(2)	0.1328(1)	1.677	1.995	2.541	0.315	0.460	-0.279	2.07
D3	0.2017(2)	0.0647(2)	0.5051(2)	2.185	2.336	1.797	0.533	0.084	-0.122	2.11
D4	0.8365(3)	0.0547(2)	0.0534(2)	1.924	1.571	2.717	-0.268	0.472	0.967	2.07
D5	0.9796(3)	0.2322(1)	0.3741(1)	2.773	1.579	1.385	0.084	-0.013	0.035	1.91

Table 6.5
Comparison of bond lengths in ammonium bicarbonate between the values as measured on *HRPD* at 10 K (note, the sample was deuterated) and determined by DFT simulations, and a single crystal X-ray diffraction experiment by Pertlik, 1981 [111].

	This work						Pertlik, 1981 [111]		
	ab initio (0 K)			*HRPD* (10 K)			X-ray (295 K)		
	H···Y (Å)	X···Y (Å)	X-H···Y (°)	D···Y (Å)	X···Y (Å)	X-D···Y (°)	H···Y (Å)	X···Y (Å)	X-H···Y (°)
N1-H(D)1···O3	1.82536	2.85863	170.1575	1.855(3)	2.872(2)	168.2(3)	2.05(2)	2.894(3)	172.0(8)
N1-H(D)2···O3	1.88672	2.89022	161.9071	1.940(3)	2.917(3)	161.4(2)	2.05(3)	2.916(3)	166.6(7)
N1-H(D)3···O3	1.87316	2.89850	167.4873	1.893(3)	2.906(2)	168.0(3)	2.07(2)	2.942(3)	168.9(6)
N1-H(D)4···O1	1.75587	2.79585	169.9146	1.814(3)	2.818(3)	168.4(3)	1.91(2)	2.818(2)	169.3(7)
O2-H(D)5···O1	1.51189	2.54471	174.5428	1.587(2)	2.594(3)	173.8(3)	1.69(2)	2.596(2)	168.8(7)

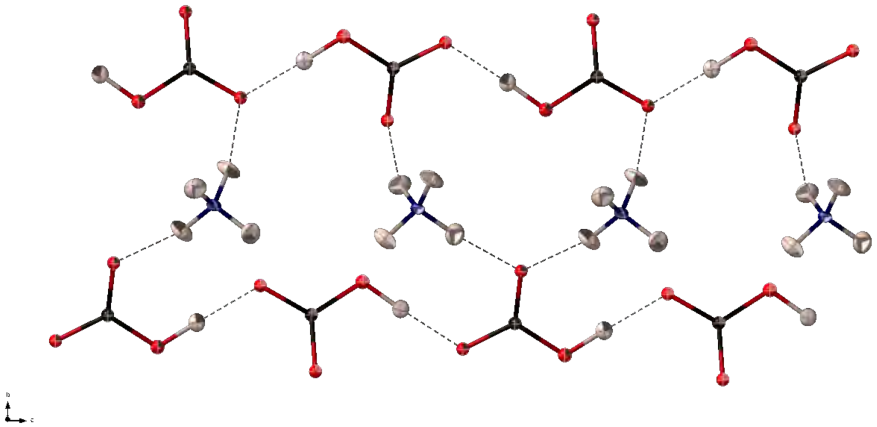

Figure 6.9
Chain motif in ND_4DCO_3 with atomic displacement ellipsoids drawn at the 50 % probability level, determined from the 10 K *HRPD* Rietveld refinement. The carbon and oxygen atoms were to be isotropic due to the low temperature of the measurement.

In the experimental structure, the D2···O3 bond is longer than the other two hydrogen bonds being accepted by the O3 atom. The D2···O3 bond is out-of plane to the chain motif, connecting to an ammonium tetrahedra in the next chain, creating a more three-dimensional hydrogen bonded structure. Although this bond length is predicted to be longer than the other two in the DFT relaxation, it is underestimated by 2.8 % compared to the experimental value.

The length of the O2···H(D)5 bond is much shorter than the other hydrogen bonds, with the highest linearity, therefore it is the strongest H-bond in the structure. This bond connects the HCO_3^- anions in a chain motif; Figure 6.9 depicts this chain motif of bicarbonate anions (HCO_3^-) running parallel to [001] with thermal displacement parameters (the carbon and oxygen atoms were set to isotropic due the very low temperature of the measurement).

6.3.2 High-pressure behaviour

6.3.2.1 Equation of state

A series of constant volume relaxations were performed over a volume range of 500 $Å^3$ to 740 $Å^3$ (corresponding to a pressure range between 12 GPa and -2 GPa). Plots of total energy against volume, *E(V)*, and pressure against volume, *P(V)*, are given in Figure 6.10, and the values of the fit to the E(V) and P(V) curves are given in Table 6.6.

There is an excellent agreement between the DFT simulations and the experimen-

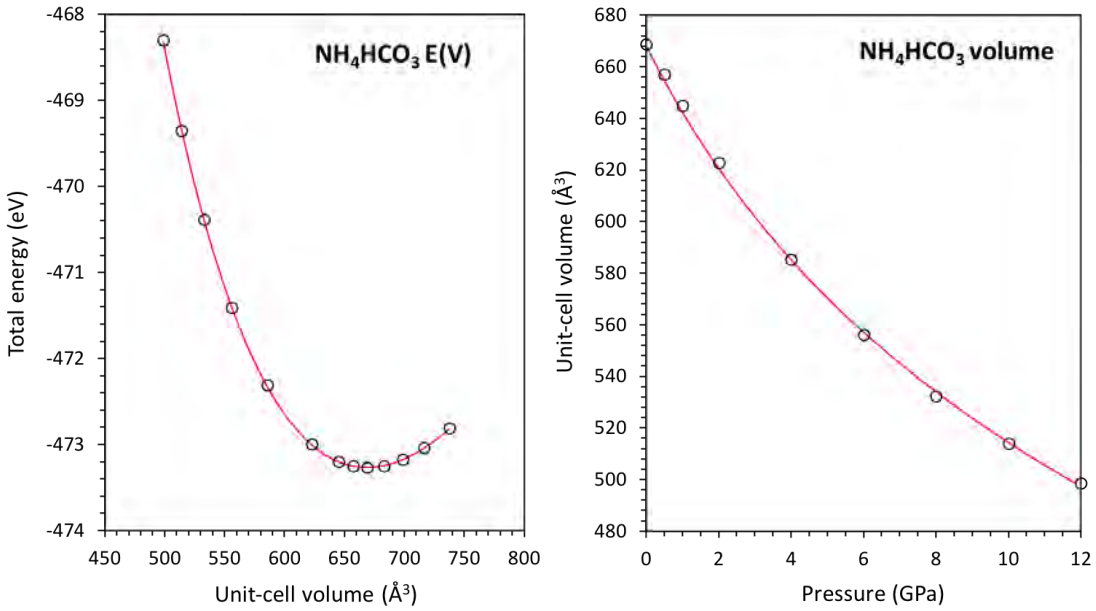

Figure 6.10
Calculated E(V) curve (*left*) and P(V) curve (*right*) of ammonium bicarbonate. The open circles are calculated points, and the solid line shows the best fit BMEOS3.

Table 6.6
Fitted EoS parameters to E(V) and P(V) curves of ammonium bicarbonate, using a BMEOS3 equation of state

	V_0 (Å^3)	K_0 (GPa)	K_0'	K_0'' (GPa^{-1})	E_0 (eV)
BMEOS3, E(V)	669.2(3)	23.6(2)	3.55(8)	-0.154(2)	-473.260(4)
BMEOS3, P(V)	668.5(9)	23.6(5)	3.7(1)	-0.156(5)	

tal values for the bulk modulus and its pressure derivatives of ammonium bicarbonate (see Table 6.7). During the high-pressure experiments on *PEARL*, an isothermal third-order Birch-Murnaghan equation of state was fitted to the high-pressure points of the ambient phase of ammonium bicarbonate for comparison with the equation of state fitted from *VASP*. The BMEOS3 was fitted to data points at 200 K, from 0.116 GPa to 4.468 GPa, with the bulk modulus set to freely refine and also $V_{0,200}$ set to that as measured on *HRPD* at 200 K. The volumetric bulk modulus from the DFT simulations is an excellent match to an experimentally obtained value of 20.8(1) GPa at 200 K, based upon an isothermal BMEOS3 fit. The value of K_0', however, is not such a good match, measured experimentally at 2.8(2) but fitted as $\sim$3.7. The pressure derivates are, for the most part, within errors of each other, and the bulk modulus - although outside of errors - allow for stiffening of the structure as T falls to zero.

There is also a good match between the relative variation of the experimental and

computational cell parameter values, as can be seen in Figure 6.11. Figure 6.11 shows the relative change in the unit-cell dimensions over the same pressure range, and over the full pressure range simulated, revealing a very similar behaviour in the unit-cell axes, albeit over a larger pressure range.

The agreement, qualitatively, is also extremely good for the elastic anisotropy; both the experiments and calculations agree that the *a*-axis is the most compressible, with the *b*-axis and *c*-axis very similar in compressibility, even showing that the *b*-axis compresses slower as a function of pressure below a few GPa, but then becomes more compressible at higher pressures. The structure of ammonium bicarbonate reveals layers of bicarbonate ions and ammonium ions running parallel to the *c*-axis, alternatively arranged along the *b*-axis. Weak hydrogen bonding between these layers along the *a*-axis means this direction is the weakest and hence most compressible.

Table 6.7
Comparison of the zero-pressure volumes, bulk modulus and it's pressure derivatives from fitting equations of state to ammonium bicarbonate based upon the high-pressure experiments on *PEARL*, the thermal expansion measurements on *HRPD* (used in the P-V-T fits), and from DFT simulations.

	Experiments on PEARL				DFT (athermal)	
	BMEOS3, 295 K	BMEOS3, 245 K	BMEOS3, 200 K	MILEOS P-V-T, 245 K	BMEOS3, E(V)	BMEOS3, P(V)
$V_{0,T}$	681.2(6)	675.2(7)	673.1(2)	676.3(2)	668.2(3)	668.5(9)
$K_{0,T}$	19.4(7)	20.9(9)	20.1(2)	19.7(2)	23.6(2)	23.6(5)
$K'_{0,T}$	2.8(6)	2.3(6)	3.1(1)	2.9(2)	3.55(8)	3.7(1)
$K''_{0,T}$	-0.21(4)	-0.24(6)	-0.187(2)	-	-0.154(2)	-0.156(5)

6.3.3 Thermal expansion

Measurements of the lattice parameters of deuterated ammonium bicarbonate (and contaminant deuterated ice *Ih*) were obtained from 10 - 300 K in 10 K increments. A simple 5^{th} order polynomial fit to the unit-cell volume, V = $AT^5 + BT^4 + CT^3 + DT^2 + V_0$, gives values $A = 1.2(1) \times 10^{-11}$ Å^5 K^{-5}, $B = -8.80(7) \times 10^{-9}$ Å^4 K^{-4}, $C = 2.0(1) \times 10^{-6}$ Å^3 K^{-3}, $D = 6(9) \times 10^{-6}$ Å^2 K^{-2}, $V_0 = 667.81(2)$ Å^3 ($R^2 = 99.991$ %).

In order to quantify the thermal expansion, two Debye models have been fitted to the unit-cell volume as measured on HRPD between 10 K and 300 K: the first, a single, first-order Debye model (see Chapter 5); the second, a single, second-order Debye

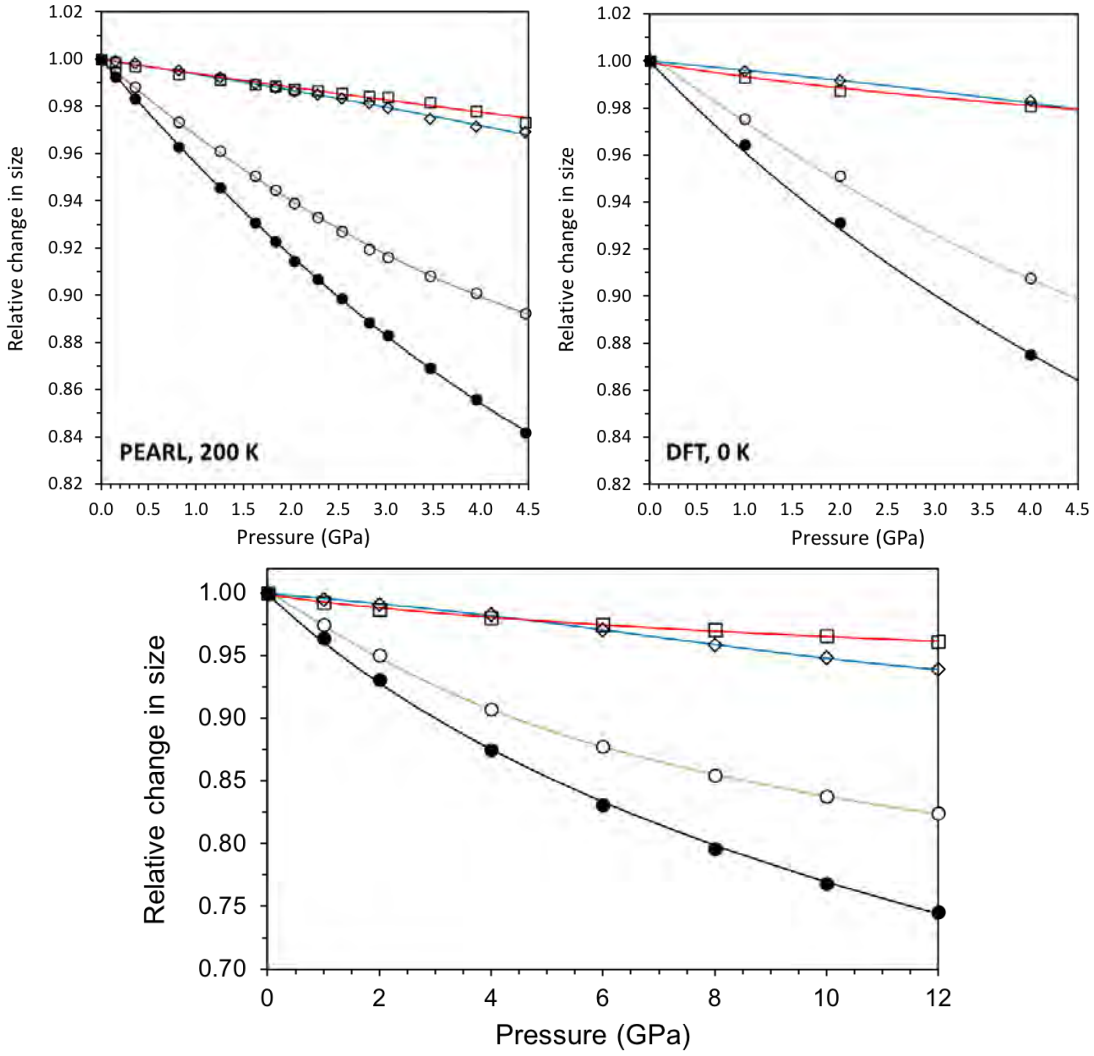

Figure 6.11
Comparison of the relative change of the unit cell dimensions with pressure of ammonium bicarbonate phase I (left panel) measured at 200 K and (right panel) from the DFT simulations. The lower panel shows the behaviour of ammonium bicarbonate phase I over the full pressure range simulated using DFT. The unit cell compresses more in the direction of the a-axis (green line, white filled circles) than the b-axis (blue line, white squares) or c-axis (red line, filled triangles), which matches *ab initio* calculations extremely well.

model. The following expression for the thermal expansion, in terms of the internal energy of the crystal to second order is [146]:

$$V(T) = \frac{V_0 U}{Q - bU} + V_0 \tag{6.1}$$

where $Q = V_0 K_0/\gamma'$ and $b = (K_0' - 1)/2$. The value γ' is a Grüneisen parameter, and K_0 and K_0' are the bulk modulus and its first derivative respectively. A second-order Debye model is used, as the first-order fit is poor; this is due to the first-order approximation being more valid at low temperatures where the change in volume is small (as was the case for α-ammonium carbamate), so the second-order is more appropriate over this larger temperature range. The values of the fitted parameters from both the first-order and second-order fits to the unit-cell volume are given in Table 6.8.

Since the Debye-type models of the thermal expansion are only dimensionally correct for the unit-cell volume, a different model is fitted to the lattice parameters to that used for the unit-cell volume of deuterated ammonium bicarbonate. There are a few models that could be used: a simple polynomial fit; a linear combination of a power-law and an exponential function; Einstein function model. In the absence of heat capacity measurements for deuterated ammonium bicarbonate, the relative simplicity of the Einstein model is preferable, while still providing some more meaningful parameters of the thermal expansion.

The lattice parameters of deuterated ammonium bicarbonate were fitted using the same equations as given in the previous Chapter (Eq's. 5.5 - 5.7). Values of the refined parameters from these fits are given in Table 6.9. The coefficients of the thermal expansion along each axis and the unit-cell volume were fitted with Eq. 5.7; plots of these fits are given in Figure 6.13.

Table 6.8
Parameters obtained by fitting a second-order single Debye model to the unit-cell parameters of ammonium bicarbonate between 10 K and 300 K.

	First-order	Second-order
V_0 (Å^3)	667.95(3)	667.865(5)
θ_D (K)	434(7)	344(3)
K_0 (GPa/γ)	45.0(5)	59.3(4)*
Q (J)	-	$3.10(3) \times 10^{-17}$
b	-	20.7(6)

* Derived from parameter Q

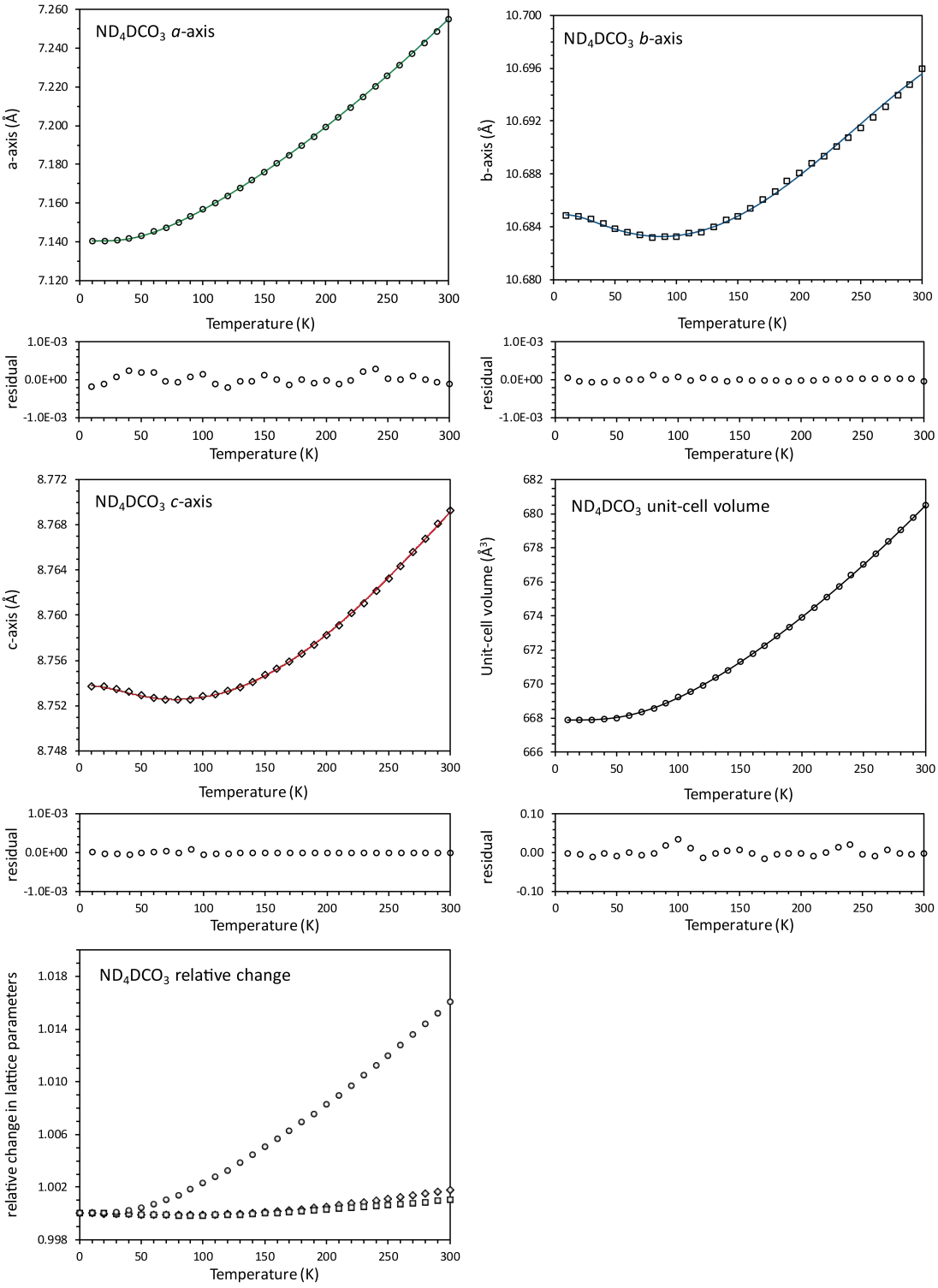

Figure 6.12
Refined unit-cell dimensions and unit-cell volume of ammonium bicarbonate from 10 - 300 K, measured on *HRPD*. The symbols and lines correspond to: (green line, open circles) *a*-axis; (blue line, open squares) *b*-axis; (red line, open diamonds) *c*-axis; (black line, open triangles) unit-cell volume. The fitted lines for the *a*-axis, *b*-axis, and *c*-axis are Einstein model fits (Eq 5.5 & 5.6) and for the unit-cell volume is a second-order Debye model. Values of the fits are given in Tables 6.9 & 6.8.

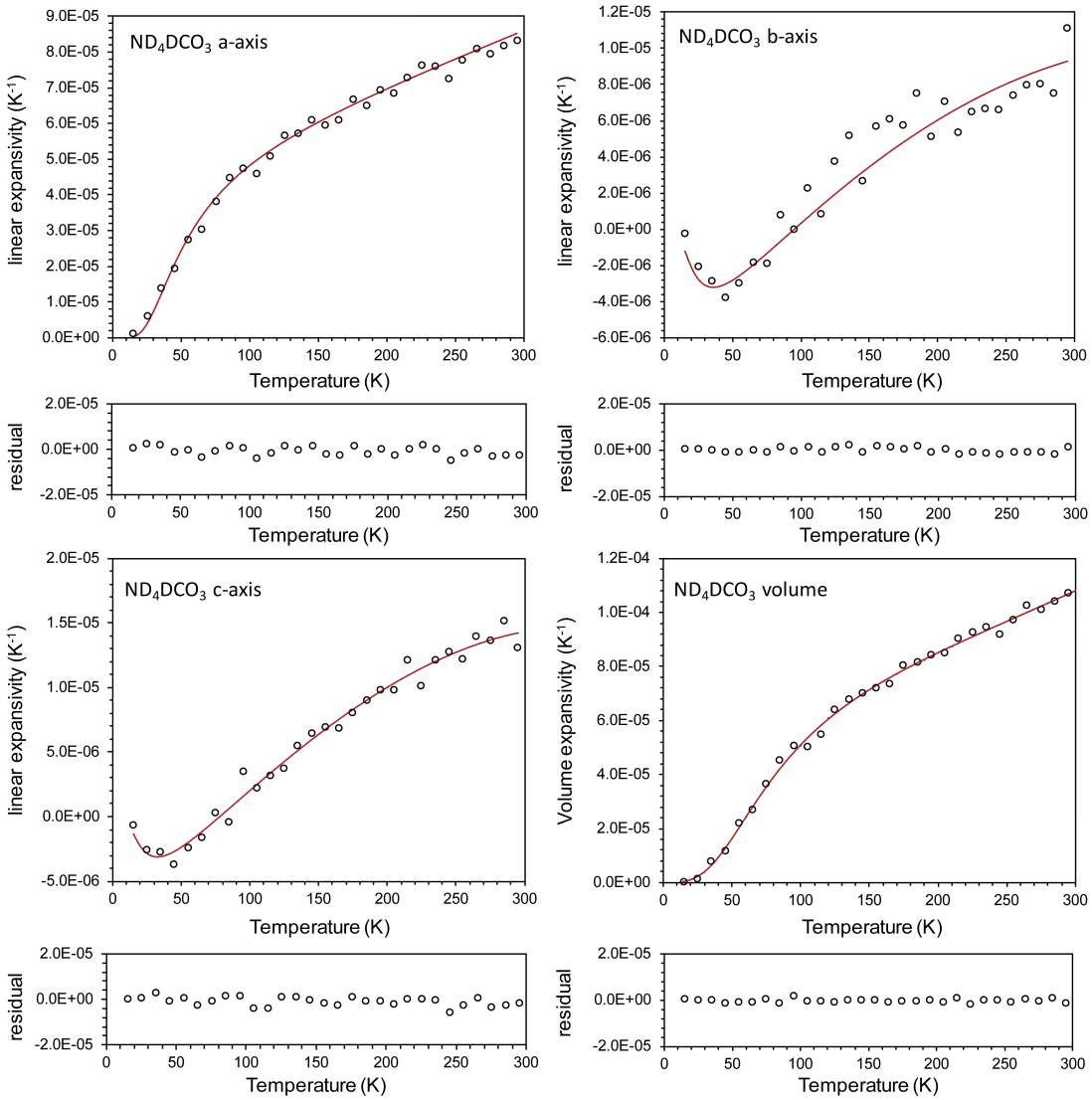

Figure 6.13
Linear and volume thermal expansion coefficients of ND_4DCO_3. The fitted lines for the *a*-axis, *b*-axis, and *c*-axis are Einstein model fits (Eq 5.7) and for the unit-cell volume is a second-order Debye model.

Almost all of the volumetric thermal expansion is due to the positive thermal expansion along the *a*-axis. The expansivity along the *b*-axis and *c*-axis is very small indeed (almost an order of magnitude smaller), and both show a small degree of negative expansivity at low temperatures (negative area expansivity, which is very uncommon); the *b*-axis has maximum negative expansivity at ∼36 K, transitioning to positive thermal expansion at ∼95 K; *c*-axis has maximum negative expansivity at ∼32 K, transitioning to positive thermal expansion at ∼78 K. The least expansion is seen in the *bc* plane due to chains of DCO_3^- ions that runs along *c*, and are linked along *b* via ND_4^+ ions, creating a rigid planar layer that resists expansion (see Figure 6.14). The greatest

Table 6.9
Parameters obtained by fitting a modified Einstein model to the unit-cell parameters of ammonium bicarbonate between 10 K and 300 K.

	a-axis	b-axis	c-axis	Volume
X_0	7.14066(8)	10.68492(7)	8.75376(3)	667.880(6)
θ_E	160(2)	70(10)	68(5)	220(2)
e_0	0.0548(2)	-0.0050(10)	-0.0041(4)	9.0(2)
e_1	$8.62(9) \times 10^{-5}$	$3.5(7) \times 10^{-5}$	$3.2(4) \times 10^{-6}$	0.0153(2)
e_2	-	$-3(1) \times 10^{-5}$	$5(9) \times 10^{-5}$	-
e_3	-	$-4.8(4) \times 10^{-4}$	$-4.0(3) \times 10^{-5}$	-
Adjusted R^2	0.99999	0.99983	0.99997	0.99999

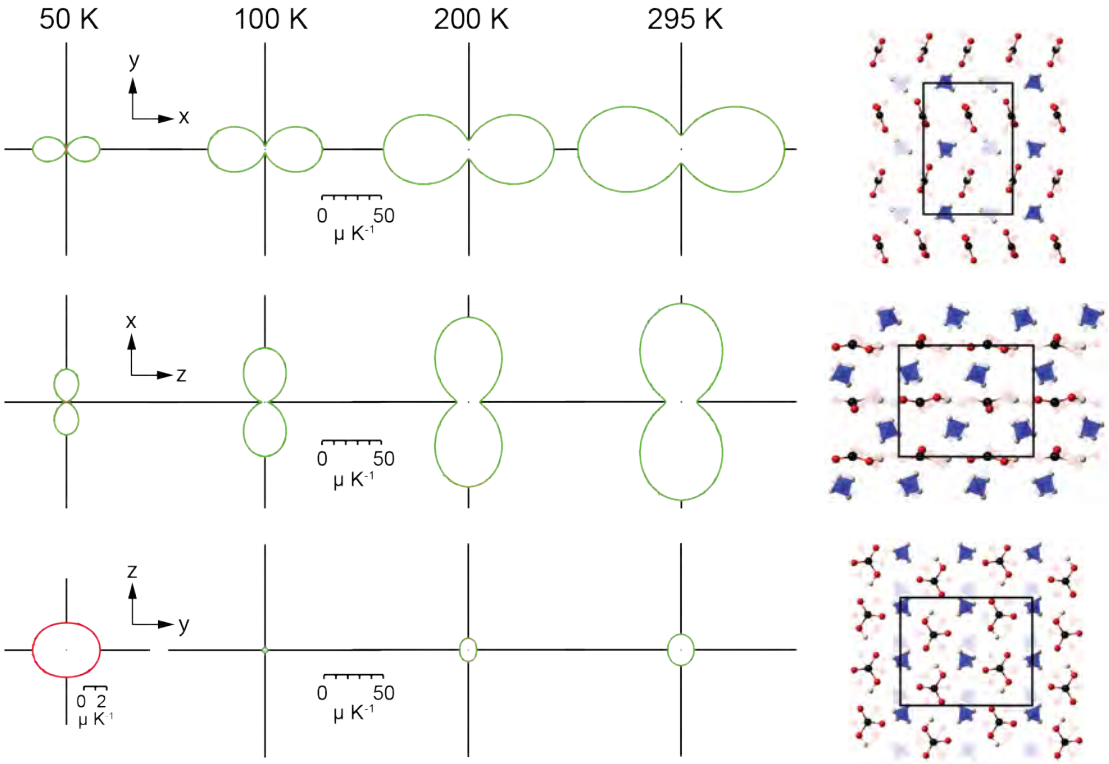

Figure 6.14
Projections of the thermal expansion coefficients of ND_4DCO_3 in the *x*-*y*, *z*-*x* and *y*-*z* plane at 50 K, 100 K, 200 K, and 300 K. The green lines indicates positive values, and the red lines indicates negative values. Projections of the corresponding structure are shown on the right. Note the projection in the y-z plane at 50 K is a different scale, due to the very small values of expansion coefficient.

expansion occurs between these planar layers, parallel to *a*.

Compared to D_2O ice I*h*, the volumetric thermal expansion of ND_4DCO_3 is greater below 117 K, at which the expansivity is the same for both ND_4DCO_3 and D_2O ice I*h*; ND_4DCO_3 expands less above this temperature.

Similar thermal expansion behaviour is seen here as in other compounds in the

$NH_3 + CO_2 \pm H_2O$ ternary system, in which there are two axes that are much stronger, and hence one large axis of expansion with the two others having much less expansivity. This is due to the generally layered character of the structures, with bonding between these layers via hydrogen bonds. Very similar thermal expansion behaviour is also seen in potassium bicarbonate $KHCO_3$ [4, 72, 79].

6.3.4 P-V-T equation of state

Using the high-pressure data collected on PEARL at 295 K, 245 K and 200 K, and also using the thermal expansion data acquired on *HRPD*, a P-V-T equation of state can be fitted to ND_4DCO_3. There is excellent agreement in the lattice parameters observed between the different instruments, allowing for both data sets to be used; all of the *PEARL* data have been used, and data from *HRPD* is limited to that between the maximum and minimum temperature values measured on *PEARL*, i.e between 200 K and 300 K.

The P-V-T data has been fitted using a Murnaghan integrated linear equation of state (MILEOS; [103]):

$$V_{P,T} = \frac{V_{0,T}}{\left[P\left(K'_{0,T}/K_{0,T}\right)+1\right]^{1/K'_{0,T}}} \tag{6.2}$$

where

$$V_{0,T} = V_{0,245} + x_1 T^* + x_2 T^{*2} + x_3 T^{*3} \tag{6.3}$$

$$K_{0,T} = K_{0,245} + \left(\delta K/\delta T\right)_p T^* \tag{6.4}$$

In the above equations, the temperature $T^* = T - 245$ K, $K_{0,T}$ is the isothermal bulk modulus, and $K'_{0,T}$ is the first pressure derivative of the bulk modulus. The reference value of T (245 K) was chosen to fall in the middle of the measured range to minimise errors around the boundary of the measured range. The MILEOS is fitted and chosen over the Birch-Murnaghan formulations due to this having an advantage in that the dependent variable easily chosen as V and not P, allowing for computation of the propagated error in V at any P, T point.

Equations 6.2 - 6.4 were fitted to the refined unit-cell volume of deuterated am-

monium bicarbonate; the fitted parameters are given in Table 6.10. A perspective view of the fitted surface as a function of P and T, with plots of the residuals, is shown in Figure 6.15.

Table 6.10
Parameters obtained by fitting a P-V-T equation of state to the lattice parameters of ND_4DCO_3. Data is from *HRPD* and *PEARL*.

	Unit-cell volume
$V_{0,245}$ (Å, Å^3)	676.3(2)
x_1	0.065(16)
x_2	3(1)E-4
x_3	4(7)E-6
$K_{0,245}$ (GPa)	19.7(2)
$\partial K/\partial T$ (GPa K^{-1})	-0.007(2)
$K'_{0,245}$	2.9(2)

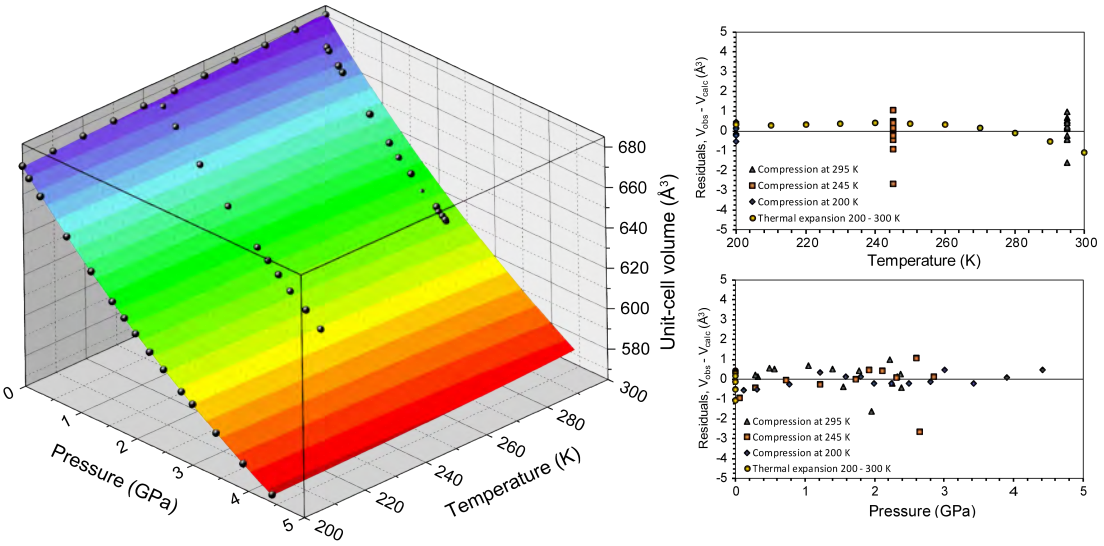

Figure 6.15
(*left*) Perspective view of the fitted P, T dependence of the unit-cell volume of deuterated ammonium bicarbonate; data points are shown as filled circles. Surface contours are in increments of 5 Å^3. (*right*) The residuals as a function of pressure and temperature.

6.3.5 Planetary parameters

Seeing how the density varies as a function of pressure in ammonium bicarbonate is important and needed for planetary modelling. The density is fitted as a function of pressure for use with a Birch-Murnaghan equation of state, Eq. 3.1, with $x = \rho/\rho_0$. The fit is given in Figure 6.16 and the parameters are given in Table 6.11.

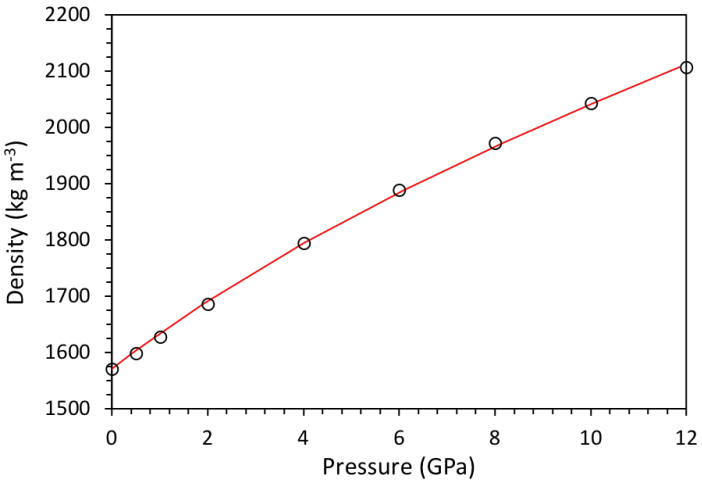

Figure 6.16
Fitted density profile as a function of pressure of ammonium bicarbonate

Table 6.11
Fitted equation parameters to the plot of density as a function of pressure for ammonium bicarbonate in the athermal limit

	K_0 GPa	K_0'	ρ_0 kg m^{-3}
BMEOS3, ρ	23.5	3.69	1570.0

6.3.6 Phase II

During the course of the first experiment on *PEARL*, three[1] new phases of d_8-ammonium bicarbonate were identified as a function of pressure and temperature. Due to the large steps in pressure and anisotropically behaving crystal structures, it is difficult to discern the difference between a new phase and a compressed sample.

The evidence for the first phase transition began at a pressure of 2.26(8) GPa (at a load of 185 bar) during Loading I. Over the course of several shorter runs, where the load was slowly increased from 185 bar to 245 bar in 10 bar increments to help induce the transition, peaks from the ambient phase disappeared and were replaced by the new phase. Once it was certain the old phase had completely disappeared, at 2.73(8) GPa (at a load of 245 bar), a long count was initiated.

To aid with indexing, *PEARL* can measure out to a d-spacing of ~ 8 Å, albeit with significantly longer counting times; counting times are longer in the longer time frame window because only 1/4 of the beam from target station 1 is collected, and the wavelength distribution of neutrons means that the neutron intensity is much lower at these

[1] Initially it was thought there were four new phases, but phase III appears to be compressed phase II.

longer wavelengths. However, the ability to measure out this far in *d*-spacing allows measurement of lower *hkl* values to better determine the indexed unit-cell metric and identify any systematic absences. For example, Figure 6.17 shows the diffractogram using the 'normal' window, but when the longer time frame window is used, an additional peak can be seen around 5.2 GPa.

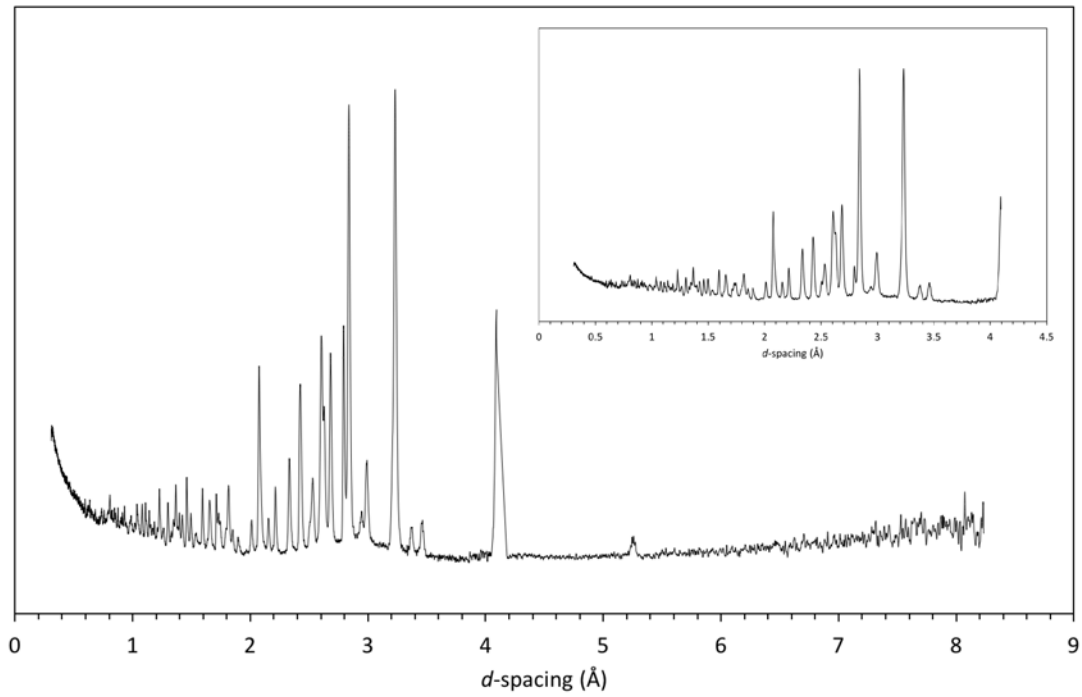

Figure 6.17
Phase II, *PEARL*. Includes contributions from lead, and the anvils (alumina and zirconia). This pattern is two windows stitched together: the inset pattern from 0.3 - 4.1 Å is the regularly used window; from 4.1 - 8.3 Å is the long time frame window.

To characterise this new phase, peak positions from the new phase were inputted into the crystallographic indexing program *DICVOL06* [18]. Careful attention was paid to ensure the peaks were only from the new phase only and not from other peaks of lead, alumina and zirconia. This was done by stack plotting diffraction patterns as the pressure was increased from 2.26(8) GPa upwards, and observing which peaks were moving and which peaks remained stationary - peaks from the anvils do not move in d-spacing as a function of pressure, and contributions from the lead amount to only three peaks in the usable diffraction pattern and therefore are easily identified and eliminated.

Two options were offered from indexing 17 peaks, both with similar unit-cell values to the ambient pressure phase but with the *a*-axis halved. The best solution was an orthorhombic unit-cell, with a = 3.39859 Å, b = 10.58048 Å, c = 8.25134 Å, V

= 296.71 Å^3, with figures of merit based upon the inputted 17 peaks M(17) = 33.0 and F(17)=30.6. The second was a monoclinic solution with essentially the same orthorhombic cell but with a β-angle close to 90 °. Since the angle is close to 90 °, and the ambient phase is an orthorhombic cell with the *a*-axis doubled, this solution was not investigated further.

Once the indexing was complete, an attempt was made to solve the structure of this new phase. To do this, the program *FOX* (Free Objects for Xstallography) [47] was used, which is an *ab initio* structure determination software package. Here, atoms can be placed in a unit-cell and models can be run from a guessed starting point to find the best fit against the measured diffraction pattern, using simulated annealing or parallel tempering multiple times to achieve the lowest possible cost and therefore, the most likely crystal structure. To improve the chances of finding the structure, a NH_4^+ ion and HCO_3^- ion were imported into the program and given fixed geometry, so as to keep the constituent parts of the structure from falling apart.

Due to a peak right at the end of the diffraction pattern at 2.26(8) GPa, $\sim$ 4 Å, the diffraction pattern used to determine the structure was measured at 4.4(1) GPa, with the unit-cell adjusted to fit the higher pressure, since F.O.X. was struggling to fit the peak intensity with a peak so close to the end. A few possible answers were output (space groups $Pmc2_1$ and $P2_12_12_1$), but the best was a unit-cell with space group $Pbc2_1$. The structure is similar to that of the ambient phase, with chains of HCO_3^- running parallel to *b* (*c* in the ambient phase) with NH_4^+ ions joining these chains together (Figure 6.18). However, the structure is repeated along *a* with no glide unlike in the ambient phase.

Once a sensible structure was found, it was imported into *VASP* in order to relax the atoms and check the veracity of the structure solution.

During the experiment on PEARL, a diffraction pattern of the new phase, measured at 245 bar at room temperature, was counted for $\sim$7 hours. Since this long-counted dataset contains greater detail in the low d-spacings of the diffraction pattern required for an accurate structure refinement, this was used for refinement using GSAS. Since the structure was found at 4.4(1) GPa, and the long-counted data set was at 2.73(8) GPa, a LeBail refinement of the unit-cell was necessary to correct for the unit-cell dimensions. Once the dimensions were found, the unit-cell of the newly-found

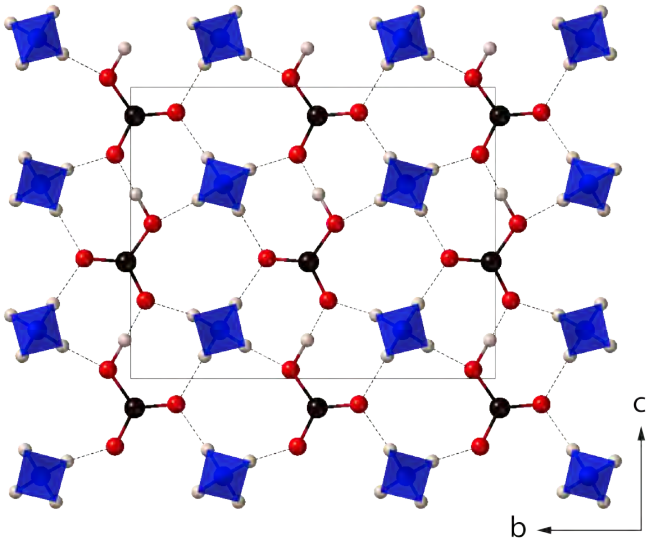

Relaxed structure from VASP.

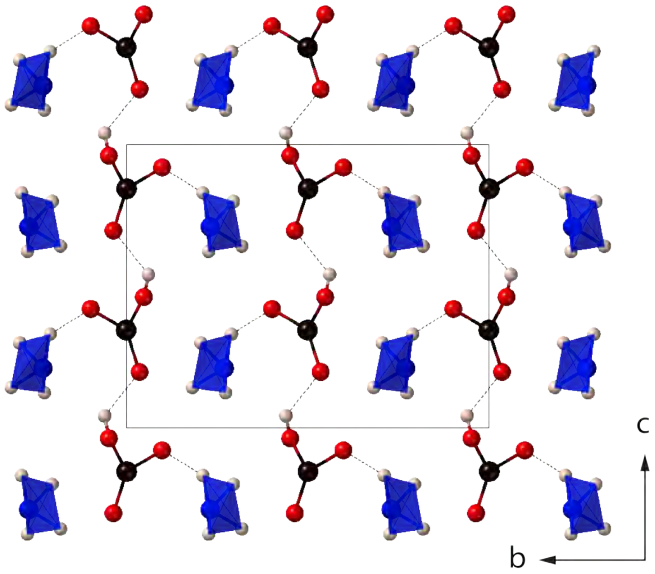

From Rietveld refinement of the structure at 2.7(2) GPa.

Figure 6.18
Possible crystal structure of ammonium bicarbonate phase II, $Pbc2_1$. The solid black line is the unit-cell outline, and the dashed lines are hydrogen bonds. The structure is similar to the ambient phase, with chains of HCO_3^- running parallel to *b* instead of *c*.

structure was adjusted, and then imported into *VASP* ready for a structure relaxation. In this, the unit-cell was kept at a fixed size, since the unit-cell dimensions are correct, but the atoms allowed to move. A k-points grid of 6x2x3, with 6 unique $\vec{k}$-points, and energy cut-off 1400 eV was used. The output from *VASP* was imported into *GSAS* for structure refinement.

As a starting point, values for U_{iso} and peak profile parameters were taken from the ambient phase. The structure required constraints to bond lengths and angles initially to stop the structure from becoming too distorted. The restraints were slowly relaxed until they were dropped completely and the structure allowed to freely refine. The overall fit to the data is excellent (Figure 6.19), although this has come at the expense at the distortion to the ammonium tetrahedra (structural parameters of this phase are given in Table 6.12).

Table 6.12
Structural parameters ammonium bicarbonate II

Ammonium bicarbonate

Formula	NH_4HCO_3	Lattice parameters	
Space group	$Pbc2_1$	*a*-axis (Å)	3.38525(6)
Z	4	*b*-axis (Å)	10.5456(4)
ρ (kg m^{-3})	1902.1	*c*-axis (Å)	8.2256(3)
Temperature (K)	295	Volume (Å^3)	293.650(6)

Label	Fractional coordinates			U_{iso}	Site
	x	y	z	(x10^2)	
C1	0.7500(30)	0.9995(16)	0.8499(17)	3.112	4a
N1	0.126(4)	0.2713(15)	0.7108(20)	1.708	4a
O1	0.994(4)	0.9005(17)	0.9181(18)	2.579	4a
O2	0.509(5)	1.0593(18)	0.9662(27)	2.579	4a
O3	0.563(5)	1.0344(17)	0.6994(20)	2.287	4a
D1	0.101(5)	0.2088(16)	0.7961(25)	2.726	4a
D2	-0.091(4)	0.1829(16)	0.6452(20)	2.726	4a
D3	-0.011(5)	0.2853(16)	0.8300(19)	2.726	4a
D4	0.316(5)	0.2752(15)	0.6211(16)	2.726	4a
D5	0.563(5)	1.0593(18)1	1.0394(18)	0.078	4a

6.3.6.1 Behaviour under pressure

This structure has been used to refine the diffraction patterns of phase II up to pressures of 5 GPa, with the lattice parameters as a function of pressure given in Figure 6.20. The behaviour, unsurprisingly, is very similar to that of the ambient phase, due to the similarity of both structures. At pressures higher than 5 GPa, the fit to the data drops in

quality; this could be indicative of a further phase transition, but it is also possible that the large pressure change between runs distorts the structure sufficiently to make fitting difficult, especially with the anisotropy in the lattice parameters observed.

The structure was also simulated under pressure to compare the computed behaviour to the experimental behaviour. Static DFT calculations (see section 3.1.1) were carried out to determine an equation of state. Convergence tests were carried out to optimise the $\vec{k}$-point sampling of the Brillouin zone within the Monkhorst-Pack scheme and the kinetic energy cut-off of the plane-wave basis set. A grid of 6x2x3, with 6 unique $\vec{k}$-points ($\sim$0.04 Å^{-1} reciprocal lattice spacing), and energy cut-off 1400 eV yielded total energy convergence better than 10^{-3} eV per unit-cell.

The BMEOS3 fit to the data gives $V_{0,0} = 330.7(4)$ Å^3, $K_0 = 14.1(3)$, $K_0' = 7.9(2)$, $K_0'' = -1.6(2)$ can be seen in Figure 6.21. The computationally calculated behaviour agrees well with the experimental behaviour, with the a-axis the most compressible.

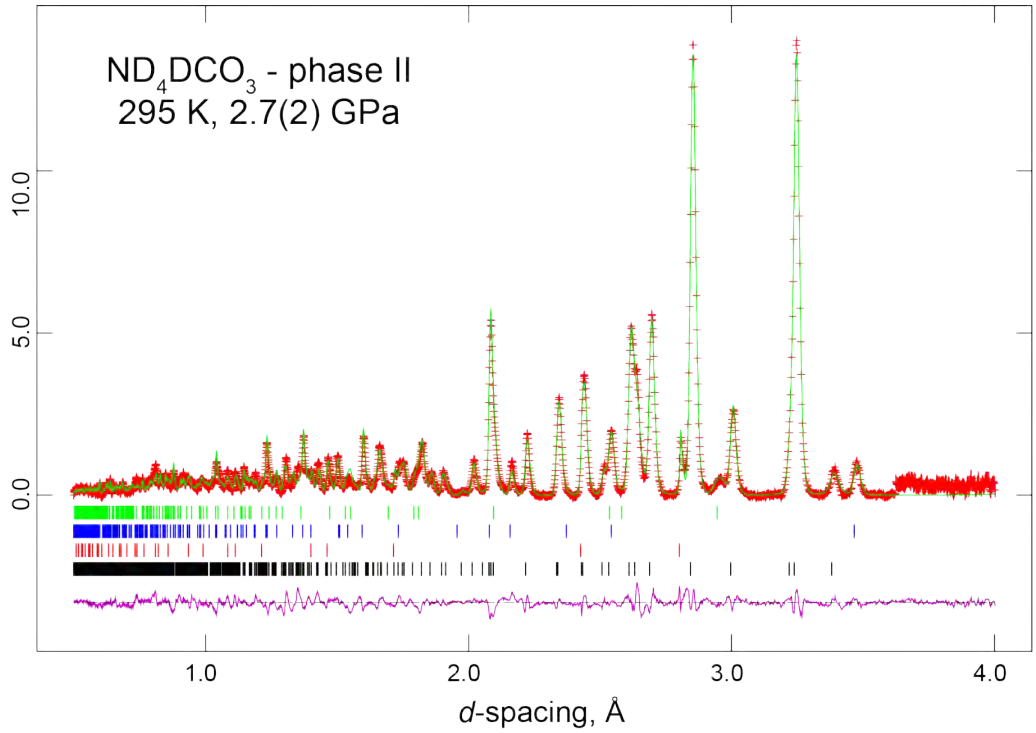

Figure 6.19
Neutron powder diffraction pattern of ND_4DCO_3 phase II, measured at 295 K and 4.4(2) GPa on *PEARL*. Red pluses represent the measured data, the solid green line the result of Rietveld refinement, the purple line the difference profile, and the tick marks the expected positions of each Bragg reflection for: (black) ND_4DCO_3 phase II; (red) lead; (blue) alumina anvils; (green) zirconia.

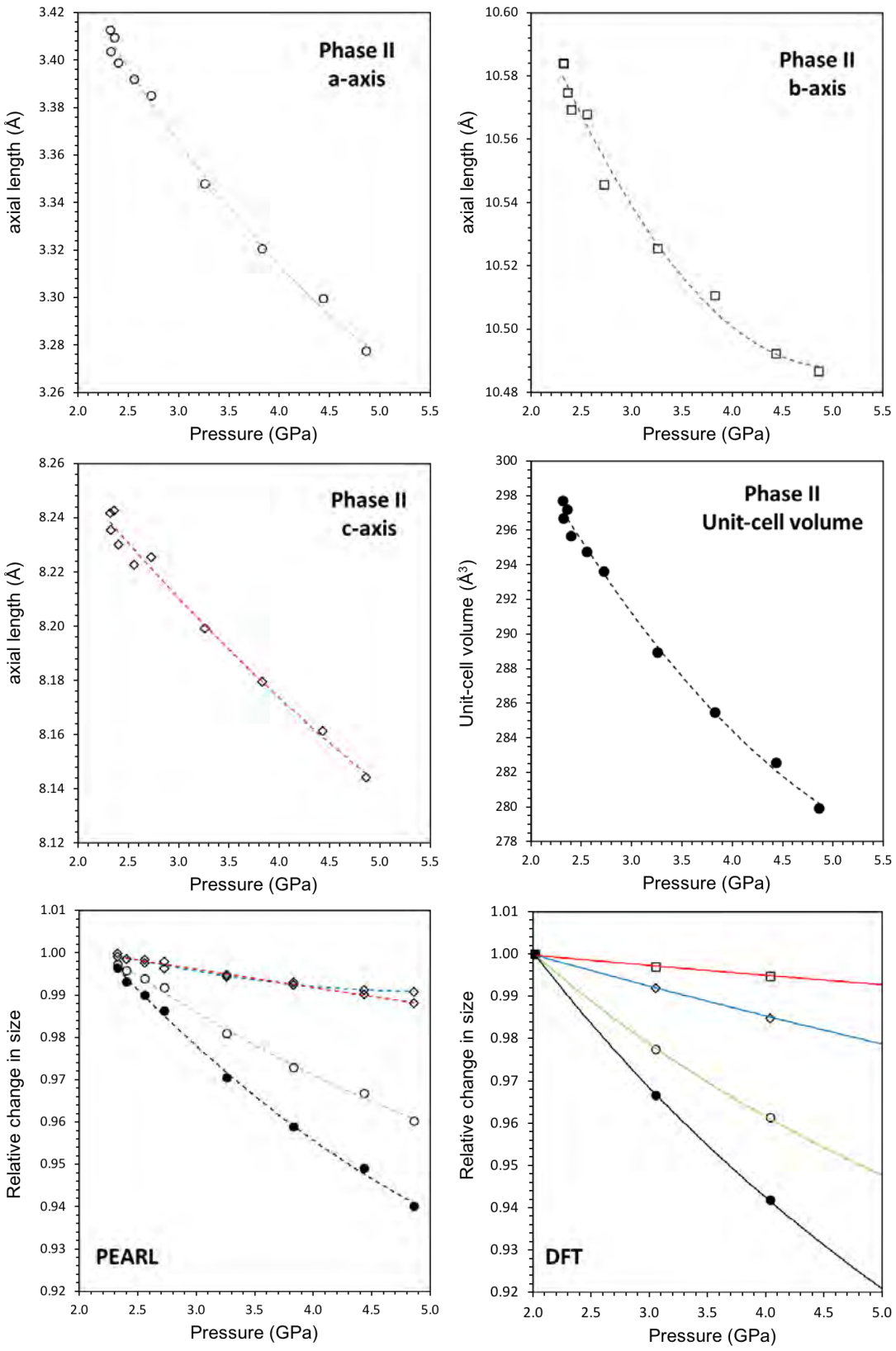

Figure 6.20
Lattice parameters of ammonium bicarbonate phase II as a function of pressure, fitted to the 295 K data from *PEARL*. The scatter of the points comes from the difficultly in fitting of the lead to obtain the sample pressure. The relative change of the lattice parameters is compared in the bottom two panels between the experimental values (left) and the computational values (right).

6.3.6.2 Relative stability

The unit-cell volume of the ambient phase at 2.39(8) GPa is 612.4(1) Å^3 (Z = 8), and phase II at the same pressure is 296.7(1) Å^3 (Z = 4). The volumetric change corresponds to a 3.1 % change between the two phases

To test the veracity of the structure solution, the proposed ammonium bicarbonate phase II structure was input into VASP and an energy - volume curve was produced to see if the curve crosses that of the ambient phase, which would suggest a phase transition. The result, seen in Figure 6.21, shows the two curves do indeed cross, suggesting a phase transition at pressure. The slope of the common tangent to the two curves gives the transition pressure, and is found to be 2 GPa; the experimental transition pressure at 295 K was ∼2.3 GPa.

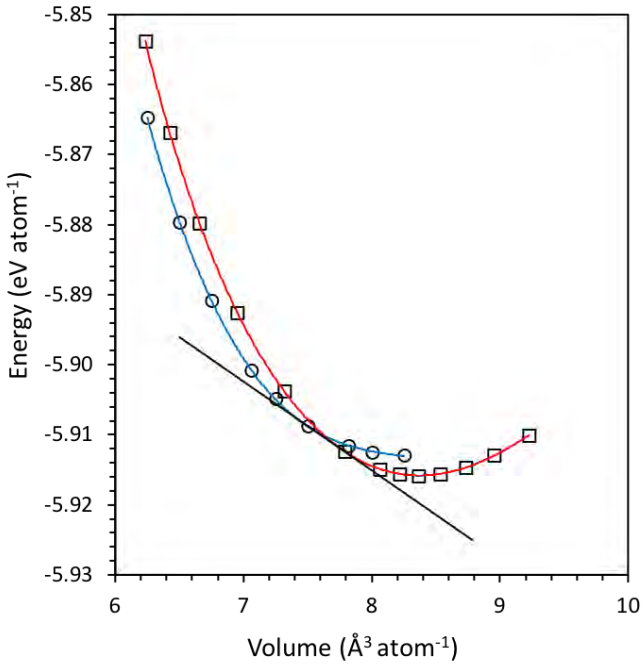

Figure 6.21
Internal energy vs volume for ammonium bicarbonate phase I (red line, open squares) and phase II (blue line, open circles). Calculated values are indicated by points, the lines being BMEOS3 fits. The common tangent to the curves for indicates that phase II will be stable for pressures greater than 2 GPa (for details see text).

6.3.7 Further phase changes

6.3.7.1 Second phase transition

The second phase transition was observed during the second loading, where the sample was compressed at 200 K, occurring at a pressure of 4.42(9) GPa. An attempt has been

made to index the structure, using the same methods as applied to the first phase transition, but since the phase transition occurs towards the upper end of the usable pressure range, the signal from the sample has decreased relative to the sample environment due to the closing of the anvils, and hence no reliable solution has yet been found.

6.3.7.2 Final phase transition

The final transition observed was at the end of the second loading, when warming the sample at maximum load available during the experiment, at 450 K and $\sim$ 4.3(2) GPa. It is not obvious that this is a new phase observed; it could be that the sample is highly anisotropic and warming 50 K has shifted the peaks sufficiently to appear to be a new phase.

6.3.7.3 Summary of phase transitions

In addition to the previously known ambient P/T phase, a further three phases were observed during the course of the high-pressure experiments conducted on PEARL. An attempt is made of the phase diagram of d_8-ammonium bicarbonate, which is very much a work in progress. Much work is needed to characterise these new phases, and map the phase transitions as a function of pressure and temperature. It is possible some of the newly discovered phases may be the same phase occurring over a range of temperatures and pressures, but the diffraction patterns may be changing sufficiently between runs that it could look like a new phase rather than a distorted version of the same phase.

6.4 Chapter summary

This chapter has given details of two experiments investigating the behaviour of deuterated ammonium bicarbonate, under conditions of variable temperature and/or pressure. The behaviour matches extremely well to the *ab initio* calculations performed previously. Several new phases of ammonium bicarbonate were observed as a function of temperature and pressure, with work ongoing to solve the structure of these new phases.

The large degree of anisotropy of the unit cell found in ammonium bicarbonate phase I matched extremely well between calculated and experimental results. The

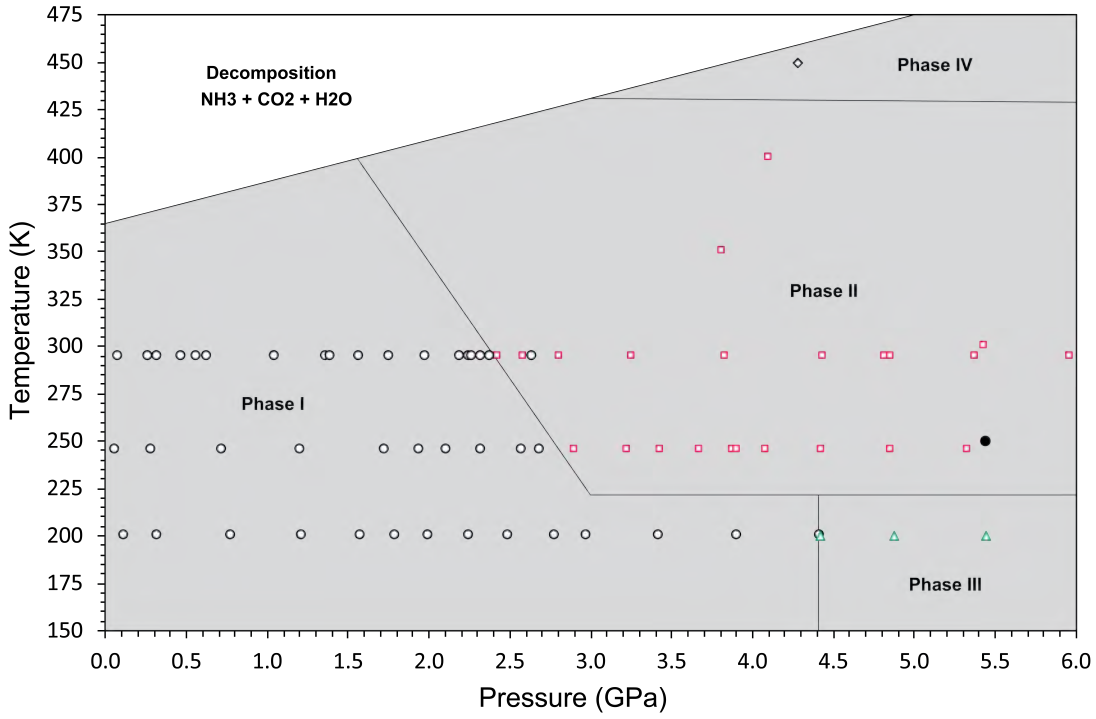

Figure 6.22
Proposed phase diagram of deuterated ammonium bicarbonate, from three experiments from *PEARL*. The melting line is an extension from its decomposition temperature (60 °C) at ambient pressure. Each of the markers corresponds to (*white circles*) phase I, (*red squares*) phase II, (*green triangles*) phase III, (*white diamond*) phase IV. The larger black circle is a measurement when warming from 200 K, yielding a slightly different diffraction pattern from phase II, but it is hard to say whether this constitutes a new phase or more simply distorted phase II. The phase boundaries are set to where the new phase appears - in the case of the transition from I $\rightarrow$ III, the new and old phase coexist together for $\sim$0.5 GPa.

equations of state determined both experimentally and computationally also match extremely well. During the experiment, several new phases were observed. A possible crystal structure of a high-pressure phase of ammonium bicarbonate, phase II, is presented. Work is on-going to index and characterise these new phases.

The work here has provided a range of values that could be used in modelling the behaviour of ammonium bicarbonate as a function of pressure and temperature. The complex high-pressure behaviour as a function of pressure and temperature is important to further constrain so that the polymorphism can be accurately incorporated into planetary models. Negative area thermal expansion was observed at low temperature in the ambient phase, which is extremely rare in materials, and could have some novel uses. The stability of this compound at room temperature means this compound will be produced in carbon-capture processes using ammonia solutions, since cooling of the

capture fluid is expensive. Therefore, the end product of the reaction of ammonium and carbon dioxide will likely produce ammonium bicarbonate - therefore understanding the material properties of ammonium bicarbonate is important.

Chapter 7

Conclusions and future work

There were two primary aims of this work: to calculate and measure the bulk properties of solids in the NH_3 + CO_2 $\pm$ H_2O ternary system *in silico* using DFT and neutron diffraction techniques, and to improve the understanding of the materials that may be present in the icy moons in the solar system by providing values necessary for use in planetary models. The work completed includes: calculations of compounds with reported crystalline structures in the ternary system; thermal expansion measurements of ammonium bicarbonate and α-ammonium carbamate; measurements of the high-pressure behaviour of ammonium bicarbonate and α-ammonium.

7.1 Discussion

7.1.1 Hydrogen bonded systems and *ab initio* simulations

The DFT simulations predicted the high-pressure behaviour and the anisotropy of the unit-cells observed in the ammonium carbonates before conducting experiments. However, although the behaviour was correctly predicted, the zero-pressure values in some instances were greatly overestimated compared to the experimental values, resulting in an under-estimated bulk modulus and affecting which phase was the most stable in compounds with more than one phase.

The importance of including a dispersion correction in the DFT simulations of materials containing hydrogen bonds has shown to be a big factor in the simulations in this work. Standard DFT methods can seriously underestimate cohesive energies in dispersion dominated structures due to the lack of dispersion interactions, translating as overestimated unit-cell volumes. The dispersion correction has improved, to varying

degrees, the zero-pressure volumes of each of the compounds in this ternary system (see Table 7.1). The best dispersion correction does not apply to all of the carbonates universally - the corrections were based upon the closest value to the zero-pressure low temperature values available either from this work or from literature values.

Interestingly, ammonium carbonate has a degree of over-binding associated with the dispersion corrections, although the magnitude is very small, at less than 1 % zero-pressure unit-cell volume. Although it appears, at first sight, that ammonium sesquicarbonate suffers the same over-binding issue seen ammonium carbonate monohydrate, this issue is due to a lack of experimental values, in particular low-temperature measurements. Since it is expected that the unit-cell volume will be smaller at cooler temperatures, it seems that this issue may be due to a lack of knowledge of the thermal behaviour of this material. Indeed, based upon the measurement at 40 K, the unit-cell volume is indeed smaller, around 1180 $Å^3$ (see Appendix B). A study to measure the thermal expansion of ammonium sesquicarbonate monohydrate would prove if this is the case.

Interestingly, the same behaviour in the lattice parameters is seen both with and without dispersion correction in materials. The biggest difference arises from the much better estimation of the unit-cell volume at a given pressure, changing the pressures at which certain behaviours are observed. For example in ammonium carbonate monohydrate without dispersion, the pressure of the onset of negative linear compressibility begins is around 5 GPa, but inclusion of a dispersion correction lowers this onset to 2-3 GPa.

To present the importance of including dispersion correction in certain hydrogen-bonded systems, a brief summary will be covered of the results of simulating the behaviour of the two phases of ammonium carbamate and the three phases of urea without the inclusion of a dispersion correction. These two systems showed greatly overestimated zero-pressure unit-cell volumes compared with available experimental data in the literature and from this work. The reader should refer to the chapters concerning ammonium carbamate (Chapter 5) and urea (Chapter 4) for the results including a dispersion correction, which, in these two cases especially has dramatically increased the accuracy of the DFT simulations.

Table 7.1
Comparison of dispersion corrected and non-dispersion corrected DFT simulations of the ammonium carbonates

	Non-dispersion corrected		Dispersion corrected	
	Volume	%	Volume	%
Ammonium carbonate monohydrate	610.00 Å^3	+3.07 %	589.43 Å^3	−0.3 %
Ammonium sesquicarbonate monohydrate[1]	1254.5 Å^3	+4.4 %	1194.40 Å^3	−0.4 %
Ammonium bicarbonate	708.3 Å^3	+5.7 %	668.92 Å^3	+0.2 %
α-ammonium carbamate	803.02 Å^3	+9.5 %	743.77 Å^3	+1.4 %
β-ammonium carbamate[2]	770.16 Å^3	+11.3 %	713.89 Å^3	+3.1 %
Urea I	155.87 Å^3	+7.2 %	144.971 Å^3	+0.1 %
Urea III	323.16 Å^3	+16.8 %	273.220 Å^3	+1.7 %
Urea IV [3]	154.82 Å^3		143.27 Å^3	

[1] Only one measurement, measured at 173(2) K and ambient pressure
[2] Only one measurement, measured at 298 K and ambient pressure
[3] Closest measurement is at 296(1) K and 3.10(5) GPa

7.1.1.1 Ammonium carbamate, α & β

The zero-pressure values without a dispersion correction included in the simulation gives unit-cell volumes of ∼820 Å^3 and ∼760 Å^3 for α-ammonium carbamate and β-ammonium carbamate respectively. The unit-cell volume of α-ammonium carbamate measured at 4.2 K - from the experiment described in Chapter 5 - is 733.225(9) Å^3. The difference therefore between the calculated and experimental unit-cell is significant, approximately 10 %. This large discrepancy between calculated and experimental values was also apparent for β-ammonium carbamate; the unit-cell measured at 298 K is 691.8 Å^3. Compare this to the calculated value of ∼765 Å^3, a difference once again of ∼10 %.

The issue with an over-estimated zero-pressure volume is that the unit-cell volume is over-estimated as a function of pressure, which reduces the bulk modulus. When dealing with a single phase this is not too problematic, although the elastic parameters are lower than the real values, but when working with a multiphase system it is important to consider this as it will also affect the relative stability.

In this instance, the dispersion correction in the DFT simulations has changed the bulk elastic properties of each phase (Table 7.2); the volumetric bulk modulus in this instance has almost doubled in value with the dispersion corrected calculations - from

Table 7.2
Fitted EoS parameters to the E(V) and P(V) curves of (top) α-ammonium carbamate and (bottom) β-ammonium carbamate, using the BMEOS3 equation of state. Dispersion corrected involved using Tkatchenko-Scheffler (TS) dispersion correction.

	DFT		Dispersion-corrected DFT		SXD
	BMEOS3, E(V)	BMEOS3, P(V)	BMEOS3, E(V)	BMEOS3, P(V)	BMEOS3, 200 K
α-ammonium carbamate					
$V_{0,T}$ (Å^3)	821.9(6)	815(3)	734.7(6)	741(2)	743.3(3)
$K_{0,T}$ (GPa)	9.42(7)	10.1(2)	16.0(3)	16.2(5)	14.4(9)
$K'_{0,T}$	5.59(5)	5.3(1)	5.35(9)	5.1(1)	8(4)
$K''_{0,T}$ (GPa^{-1})	-0.85(2)	-0.68(4)	-0.44(3)	-0.38(4)	-2(3)
β-ammonium carbamate					
$V_{0,T}$ (Å^3)	764.1(4)	766(2)	711.6(2)	714.5(4)	
$K_{0,T}$ (GPa)	13.9(2)	14.6(4)	23.3(1)	23.5(2)	
$K'_{0,T}$	6.6(2)	5.6(1)	4.51(8)	4.30(8)	
$K''_{0,T}$ (GPa^{-1})	-0.95(2)	-0.47(4)	-0.200(8)	-0.182(7)	

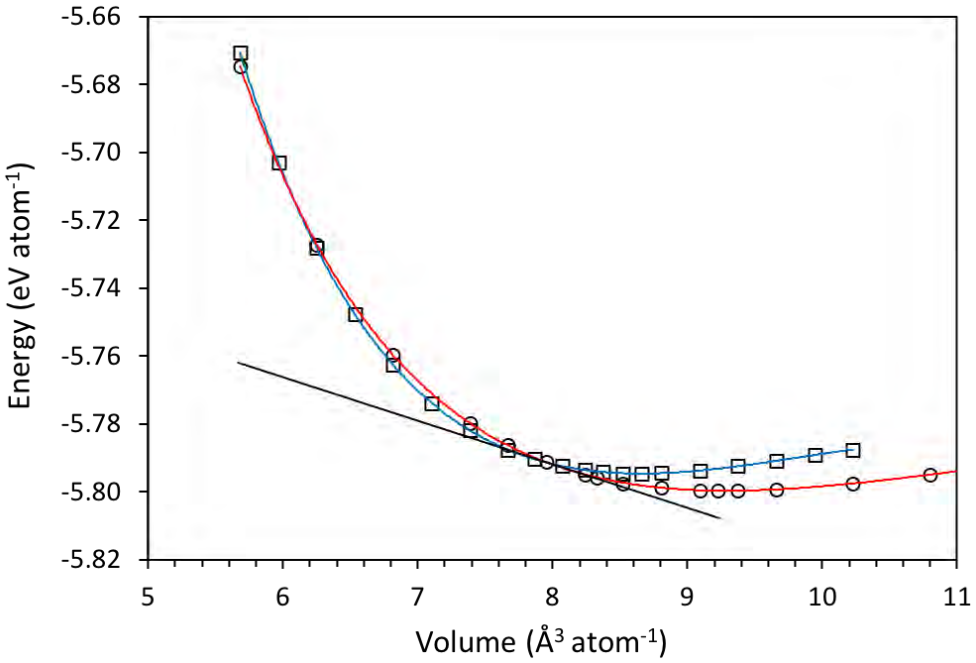

Figure 7.1
Calculated E(V) curves (without a dispersion correction) of α-ammonium carbamate (red line, open circles) and β- ammonium carbamate (blue line, open squares). The common tangent to the curves indicates that β-ammonium carbamate will be stable for pressures greater than 2 GPa.

∼10 GPa to ∼16 GPa for α-ammonium carbamate and from ∼14 GPa to ∼24 GPa for β-ammonium carbamate. The other significant result of including dispersion correction is the change of the relative stability of the two polymorphs. Without a dispersion correction, the α-carbamate is still the thermodynamically stable phase at 0 K, but the common tangent to the two curves suggests a transition pressure to β-ammonium car-

bamate of $\sim$ 2 GPa - compare this with the dispersion corrected calculations, which give a transition pressure of $\sim$0.4 GPa (Figure 7.1).

7.1.1.2 Urea

As was the case for both phases of ammonium carbamate, the zero-pressure volumes for DFT simulations not including a dispersion correction were greatly over-exaggerated for all three phases of urea. The calculated zero-pressure volumes were: urea I, $\sim$158 Å^3; urea III, $\sim$322 Å^3; urea IV, $\sim$158 Å^3. Although there are no experimental lattice parameters below room temperature for urea IV, there are literature values for urea I at low temperature, and the measurements on HRPD include unit-cell values for phase III at 10 K (Appendix A). Comparing these literature values to the relaxations, the unit-cell volumes are overestimated by 9 % and 20 % for phases I and III respectively.

In this case, the estimated bulk modulus of urea I and urea III was $\sim$9 GPa and $\sim$5 GPa respectively. The value of phase III is much lower than the experimentally derived value, determined to be 10.8 GPa at room temperature. The inclusion of a dispersion correction has, in this case, drastically changed the bulk elastic properties of each phase of urea, with values broadly in line with experimental values (see Chapter 4).

7.1.1.3 Summary

It is interesting that the two compounds that most required dispersion correction due to very large errors on the zero-pressure volumes, urea and ammonium carbamate, contain 'strong' intramolecular and intermolecular motif structures: urea has two-centre $C_2^1(6)$ and chelated $R_2^1(6)$ hydrogen bond motifs; α and β ammonium carbamate have ring $R_2^2(6)$ hydrogen bond motifs. It seems apparent that the molecular structures in this case must be dominated by dispersion forces, as was suggested for urea in previous DFT simulations (e.g. [27, 55]). The addition of a dispersion correction in the DFT simulations give zero-pressure unit-cell volumes extremely close to what has been measured, and must therefore be correcting for underestimate in the cohesive energies in these structures.

This is extremely important for providing accurate bulk properties of the ammonium carbonates, and other H-bonded materials, for use in models. For this project, it is very important to provide accurate values for use in planetary models and industrial models, and to be able to predict the behaviour of these materials in a variety of uses.

Therefore, when simulating hydrogen-bonded materials, the bonding geometry and any larger scale motif structures in a system, careful consideration needs to be taken since it may adversely affect the low-pressure behaviour of the material. The choice of dispersion correction in the DFT simulations also needs to be considered, as there is not a one-fits-all correction. Ideally, a low temperature value for the unit-cell volume will be available before commencing the DFT simulations so the two values can be compared to assess if a dispersion correction is necessary and which correction should be applied.

7.1.2 Implications for planetary science

Without the present ability to collect samples *in situ* from the surface of icy moons, or to unambiguously characterise their surface mineralogy by *in situ* diffraction measurements, the only methods available to constrain the internal structure of these planetary bodies is by modelling the body in question using compounds that are thought likely to be present. By comparing these models with data measured from passing or orbiting spacecraft, usually in the form of gravitational field measurements, an estimate of the internal structure of these bodies can be obtained.

This thesis has provided numerical values for how the density varies with pressure for all of the compounds, and bulk properties that will affect how the materials behave with pressure. There are still data that would need to be collected for complete implementation of these compounds in planetary models (such as how the unit-cell volumes varies as a function of temperature), and for the detection of these compounds in planetary environments from spacecraft (such as absorption/reflectivity data).

Since ammonia was only condensed past the ‘snow line’ in the early solar system, the detection of the ammonium carbonates in planetary environments may help to determine how the planetary body evolved.

Further data are needed to understand the phase behaviour of the ammonium carbonates, since these different phases could have affected how a planetary environment evolved, or could alter the chemical equilibrium of such a body. Phase changes in planetary interiors of icy moons are important to understand as a function of pressure, requiring data at low temperatures. Volumetric changes, as well as the chemical properties of each phase will determine the stability of different layers inside a planetary

body, and will therefore affect the overall structure.

7.1.3 Implications for terrestrial science

Back on Earth, accurate and precise crystal structures as a function of temperature and/or pressure may help in simulating the the behaviour of the ammonium carbonates in practical applications, such as in carbon-capture processes. The use of modelling could be used to simulate the carbon-capture process, improving the efficiency, or to simulate ammonia slip that is an inherent problem in such processes and perhaps to minimise this effect.

Understanding the phase behaviour as a function of temperature and/or pressure is extremely important in industrial processes, since, for example, it could drastically alter the chemical behaviour, or indeed the stability of the system.Variations in the physical properties of each polymorph, which can be in the form of crystal habit, solubility, hardness, optical properties, melting point or chemical reactivity play an important role in industrial applications. A good example of the importance of understanding the phase behaviour in systems can be seen in the pharmaceutical industry, where certain phases can be desirable for end use, for example, if the crystal is more soluble it is easier to digest when taken orally. The polymorphism exhibited in this ternary system, therefore, is an important property to understand when incorporating the ammonium carbonates into industrial processes, as well as material properties of how each phase varies with pressure and temperature.

7.2 Summary of completed work

This section provides an overview of the findings of each of the compounds studied in this ternary system, and how the results of the behaviour and properties found in this work are important in planetary and earthly matters.

7.2.1 Ammonium carbonate monohydrate

A highly anisotropic material, the *c*-axis being the least compressible, with the *b*-axis the most compressible direction. The high-pressure simulations match the thermal expansivity behaviour that was measured experimentally (Appendix B, & [53]). The negative linear thermal expansion along *c* manifests in the high-pressure calculations as having negative linear compressibility above 2 GPa. The extent of the negative linear

compressibility (NLC) is over a very large pressure range (∼2 - 11 GPa) and is high in magnitude - similar behaviour is seen in ammonium oxalate monohydrate [115].

NLC is a highly attractive mechanical property, having various applications, such as in the design of pressure sensors, artificial muscles and actuators [15], but, even with ever more materials found exhibiting this behaviour, it is still a relatively rare phenomenon. The extent of the NLC calculated to be in ammonium carbonate monohydrate is quite important, being both high in magnitude and persisting over a large pressure range. Since ammonium carbonate is only stable below 273 K at ambient pressure, it does place a limit on the range of applications. There could be a novel industrial use of the NLC predicted to be present ammonium carbonate monohydrate, due to its low temperature requirement.

In a planetary environment, NLC would have a major impact on the internal structure of an icy moon, since, in one direction, ammonium carbonate monohydrate would increase in size. The internal pressures required to reach the region of negative compressibility means only very large icy bodies would be affected by this phenomena.

7.2.2 Ammonium sesquicarbonate monohydrate

In this structure, the *a*-axis is much more compressible than the other two crystallographic directions, due to the strongly layered character of this structure. The structure was stable over the pressure range simulated, with no evidence of a phase change present. The bulk modulus of this material places this above that of ammonium bicarbonate, but below ammonium carbonate monohydrate in terms of stiffness. There is no sign of any negative compressibility over a large pressure range, and so would most likely not show any negative thermal expansivity either.

The anisotropy observed in this structure is important to understand when incorporating this compound into structural models of icy bodies, and the bulk elastic properties presented in this work will help to determine the stability of this compound in such environments.

7.2.3 Urea I, III and IV

Dispersion correction was required in the urea simulations to prevent the unit-cell being overestimated by several percent. This was most apparent in the high-pressure phases, particularly urea III. The dispersion calculations are a much better match to experimen-

tal values for urea I and III, and the structural similarity of urea IV to urea I means the zero-pressure unit-cell volumes are quite similar.

In the athermal limit, urea III is the stable phase over the pressure range simulated. Experiments show that urea III is most likely the thermodynamically stable phase at low temperatures, but transition from phase I $\rightarrow$ III may be inhibited. Urea I shows no structural changes of the pressure range simulated, and the behaviour matches a previous DFT study. This work however is more accurate in terms of values, matching the 2 K experimental value extremely well, and correctly predicting the anisotropic behaviour. Urea III values are an excellent match to the measured zero-pressure volumes and the bulk modulus and its pressure derivatives. There was a small degree of relaxation in the *b*-axis, and the deformation under pressure suggests how the phase change mechanism, from III $\rightarrow$ IV, takes place. Urea IV shows some very interesting behaviour below 2 GPa, relaxing back into a similar shape as urea I - this could also explain how phase IV has been suggested to be phase II.

On the basis of this work, it is highly likely that, if urea is present, urea III is the phase that would be observed in planetary interiors of the outer solar system, since it is the stable phase at temperatures applicable to these bodies. There is still a considerable lack of data on the compressibility of urea at temperatures applicable to these bodies - determining where, if any, phase transitions occur at temperatures relevant to these bodies is important for understanding and modelling of urea in planetary environments. This work has provided bulk elastic properties and accurate crystal structures for each phase that could be incorporated into planetary models.

Understanding the phase behaviour of urea is important for matters here on Earth. Carbon-capture processes involving urea will most likely be in the form of the ambient phase of urea, phase I, but small amounts of pressure could form phase III, changing the physical properties of the system and potentially affecting the CO_2 absorption process. Changing the conditions used in hydrogen fuel cells may alter the chemistry of the system by changing the phase of urea, potentially for the better (or worse). The accurate crystal structures provided of each phase by this work can be included in any modelling of urea.

7.2.4 Ammonium carbamate α and β

The initial DFT calculations successfully predicted the anisotropic behaviour of the unit-cell as a function of pressure that was subsequently observed experimentally; a high-pressure experiment to measure deuterated α-ammonium carbamate was performed on *SXD*. However, the zero-pressure unit-cell volume calculated was greatly overestimated relative to the measured unit-cell volume at 4 K - as part of the thermal expansion measurement on *HRPD*. Calculations were performed using a dispersion correction, which largely corrected the problem.

In α-ammonium carbamate, there was also a prediction for NLC in the structure above 5 GPa and once again above 9 GPa. However, whether this would be seen experimentally is difficult to assess, since a phase change between α and β is predicted well below this pressure. Unlike ammonium carbonate monohydrate, which also exhibits NLC, there is no negative thermal expansion in α-ammonium carbamate, remaining positive in all directions at all temperatures.

Ammonium carbamate will most likely form in planetary environments with low concentrations of H_2O available. The complex behaviour as a function of pressure would affect the evolution and stability of large icy bodies. Determining the phase behaviour as a function of pressure and temperature is important for modelling this compound.

7.2.5 Ammonium bicarbonate

The DFT simulations in this case match the values obtained over several experiments, and successfully predicted the observed anisotropic behaviour of the unit-cell, although to higher pressures than measured.

The thermal expansion of deuterated ammonium bicarbonate was determined on *HRPD* from 10 - 300 K; the *b*-axis show a small degree of negative area thermal expansion below 78 K, with almost all the positive volume thermal expansion as a result of the expansion along the *a*-axis. This anisotropy was also measured in several high-pressure experiments on PEARL, in which a few new phases were also discovered. Measurements of the compressibility over three temperatures - 200 K, 245 K and 295 K - allowed for an equation of state to be fitted to the volume of the ambient phases as a function of P and T. The powder diffraction pattern of one of the new phases dis-

covered has successfully been indexed and the crystal structure has been solved, being found to involve a change in space group from *Pccn* to $Pbc2_1$. Further new phases were observed but remain unsolved

Negative area expansivity is a rare phenomena, and has been proposed to be used in controlling the thermal expansion of composites by addition of positive and negative expanding materials to produce the desired expansivity. The negative area thermal expansion observed at low temperatures will have a dramatic impact on the stability and evolution of planetary bodies containing ammonium bicarbonate.

The complex phase behaviour observed in the experiments as a function of pressure and temperature is important to understand and characterise, in order to accurately predict the behaviour of ammonium bicarbonate in planetary interiors. Further investigations are required to map the phase boundaries and characterise the high-pressure phases observed.

Since ammonium bicarbonate is stable in air, this compound would be ideal for use in hydrogen fuel cells, requiring little in the way of storage needs. Carbon-capture processes, by which ammonium hydroxide solutions are exposed to CO_2, would most likely form ammonium bicarbonate due to the stability of this compound. The bulk elastic properties provided in this thesis can be used in modelling of ammonium bicarbonate in a variety of uses, such as understanding the behaviour in high-pressure environments.

7.3 Future work

There is a large amount of future work that can be implemented on the compounds that form this ternary system. Perhaps one of the most interesting, at least from a materials science point, is the presence of negative linear thermal expansion and negative compressibility calculated to occur in ammonium carbonate monohydrate. It would be very worthwhile to measure the behaviour of this compound as a function of temperature and pressure in order to confirm the negative thermal expansion and precisely measure its magnitude, and to confirm if the negative linear compressibility is seen experimentally.

This could be done by a high accuracy and precision powder diffraction study to determine the lattice parameters as a function of temperature, using, for example, *HRPD* at ISIS, due to its high resolution, allowing the highest precision in refined lattice

parameters. A second experiment would be to measure the behaviour of ammonium carbonate monohydrate as a function of pressure - this could be done at ISIS on *PEARL*, since it allows hydrostatic compression of materials to high-pressures. However, since the calculated negative compressibility behaviour occurs up to 12 GPa, other methods to reach high-pressure, such as a diamond anvil cell, may be more useful to measure this compound over a large pressure range. There are a few issues that need to be addressed for this to take place.

Firstly, this compound is only stable below room temperature, so it will require loading into a sample environment cold. Whilst this is not too difficult for a thermal expansion measurement, as loading into a cold stage has already been done during this work, loading the sample into high-pressure equipment below room temperature would require careful planning. This work however would be of interest, not only in terms of material science - since NLC is quite rare - but also to planetary science, since mixtures of ammonia, water and carbon dioxide at low temperatures would likely yield this compound.

Further experiments are also needed for the other compounds in this ternary system. Ammonium sesquicarbonate has only one measurement in the literature, so there are no data available on the temperature and pressure dependence of the structure, which is particularly important to understand and constrain this behaviour for incorporation into planetary models. Urea has only been measured as a function of pressure at room temperature, so data are missing on the phase behaviour and stability at temperatures most applicable to icy moons; also for urea, phase V is reported to exist in the literature but thus far the crystal structure is unknown. Further high-pressure experiments are required to address this lack of data. The phase changes in ammonium bicarbonate warrant further investigation, mapping out the phase boundaries and characterising the unsolved phases measured in this work.

Finally, since the only way to measure the existence of such compounds in planetary environments is from remote sensing, spectroscopic information is required for all these compounds in environments similar to those seen on the surfaces of icy moons, to complete the data on these compounds for planetary applications. The most useful would be in the form of infra-red absorption and reflectivity measurements at low temperatures.

Appendix A

Recovery of deuterated urea phase III from high pressure

This was an experiment based upon the recovery of the high pressure phase of urea, phase III, to ambient pressures by quenching the sample under liquid nitrogen using the new piston-cylinder press at UCL [147]. The lattice parameters were then measured as a function of temperature upon warming to determine the thermal expansion and the anisotropy seen in the high pressure DFT simulations, and to observe the phase transition from phase III $\rightarrow$ I. The work provided an accurate structure for use in the DFT calculations for phase III, and for future studies of urea.

A.1 Methods

A.1.1 Sample preparation

Powdered deuterated urea (Sigma Aldrich 176087, $>$98 atom % D) was lightly ground using a mortar and pestle before being loaded inside a PTFE sample capsule, which was put into the piston-cylinder cell at UCL and mounted on the Paris-Edinburgh press at room temperature. The sample was compressed to a maximum oil pressure of 100 bar, equivalent (ignoring friction) to a pressure on the sample of 0.88 GPa. At this temperature, the phase transition from phase I to III is expected at 0.48 GPa [106]. As can be seen in Figure A.1, the transition begins at $\sim$75 bar, equivalent to a pressure on the sample of 0.66 GPa. The higher transition pressure observed during this compression could be due to friction.

Once compressed to $\sim$0.9 GPa, the sample was cooled under load to 80 K (Figure

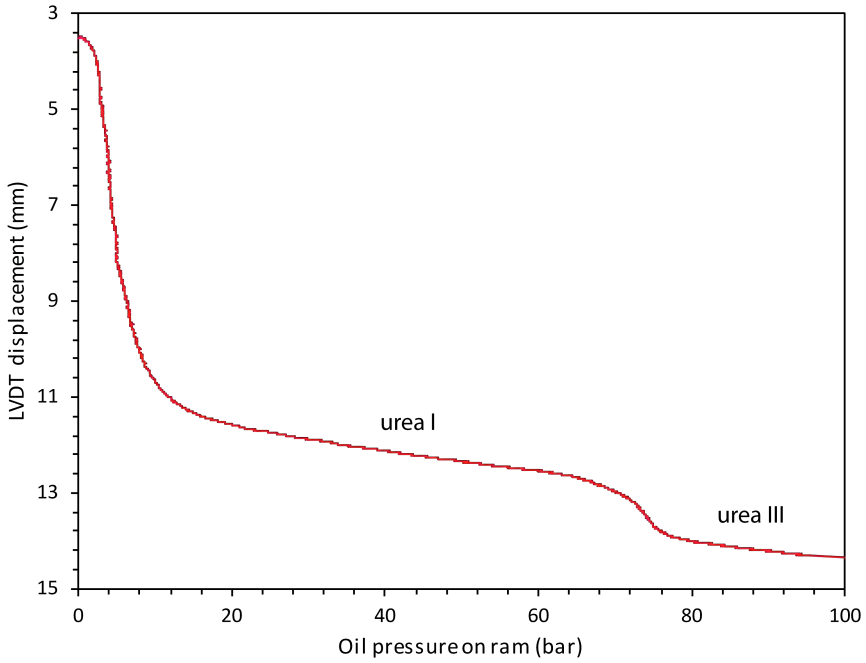

Figure A.1
The compression of deuterated urea at room temperature. The large displacement below 15 bar oil pressure is due to the initial compression of the sample in the PTFE capsule. The phase transition between phase I and III is clearly visible.

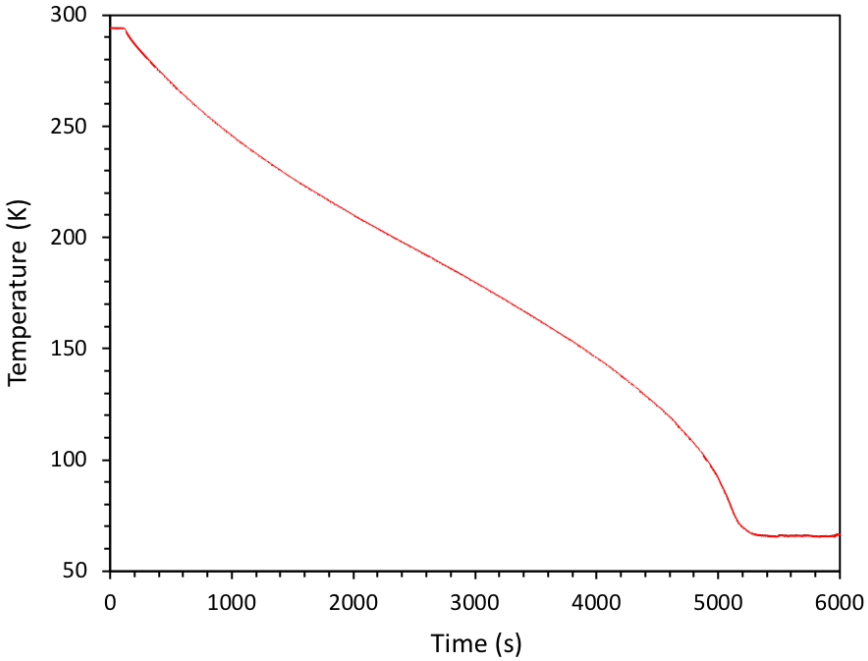

Figure A.2
Temperature log (at 1s intervals) showing the cooling curve of urea compressed at 100 bar oil pressure when cooling at the maximum rate. Note the base temperature recorded by the logging system is too low for liquid nitrogen, due to the K-type thermocouple not being calibrated at low temperatures.

A.2), after which the load was gradually reduced to zero and the sample pushed out of the pressure vessel into liquid nitrogen. The sample, still inside the PTFE capsule, was transported to the ISIS neutron spallation source whilst kept submerged in liquid nitrogen.

At ISIS, the sample was extracted from the capsule and ground under liquid nitrogen in a stainless steel cryo-mortar. Once fully ground, the material was loaded into an aluminium-framed slab-geometry can with 10 mm depth, which was transferred to a CCR pre-cooled to 100 K. The CCR centre-stick was lowered into the CCR and the temperature reduced to 10 K for measurements to begin.

A.1.1.1 Data Acquisition

Time-of-flight neutron powder diffraction data were collected at 10 K in the 30-130 ms window using the backscattering detectors (2θ = 168°, d-spacing range 0.65 - 2.6 Å) for high resolution structural refinement, counting for ∼4 hr (corresponding to an integrated proton-beam current of 160 μA hr); this well counted dataset was used for precise structural refinement. Subsequent data were collected on warming in 10 K increments, with two longer counts initiated at 100 K and 190 K, up to 270 K. Each measurement lasted for ∼30 mins (corresponding to an integrated proton-beam current of 20 μA hr per step), with the longer counts lasting for ∼4 hours (corresponding to an integrated proton-beam current of 160 μA hr per step). The diffraction data were focussed, normalised to the incident beam spectrum and corrected for detector efficiency by reference to a vanadium standard using *Mantid* [7], and exported to a format suitable for analysis with *GSAS/Expgui* [87, 138].

A.1.1.2 Structure refinement

Neutron powder diffraction data were analysed at 10 K by the Rietveld method using *GSAS/Expgui* [87, 138], starting from the high pressure structure measured at 0.80(5) GPa and 296 K given by Olejniczak et al., 2009 [106]. Phase pure deuterated urea III was identified in the initial 10 K dataset by inspection of peak positions. Data were fitted by refinement of unit-cell parameters, scale factors and phase fractions, peak-profile coefficients (*GSAS* profile function 3), and an eight term Chebyschev polynomial. Atomic coordinates were refined independently without restraints, whilst the thermal displacement parameters, U_{iso}, were fixed at two values, one for all the deuterons

(0.01909 Å^2), the other for all non-deuterons (0.00730 Å^2), to prevent some values becoming negative. The final fit to the data is given in Figure A.3.

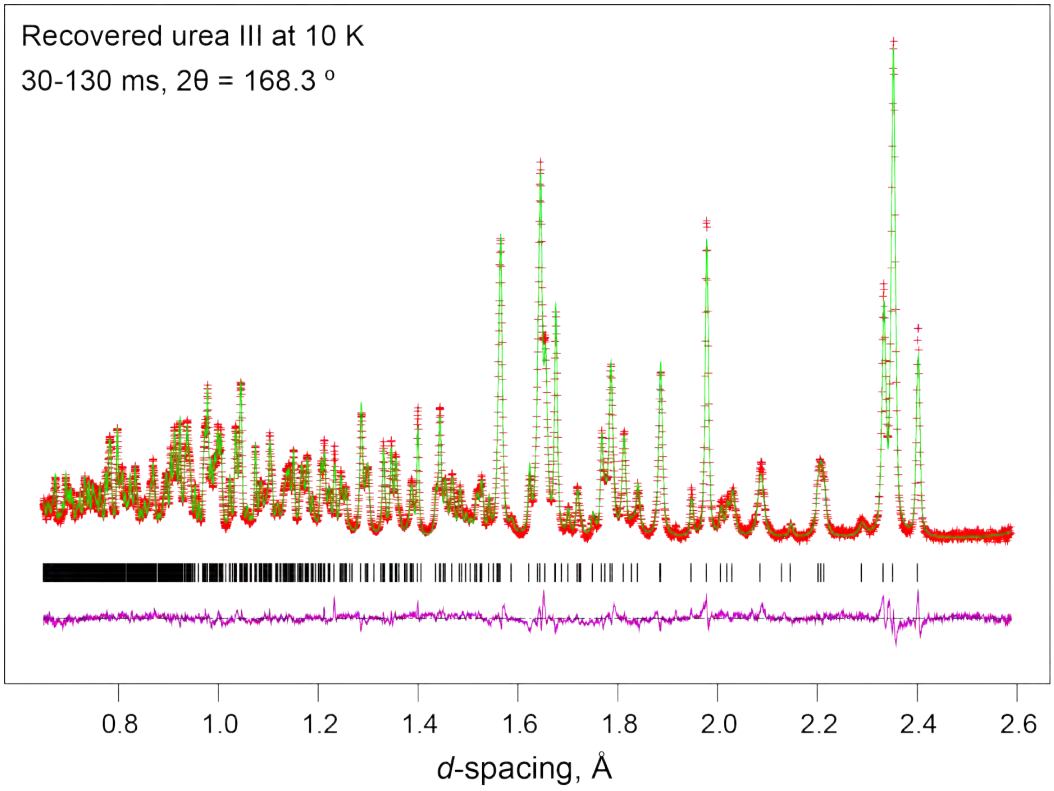

Figure A.3
Neutron powder diffraction pattern of recovered deuterated urea III acquired at 10 K in the highest resolution backscattering bank of *HRPD*. Red pluses represent the measured data, the solid green line the result of Rietveld refinement, the purple line the difference profile, and the black tick marks the expected positions of each Bragg reflection for urea III

A.2 Results

In this section, I will give a brief account of the results of the thermal expansion behaviour of recovered deuterated urea III, and the back transformation to the ambient phase.

From the Rietveld refinement at 10 K, the unit-cell volume at ambient pressure and 10 K is 268.717(4) Å^3 (see Table A.1 for the detailed crystal structure). The conditions of this measurement are much different to those that have been used before - all other experiments involving urea III have been conducted at pressures greater than 0.5 GPa and at room temperature.

Table A.1
Structural parameters of urea III measured on *HRPD* at 10 K

Deuterated urea III

Formula	$CO(ND_2)_2$	Lattice parameters	
Space group	$P2_12_12_1$	*a*-axis (Å)	3.65620(4)
Z	4	*b*-axis (Å)	8.34391(9)
ρ (kg m^{-3})	1583.98	*c*-axis (Å)	8.8084(1)
Temperature	10 K	Volume (Å^3)	268.717(4)

Label	Fractional coordinates			Site
	x	y	z	
C1	0.1631(4)	0.47847(17)	0.05904(18)	4a
O1	0.0822(5)	0.44135(20)	-0.07569(19)	4a
N1	0.32739(31)	0.37577(12)	0.15229(11)	4a
N2	0.09712(28)	0.63097(13)	0.11092(11)	4a
D1A	0.4110(6)	0.26826(20)	0.11298(22)	4a
D1B	0.4033(5)	0.41569(20)	0.25677(20)	4a
D2A	-0.0986(5)	0.69020(20)	0.05294(23)	4a
D2B	0.1076(6)	0.64503(18)	0.22353(19)	4a

A.2.1 Thermal expansion

There is a very good agreement between the DFT simulations and this thermal expansion work for the behaviour of the crystal structure when subject to external stimuli. Urea III has a large degree of anisotropy when subject to external stimuli. Looking at Figure A.4, virtually all of the volumetric thermal expansion is attributed to the expansion of the *a*-axis, which equates in the crystal structure to be perpendicular to the sheets of urea molecules in the bc plane, with fewer hydrogen bonds connecting these sheets. In the DFT simulations, this axis exhibits the highest compressibility.

The *c*-axis has a small degree of positive linear expansion over the measured temperature range, but this expansion is negated by an almost equal contraction along the *b*-axis, which exhibits negative linear thermal expansion over the full temperature range where urea III is stable. There is also a small degree of negative compressibility predicted in the DFT simulations along the *b-axis*. This behaviour is similar to that seen in ammonium carbonate monohydrate (see Appendix B).

A.2.2 Phase transition

Urea III remained stable from 10 K to 180 K. Peaks of urea I appeared between the 180 K and 190 K runs (Figure A.5), with peaks from phase III disappearing between the 210 K and 220 K runs (a total of 5 hr 45 mins between the beginning of the 190 K run to the

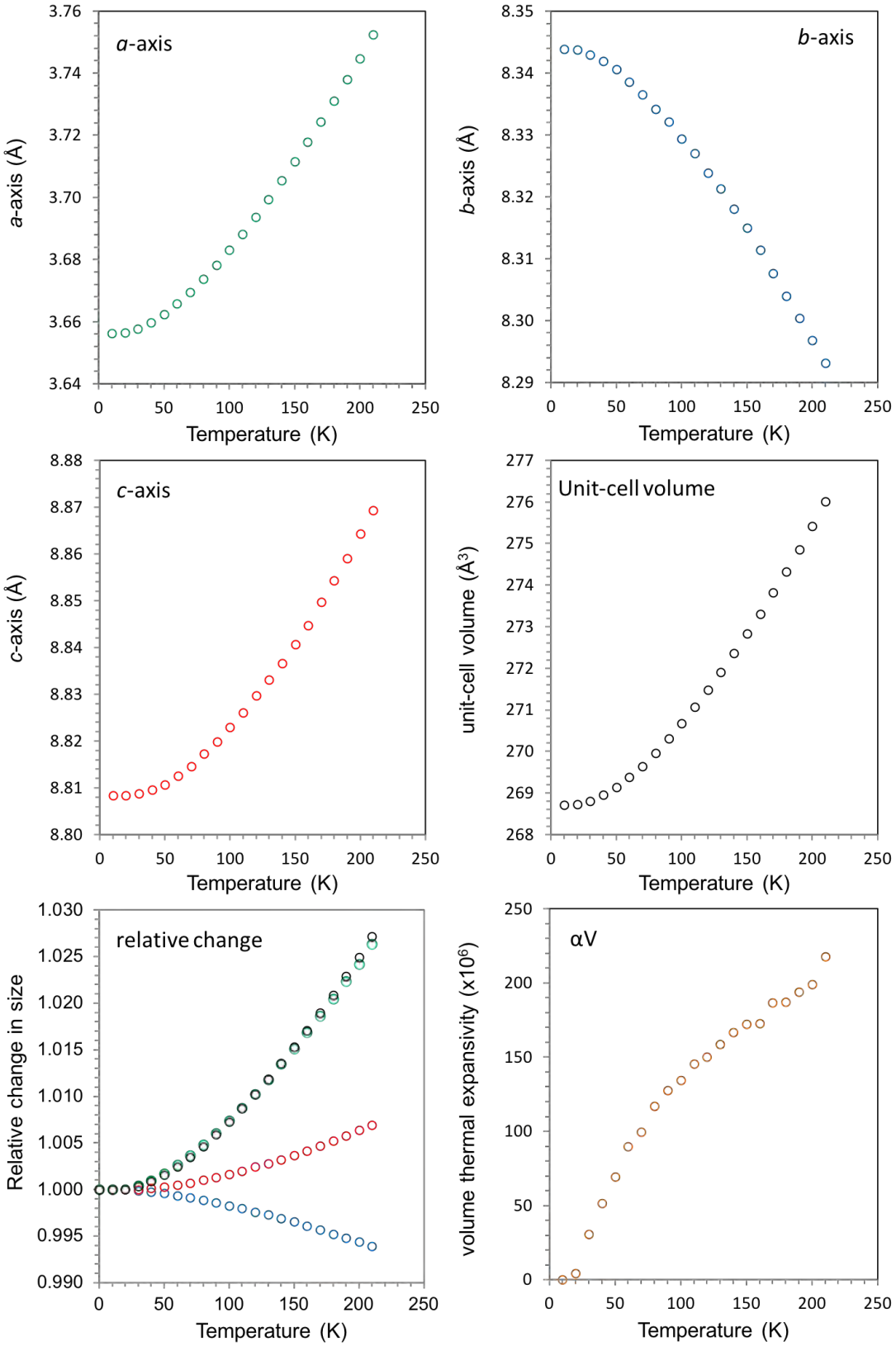

Figure A.4
Lattice parameters, relative change in size and volumetric thermal expansivity of deuterated urea III as a function of temperature from *HRPD*.

start of the 220 K run to transform). The peaks of urea I showed a degree of anisotropic strain broadening after the phase transition; this behaviour has been observed before in urea I during a thermal expansion measurement (see Birkedal et al., 2004), but in their experiment no phase transition occurred.

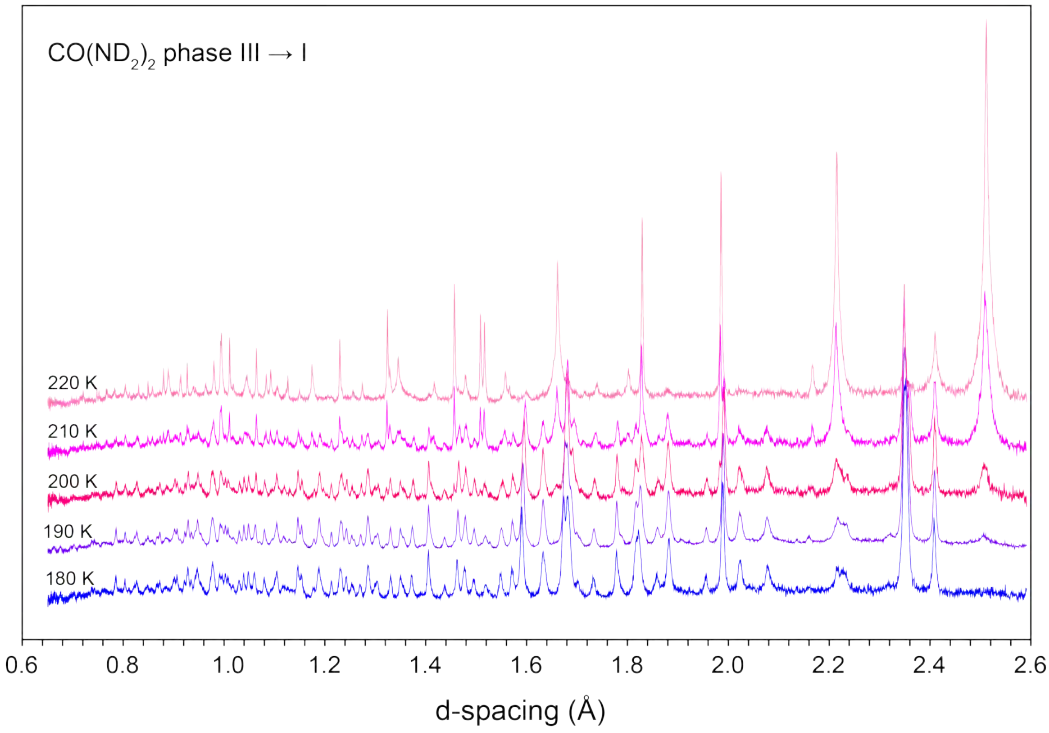

Figure A.5
Stack plot of neutron powder diffraction patterns through the back-transformation of deuterated urea III →I as measured on *HRPD*, from 180 K (at the bottom) to 220 K (at the top). The onset of the phase transition occurred between the 180 K and 190 K measurements.

A.3 Conclusion

The results have shown the large anisotropy calculated under pressure using DFT is also manifests in large anisotropic thermal expansivity, with the *b*-axis exhibiting negative linear thermal expansivity from 10 K to 180 K. The phase transition from phase III→I was observed between 180 K and 190 K, after which urea I showed some anisotropic strain broadening. Further work is planned to try and recover urea phase II - discovered by Bridgman in 1916 [19], to prove whether this is indeed phase IV as suggested by Dziubek *et al.*, 2017 [42]. However, this will require some modification to the recovery press to allow heating of the sample before compressing, quenching and extraction.

Appendix B

Thermal expansion of ammonium carbonate monohydrate

This was an experiment to determine the thermal expansion of ammonium carbonate monohydrate using the Phenix-FL CCR mounted on the X-ray powder diffractometer in UCL.

B.1 Methods

Crystals were grown by exposing a beaker filled with aqueous ammonia to a CO_2-rich atmosphere inside a small plastic container with lid placed loosely filled with dry-ice pellets. Crystals were extracted from the mother liquor inside UCL Earth Science's Cold Room suite to minimise their breakdown during sample preparation, and ground under liquid nitrogen using a stainless-steel pestle and mortar. The resulting powder was loaded into the Phenix-FL sample holder, also kept under liquid N_2, and placed into the diffractometer at liquid nitrogen temperature. The sample was then cooled to 40 K to begin measurement.

X-ray powder diffraction data were collected using a PANalytical X'Pert Pro diffractometer with Ge monochromated Co $K\alpha_1$ radiation (λ= 1.789001 Å), measuring from 40 K to 100 K in 10 K steps, then from 100 K to 160 K in 20 K steps. At each temperature step, the measurement lasted for 4.5 hrs, with 2θ ranging from 10 - 155°. Peaks were identified from ammonium carbonate monohydrate, ammonium sesquicarbonate monohydrate, and water ice. Powder diffraction data were analysed using *GSAS/Expgui* [87, 138], and refined using the Rietveld method.

B.2 Results and conclusion

The diffractogram shows peak shapes that are split and poorly defined. As can be seen in the Figure B.2, the difference curve is extremely large, due to the peak profile shapes not accurately reproducing the data. The peak splitting is likely caused by an uneven sample surface. However, although the fit is quite poor, it does manage to produce a good estimate of the thermal expansion of ammonium carbonate monohydrate (see Figure B.1).

The thermal expansion seen is a good match to that of Fortes *et al.*, 2014 [53]. It can be seen in the data that the *c*-axis does exhibit negative thermal expansivity in the temperature range measured here, with the *ab* plane exhibiting positive thermal expansion to a high enough degree that the volumetric thermal expansivity remains positive in this temperature range. A further experiment is needed to measure the behaviour of ammonium carbonate monohydrate as a function of temperature to accurately and precisely measure the negative expansivity along *c*.

This work has also provided a measurement of the lattice parameters of ammonium sesquicarbonate monohydrate at 40 K. The lattice parameters are as follows: a = 7.1391(3) Å, b = 15.817(1) Å, c = 10.4494(7) Å, V = 1179.9(1) Å^3. Due to the small quantity of this compound in the sample, the peaks are very small so the quality of the data is not sufficient to get an estimate of the thermal expansivity. It does however serve to prove that the apparent 'overbinding' of the unit-cell volume in the DFT calculations is actually due to the lack of low temperature lattice parameters, with the unit-cell contracting in volume as the temperature is reduced.

A study to measure the thermal expansion of ammonium sesquicarbonate monohydrate is required to understand and characterise the behaviour of this compound, with the values important for use in structural planetary models.

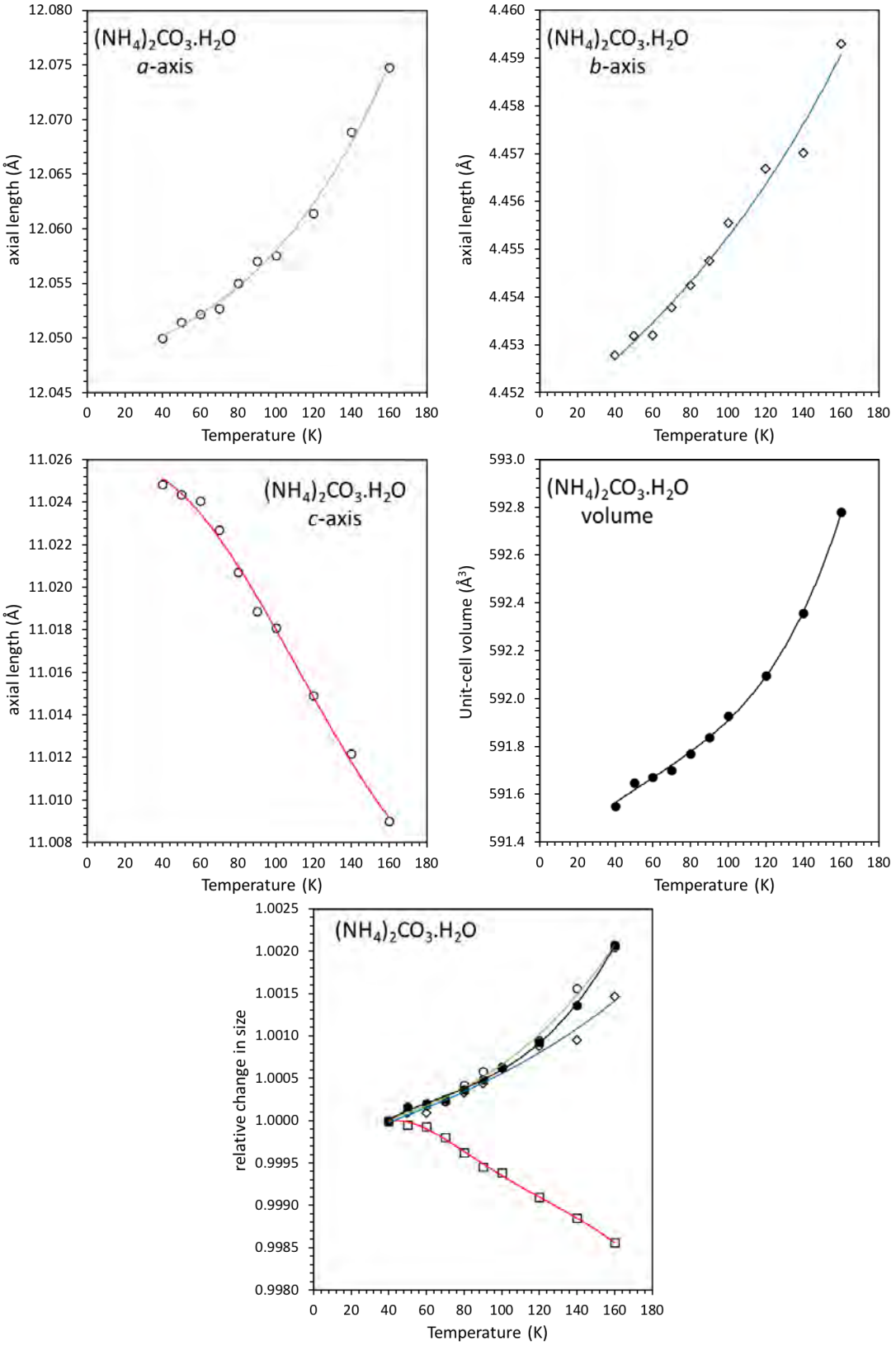

Figure B.1
Lattice parameters and relative change in size of $(NH_4)_2CO_3 \cdot H_2O$ as a function of temperature. The lines are fitted polynomials to guide the eye only.

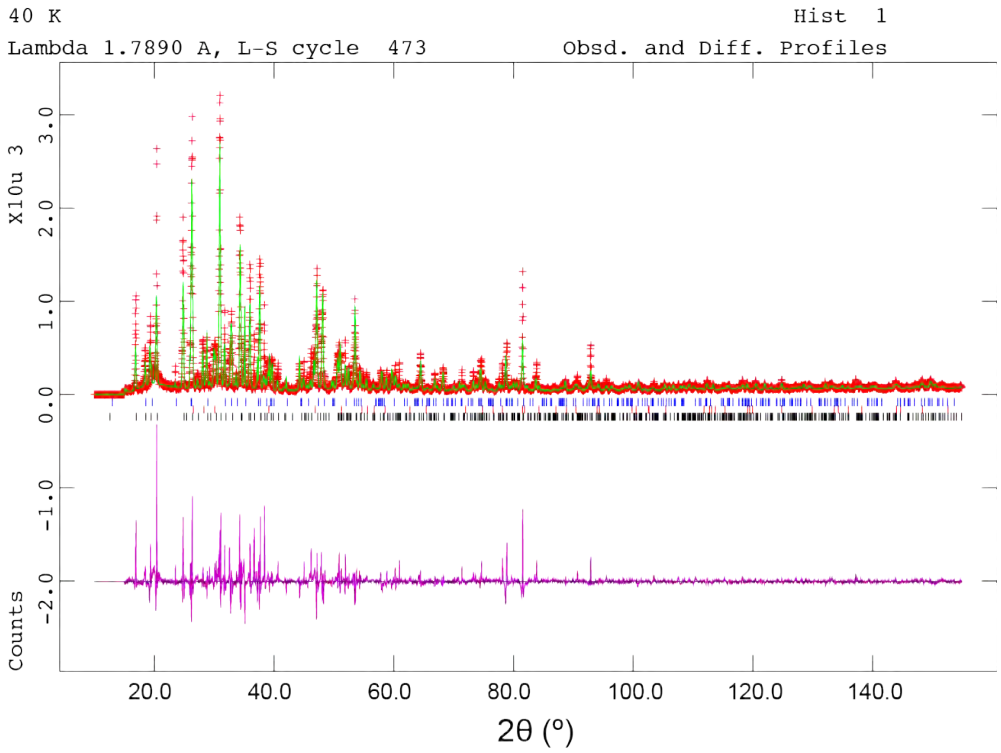

X-ray powder diffraction pattern with difference curve plotted

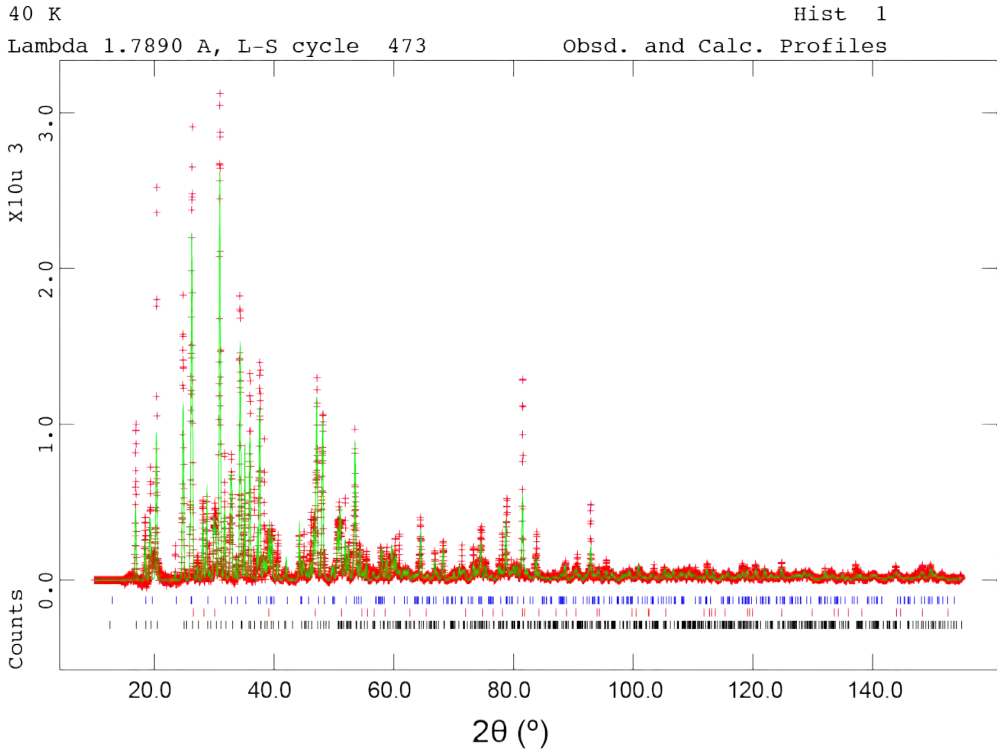

X-ray powder diffraction pattern without difference curve plotted

Figure B.2
X-ray powder diffraction pattern obtained at 40 K using the Phenix-FL CCR. Red symbols represent the measured data, green lines the result of Rietveld refinement, pink line is the difference profile, and the tick marks the expected positions of each Bragg reflection for; ammonium carbonate monohydrate (black); water ice (red); ammonium sesquicarbonate monohydrate (blue).

Bibliography

[1] M. Abu-Zahra, Z. Abbas, P. Singh, and P. Feron. *Materials and Processes fro Energy: Communicating Current Research and Technological Developments*, chapter Carbon dioxide post-combustion capture: solvent technologies overview, status and future directions, pages 923–934. 1. Formatex Research Center, 2013.

[2] J. M. Adams and R. W. H. Small. The crystal structure of ammonium carbamate. *Acta Crystallographica Section B*, 29(11):2317–2319, 1973.

[3] C. Ahn, K. Han, M. Lee, J. Kim, H. Chun, Y. Kim, and J. Park. Experimental studies of additives for suppression of ammonia vaporization in the ammonia based CO_2 capture process. *Energy Procedia*, 37:7108–7116, 2013.

[4] D. Allan, W. G. Marshall, and C. Pulham. The high-pressure crystal structure of potassium hydrogen carbonate ($KHCO_3$). *American Mineralogist*, 92(7):1018–1025, 2007.

[5] E. Anders and N. Grevesse. Abundances of the elements: Meteoritic and solar. *Geochimica et cosmochimica acta*, 53(1):197–214, 1989.

[6] O. Andersson and R. Ross. Phase behavior and thermal conductivity of urea at pressures up to 1 GPa and at temperatures in the range 50–370 K. *International Journal of Thermophysics*, 15(3):513–524, 1994.

[7] O. Arnold, J. C. Bilheux, J. M. Borreguero, A. Buts, S. I. Campbell, L. Chapon, M. Doucet, N. Draper, R. Ferraz Leal, M. A. Gigg, V. E. Lynch, A. Markvardsen, D. J. Mikkelson, R. L. Mikkelson, R. Miller, K. Palmen, P. Parker, G. Passos, T. G. Perring, P. F. Peterson, S. Ren, M. A. Reuter, A. T. Savici, J. W. Taylor, R. J. Taylor, R. Tolchenov, W. Zhou, and J. Zikovsky. Mantid - Data analysis

and visualization package for neutron scattering and μSR experiments. *Nuclear instruments & methods in physics research. Section A, Accelerators, spectrometers, detectors and associated equipment*, 764:156–166, 2014.

[8] E. Arunan, G. R. Desiraju, R. A. Klein, J. Sadlej, S. Scheiner, I. Alkorta, D. C. Clary, R. H. Crabtree, J. J. Dannenberg, P. Hobza, H. G. Kjaergaard, A. C. Legon, B. Mennucci, and D. J. Nesbitt. Definition of the hydrogen bond (IUPAC recommendations 2011). *Pure Applied Chemistry*, June 2011.

[9] S. K. Atreya, T. M. Donahue, and W. R. Kuhn. Evolution of a Nitrogen Atmosphere on Titan. *Science*, 201(4356):611–613, 1978.

[10] S. A. Azhagan and S. Ganesan. Linear and nonlinear optical studies of γ-glycine single crystals from ammonium carbonate for optoelectronic applications. *Optik - International Journal for Light and Electron Optics*, 124(6):526 – 528, 2013.

[11] U. Baisch, S. Pagano, M. Zeuner, and W. Schnick. Carbon dioxide fixation by organolanthanides and thermal degradation into amorphous and higher condensed Ln/O/C/N solids. *European Journal of Inorganic Chemistry*, 17:3517–3524, 2006.

[12] M. A. Barucci, F. Merlin, A. Guilbert, C. de Bergh, A. Alvarez Candal, O. Hainaut, A. Doressoundiram, C. Dumas, T. Owen, and A. Coradini. Surface composition and temperature of the TNO Orcus. *Astronomy and astrophysics*, 479(1):L13–L16, 2008.

[13] F. Barzagli, F. Mani, and M. Peruzzini. Carbon dioxide uptake as ammonia and amine carbamates and their efficient conversion into urea and 1,3-distributed ureas. *Journal of CO_2 Utilization*, 13:81–89, 2016.

[14] J. M. Bauer, T. L. Roush, T. R. Geballe, K. Meech, and T. C. Owen. The near infrared spectrum of Miranda evidence of crystalline water ice. *Icarus*, 158(1):178–190, 2002.

[15] R. H. Baughman, S. Stafström, C. Cui, and S. O. Dantas. Materials with negative compressibilities in one or more dimensions. *Science*, 279(5356):1522–1524, 1998.

[16] J. M. Besson, S. Klotz, G. Hamel, W. G. Marshall, R. J. Nelmes, and J. S. Loveday. Structural instability in ice VIII under pressure. *Phys. Rev. Lett.*, 78:3141–3144, Apr 1997.

[17] P. E. Blöchl. Projector augmented-wave method. *Phys. Rev. B*, 50:17953–17979, Dec 1994.

[18] A. Boultif and D. Louer. "Program for the Automatic Indexing of Powder Diffraction Patterns by the Successive Dichotomy Method". *Journal of Applied Crystallography*, 37:724–731, 2004.

[19] P. W. Bridgman. Polymorphism at high pressures. *Proceedings of the American Academy of Arts and Sciences*, 52(3):pp. 91–187, 1916.

[20] R. Brooks and T. C. Alcock. Crystal structure of ammonium bicarbonate and a possible relationship with ammonium hypophosphate. *Nature*, 166(4219):435–436, 09 1950.

[21] P. R. L. Brown. Occurence of Teschemacherite in a geothermal well at Broadlands, New Zealand. *American Mineralogist*, 57:1304–1305, 1972.

[22] R. Brown, R. Clark, B. Buratti, D. Cruikshank, J. Barnes, G. Bellucci, J. Bauer, S. Newman, T. Momary, K. H. Baines, F. Capaccioni, P. Cerroni, M. Combes, A. Coradini, P. Drossart, V. Formisano, R. Jaumann, Y. Langevin, D. L. Matson, T. B. McCord, R. M. Nelson, P. D. Nicholson, B. Sicardy, and C. Sotin. Composition and physical properties of Enceladus' surface. *Science*, 311(5766):1425–1428, 2006.

[23] C. Bull, N. Funnell, M. Tucker, S. Hull, D. Francis, and W. Marshall. PEARL: the high pressure neutron powder diffractometer at ISIS. *High Pressure Research*, 36(4):493–511, 2016.

[24] R. J. Candal, A. E. Regazzoni, and M. A. Blesa. Precipitation of copper(II) hydrous oxides and copper(II) basic salts. *J. Mater. Chem.*, 2:657–661, 1992.

[25] S. B. Charnley and S. D. Rodgers. The end of interstellar chemistry as the origin of nitrogen in comets and meteorites. *Astrophysical journal*, 569(2):L133–L137, 2002.

[26] Y. Chen, Y. Cao, X. Sun, C. Yan, and T. Mu. New criteria combined of efficiency, greenness, and economy for screening ionic liquids for CO_2 capture. *International Journal of Greenhouse Gas Control*, 16:13–20, 2013.

[27] B. Civalleri, K. Doll, and C. M. Zicovich-Wilson. Ab initio investigation of structure and cohesive energy of crystalline urea. *The Journal of Physical Chemistry B*, 111(1):26–33, 2007.

[28] W. W. Cochran. *The dynamics of atoms in crystals*. New York : Crane, Russak, 1973. Includes bibliographical references.

[29] U. Costantino, F. Marmottini, M. Nocchetti, and R. Vivani. New synthetic routes to hydrotalcite-like compounds characterisation and properties of the obtained materials. *European Journal of Inorganic Chemistry*, 1998(10):1439–1446, 1998.

[30] D. P. Cruikshank, T. L. Roush, T. C. Owen, T. R. Geballe, C. de Bergh, B. Schmitt, R. H. Brown, and M. J. Bartholomew. Ices on the surface of Triton. *Science*, 261(5122):742–745, 1993.

[31] D. P. Cruikshank, B. Schmitt, T. L. Roush, T. C. Owen, E. Quirico, T. R. Geballe, C. de Bergh, M. J. Bartholomew, C. M. D. Ore, S. Douté, and R. Meier. Water ice on Triton. *Icarus*, 147(1):309 – 316, 2000.

[32] H. Davy. *Researches, Chemical and Philosophical: Chiefly concerning nitrous oxide, or dephlogisticated nitrous air and its respiration*. London: J Johnson, 1800.

[33] R. de Kok, P. Irwin, N. Teanby, E. Lellouch, B. Bézard, S. Vinatier, C. Nixon, L. Fletcher, C. Howett, S. Calcutt, N. Bowles, F. Flasar, and F. Taylor. Oxygen compounds in Titan's stratosphere as observed by Cassini CIRS. *Icarus*, 186(2):354 – 363, 2007.

[34] M. C. De-Sanctis, E. Ammannito, A. Raponi, S. Marchi, T. B. McCord, M. C. De Sanctis, H. Y. McSween, F. Capaccioni, M. T. Capria, F. G. Carrozzo, M. Ciarniello, A. Longobardo, F. Tosi, S. Fonte, M. Formisano, A. Frigeri, M. Giardino, G. Magni, E. Palomba, D. Turrini, F. Zambon, W. Feldman, R. Jaumann, L. A. McFadden, C. M. Pieters, C. A. Toplis, M. Raymond, C. T. Russell, and T. Prettyman. Ammoniated phyllosilicates with a likely outer Solar System origin on Ceres. *Nature*, 528(7581):241–244, 2015.

[35] M. C. De Sanctis, A. Raponi, E. Ammannito, M. Ciarniello, M. J. Toplis, H. Y. McSween, J. C. Castillo-Rogez, B. L. Ehlmann, F. G. Carrozzo, S. Marchi, F. Tosi, F. Zambon, F. Capaccioni, M. T. Capria, S. Fonte, M. Formisano, A. Frigeri, M. Giardino, A. Longobardo, G. Magni, E. Palomba, L. A. McFadden, C. M. Pieters, R. Jaumann, P. Schenk, R. Mugnuolo, C. A. Raymond, and C. T. Russell. Bright carbonate deposits as evidence of aqueous alteration on (1) Ceres. *Nature*, 536:54 EP –, 06 2016.

[36] A. Delsanti, F. Merlin, A. Guilbert Lepoutre, J. Bauer, B. Yang, and K. J. Meech. Methane, ammonia, and their irradiation products at the surface of an intermediate-size KBO? *Astronomy and astrophysics*, 520:A40, 2010.

[37] F. E. DeMeo, C. Dumas, J. C. Cook, B. Carry, F. Merlin, A. J. Verbiscer, and R. P. Binzel. Spectral variability of Charon's 2.21-μm feature. *Icarus*, 246:213 – 219, 2015. Special Issue: The Pluto System.

[38] S. J. Desch, J. C. Cook, T. Doggett, and S. B. Porter. Thermal evolution of Kuiper belt objects, with implications for cryovolcanism. *Icarus*, 202(2):694 – 714, 2009.

[39] E. Divers. XXIII.-On the combinations of carbonic anhydride with ammonia and water. *J. Chem. Soc.*, 23:171–279, 1870.

[40] M. Dixit, G. N. Subbanna, and P. V. Kamath. Homogeneous precipitation from solution by urea hydrolysis: a novel chemical route to the α-hydroxides of nickel and cobalt. *J. Mater. Chem.*, 6:1429–1432, 1996.

[41] L. Dumee, C. Scholes, G. Stevens, S. Kentish, and L. Dumée. Purification of aqueous amine solvents used in post combustion CO_2 capture: A review. *International Journal of Greenhouse Gas Control*, 10:443–455, 2012.

[42] K. Dziubek, M. Citroni, F. Samuele, C. Andrew, and B. Roberto. High-pressure high-temperature structural properties of urea. *The Journal of Physical Chemistry C.*, 121(4):2380–2387, 2017.

[43] U. Eberle, M. Felderhoff, F. Schueth, and F. Schüth. Chemical and physical solutions for hydrogen storage. *Angewandte Chemie (International ed.)*, 48(36):6608–6630, 2009.

[44] J. P. Emery, D. M. Burr, D. P. Cruikshank, R. H. Brown, and J. B. Dalton. Near-infrared (0.8–4.0 μm) spectroscopy of Mimas, Enceladus, Tethys, and Rhea. *Astronomy and astrophysics*, 435(1):353–362, 2005.

[45] M. C. Etter, J. C. MacDonald, and J. Bernstein. Graph-set analysis of hydrogen-bond patterns in organic crystals. *Acta Crystallographica Section B*, 46(2):256–262, Apr 1990.

[46] Evans K. E. and Alderson A. Auxetic materials: Functional materials and structures from lateral thinking! *Advanced Materials*, 12(9):617–628, 2000.

[47] V. Favre-Nicolin and R. Černý. *FOX*, 'Free Objects for Crystallography': a modular approach to *ab initio* structure determination from powder diffraction. *Journal of Applied Crystallography*, 35(6):734–743, Dec 2002.

[48] B. Fegley and R. G. Prinn. Kinetic inhibition of CO and N_2 reduction in circumplanetary nebulae - Implications for satellite composition. *Astrophysical Journal*, 249(1):308–317, 1981.

[49] B. Fleury, N. Carrasco, T. Gautier, A. Mahjoub, J. He, C. Szopa, E. Hadamcik, A. Buch, and G. Cernogora. Influence of CO on Titan atmospheric reactivity. *Icarus*, 238:221 – 229, 2014.

[50] A. Fortes, I. Wood, and K. Knight. The crystal structure and thermal expansion tensor of $MgSO_4 \cdot 11\,D_2O$ (meridianiite) determined by neutron powder diffraction. *Physics and Chemistry of Minerals*, 35(4):207–221, 2008.

[51] A. D. Fortes. *Computational and experimental studies of solids in the ammonia - water system*. PhD thesis, UCL, January 2004.

[52] A. D. Fortes. Accurate and precise lattice parameters of H_2O and D_2O ice I*h* between 1.6 and 270K from high-resolution time-of-flight neutron powder diffraction data. *Acta Crystallographica Section B*, 74(2):196–216, Apr 2018.

[53] A. D. Fortes, I. G. Wood, D. Alfè, E. R. Hernández, M. J. Gutmann, and H. A. Sparkes. Structure, hydrogen bonding and thermal expansion of ammonium carbonate monohydrate. *Acta Crystallographica Section B*, 70(6):948–962, 2014.

[54] Y. A. Galkina, N. A. Kryuchkova, M. A. Vershinin, and B. A. Kolesov. Features of strong O-H$\cdots$O and N-H$\cdots$O hydrogen bond manifestation in vibrational spectra. *Journal of Structural Chemistry*, 58(5):911–918, Sep 2017.

[55] J. George, R. Wang, U. Englert, and R. Dronskowski. Lattice thermal expansion and anisotropic displacements in urea, bromomalonic aldehyde, pentachloropyridine, and naphthalene. *The Journal of Chemical Physics*, 147(7):074112, 2017.

[56] C. R. Glein, S. J. Desch, and E. L. Shock. The absence of endogenic methane on Titan and its implications for the origin of atmospheric nitrogen. *Icarus*, 204(2):637 – 644, 2009.

[57] F. Gourgeot, C. Dumas, F. Merlin, P. Vernazza, and A. Alvarez Candal. Near-infrared spectroscopy of Miranda. *Astronomy and Astrophysics*, 562:A46, 2014.

[58] T. Grant, C. Anderson, and B. Hooper. Comparative life cycle assessment of potassium carbonate and monoethanolamine solvents for CO_2 capture from post combustion flue gases. *International Journal of Greenhouse Gas Control*, 28:35–44, 2014.

[59] S. Grimme, J. Antony, S. Ehrlich, and H. Krieg. A consistent and accurate ab initio parametrization of density functional dispersion correction (DFT-D) for the 94 elements H-Pu. *The Journal of Chemical Physics*, 132(15):154104, 2010.

[60] S. Grimme, S. Ehrlich, and L. Goerigk. Effect of the damping function in dispersion corrected density functional theory. *Journal of Computational Chemistry*, 32(7):1456–1465, 2011.

[61] T. Gruene, H. W. Hahn, A. V. Luebben, F. Meilleur, and G. M. Sheldrick. Refinement of macromolecular structures against neutron data with *SHELXL2013*. *Journal of Applied Crystallography*, 47(1):462–466, Feb 2014.

[62] W. Grundy, L. Young, J. Stansberry, M. Buie, C. Olkin, and E. Young. Near-infrared spectral monitoring of Triton with IRTF/SpeX II: Spatial distribution and evolution of ices. *Icarus*, 205(2):594 – 604, 2010.

[63] W. M. Grundy, R. P. Binzel, B. J. Buratti, J. C. Cook, D. P. Cruikshank, C. M. Dalle Ore, A. M. Earle, K. Ennico, C. J. A. Howett, A. W. Lunsford, C. B. Olkin, A. H. Parker, S. Philippe, S. Protopapa, E. Quirico, D. C. Reuter, B. Schmitt, K. N. Singer, A. J. Verbiscer, R. A. Beyer, M. W. Buie, A. F. Cheng, D. E. Jennings, I. R. Linscott, J. W. Parker, P. M. Schenk, J. R. Spencer, J. A. Stansberry, S. A. Stern, H. B. Throop, C. C. C. Tsang, H. A. Weaver, G. E. Weigle, and L. A. a. Young. Surface compositions across Pluto and Charon. *Science*, 351(6279), 2016.

[64] M. J. Gutmann. SXD2001. Technical report, ISIS Facility, Rutherford Appleton Laboratory, Oxfordshire, England., 2005.

[65] K. Han, C. K. Ahn, M. S. Lee, C. H. Rhee, J. Y. Kim, and H. D. Chun. Current status and challenges of the ammonia-based CO_2 capture technologies toward commercialization. *International Journal of Greenhouse Gas Control*, 14(0):270 – 281, 2013.

[66] N. Haque, A. Hughes, S. Lim, and C. Vernon. Rare earth elements: Overview of mining, mineralogy, uses, sustainability and environmental impact. *Resources*, 3(4):614–635, 2014.

[67] S. B. Hendricks. The crystal structure of urea and the molecular symmetry of thiourea. *Journal of the American Chemical Society*, 50(9):2455–2464, 1928.

[68] P. Hohenberg and W. Kohn. Inhomogeneous electron gas. *Phys. Rev.*, 136:B864–B871, Nov 1964.

[69] B. Holler, L. Young, M. Buie, W. Grundy, J. Lyke, E. Young, and H. Roe. Measuring temperature and ammonia hydrate ice on Charon in 2015 from Keck/OSIRIS spectra. *Icarus*, 284(Supplement C):394 – 406, 2017.

[70] R. Idem, T. Supap, H. Shi, D. Gelowitz, M. Ball, C. Campbell, and P. Tontiwachwuthikul. Practical experience in post-combustion CO_2 capture using reactive solvents in large pilot and demonstration plants. *International Journal of Greenhouse Gas Control*, 40(supplement):6–25, 2015.

[71] D. Jewitt and J. Luu. Crystalline water ice on the Kuiper belt object (50000) Quaoar. *Nature*, 432(7018):731–733, 2004.

[72] H. Kagi, T. Nagai, K. Komatsu, T. Okada, C. Wada, J. Loveday, and J. Parise. Pressure response on hydrogen bonds in potassium hydrogen carbonate and sodium hydrogen carbonate. *Journal of Neutron Research*, 13(1-3):21–26, 2005.

[73] W. Kaminsky. Wintensor 1.5. http://cad4.cpac.washington.edu/WinTensorhome/WinTensor.htm 2014.

[74] D. A. Keen, M. J. Gutmann, and C. C. Wilson. SXD – the single-crystal diffractometer at the ISIS spallation neutron source. *Journal of Applied Crystallography*, 39(5):714–722, Oct 2006.

[75] M. Khajelakzay, R. Razavi, M. Barekat, M. Naderi, M. Milani, and R. Shoja Razavi. Synthesis of yttria nanopowders by two precipitation methods and investigation of synthesis conditions. *International Journal of Applied Ceramic Technology*, 13(1):209–218, 2016.

[76] S. Klotz, K. Komatsu, H. Kagi, K. Kunc, A. Sano-Furukawa, S. Machida, and T. Hattori. Bulk moduli and equations of state of ice VII and ice VIII. *Phys. Rev. B*, 95:174111, May 2017.

[77] S. Klotz and J. S. Loveday. Rb 10412. ISIS experimental report (POLARIS)., 1999.

[78] W. Kohn and L. J. Sham. Self-consistent equations including exchange and correlation effects. *Phys. Rev.*, 140:A1133–A1138, Nov 1965.

[79] K. Komatsu, H. Kago, Y. Kudoh, T. Nagai, T. Kuribayashi, and J. Parise. Single-crystal X-ray diffraction study of high-pressure phases of $KHCO_3$. *American Mineralogist*, 92(8-9):1270, 2007.

[80] G. Kresse and J. Furthmüller. Efficient iterative schemes for *ab initio* total-energy calculations using a plane-wave basis set. *Phys. Rev. B*, 54:11169–11186, Oct 1996.

[81] G. Kresse and D. Joubert. From ultrasoft pseudopotentials to the projector augmented-wave method. *Phys. Rev. B*, 59:1758–1775, Jan 1999.

[82] N. Kuhn, M. Ströbele, and H.-J. Meyer. Über die identität eines sogenannten ammoniumcarbonat-präparates. *Zeitschrift für anorganische und allgemeine Chemie*, 633(4):653–656, 2007.

[83] S. Kumar, J. Cho, and I. Moon. Ionic liquid-amine blends and CO_2 BOLs: Prospective solvents for natural gas sweetening and CO_2 capture technology - a review. *International Journal of Greenhouse Gas Control*, 20:87–116, 2014.

[84] N. E. T. Laboratory. DOE/NETL advanced carbon dioxide capture R&D program: Technology update. Technical report, U.S. Department of Energy, May 2013.

[85] F. J. Lamelas, Z. A. Dreger, , and Y. M. Gupta. Raman and X-Ray scattering studies of high-pressure phases of urea. *The Journal of Physical Chemistry B*, 109(16):8206–8215, 2005.

[86] R. Lan, J. T. Irvine, and S. Tao. Ammonia and related chemicals as potential indirect hydrogen storage materials. *International Journal of Hydrogen Energy*, 37(2):1482 – 1494, 2012. 10th International Conference on Clean Energy 2010.

[87] A. C. Larson and R. B. Von Dreele. General Structure Analysis System (GSAS). Technical Report 86-748, Los Alamos National Laboratory, 2004.

[88] L. Leiserowitz and A. T. Hagler. The generation of possible crystal structures of primary amides. *Proceedings of the Royal Society A*, 388:133–175, 1983.

[89] K. Lodders. Solar system abundances and condensation temperatures of the elements. *Astrophysical journal*, 591(2):1220–1247, 2003.

[90] A. Lundin, R. G. Ross, and G. Bäckström. Apparatus for equation-of-state measurements. *High Temperature High Pressure*, 26(5):477–496, 1994.

[91] G. Margraf, H.-W. Lerner, M. Bolte, and M. Wagner. Synthese und struktur des ammoniumsesquicarbonat monohydrates $(NH_4)_4[H_2(CO_3)_3]\cdot H_2O$. *Z. Naturforsch*, 58b:511–513, 2003.

[92] G. Marion, J. Kargel, D. Catling, and J. Lunine. Modeling ammonia-ammonium aqueous chemistries in the Solar System's icy bodies. *Icarus*, 220(2):932 – 946, 2012.

[93] M. M. Maroto-Valer, V. Cortes, F. Vega, A. Sanna, B. Navarrete, M. M. Maroto Valer, and V. Cortés. Degradation of amine-based solvents in CO_2 capture process by chemical absorption. *Greenhouse Gases: Science and Technology*, 4(6):707–733, 2014.

[94] W. G. Marshall and D. J. Francis. Attainment of near-hydrostatic compression conditions using the Paris–Edinburgh cell. *Journal of Applied Crystallography*, 35(1):122–125, Feb 2002.

[95] C. P. McKay, T. W. Scattergood, J. B. Pollack, W. J. Borucki, and H. T. V. Ghyseghem. High-temperature shock formation of N_2 and organics on primordial Titan. *Nature*, 332(6164):520–522, 04 1988.

[96] S. Meher, P. Justin, and G. R. Rao. Nanoscale morphology dependent pseudocapacitance of NiO: Influence of intercalating anions during synthesis. *Nanoscale*, 3(2):683–692, 2011.

[97] M. Miao, V. V. Doren, R. Keuleers, H. Desseyn, C. V. Alsenoy, and J. L. Martins. Density functional calculations of the structure of crystalline urea under high pressure. *Chemical Physics Letters*, 316(3):297 – 302, 2000.

[98] H. J. Monkhorst and J. D. Pack. Special points for brillouin-zone integrations. *Phys. Rev. B*, 13:5188–5192, Jun 1976.

[99] R. C. L. Mooney. Crystal structure of ammonium bicarbonate. In *Minutes of the New Orleans Meeting, December 29-30, 1931*, volume 39, pages 861–862. University of Chicago, American Physical Society, 1932.

[100] J. M. Moore, W. B. McKinnon, J. R. Spencer, A. D. Howard, P. M. Schenk, R. A. Beyer, F. Nimmo, K. N. Singer, O. M. Umurhan, O. L. White, S. A. Stern, K. Ennico, C. B. Olkin, H. A. Weaver, L. A. Young, R. P. Binzel, M. W. Buie, B. J. Buratti, A. F. Cheng, D. P. Cruikshank, W. M. Grundy, I. R. Linscott, H. J. Reitsema, D. C. Reuter, M. R. Showalter, V. J. Bray, C. L. Chavez, C. J. A. Howett, T. R. Lauer, C. M. Lisse, A. H. Parker, S. B. Porter, S. J. Robbins, K. Runyon, T. Stryk, H. B. Throop, C. C. C. Tsang, A. J. Verbiscer, A. M. Zangari, A. L. Chaikin, and D. E. a. Wilhelms. The geology of Pluto and Charon through the eyes of New Horizons. *Science*, 351(6279):1284–1293, 2016.

[101] K. Mumford, K. Smith, C. Anderson, S. Shen, W. Tao, Y. Suryaputradinata, D. Quyn, A. Qader, B. Hooper, R. Innocenzi, S. Kentish, and G. Stevens. Post-combustion capture of CO_2: Results from the solvent absorption capture plant at Hazelwood Power Station using potassium carbonate solvent. *Energy & Fuels*, 26(10):6449–6449, 2012.

[102] K. Mumford, Y. Wu, K. Smith, and G. Stevens. Review of solvent based carbon-dioxide capture technologies. *Frontiers of Chemical Science and Engineering*, 9(2):125–141, 2015.

[103] F. D. Murnaghan. The compressibility of media under extreme pressures. *Proceedings of the National Academy of Sciences*, 30(9):244–247, 1944.

[104] H. B. Niemann, S. K. Atreya, J. E. Demick, D. Gautier, J. A. Haberman, D. N. Harpold, W. T. Kasprzak, J. I. Lunine, T. C. Owen, and F. Raulin. Composi-

tion of Titan's lower atmosphere and simple surface volatiles as measured by the Cassini-Huygens probe gas chromatograph mass spectrometer experiment. *Journal of Geophysical Research: Planets*, 115(E12), 2010. E12006.

[105] F. C. T. Office. Hydrogen storage. In *Multi-Year Research, Development, and Demonstration Plan*, chapter 3.3. U.S. Department of Energy, 2015.

[106] A. Olejniczak, K. Ostrowska, and A. Katrusiak. H-bond breaking in high-pressure urea. *The Journal of Physical Chemistry C*, 113(35):15761–15767, 09 2009.

[107] C. Pak, H. M. Lee, J. C. Kim, D. Kim, and K. S. Kim. Theoretical investigation of normal to strong hydrogen bonds. *Structural Chemistry*, 16(3):187–202, 2005.

[108] C. Palache, H. Berman, and C. Frondel. *The System of Mineralogy of James Dwight Dana and Edward Salisbury Dana, Yale University 1937-1892*, volume II. J. Wiley & sons, 1892.

[109] H. Palme, K. Lodders, and A. Jones. 2.2 - Solar System Abundances of the Elements. In H. D. Holland and K. K. Turekian, editors, *Treatise on Geochemistry*, pages 15 – 36. Elsevier, Oxford, second edition, 2014.

[110] J. P. Perdew, K. Burke, and M. Ernzerhof. Generalized gradient approximation made simple. *Phys. Rev. Lett.*, 77:3865–3868, Oct 1996.

[111] F. Pertlik. Refinement of the crystal structure of teschemacherite, $NH_4CO_2(OH)$. *Tschermaks mineralogische und petrographische Mitteilungen*, 29(2):67–74, 1981.

[112] T. L. Phipson. XII.-Note on the bicarbonate of ammonia of the Chinca isles. *J. Chem. Soc.*, 16:74–76, 1863.

[113] J. C. Poggendorff. *Annalen der Physik und Chemie*, volume 46 of *1*, chapter Third Piece: I. On the Connections of Ammonia with Carbonic Acid; by Heinrich Rose., pages 353–411. J.A. Barth., 1839.

[114] P. Pruzan, J. C. Chervin, E. Wolanin, B. Canny, M. Gauthier, and M. Hanfland. Phase diagram of ice in the VII-VIII-X domain. vibrational and structural data for strongly compressed ice VIII. *Journal of Raman Spectroscopy*, 34:591–610, 2003.

[115] Y. Qiao, K. Wang, H. Yuan, K. Yang, and B. Zou. Negative linear compressibility in organic mineral ammonium oxalate monohydrate with hydrogen bonding wine-rack motifs. *The Journal of Physical Chemistry Letters*, 6(14):2755–2760, 2015.

[116] L. C. Quick, D. L. Buczkowski, O. Ruesch, J. E. Scully, J. Castillo-Rogez, C. A. Raymond, P. M. Schenk, H. G. Sizemore, and M. V. Sykes. A possible brine reservoir beneath Occator crater: Thermal and compositional evolution and formation of the Cerealia Dome and Vinalia Faculae. *Icarus*, 2018.

[117] M. Rabensteiner, G. Kinger, M. Koller, G. Gronald, S. Unterberger, and C. Hochenauer. Investigation of the suitability of aqueous sodium glycinate as a solvent for post combustion carbon dioxide capture on the basis of pilot plant studies and screening methods. *International Journal of Greenhouse Gas Control*, 29:1–15, 2014.

[118] N. Radenahmad, A. Afif, P. I. Petra, S. M. Rahman, S.-G. Eriksson, and A. K. Azad. Proton-conducting electrolytes for direct methanol and direct urea fuel cells – a state-of-the-art review. *Renewable and Sustainable Energy Reviews*, 57:1347 – 1358, 2016.

[119] A. Raponi, M. D. Sanctis, F. Carrozzo, M. Ciarniello, J. Castillo-Rogez, E. Ammannito, A. Frigeri, A. Longobardo, E. Palomba, F. Tosi, F. Zambon, C. Raymond, and C. Russell. Mineralogy of Occator crater on Ceres and insight into its evolution from the properties of carbonates, phyllosilicates, and chlorides. *Icarus*, 2018.

[120] A. Reynolds, T. V. Verheyen, S. Adeloju, E. Meuleman, and P. Feron. Towards commercial scale postcombustion capture of CO_2 with monoethanolamine solvent: Key considerations for solvent management and environmental impacts. *Environmental Science & Technology*, 46(7):3643–3654, 2012.

[121] A. Rollinson, J. Jones, V. Dupont, and M. Twigg. Urea as a hydrogen carrier: a perspective on its potential for safe, sustainable and long-term energy supply. *Energy & Environmental Science*, 4(4):1216–1224, 2011.

[122] K. Röttger, A. Endriss, J. Ihringer, S. Doyle, and W. F. Kuhs. Lattice constants and thermal expansion of H_2O and D_2O ice I*h* between 10 and 265 K. *Acta Crystallographica Section B*, 50(6):644–648, Dec 1994.

[123] H. Sainte-Claire Deville. *Memoire sur la forme et la composition des carbonates ammoniacaux*, volume 40, pages 87–98. Crochard (Paris), V. Masson (Paris), 1854.

[124] S. Salentinig, P. Jackson, and M. Attalla. Strategic vapor suppressing additives for ammonia based CO_2 capture solvent. *Energy Procedia*, 37:241–246, 2013.

[125] V. N. Salinas, M. R. Hogerheijde, E. A. Bergin, L. Ilsedore Cleeves, C. Brinch, G. A. Blake, D. C. Lis, G. J. Melnick, O. Panić, J. C. Pearson, L. Kristensen, U. A. Yldz, and E. F. van Dishoeck. First detection of gas-phase ammonia in a planet-forming disk - NH_3, N_2H^+, and H_2O in the disk around TW Hydrae. *A&A*, 591:A122, 2016.

[126] E. L. Schaller and M. E. Brown. Detection of methane on Kuiper Belt Object (50000) Quaoar. *The Astrophysical Journal Letters*, 670(1):L49, 2007.

[127] K. R. Schwarz and E. A. Bergin. The effects of initial abundances on nitrogen in protoplanetary disks. *The Astrophysical Journal*, 797(2):113, 2014.

[128] C. Sclar and L. Carrison. Phase composition of commercial ammonium carbonate. *Science*, 140(357):1205, 1963.

[129] G. M. Sheldrick. A short history of SHELX. *Acta Crystallographica Section A*, 64(1):112–122, Jan 2008.

[130] S. Sikka and S. M. Sharma. The hydrogen bond under pressure. *Phase Transitions*, 81(10):907–934, 2008.

[131] R. Sims, R. Schaeffer, F. Creutzig, X. Cruz-Núñez, M. D'Agosto, D. Dimitriu, M. J. Figueroa Meza, L. Fulton, S. Kobayashi, O. Lah, A. McKinnon, P. Newman, M. Ouyang, J. J. Schauer, D. Sperling, and G. Tiwari. Contribution of Working Group III to the Fifth Assessment Report of the Intergovernmental Panel on Climate Change. In O. Edenhofer, R. Pichs-Madruga, Y. Sokona, E. Farahani, S. Kadner, K. Seyboth, A. Adler, I. Baum, S. Brunner, P. Eickemeier, B. Kriemann, J. Savolainen, S. Schlömer, C. von Stetchow, T. Zwickel, and J. C. Minx, editors, *Climate Change 2014: Mitigation of Climate Change.*, chapter Transport. Cambridge University Press, Cambridge, United Kingdom and New York, NY, USA, 2014.

[132] A. Sodiq, A. Rayer, A. Olanrewaju, and A. A. Olanrewaju. Reaction kinetics of carbon dioxide (CO_2) absorption in sodium salts of taurine and proline using a stopped-flow technique. *International Journal of Chemical Kinetics*, 46(12):730–745, 2014.

[133] V. Štengl, S. Bakardjieva, and N. Murafa. Preparation and photocatalytic activity of rare earth doped TiO_2 nanoparticles. *Materials chemistry and physics*, 114(1):217–226, 2009.

[134] J. Ŝubrt. Homogeneous precipitcation with urea - versatile way to metal oxide nanoparticles. In C. M. Muñoz and A. M. Fernández, editors, *Urea: Synthesis, properties and uses*, number ISBN 978-1-62257-061-4 in 1, pages 109–148. Nova Science Publishers, 2012.

[135] S. Swaminathan, B. M. Craven, and R. K. McMullan. The crystal structure and molecular thermal motion of urea at 12, 60 and 123 K from neutron diffraction. *Acta Crystallographica Section B*, 40(3):300–306, Jun 1984.

[136] E. Teschemacher. Lxxxiv. an account of various substances found in the guano deposits and in their vicinity. *Philosophical Magazine*, 28(190):546–550, 1846.

[137] E. C. Thomas, T. H. Vu, R. Hodyss, P. V. Johnson, and M. Choukroun. Kinetic effect on the freezing of ammonium-sodium-carbonate-chloride brines and implications for the origin of ceres' bright spots. *Icarus*, 2017.

[138] B. H. Toby. *EXPGUI*, a graphical user interface for *GSAS*. *Journal of Applied Crystallography*, 34(2):210–213, Apr 2001.

[139] D. E. Trilling. The surface age of Sputnik Planum, Pluto, must be less than 10 million years. *PLoS ONE*, 11(1):1–5, 01 2016.

[140] J. S. Tse and D. D. Klug. Anomalous isostructural transformation in ice VIII. *Phys. Rev. Lett.*, 81:2466–2469, Sep 1998.

[141] G. L. Ulex. Ueber naturliches zweifach-kohlensaures ammoniak. *Ann. Chim*, 66:44–45, 1848.

[142] A. Verbiscer, D. Peterson, M. Skrutskie, M. Cushing, P. Helfenstein, M. Nelson, J. D. Smith, and J. Wilson. Near-infrared spectra of the leading and trailing hemispheres of Enceladus. *Icarus*, 182(1):211–223, 2006.

[143] R. B. Von Dreele. *X-ray and Neutron Crystallography*. Government Printing Office, 1990.

[144] J. H. Waite, M. Combi, W.-H. Ip, T. Cravens, R. McNutt, W. Kasprzak, R. Yelle, J. Luhmann, H. Niemann, D. Gell, B. Magee, G. Fletcher, J. Lunine, and W.-L. Tseng. Cassini Ion and Neutral Mass Spectrometer: Enceladus Plume Composition and Structure. *Science*, 311(5766):1419–1422, 2006.

[145] J. H. Waite, C. R. Glein, R. S. Perryman, B. D. Teolis, B. A. Magee, G. Miller, J. Grimes, M. E. Perry, K. E. Miller, A. Bouquet, J. I. Lunine, T. Brockwell, and S. J. Bolton. Cassini finds molecular hydrogen in the enceladus plume: Evidence for hydrothermal processes. *Science*, 356(6334):155–159, 2017.

[146] D. Wallace. *Thermodynamics of Crystals*. Dover books on physics. Dover Publications, 1998.

[147] W. Wang, A. D. Fortes, D. P. Dobson, C. M. Howard, J. Bowles, N. J. Hughes, and I. G. Wood. Investigation of high-pressure planetary ices by cryo-recovery. II. High-pressure apparatus, examples and a new high-pressure phase of $MgSO_4{\cdot}5H_2O$. *Journal of Applied Crystallography*, 51(3):692–705, Jun 2018.

[148] H. P. Weber, W. G. Marshall, and V. Dmitriev. High-pressure polymorphism in deuterated urea. *Acta Crystallographica Section A*, 58(s1):C174, Aug 2002.

[149] C.-C. Wei, G. Puxty, and P. Feron. Amino acid salts for CO_2 capture at flue gas temperatures. *Chemical Engineering Science*, 107:218–226, 2014.

[150] C. C. Wilson, P. F. Henry, M. Schmidtmann, V. P. Ting, E. Williams, and M. T. Weller. Neutron powder diffraction – new opportunities in hydrogen location in molecular and materials structure. *Crystallography Reviews*, 20(3):162–206, 2014.

[151] I. G. Wood, A. D. Fortes, D. P. Dobson, W. Wang, L. Pajdzik, and J. Cosier. Investigation of high-pressure planetary ices by cryo-recovery. I. An apparatus for X-ray powder diffraction from 40 to 315 K, allowing 'cold loading' of samples. *Journal of Applied Crystallography*, 51(3):685–691, Jun 2018.

[152] H. Yamawaki, H. Fujihisa, M. Sakashita, A. Nakayama, and K. Aoki. Powder X-ray diffraction study of the volume change of ice VIII under high pressure. *Physica B: Condensed Matter*, 344(1):260 – 264, 2004.

[153] S. Yan, Q. He, S. Zhao, H. Zhai, M. Cao, and P. Ai. CO_2 removal from biogas by using green amino acid salts: Performance evaluation. *Fuel Processing Technology*, 129:203–212, 2015.

[154] N. Yang, H. Yu, L. Li, D. Xu, W. Han, and P. Feron. Aqueous ammonia (NH_3) based post combustion CO_2 capture: A review. *Oil & Gas Science and Technology*, 69(5):931–945, 2014.

[155] Z.-Z. Yang, Y.-N. Zhao, and L.-N. He. CO_2 chemistry: task-specific ionic liquids for CO_2 capture/activation and subsequent conversion. *RSC Advances*, 1(4):545–567, 2011.

[156] A. Yoshihara and E. R. Bernstein. Brillouin and rayleigh studies of urea single crystals. *The Journal of Chemical Physics*, 77(11):5319–5326, 1982.

[157] H. Yu, S. Morgan, A. Allport, A. Cottrell, T. Do, J. McGregor, L. Wardhaugh, and P. Feron. Results from trialling aqueous NH_3 based post-combustion capture

in a pilot plant at Munmorah power station: Absorption. *Chemical Engineering Research and Design*, 89(8):1204–1215, 2011.

[158] H. Yu, Q. Xiang, M. Fang, Q. Yang, and P. Feron. Promoted CO_2 absorption in aqueous ammonia. *Greenhouse Gases: Science and Technology*, 2(3):200–208, 2012.

[159] Q. Zhuang, B. Clements, and Y. Li. From ammonium bicarbonate fertilizer production process to power plant CO_2 capture. *International Journal of Greenhouse Gas Control*, 10:56–63, 2012.

[160] A. Züttel, A. Remhof, A. Borgschulte, and O. Friedrichs. Hydrogen: the future energy carrier. *Philosophical Transactions of the Royal Society A*, 368(1923):3329–3342, June 2010.